Interactions and Assemblies of Polymeric Materials and Colloidal Nanocrystals

by

Teresa Elaine Williams

A dissertation submitted in partial satisfaction of the

requirements for the degree of

Doctor of Philosophy

in

Engineering – Applied Science and Technology

in the

Graduate Division

of the

University of California, Berkeley

Committee in charge:

Doctor Brett A. Helms, Co-Chair

Professor Ting Xu, Co-Chair

Professor Ronald Gronsky

Professor Matthew B. Francis

Spring 2017

Interactions and Assemblies of Polymeric Materials and Colloidal Nanocrystals

by

Teresa Elaine Williams

Abstract

Interactions and Assemblies of Polymeric Materials and Colloidal Nanocrystals

by

Teresa Elaine Williams

Doctor of Philosophy in Engineering – Applied Science and Technology

University of California, Berkeley

Doctor Brett A. Helms, Co-Chair

Professor Ting Xu, Co-Chair

Our need to reduce global energy use is well known and without question, not just from an economic standpoint but also to decrease human impact on climate change. Emerging advances in this area result from the ability to tailor-make materials and energy-saving devices using solution–phase chemistry and deposition techniques. Colloidally synthesized nanocrystals, with their tunable size, shape, and composition, and unusual optical and electronic properties, are leading candidates in these efforts. Because of recent advances in colloidal chemistries, the inventory of monodisperse nanocrystals has expanded to now include metals, semiconductors, magnetic materials, and dielectric materials. For a variety of applications, an active layer composed of a thin film of randomly close-packed nanocrystals is not ideal for optimized device performance; here, the ability to arrange these nano building units into mesoporous (2 nm < d < 50 nm) architectures is highly desirable. Given this, the goal of the work in this dissertation is to determine and understand the design rules that govern the interactions between ligand-stripped nanocrystals and polymeric materials, leading to their hierarchical assembly into colloidal nanocrystal frameworks. I also include the development of quantitative, and novel, characterization techniques, and the application of such frameworks in energy efficiency devices such as electrochromic windows.

Understanding the local environment of nanocrystal surfaces and their interaction with surrounding media is vital to their controlled assembly into higher-order structures. Though work has continued in this field for over a decade, researchers have yet to provide a simple and straightforward procedure to scale across nanoscale material systems and applications allowing for synthetic and structural tunability and quantitative characterization. In this dissertation, I have synthesized a new class of amphiphilic block copolymer architecture-directing agents based upon poly(dimethylacrylamide)-*b*-poly(styrene) (PDMA-*b*-PS), which are strategically designed to enhance the interaction between the hydrophilic PDMA block and ligand-stripped nanocrystals. As a result, stable assemblies are produced which, following solution deposition and removal of the block copolymer template, renders a mesoporous framework. Leveraging the use of this sacrificial block copolymer allows for the formation of highly tunable structures, where

control over multiple length scales (e.g., pore size, film thickness) is achieved through the judicious selection of the two building blocks. I also combine X-ray scattering, electron imaging, and image analysis as novel quantitative analysis techniques for the physical characterization of the frameworks.

Last, I demonstrate the applicability of these porous frameworks as platforms for chemical transformation and energy efficiency devices. Examining the active layer in an electrochromic window, I show a direct comparison between, and improved performance for, devices built from both randomly close-packed nanocrystals and those arranged in mesoporous framework architectures. I show that the framework also serves as a scaffold for in-filling with a second active material, rendering a dual–mode electrochromic device. These results imply that there may exist a broad application space for these techniques in the development of ordered composite architectures.

Be yourself; everyone else is already taken.

–Oscar Wilde

Table of Contents

List of Acronyms and Symbols

ADA(s)	architecture-directing agent(s)
ATRP	atom-transfer radical polymerization
BCP(s)	block copolymer(s)
BF	bright-field
BTU	British thermal units
CE	coloration efficiency
cmc	critical micelle concentration
CNF(s)	colloidal nanocrystal framework(s)
CRP	controlled/living radical polymerization
CTA	chain transfer agent
CV	cyclic voltammetry
D_h	hydrodynamic radius
DLS	dynamic light scattering
DMP	dodecylsulfanylthiocarbonylsulfanyl-2-methylpropionic acid
D_t	diffusion coefficient
EDL(s)	electrical double layer(s)
EDS	Energy-Dispersive X-ray spectroscopy
EP	ellipsometric porosimetry
FITC	fluorescein
FT-IR	Fourier transform infrared spectroscopy
FTO	fluorine-doped tin oxide
GISAXS	grazing-incidence small angle X-ray scattering
HATR	Horizontal Attenuated Total Reflectance
ICDD–PDF	International Center for Diffraction Data–Powder Diffraction File
ICP–OES	inductively coupled plasma–optical emission spectroscopy
l_0	micelle coronal width
LSPR	localized surface plasmon resonance
M_n	number average molecular weight
M_w	weight average molecular weight
MWCO	molecular weight cutoff
N	degree of polymerization
$n \sin \alpha$	numerical aperture
NC(s)	nanocrystal(s)
NIR	Near-infrared
NMP	nitroxide-mediated polymerization
NMR	nuclear magnetic resonance
NP	nanoparticle
ODT	order-disorder transition
PDI	polydispersity index
PDMA-*b*-PS	poly(dimethylacrylamide)-*b*-poly(styrene)
PLQY	photoluminescence quantum yield
POM	polyoxometalate
PPE	plasticized polymer electrolyte
R_0	root-mean-squared end-to-end distance

RAFT	reversible addition–fragmentation chain transfer
RBS	Rutherford Backscattering
R_c	micelle core radius
R_g	radius of gyration
R_h	hydrodynamic radius
R_m	micelle radius
$\mathrm{S}(q)$	structure factor
SAD	selected-area diffraction
SAXS	small angle X-ray scattering
SEC	size exclusion chromatography
SEM	scanning electron microscopy
T	transmittance
TEM	transmission electron microscopy
TGA	thermogravimetric analysis
UV	Ultraviolet
UV-Vis-NIR	Ultraviolet-Visible Near-infrared
Vis	Visible
XRD	X-ray diffraction
Z	aggregation number
$\mathit{\Delta}$	phase difference
η	viscosity
τ	time constant
χ	Flory-Huggins interaction parameter
$\mathit{\Psi}$	amplitude ratio

Acknowledgements

I dedicate this dissertation to Betty Jane Williams, my grandmother, for blazing the path; she did things that no one ever expected her to do and set the example. This journey would never have begun, nor would I have achieved success as a graduate student, without the support and encouragement of my mentor, Dr. Brett Helms. His patience was crucial as I held dual roles as graduate student and full-time Foundry staff. It's been an honor working together; we will forever be bonded by friendship and science, and for that I am truly grateful.

Many thanks also to Professor Ting Xu for helping me find my way to the Applied Science and Technology program as well as all of her support, guidance and navigation throughout the program. I also want to thank Professor Ron Gronsky for always being there to listen, offer advice, and keep me on track during the most challenging times. I am grateful to Professor David Attwood for encouraging me to step up and do things that are hard. I want to thank Professor Matt Francis for being a wonderful role model and leader while acting as interim director of the Organic facility; his critical feedback of my performance and ability to mediate difficult situations made a huge difference during a much-needed time. These professors have supported me on my preliminary exam, qualifying exam, and dissertation committee and have provided mentorship to help me develop into the scientist that I have become. I will continue to grow and learn and make them proud!

The support of the Tuition Assistance Program at Lawrence Berkeley National Lab made this dream a reality; I thank Dr. Jeffrey Neaton for the support. I also must thank Dr. Frantisek (Frank) Svec, Professor Rachel Segalman, and Professor Daryl Chrzan for filling many roles as advisors, mentors, advice-givers, and listeners. Thank you for caring about me and helping me achieve my goals. I will always remember Frank's statement: "you are never too old to learn."

Graduate school has brought some amazing women into my life and, along with it, a wonderful network of friends and colleagues whom I want to honor and acknowledge: I am indebted to Virginia for sharing her skills, being patient, and training me as an electron microscopist; many thanks to Mahati and Hilda whose support and energy were so needed during my first semester as a graduate student; much love to Evie, my dear friendo and partner in crime/dancing; gratitude to Delia for her collaboration and being a strong role model as a woman in science; huge hugs to Laleh for telling my story; warm regards to dear colleagues Cindy, Gordana, Caroline, Deirdre, Tracy, and Karen for being there for me. I am truly grateful to Sibel for being my mentor, for telling me it's ok to ask for help, and getting me through Solid State Physics; her support, advice, and friendship made the difference at EVERY point when I was struggling to stay afloat. And though not women, to fellow Helms group members Andy, Pete F., and Steve, thank you for your friendship, kindness and collaboration.

Finally, I want to recognize two very special people with whom I have shared so much over the last six years. Wendy, your friendship brings joy and growth into my life every day. You help keep me present and honest with others and myself. To my Starbuck: all the twists and turns along the way have been a gift and made us stronger. You bring out the best in me, including my spirit and passion for living, learning and loving. As this chapter comes to a close and the next one begins I can’t imagine sharing the journey with anyone other than you. I love you, David.

Introduction

Chapter 1

Motivation

The need to reduce global energy use is well known and without question, not just from an economic standpoint, but also to decrease human impact on global warming. The United States (U. S.) Energy Information Administration (EIA) reported in 2015 that ~40% of total U.S. energy consumption was in residential and commercial buildings; this amounts to 39 quadrillion British thermal units (BTU),[1] with commercial buildings accounting for 18 quadrillion BTU.[2] In commercial buildings, this energy use is primarily in the form of HVAC (heating, ventilation, air conditioning) and lighting (Figure 1.1). Given this, one potential area that could offer large energy savings is in the adoption of energy efficient windows into commercial buildings. Windows are ubiquitous; they allow for natural light into a space and, often, allow occupants to enjoy the view outside. Unfortunately, as the sun moves throughout the day, its changing position often accompanies the need to draw shades and turn on lights, and perhaps even use HVAC to regulate the solar heat gain within the space. Electrochromic windows have the ability to control how much of the sun's heat and light enter through the window, ideally with independent and tunable control over each. A 2004 report projected that 40% market penetration of electrochromic window technology, with daylighting controls, would save approximately 91.5–97.3 10^{12} BTU in the year 2030 compared to a typical spectrally selective low-E window with manually-controlled interior shades and no daylighting controls.[3]

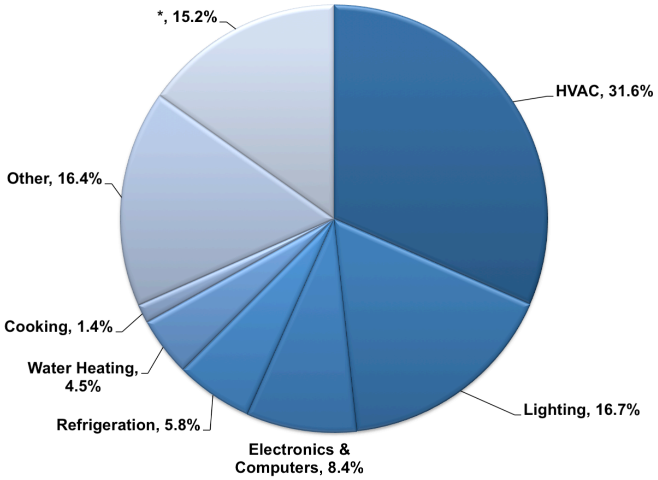

Figure 1.1. Commercial energy end-use splits for 2015. Note: 'Other' includes service station equipment, ATMs, telecommunications equipment, medical equipment, pumps, emergency electric generators, combined heat and power in commercial buildings, and manufacturing performed in commercial buildings; '*' indicates an energy adjustment EIA uses to relieve discrepancies between data sources. Chart produced from data presented in reference 2.

In the design, the window is an electrochemical cell in which two conducting glass panes are separated by a solid electrolyte material. The electrochromic active layer is an electrode composed of a conductive metal oxide nanocrystal film, deposited on one pane, with a counter electrode deposited on the other pane. In one design, and depending on the choice of material, voltage bias switches the window from near-infrared (NIR)-

transmitting to NIR-blocking states, with power required only to make the switch (typically less than 1 W needed) (Figure 1.2a,b). The device could also be designed with dual-mode function, with the active layer composed of two distinct materials in a composite, and the second material providing tunability for the visible (Vis) spectrum, thereby blocking light (Figure 1.2c).

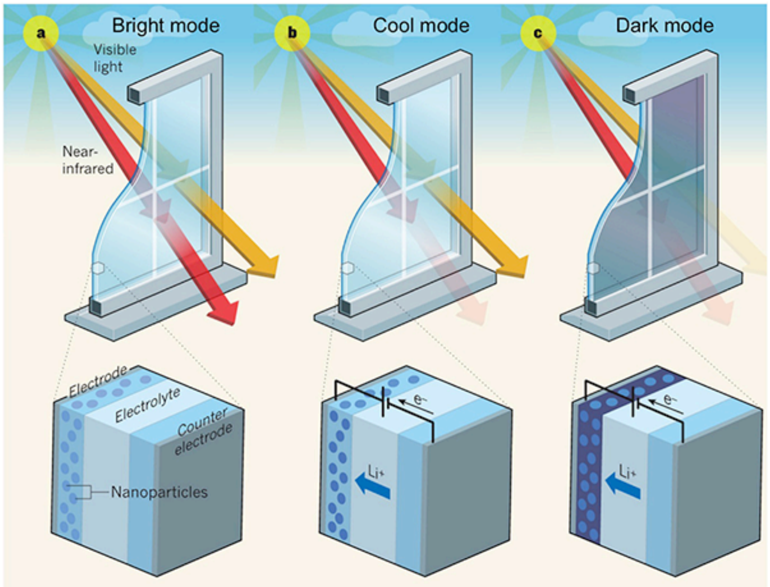

Figure 1.2. Illustration of a dual-mode electrochromic window that controllably and selectively absorbs near-infrared light (heat) and visible light: (a) depicts ‘Bright mode’, in which the window is transparent to both near-infrared light and visible light; (b) depicts ‘Cool mode’ where the active material blocks most incoming near-infrared light upon application of an intermediate voltage; (c) depicts ‘Dark mode’ where, at lower voltages, if present, a second active material blocks most incoming visible light. Image adapted from reference 4.

Without the application of an electrical load, the window is transparent to Vis and NIR light (Figure 1.2a). When an intermediate voltage is applied, charge carriers (lithium ions, Li^+, and electrons, e^-) move through the circuit. The nanocrystal active layer in the composite is chemically reduced, thereby blocking most incoming near-infrared light (Figure 1.2b). The second, Vis-active compound can also then become reduced at lower voltages and block most incoming visible light. The choice of the active materials is key in order to tailor the device properties to provide dual-mode functionality.

The active layer electrode in Figure 1.2 is depicted as a thin film of randomly close-packed nanocrystals. Though this type of architecture is valuable for a variety of applications, recent work shows it may not to be ideal for optimized device performance.[5] Rather, the ability to arrange these nano building units into mesoporous (2 nm < d < 50 nm) framework architectures is highly desirable to improve ion or mass transport (Figure 1.3) throughout the thickness of the electrode. Here, as the charging process is capacitive, it was shown that the ability to reduce the overlap of the electrical double layer is advantageous to improve charging kinetics and overall capacity.[6,7]

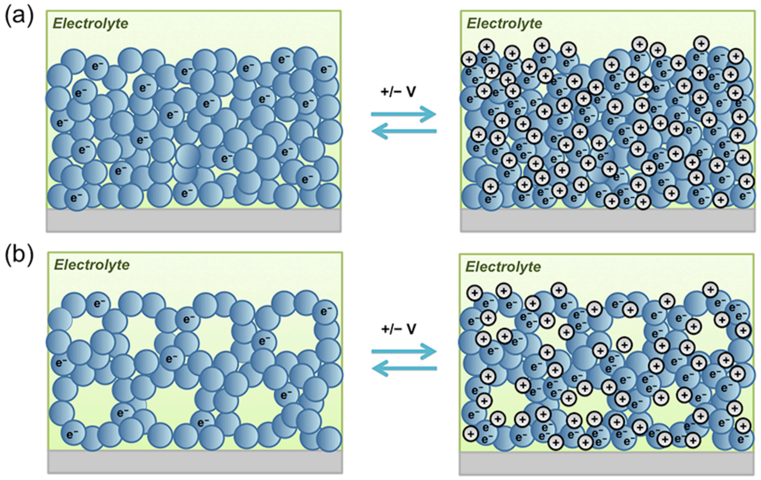

Figure 1.3. Depiction of charged and uncharged states for an electrode composed of: (a) randomly close-packed nanocrystals; (b) mesoporous nanocrystal framework.

My research interests are based on the hypothesis that templating agents can direct the assembly of nanocrystals into such porous structures; moreover, these templates can be hard (i.e. siliceous colloids, sacrificial porous inorganics[8,9]) or soft (i.e. surfactant or polymeric[10,11]). In either case, a physical or chemical removal post-assembly is required to reveal the framework's porous architecture. In the case of soft templating agents, such as block copolymers, when combined with nanocrystals it is vital to understand the local environment of the nanocrystal's surface and its interaction with the polymer templating agent to exert control over their assembly into higher-order structures. Though work has been ongoing in this field for over a decade, a simple and straightforward procedure to scale across materials systems and applications allowing for synthetic and structural tunability and quantitative analysis has not yet been determined.

The goal of the work presented in this dissertation is to understand the design rules that govern the interactions between bare nanocrystal surfaces and polymeric materials. This leads to the hierarchical assembly of nanocrystals with block copolymer architecture-directing agents into colloidal nanocrystal frameworks; quantitative characterization techniques of both the assemblies and the frameworks are presented, as well as their application in electrochromic windows. Recent advances in this area are driven by the development of techniques to tailor-make materials and devices using solution phase chemistry and deposition techniques. Colloidally-synthesized nanocrystals, with their tunable size, shape, and composition, as well as interesting optical and electronic properties, are leading in these efforts.

In this work, I first investigated how functionalized polyacrylic acid interacts with the surface of a variety of ligand-stripped colloidal nanocrystals, thereby rendering them dispersible in aqueous media. As typical inorganic nanomaterials are hydrophobic in nature, this technique allows these assemblies to find use in a range of biological applications, such as drug delivery or bioimaging.[12–14] Next, as these results led to the investigation of how to further enhance interactions and impart functionality between polymers and nanocrystals, I designed and synthesized a new class of block copolymer architecture-directing agents based upon poly(dimethylacrylamide)-*b*-poly(styrene), PDMA-*b*-PS. As a result of the enhanced interaction between PDMA-*b*-PS and ligand-stripped colloidal nanocrystals, stable assemblies were produced which, following solution deposition and removal of the block copolymer template, afforded a mesoporous nanocrystal framework. Leveraging the use of this sacrificial block copolymer allowed for the formation of highly tunable structures, where control over multiple length scales (e.g., pore size, film thickness) was achieved through polymer synthesis techniques and choice of nanocrystal. I developed quantitative analysis techniques for the physical characterization of the frameworks through the use of X-ray scattering and electron imaging, combined with image analysis. Thus, the first part of my dissertation is focused on the development and characterization of these materials.

As the choice of nanocrystal drives the ability to impart functionality in the framework, the focus of the second part of my dissertation is in their application as a platform for chemical transformation as well as energy efficiency devices. By applying a tin-doped indium oxide nanocrystal framework as the active layer in an electrochromic window, I designed experiments to understand the differences in performance for devices built from both randomly close-packed nanocrystals and those arranged in mesoporous framework architectures. I also investigated the use of the framework to serve as a scaffold for in-filling with a second active material, rendering the design for a dual-mode electrochromic device. These results imply that there may exist a broad application space for these techniques in the development of ordered composite architectures.

This dissertation is organized into chapters meant to distinguish the background information from various experimental works focused on understanding polymer–nanocrystal interactions and their subsequent assemblies and characterization, and finally their potential applications. Chapters 2–4 serve as an introduction describing the nanocrystal and polymeric materials of interest, block copolymer–nanocrystal assembly, and an overview of the characterization techniques utilized in my experimental work, respectively. The subsequent sections contain my scientific output. Chapters 5 and 6 investigate the interaction of different polymeric materials with nanocrystal surfaces. A thorough assessment of their assembly properties is presented in Chapters 7 and 8, from a scattering perspective as well as image analysis of electron micrographs. The last section, Chapters 9–11, is focused on investigating the application of mesoporous colloidal nanocrystal frameworks as both a platform for chemical transformation and their use in electrochromic devices. All of the scientific output chapters represent a published, peer-reviewed article or a manuscript for publication of which I am one of the main authors. Finally, a conclusion chapter summarizes my results.

References

1. Department of Energy, 2015 Buildings Energy Data Book, Section 1.1.5, 2015. http://buildingsdatabook.eren.doe.gov/docs/xls_pdf/1.1.5.pdf
2. Department of Energy, 2015 Buildings Energy Data Book, Section 3.1.5, 2015. http://buildingsdatabook.eren.doe.gov/docs/xls_pdf/3.1.5.pdf
3. Lee, E. S.; Yazdanian, M.; Selkowitz, S. S. B.E. 2004. LBL-54966, Lawrence Berkeley National Laboratory, Berkeley, California.
4. Korgel, B. A. "Materials science: Composite for smarter windows" *Nature* **2013**, *500*, 278–279.
5. Minakshi, M.; Appadoo, D.; Martin, D. E. "The Anodic Behavior of Planar and Porous Zinc Electrodes in Alkaline Electrolyte" *Electrochemical and Solid-State Lett.* **2010**, *13*, A77–A80.
6. Largeot, C.; Portet, C.; Chmiola, J.; Taberna, P.-L.; Gogotsi, Y.; Simon, P. "Relation between the Ion Size and Pore Size for an Electric Double-Layer Capacitor" *J. Am. Chem. Soc.* **2008**, *130*, 2730–2731.
7. Brezesinski, T.; Wang, J.; Polleux, J.; Dunn, B.; Tolbert, S. H "Templated Nanocrystal-Based Porous TiO_2 Films for Next-Generation Electrochemical Capacitors" *J. Am. Chem. Soc.* **2009**, *131*, 1802–1809.
8. Yang, H.; Zhao, D. "Synthesis of replica mesostructures by the nanocasting strategy" *J. Mater. Chem*. **2005**, *15*, 1217–1231.
9. Lu, A.-H.; Schüth, F. "Nanocasting: A Versatile Strategy for Creating Nanostructured Porous Materials" *Adv. Mater*. **2006**, *18*, 1793–1805.
10. Blin, J. L., Léonard, A., Yuan, Z. Y., Gigot, L., Vantomme, A., Cheetham, A. K., & Su, B. L. "Hierarchically Mesoporous/Macroporous Metal Oxides Templated from Polyethylene Oxide Surfactant Assemblies" *Angew. Chem*. **2003**, *115*, 2978 –2981.
11. Warren, S. C.; Messina, L. C.; Slaughter, L. S.; Kamperman, M.; Zhou, Q.; Gruner, S. M.; DiSalvo, F. J.; Wiesner, U. *Science* **2008**, *320*, 1748–1752.
12. Kim, J.; Kim, H.-S.; Lee, N.; Kim, T.; Kim, H.; Yu, T.; Song, I.-C.; Moon, W.-K.; Hyeon, T. "Multifunctional uniform nanoparticles composed of a magnetite nanocrystal core and a mesoporous silica shell for magnetic resonance and fluorescence imaging and for drug delivery" *Angew. Chem. Int. Ed*. **2008**, *47*, 8438–8441.
13. Liu, G. L.; Yin, Y.; Kunchakarra, S.; Mukherjee, B.; Gerion, D.; Jett, S. D.; Bear, D. G.; Gray, J. W.; Alivisatos, A. P.; Lee, L. P.; Chen, F. F. "A nanoplasmonic molecular ruler for measuring nuclease activity and DNA footprinting" *Nat. Nanotechnol.* **2006**, *1*, 47–52.
14. Norris, D. J.; Efros, A. L.; Erwin, S. C. "Doped nanocrystals" *Science* **2008**, *319*, 1776–1779.

Chapter 2

Components of interest: colloidal nanocrystals and polymeric materials

Colloidal nanocrystals have been proposed as functional building units for preparing mesostructured materials,[1] and block copolymers (BCPs) have been used to direct the assembly of preformed nanocrystals into these types of open-pore structures.[2–5] A thorough understanding of the fundamental properties and chemistries of each of these components is vital to determining the design rules for their co-assembly and their evaluation into ordered architectures. A brief overview of each material is presented, with the inclusion of several references to provide a more in-depth description.

2.1 Colloidal nanocrystal synthesis

Colloidal nanocrystals are prepared using solution-based chemistry techniques. They typically range in size from 1 to 20 nm in diameter[6] and take the shape of spheres, cubes, or anisotropic structures such as rods or tetrapods.[7,8] Compositionally, they range from metal oxides, metal pnictides, metal chalcogenides, metal halides, perovskites, etc.[9–11] Advances in synthetic chemistry techniques over the last two decades now allow scientists to prepare monodisperse (≤ 5%) materials with tunability and control over unique, size and shape-dependent physical properties.[10,12–14] It is beyond the scope of this dissertation to include an in-depth analysis of colloidal nanocrystals, their synthesis, and applications; however, detailed information can be found in references 14 and 15.

High-temperature synthesis routes are used to prepare colloidal nanocrystals from inorganic salts or organometallics in the presence of both coordinating and non-coordinating solvents, which serve to exert control over their size, morphology, and composition.[8,16] Though the first reported synthesis methods had used a ‘hot-injection’ technique,[17] where synthesis initiates with the rapid injection of organometallic reagents into a hot coordinating solvent, more recent synthetic efforts take advantage of the ‘heat-up’ method, in which synthesis precursors are heated within a reaction medium to induce a chemical reaction that yields monomer for nucleation and growth.[15] The heat-up technique circumvents the pitfalls of mixing time and poor heat management inherent to classical ‘hot-injection’ methods. Nanocrystal nucleation and growth typically follows a model first proposed by LaMer, which described that the production of monodisperse colloids required a temporally discrete nucleation event followed by slower controlled growth on the existing nuclei,[18] as described in Figure 2.1. Temperature plays a role in this process, with an increase in temperature allowing precursors to react to form monomer (Figure 2.1c).[15] A detailed overview of nucleation theory can be found in references 18 and 19.

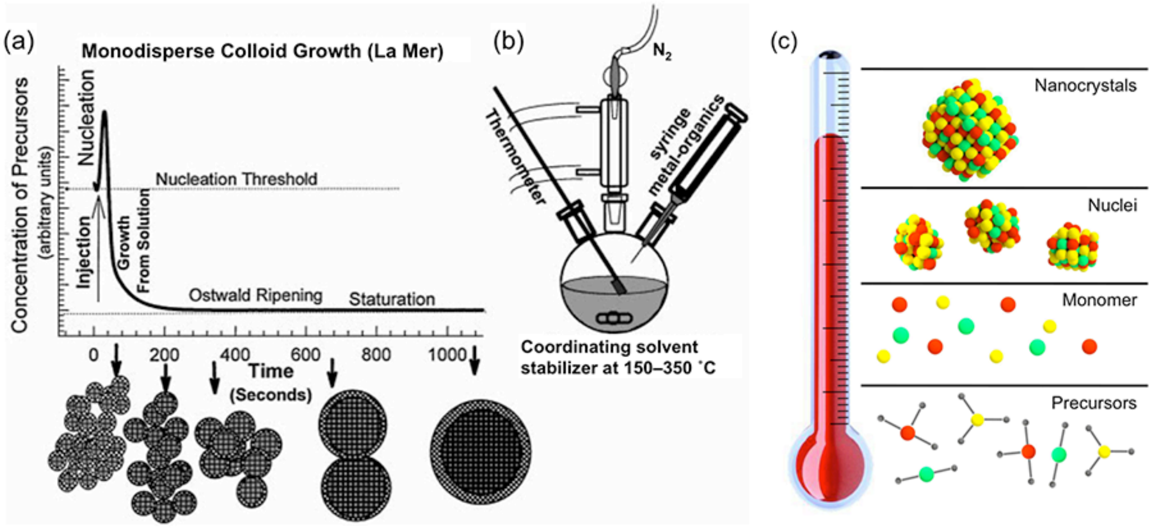

Figure 2.1. Illustration depicting colloidal nanocrystal synthesis: (a) stages of nucleation and growth for the preparation of monodisperse nanocrystals in the framework of the LaMer model; (b) representation of the simple synthetic apparatus employed in the preparation of monodisperse nanocrystal samples; (c) depiction of heat-up synthesis process as related to increasing reaction temperature. Graphics adapted from references 14 (a,b) and 15 (c) .

In order to prevent aggregation and precipitation of the nanocrystals during growth, and stabilizing agents in the form of coordinating solvents are present in the reaction mixture. These stabilizing molecules are attached to the NC surface as a monolayer through covalent, dative, or ionic bonds, they are referred to as capping groups.[20] These capping groups serve to mediate NC growth, sterically stabilize NCs in solution, and passivate surface electronic states in semiconductor NCs. This surface capping is analogous to the binding of ligands in more traditional coordination chemistry.[14] Synthetic organic techniques allow the tail and head groups to be independently tailored through well-established chemical substitutions.[14] The capping groups provide a repulsive force strong enough to counteract the inherent van de Waals attraction between NCs; this is how they are rendered a stable dispersion and resist aggregation. The energetic barrier to aggregation provided by the capping groups is strongly dependent on the energy of mixing between the tethered capping groups and the solvent.[14] Nanocrystals are typically separated from reaction by-products and purified by several rounds of precipitation. Here, a non-solvent, miscible with the by-products and original dispersing solvent, destabilizes the NC dispersions such that flocculation to separate the components. Solids can then be collected *via* centrifugation, and the process is repeated several times using fresh solvent allows for the isolation of the desired product. As capping groups are typically hydrophobic in nature, as-synthesized NCs are rendered dispersible in non-polar ‘good’ solvents (i.e., toluene, hexanes); therefore, polar solvents, such as acetone or isopropanol, are commonly used for the precipitation process.

2.2 Colloidal nanocrystal surfaces and ligands

Traditional surface science has established that the surfaces of large crystals can lower their energy by moving surface atoms away from lattice sites in the process of surface reconstruction, dangling bonds can introduce new electronic states, and foreign molecules (surfactants or adsorbates) can alter the energy and reactivity of a crystal surface.[21] All of these apply to colloidal nanocrystals. The relationship of the chemical bond between a NC surface atom and surfactant molecule is similar to that of a metal ion and ligand in a coordination complex; these principles thereby offer a useful analogy between NCs and molecular compounds.[21]

The interaction between the NC core and ligand head group can be rationalized using the classification of ionic or covalent bonds, originally proposed for metal coordination complexes and adapted to NCs by Owen and coworkers.[22–24] Three classes of metal–ligand interaction are distinguished based on the number of electrons involved, and the identity of the electron donor and acceptor groups.[21] L-type ligands are neutral two-electron donors with a lone electron pair that datively coordinates surface metal atoms.[21] X-type ligands, in neutral form, have an odd number of valence-shell electrons, requiring one electron from the NC surface site to form a two-electron covalent bond.[21] Z-type ligands bind through the metal atom as two-electron acceptors.[23] Reference 25 can be consulted for full account of the technical details of these classifications. Figure 2.2 depicts the different types of bonding on a NC surface and examples of ligands, by type.

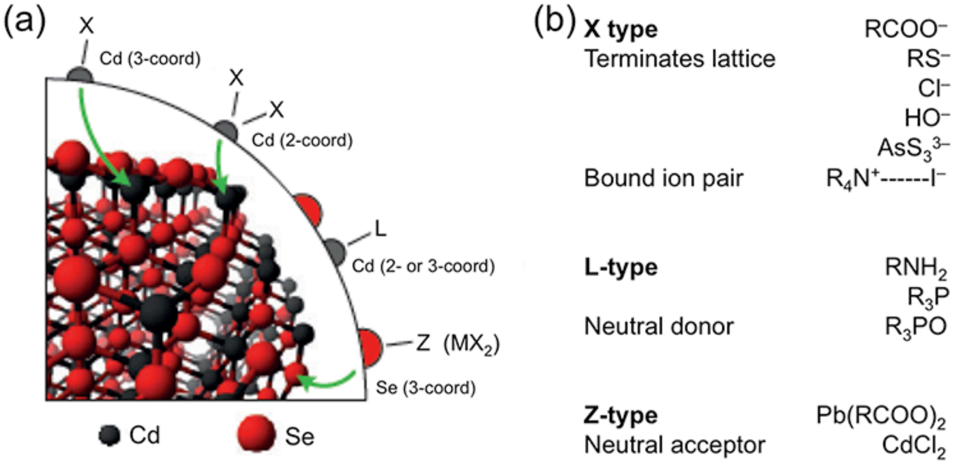

X type	$RCOO^-$
Terminates lattice	RS^-
	Cl^-
	HO^-
	AsS_3^{3-}
Bound ion pair	R_4N^+------I^-
L-type	RNH_2
	R_3P
Neutral donor	R_3PO
Z-type	$Pb(RCOO)_2$
Neutral acceptor	$CdCl_2$

Figure 2.2. Nanocrystal surface bonding motifs. (a) Illustration depicting the three classifications of metal–ligand interaction; (b) examples of surface ligands, by type. Image adapted from reference 21.

The "native" ligands that coordinate to NC surfaces provide steric stabilization in organic solvents, facilitating assembly and deposition of uniform films.[26] While these capping ligands are necessary, post-synthesis, to prevent particle aggregation, they are also hydrophobic and highly insulating. This constitutes a significant barrier for charge or ion transport in devices configured from these materials, and in many cases these ligands must be replaced by other surface-binding species better suited to the end application.[21,27] Producing a stable dispersion of NCs with ‘bare’ surfaces poses a significant challenge and often results in undesirable consequences. For example, removal of native ligands from nanocrystal dispersions usually results in aggregation or etching, while in thin films their chemical displacement (e.g., by hydrazine or formic acid) often gives inefficient removal of surface ligands.[27] Thermal treatments inevitably leave behind an undesirable residue, require lengthy annealing times, or result in particle sintering.[28] Ligand exchange reactions have been well documented and references 21 and 24 provide in-depth information on the subject. Here, the focus will be on chemistries to strip native ligands, rendering a ‘bare’ surface.

2.3 Nanocrystal ligand stripping

As a bare NC surface lacks the native coordinating ligands acquired during synthesis, the loss of those chemical bonds between the ligands and surface metal ions produces a charge imbalance. By virtue of electrostatics this often leads to adjacent NCs ‘bonding’ and aggregating. One of the first examples of chemistries leading to a charge-balanced surface employed reactive ligand stripping using the strongly oxidizing and Lewis acidic nitrosyl tetrafluoroborate ($NOBF_4$).[29] The simple procedure showed that a dispersion of hydrophobic, as-synthesized NCs could be efficiently transferred to a polar solvent, such as *N,N*-dimethylformamide (DMF), within stirring for five minutes following introduction of $NOBF_4$ (Figure 2.3). The ligand-stripped NCs could then be purified using a flocculation technique similar to that described previously. Reversibility was also demonstrated, with addition of the original surface ligands (e.g., oleyl amine, oleic acid, etc.), dissolved in hexanes, to the NC dispersion in DMF; the NCs were found to transfer immediately (<1 min) from the DMF layer to the hexane layer.

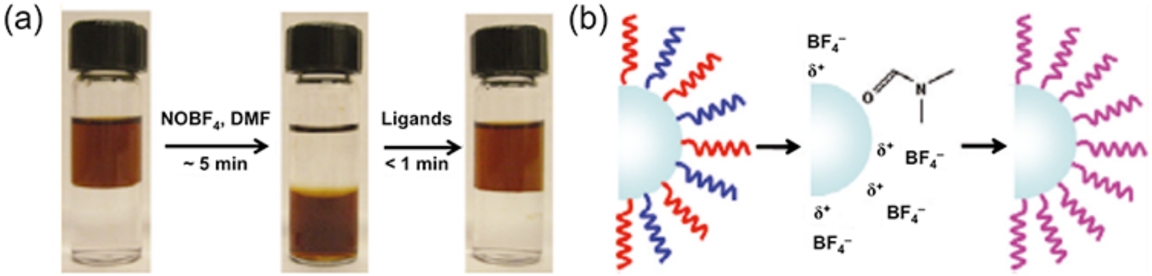

Figure 2.3. Nanocrystal stripping using $NOBF_4$: (a) images depicting transfer of hydrophobic NCs following stripping (left) to DMF (center), highlighting reversibility of the process (right); (b) illustration of the same, with blue and red ligands illustrating applicability to different ligand types. Image adapted from reference 29.

The proposed reaction mechanism is described in Figure 2.4. Trace amounts of water in the NC dispersion first react with $NOBF_4$ to form nitrous acid and fluoroboric acid. The low pKa of fluoroboric acid means it readily gives up an acidic proton, which protonates the organic surface ligands, releasing them from their surface bonds. Remaining BF_4^- ions, present in excess, are able to coordinate to the NC surface.[30] The dispersion remains acidic even after precipitation (pH ~ 3–5). It was demonstrated that BF_4^- ions formed an electrostatic stabilization with the open metal coordination sites on the NC surface. Most importantly, it is noted that DMF and other polar solvents such as hexamethylphosphoramide (HMPA) were shown to displace those ions to form dative coordination bonds of their own; this accounted for the very high (>120 mg mL^{-1}) dispersibility of the NCs in DMF and HMPA.[29]

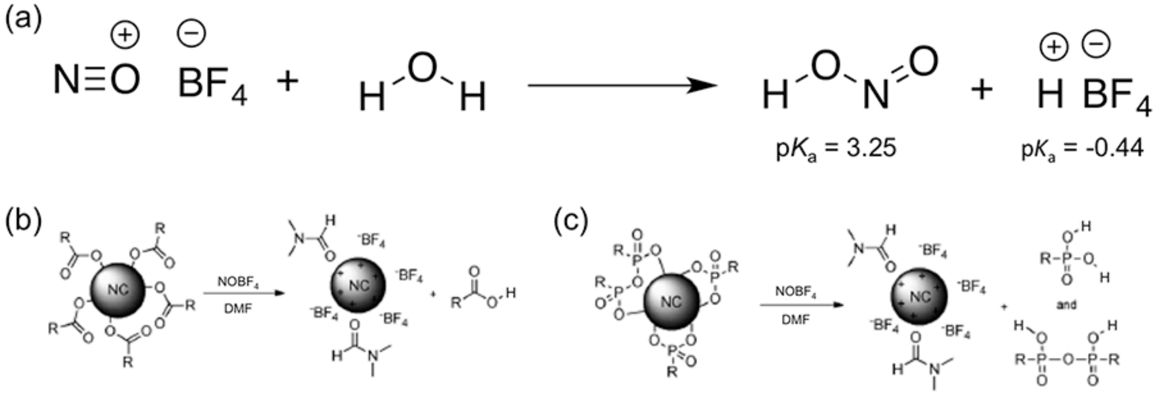

Figure 2.4. Proposed mechanism for nanocrystal stripping using $NOBF_4$: (a) reaction of $NOBF_4$ with water, forming nitrous acid and fluoroboric acid; depiction of $NOBF_4$ reaction with (b) oleate surface ligands or (c) phosphonate ligands. Images b,c adapted from reference 27.

The generality of this ligand-stripping approach was demonstrated for various NCs having different compositions (e.g., metal oxides, metals, dielectrics, some semiconductors), sizes, and shapes, as well as applicability to dispersions of NCs or thin films.[29] However, due to the strong Lewis acid character of $NOBF_4$,[31] certain classes of NCs (e.g., metal chalcogenides and both doped and undoped ZnO) were not amenable to the procedure. It was reported that the oxidative ability of the nitrosonium cation was not compatible with materials having limited chemical stability. A milder reagent, Meerwein's salt (i.e., triethyloxonium tetrafluoroborate, or Et_3OBF_4), showed applicability to these more sensitive classes of NCs (e.g., PbSe, CdSe, TiO_2) as it is a non-oxidizing and non-acidic reagent.[27] Nonetheless, both reagents facilitated the preparation of stable colloidal dispersions in polar solvents.[27,29] Dispersions of ligand-stripped colloidal NCs, accessible via these chemistries and others,[32,33] are already finding their way into device preparation techniques for applications ranging from thin-film transistors,[34] NC photovoltaic cells,[35] and plasmonic devices.[36]

2.4 Polymeric materials

Ever since 1907 when Leo Baekeland invented the first synthetic polymer, Bakelite, a phenol-formaldehyde resin, society at large has benefitted from these unique synthetic materials. *Poly*, meaning many, and *mer*, meaning parts, polymers, also known as 'plastics', are ubiquitous in everyday life, from household items to clothing, sporting goods, and computers. Advantages are their low cost and useful, tunable properties (e.g., low density, transparency, flexibility). The International Union of Pure and Applied Chemistry (IUPAC) provides a standard to polymer nomenclature, and distinguishes that a polymer is a substance composed of macromolecules.[37] It is highly unusual for a polymer to be completely monodisperse and composed entirely of perfectly identical chain sizes/lengths; rather, polymers have a range of molar masses (unit: g mol^{-1}).[38] The measurement of dispersity is defined as the ratio of the weight average molecular weight ($M_w \equiv \sum N_i M_i / \sum N_i$) to the number average molecular weight ($M_n \equiv \sum N_i M_i^2 / \sum N_i\, M_i$), where M_i is the molecular weight of a chain and N_i is the number of chains of that molecular weight. The simplest material, a homopolymer, is composed of a single type of repeat unit, or monomer, covalently bonded to adjacent 'mers', and can take on different structures, such as linear, branched, or cross-linked. A homopolymer is named using the name of the monomer from which it is derived, e.g., poly(styrene). When two or more 'mers' compose the polymer, it is referred to as a copolymer. These more complex materials can similarly take on the structures described for homopolymers, but with the addition of qualifier (e.g., statistical, random, graft, or block) to describe their physical placement on the polymer backbone. A complete pedagogy on polymer types, nomenclature, physical properties, and synthesis techniques can be found in references 39 and 40. Block copolymers will be the focus for the experiments carried out in this dissertation.

2.5 Block copolymers

Block copolymers (BCPs) are macromolecules composed of sequences, or blocks, of chemically distinct repeat units. The simplest combination is derived from two different monomer types, covalently bound to link their individual chains (e.g., methyl methacrylate and styrene). This leads to a class of materials referred to as A–B block copolymers, which can be synthesized systematically, with the B-block initiating off the A-block chain end, or by bringing together individual A and B homopolymer chains and forming a covalent bond to link them. Chemistries allowing access to such materials have evolved over the last several decades since to the discovery of anionic polymerization,[41–42] and more recently, with controlled/living radical polymerization (CRP).[43] These are known as chain-growth polymerization techniques, in which the active site on a growing polymer chain end reacts with, and adds, monomer one at a time. It was the work of Paul Flory in 1953 that first made the distinction between step-growth polymerization and chain-growth polymerization, with step-growth reaction mechanism using the functional groups of the monomers to react and form dimers, trimers, and eventually long polymer chains.[44]

Developments in chain-growth polymerization allow for the preparation of well-defined polymers with controlled molecular weight, polydispersity, composition, chain architecture, and site-specific functionality.[45] The field has branched into three fundamental types of CRP: atom-transfer radical polymerization (ATRP), nitroxide-mediated polymerization (NMP), and reversible addition–fragmentation chain transfer polymerization (RAFT). In each of these techniques the polymer forms *via* successive addition of free radical building blocks that are typically generated from separate initiator molecules (e.g., azobisisobutyronitrile, or AIBN). Polymers synthesized *via* RAFT are the focus of this work, with reviews covering ATRP and NMP included in references 46 and 47, respectively. The proposed reaction mechanism[48] for polymerization by RAFT, consisting of four steps (initiation, propagation, transfer, and termination), is shown in Figure 2.5.

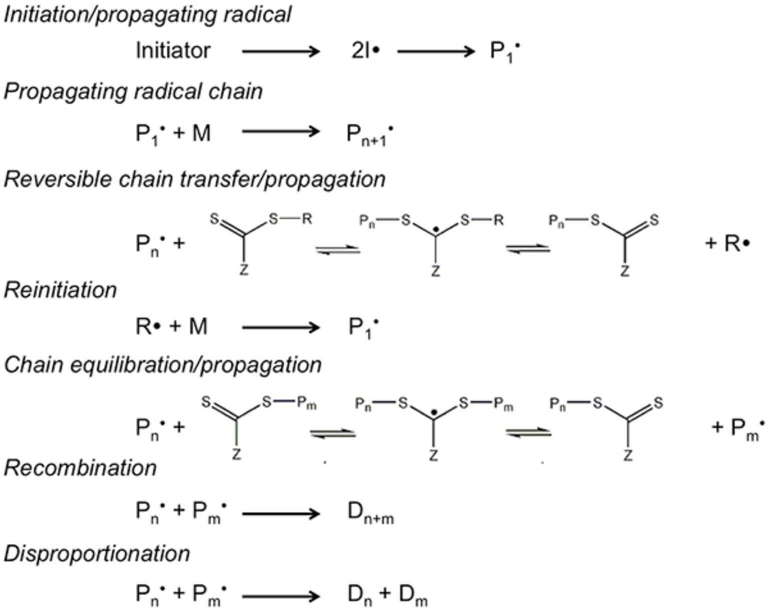

Figure 2.5. Proposed mechanism for polymerization by RAFT, with R• = radical, M = monomer, and P_x = polymer chain. Scheme adapted from reference 48.

At the start, radical initiators are typically formed *via* the homolytic cleavage of organic peroxides or azo compounds, generating two radicals per initiator molecule. The radical reacts with the first monomer unit, forming polymer $P_1^\bullet$; this active chain end can propagate and continue adding monomer units. Concurrently, this propagating radical chain can also transfer its active chain end with the chain transfer agent (CTA). The CTA, depicted here in Figure 2.5 as a dithiocarbamate, has two functions: to provide fast rates of both addition and fragmentation, relative to the rate of propagation, and to allow for the capability of the expelled radical (R•) to reinitiate polymerization.[48] This keeps the concentration of active radicals low thereby suppressing side reactions such as recombination or disproportionation. The establishment of a dynamic equilibrium between propagating radicals and various dormant species is central to all CRP systems.[50,51] Polymers can then either continue propagating off the transferred chain, as shown in the chain equilibration step, or initiate new polymers from the expelled radical. Two termination events are possible: either radical–radical recombination, where the radicals on the ends of two active chains form a covalent bond, or disproportionation, where two chain ends exchange a proton leaving a saturation on one end and a terminal alkene on the other.[49] The reaction can also be stopped at any point, at moderate conversions, which lowers the chance of termination.[50]

Unlike RAFT, in traditional radical polymerization chain transfer and termination are impossible to control. As the reaction proceeds and monomer is consumed, the concentration of free radicals grows such that the proportion of termination to propagation also sees a dramatic increase.[40] This control is the key advantage to the RAFT technique, as depicted in Figure 2.6.

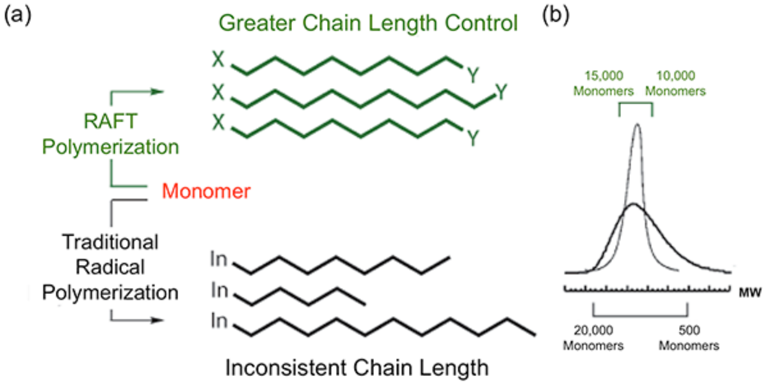

Figure 2.6. Comparison between RAFT and traditional radical polymerization: (a) scheme depicting greater chain length control; (b) overlay of size-exclusion chromatography traces for the same two types of polymerizations. Graphics adapted from Sigma-Aldrich.

A more complete description of controlled radical polymerization can be found in reference 43. Block copolymers are prepared *via* RAFT by using the as-synthesized homopolymer as a macro-CTA; the second monomer adds to the dithiocarbamate, or other CTA functional group, and propagates as described in Figure 2.5. As the RAFT process is amenable to a wide variety of monomers (e.g., (meth)acrylates, (meth)acrylamides, acrylonitrile, styrenes, dienes, vinyl monomers) a wealth of possibilities exist for new materials.

When a BCP contains both hydrophilic (polar, water-loving) and hydrophobic (apolar, water-repelling) qualities within a single material it is known as an amphiphilic BCP. These characteristics are derived from the selection of monomer for each block; styrene–methyl methacrylate and ethylene–ethylene glycol are well known examples. As the blocks are composed of chemically distinct species the segments often have a desire to demix completely but they cannot due to their covalent attachment. Block copolymers instead, as a compromise of sorts, undergo a process known as microphase separation. The morphology and length scale accessible by this phase separation depends on many factors, namely the volume fraction of a block, f, the total chain length or degree of polymerization, N, and the degree of compatibility of the blocks, χ, also known as the Flory-Huggins interaction parameter.[41] Typically, phase-separation gives access to structures having length scale 2–100 nm.[52] A more in-depth description of the concepts presented here can be found in reference 52.

2.6 Self-assembly of block copolymers

Block copolymer (BCP) self-assembly has attracted considerable attention for several decades as it yields ordered structures in a wide range of morphologies,[52] as depicted in Figure 2.7. The foundation for the science comes from the work of F. S. Bates in 1990, describing the theory and experiment behind BCP thermodynamics, including their composition-dependent architectures and microphase separation. Reference 41 provides a complete description and should be consulted for further details, with a brief description of concepts relevant to the work in this dissertation covered below.

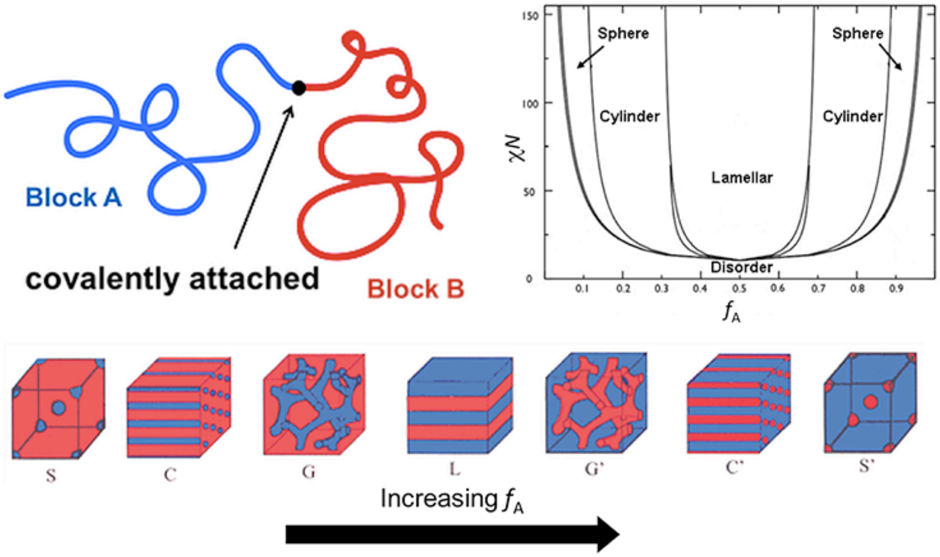

Figure 2.7. Block copolymer bulk phase separation and self-assembly. Possible structures are spheroid (S), cylinder (C), gyroid (G), and lamellar (L), with the phase diagram showing four equilibrium morphologie. Graphics adapted from reference 53.

According to self-consistent mean-field theory predictions,[54] at equilibrium a dense collection of monodisperse BCP chains will arrange themselves in minimum free energy configurations.[53] The phase diagram in Figure 2.7 depicts at what polymer block fraction, f, with respect to the other block, will lead to either spheroid, cylinder, or lamellar structures. The term χN also factors into the phase separation, noting that larger values (> 50) lead to a greater degree of order within the system. Thermodynamically, entropy is the key player. The terms for f and N, controlled through polymerization stoichiometry, contribute to the translational and configurational entropy of the system.[52] Enthalpic considerations and the magnitude of χ arise from the selection of the A–B monomer pair, with the self-assembly process driven by an unfavorable mixing enthalpy coupled with a small mixing entropy.[52] Additionally, there is a temperature dependence to the enthalpic contribution of the Flory-Huggins interaction parameter, noted here as χ_{AB} for the A–B monomer pair, and given by $\chi_{AB} = \left(\frac{z}{k_B T}\right)\left[\varepsilon_{AB} - \frac{1}{2}(\varepsilon_{AA} + \varepsilon_{BB})\right]$. Here, z is the number of nearest neighbors per repeat unit in the polymer, k_BT is the thermal energy, ε_{AB}, ε_{AA}, and ε_{BB} are the interaction energies per repeat unit for A–B, A–A, and B–B, respectively. The complete pedagogy covering this topic can be found in references 52 and 53.

The introduction of solvent increases the level of complexity for BCP self-assembly in solution, with non-equilibrium structures potentially becoming accessible as a block copolymer is dispersed in a single, or mixture of, solvent. Similarly to surfactants, and when dispersed in the appropriate solvent(s), amphiphilic BCPs can self-associate to form spherical aggregates through a closed association process, forming micelles.[55] This manifests as a way to release the surface tension which builds as a result of the increase in polymer concentration. Two distinct types of BCP micelle have been identified: star-like and crew-cut structures (Figure 2.8a,b), with star-like micelles having a small core compared to the corona and crew-cut micelles having a large core and highly stretched coronal chains.[55]

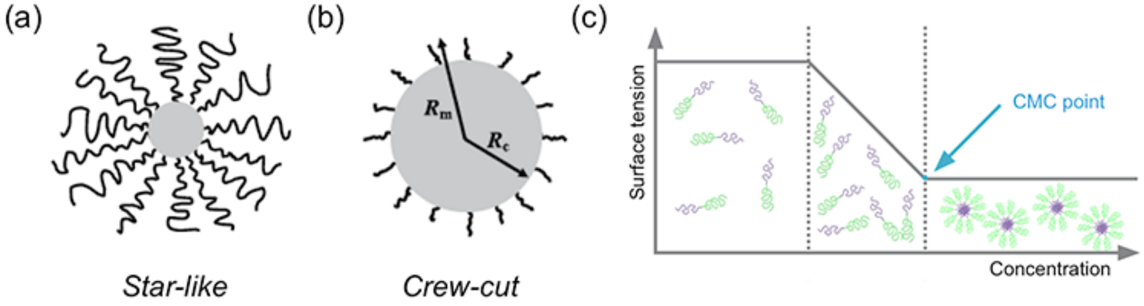

Figure 2.8. Micelle aggregates, formed by the closed association of amphiphilic BCPs: (a) star-like and (b) crew-cut structures; (c) critical micelle point as a function of surface tension and BCP concentration. Graphics a,b adapted from reference 55; image c adapted from Biolin Scientific.

The parameter R_c (Figure 2.8b) describes the radius of the core and R_m describes the overall radius of a micelle. The dimension of a micelle can also be defined by the radius of gyration, R_g, and the hydrodynamic radius, R_h;[56] both are defined elsewhere and will be discussed in the experimental work to follow. Another parameter, b, is defined as the grafting distance between neighboring blocks at the core–corona interface, with b^2 as the area occupied by one chain at that interface. This area can be compared to the area occupied by a head group for low molecular weight surfactant micelles.[57] Micelles form above a certain BCP concentration, known as the critical micelle concentration (cmc) (Figure 2.8c) and are quantified by their aggregation number, Z, the number of BCP chains contained within the micelle. The degree of polymerization of the polymer blocks,

N_A and N_B, and the Flory–Huggins interaction parameter, χ, are responsible for controlling R_c, R_m, b, and Z.[55]

Choice of solvent, or for that matter, co-solvent also impacts assembly trajectories. Micelles from an A–B block copolymer can form in a single solvent that is a 'good' solvent for (i.e., solubilizes) the B block and a non-solvent for the A block. An example are micelles formed from polystyrene-*block*-poly(ethylene oxide) (PS-*b*-PEO) in water, which have been studied extensively;[58,59] these references can be consulted for further information. In others cases, and for the experiments described in this dissertation, a solvent mixture is used, with the BCP first dissolved in a good solvent for both blocks, with the micelle forming upon the addition of a selective solvent for the A block.[61] Here the B block collapses to minimize the interaction with the selective solvent with the A block is extended at the interface. A more thorough description can be found in references 55 and 60. What is important to note for micelles formed by this technique is that a BCP with $f_A \sim f_B$ would typically form a lamellar phase in the bulk. However, here, access to a spherical, non-equilibrium shape is made possible by the solvent effect, which has been shown for a series of PEO-based amphiphilic BCPs.[62]

Micelles formed from amphiphilic block copolymers have quickly found use as biological applications as vehicles for drug delivery of targeted therapeutics, release of channel proteins or metal nanoparticles, or as synthetic cellular reactors.[63,64] Further discussion on this topic will be presented in the scientific work of this dissertation.

2.7 References

1. Milliron, D. J.; Buonsanti, R.; Llordes, A.; Helms, B. A. "Constructing functional mesostructured materials from colloidal nanocrystal building blocks" *Acc. Chem. Res*. **2014**, *47*, 236−246.
2. Bockstaller, M. R.; Mickiewicz, R. A.; Thomas, E. L. "Block Copolymer Nanocomposites: Perspectives for Tailored Functional Materials" *Adv. Mater*. **2005**, *17*, 1331−1349.
3. Kao, J.; Thorkelsson, K.; Bai, P.; Rancatore, B. J.; Xu, T. "Toward functional nanocomposites: taking the best of nanoparticles, polymers, and small molecules" *Chem. Soc. Rev*. **2013**, *42*, 2654−2678.
4. Hoheisel, T. N.; Hur, K.; Wiesner, U. B. "Block copolymer–nanoparticle hybrid self-assembly" *Prog. Polym. Sci*. **2015**, *40*, 3−32.
5. Helms, B. A.; Williams, T. E.; Buonsanti, R.; Milliron, D. J. "Colloidal Nanocrystal Frameworks" *Adv. Mater*. **2015**, *27*, 5820–5829.
6. Puntes, V. F.; Krishnan, K. M.; Alivisatos, A. P. "Colloidal nanocrystal shape and size control: the case of cobalt" *Science* **2001**, *291*, 2115–2117.
7. Milliron, D. J.; Hughes, S. M.; Cui, Y.; Manna, L.; Li, J.; Wang, L.-W.; Alivisatos, A. P. "Colloidal nanocrystal heterostructures with linear and branched topology" *Nature* **2004**, *430*, 190–195.
8. Jun, Y.-W.; Choi, J.-S.; Cheon, J. "Shape control of semiconductor and metal oxide nanocrystals through nonhydrolytic colloidal routes" *Angew. Chem. Int. Ed*. **2006,** *45*, 3414–3439.
9. Y. Yin, Alivisatos. A. P.; "Colloidal nanocrystal synthesis and the organic–inorganic interface" *Nature* **2005**, *437*, 664–670.
10. Cozzoli, P. D.; Pellegrino, T.; Manna, L. "Synthesis, properties and perspectives of hybrid nanocrystal structures" *Chem. Soc. Rev*. **2006**, *35*, 1195–1208.
11. Buonsanti, R.; Milliron, D. J. "Chemistry of Doped Colloidal Nanocrystals" *Chem. Mater*. **2013**, *25*, 1305–1317.
12. Alivisatos, A. P. "Semiconductor Clusters, Nanocrystals, and Quantum Dots" *Science* **1996**, *271*, 993–937.
13. Alivisatos, A. P. "Perspectives on the Physical Chemistry of Semiconductor Nanocrystals" *J. Phys. Chem. C* **1996**, *100*, 13226–13239.
14. Murray, C. B.; Kagan, C. R.; Bawendi, M. G. "Synthesis and Characterization of Monodisperse Nanocrystals and Close-Packed Nanocrystal Assemblies" *Annu. Rev. Mater. Sci*. **2000**, *30*, 545–610.
15. van Embden, J.; Chesman, A. S. R.; Jasieniak, J. J. "The Heat-Up Synthesis of Colloidal Nanocrystals" *Chem. Mater*. **2015**, *27*, 2246−2285.
16. Laurent, S.; Forge, D.; Port, M.; Roch, A.; Robic, C.; Elst, L. V.; Muller, R. N. "Magnetic Iron Oxide Nanoparticles: Synthesis, Stabilization, Vectorization, Physicochemical Characterizations, and Biological Applications" *Chem. Rev*. **2008**, *108*, 2064–2110.
17. Murray, C. B.; Norris, D. J.; Bawendi, M. G. "Synthesis and Characterization of Nearly Monodisperse CdE (E = S, Se, Te) Semiconductor Nanocrystallites" *J. Am. Chem. Soc.* **1993**, *115*, 8706–8715.

18. LaMer, V. K.; Dinegar, R. H. “Theory, Production and Mechanism of Formation of Monodispersed Hydrosols” *J. Am. Chem. Soc.* **1950**, *72*, 4847−4854.
19. Thanh, N. T. K.; Maclean, N.; Mahiddine, S. “Mechanisms of Nucleation and Growth of Nanoparticles in Solution” *Chem. Rev.* **2014**, *114*, 7610−7630.
20. Steigerwald, M. L.; Alivisatos, A. P.; Gibson, J. M.; Harris, T. D.; Kortan, A. R.; Muller, A. J.; Thayer, A. M.; Duncan, T. M.; Douglass, D. C.; Brus, L. E. “Surface Derivatization and Isolation of Semiconductor Cluster Molecules” *J. Am. Chem. Soc.* **1988**, *110*, 3046–3051.
21. Boles, M. A.; Ling, D.; Hyeon, T.; Talapin, D. V. “The surface science of nanocrystals” *Nat. Mater.* **2016**, *15*, 141–153.
22. Green, M. L. H. “A new approach to the formal classification of covalent compounds of the elements” *J. Organomet. Chem.* **1995**, *500*, 127–148.
23. Anderson, N. C.; Hendricks, M. P.; Choi, J. J.; Owen, J. S. “Ligand exchange and the stoichiometry of metal chalcogenide nanocrystals: spectroscopic observation of facile metal–carboxylate displacement and binding” *J. Am. Chem. Soc.* **2013**, *135*, 18536–18548.
24. Owen, J. S. “The coordination chemistry of nanocrystal surfaces” *Science*, **2015**, *347*, 615–616.
25. Green, M. L. H.; Parkin, G. “Application of the covalent bond classification method for the teaching of inorganic chemistry” *J. Chem. Educ.* **2014**, *91*, 807–816.
26. Milliron, D. J.; Buonsanti, R.; Llordes, A.; Helms, B. A. “Constructing Functional Mesostructured Materials from Colloidal Nanocrystal Building Blocks” *Acc. Chem. Res.* **2014**, *47*, 236–246.
27. Rosen, E. L.; Buonsanti, R.; Llordes, A.; Sawvel, A. M.; Milliron, D. J.; Helms, B. A. “Exceptionally Mild Reactive Stripping of Native Ligands from Nanocrystal Surfaces by Using Meerwein’s Salt” *Angew. Chem. Int. Ed.* **2012**, *51*, 684–689.
28. Voitekhovich, S. V.; Talapin, D. V.; Klinke, C.; Kornowski, A.; Weller, H. “CdS Nanoparticles Capped with 1-Substituted 5-Thiotetrazoles: Synthesis, Characterization, and Thermolysis of the Surfactant” *Chem. Mater.* **2008**, *20*, 4545–4547.
29. Dong, A.; Ye, X.; Chen, J.; Kang, Y.; Gordon, T.; Kikkawa, J. M.; Murray, C. B. “A Generalized Ligand-Exchange Strategy Enabling Sequential Surface Functionalization of Colloidal Nanocrystals” *J. Am. Chem. Soc.* **2011**, *133*, 998–1006.
30. Kim, S. B.; Cai, C.; Kim, J.; Sun, S.; Sweigart, D. A. “Surface Modification of Fe_3O_4 and FePt Magnetic Nanoparticles with Organometallic Complexes” *Organometallics* **2009**, *28*, 5341–5348.
31. Connelly, N. G.; Geiger, W. E. “Chemical Redox Agents for Organometallic Chemistry” *Chem. Rev.* **1996**, *96*, 877–910.
32. Webber, D. H.; Brutchey, R. L. “Ligand Exchange on Colloidal CdSe Nanocrystals Using Thermally Labile tert-Butylthiol for Improved Photocurrent in Nanocrystal Films” *J. Am. Chem. Soc.* **2012**, *134*, 1085–1092.
33. Doris, S. E.; Lynch, J. J.; Li, C.; Wills, A. W.; Urban, J. J.; Helms, B. A. "Mechanistic Insight into the Formation of Cationic Naked Nanocrystals

Generated under Equilibrium Control" *J. Am. Chem. Soc.* **2014**, *136*, 15702–15710.

34. Rosen, E. L.; Sawvel, A. M.; Milliron, D. J.; Helms, B. A. “Influence of Surface Composition on Electronic Transport Through Naked Nanocrystal Networks” *Chem. Mater.* **2014**, *26*, 2214–2217.
35. Panthani, M. G., Kurley, J. M., Crisp, R. W., Dietz, T. C., Ezzyat, T., Luther, J. M., & Talapin, D. V “High Efficiency Solution Processed Sintered CdTe Nanocrystal Solar Cells: The Role of Interfaces” *Nano Lett.* **2014**, *14*, 670–675.
36. Garcia, G.; Buonsanti, R.; Runnerstrom, E. L.; Mendelsberg, R. J.; Llordes, A.; Anders, A.; Richardson, T. J.; Milliron, D. J. “Dynamically Modulating the Surface Plasmon Resonance of Doped Semiconductor Nanocrystals” *Nano Lett.* **2011**, *11*, 4415–4420.
37. Hiorns, R. C.; Boucher, R. J.; Duhlev, R.; Hellwich, K. H.; Hodge, P.; Jenkins, A. D.; Jones, R. G.; Kahovec, J.; Moad, G.; Ober, C. K.; Smith, D. W. “A brief guide to polymer nomenclature” *Polymer*, **2012**, *201354*, 3–4.
38. Cho, K. S. Viscoelasticity of Polymers: Theory and Numerical Algorithms. New York: Springer, 2016. Print.
39. Cowie, J. M. G.; Arrighi, V. *Polymers: Chemistry and Physics of Modern Materials, 3rd Edition*. Boca Raton; CRC Press, 2008. Print.
40. Odian, G. *Principles of Polymerization, 4th edition*. Hoboken: John Wiley & Sons, 2004. Print.
41. Bates, F. S.; Fredrickson, G. H. “Block Copolymer Thermodynamics: Theory and Experiment” *Annu. Rev. Phys. Chem*. **1990**, *41*, 525–57.
42. Szwarc, M.; Levy, M.; Milkovich, R. “Polymerization initiated by electron transfer to monomer. A new method of formation of block copolymers” *J. Am. Chem. Soc*. **1956**, *78*, 2656–2657.
43. Braunecker, W.; Matyjaszewski, K. “Controlled/living radical polymerization: Features, developments, and perspectives” *Prog. Polym. Sci*. **2007**, *32*, 93–146.
44. Flory, P. J. *Principles of Polymer Chemistry*. New York: Cornell University Press, 1953. Print.
45. Matyjaszewski, K.; Spanswick, J. “Controlled/living radical polymerization” *Materials Today*, **2005**, *8*, 26–33.
46. Patten, T. E.; Matyjaszewski, K. “Atom transfer radical polymerization and the synthesis of polymeric materials” *Adv. Mater*. **1998**, *10*, 901–915.
47. Hawker, C. J.; Bosman, A. W.; Harth, E. “New polymer synthesis by nitroxide mediated living radical polymerizations” *Chem. Rev*. **2001**, *101*, 3661–3688.
48. Mayadunne, R. T.; Rizzardo, E.; Chiefari, J.; Chong, Y. K.; Moad, G.; Thang, S. H. “Living radical polymerization with reversible addition−fragmentation chain transfer (RAFT polymerization) using dithiocarbamates as chain transfer agents” *Macromolecules*, **1999**, *32*, 6977–6980.
49. Chiefari, J.; Chong, Y. K.; Ercole, F.; Krstina, J.; Jeffery, J.; Le, T. P. T.; Mayadunne, R. T. A.; Meijs, G. F.; Moad, C. L.; Moad, G.; Rizzardo, E.; Thang, S. H. “Living Free-Radical Polymerization by Reversible Addition−Fragmentation Chain Transfer: The RAFT Process” *Macromolecules* **1998**, *31*, 5559–5562.

50. Greszta, D.; Mardare, D.; Matyjaszewski, K. '''Living' radical polymerization. I. Possibilities and limitations" *Macromolecules* **1994,** *27*, 638–44.
51. Goto, A.; Fukuda, T. "Kinetics of living radical polymerization" *Prog Polym Sci* **2004**, *29*, 329–385.
52. Mai, Y.; Eisenberg, A. "Self-assembly of block copolymers" *Chem. Soc. Rev*. **2012**, *41*, 5969–5985.
53. Bates, F. S. Fredrickson, G. H. "Block Copolymers–Designer Soft Materials" *Physics Today*, **1999**, *52*, 32–38.
54. Matsen, M. W.; Bates, F. S. "Unifying Weak- and Strong-Segregation Block Copolymer Theories" *Macromolecules*, **1996**, *29*, 1091–1098.
55. Gohy, J.-F. "Block Copolymer Micelles" *Adv. Polym. Sci*. **2005**, *190*, 65–136.
56. Brown, W.; editor. *Dynamic light scattering*. Oxford: Oxford University Press, 1972. Print.
57. Israelachvili, J. N.; editor. *Intermolecular and surface forces, 2nd Edition*. London: Academic Press, 1985. Print.
58. Jada, A.; Hurtrezb, G.; Siffert, B.; Riess, G. 'Structure of polystyrene-*block*-poly(ethy1ene oxide) diblock copolymer micelles in water" *Macromol. Chem. Phys*. **1996**, *197*, 3697–3710.
59. Xu, R.; Winnik, M. A.; Hallett, F. R.; Riess, G.; Croucher, M. D. "Light-scattering study of the association behavior of styrene-ethylene oxide block copolymers in aqueous solution" *Macromolecules* **1991**, *24*, 87–93.
60. Matijevic, E.; editor. *Surface and colloid science, Volume 15*. New York: Plenum, 1993. Print.
61. Kelley, E. G.; Smart, T. P.; Jackson, A. J.; Sullivan, M. O.; Epps, T. H. "Structural changes in block copolymer micelles induced by cosolvent mixtures" *Soft Matter*, **2011**, *7*, 7094–7102.
62. Rauda, I. E.; Buonsanti, R.; Saldarriaga-Lopez, L. C.; Benjauthrit, K.; Schelhas, L. T.; Stefik, M.; Augustyn, V.; Ko, J.; Wiesner, U.; Milliron, D. J.; Tolbert, S. H. "General method for the synthesis of hierarchical nanocrystal-based mesoporous materials" *ACS Nano* **2012**, *6*, 6386–6399.
63. Rösler, A.; Vandermeulen, G. W.; Klok, H. A. "Advanced drug delivery devices via self-assembly of amphiphilic block copolymers" *Advanced Drug Delivery Reviews* 2012, 64, 270–279.
64. Blanazs, A.; Armes, S. P.; Ryan, A. J. "Self-Assembled Block Copolymer Aggregates: From Micelles to Vesicles and their Biological Applications" *Macromol. Rapid Commun*. **2009**, *30*, 267–277.

Chapter 3

Block copolymer–nanocrystal interactions and assembly

Micelles derived from amphiphilic block copolymers have proven their utility as delivery vehicles for a variety of biologial applications, as described in Chapter 2. Their enhanced funtionality is derived from the combination of the micelle with a secondary component (e.g., proteins, therapeutic medicines, magnetic nanoparticles). It should follow that combinations of micelles with other types of components could be of high value for other applications, particularly those where the nature of the initial micellar structure (i.e., physical size and shape) could be leveraged as a template for final device architecture. Specifically, devices featuring porous structures or high surface area films could be imagined to benefit from exploring these types of new functional assemblies. This chapter will highlight methods looking at different ways to interface amphilic block copolymers with inorganic or metal nanoparticles, with a discussion of kinetic vs. thermodynamic assembly pathways and brief review of types and strengths of BCP–NC interactions.

The ability to assemble two or more dissimilar materials into a higher-order structure is of great importance to researchers, as the blending of the two materials could impart enhanced function to one material when in combination with the other. When a block copolymer (BCP) and a colloidal nanocrystal (NC) are brought together there are many important factors to consider, namely how to control and enhance the interaction between the two materials, and how to predict and tune the local and long range order of the resulting structures. The soft, polymeric material, used as a template to direct the arrangement of the nanocrystals into an ordered architecture, is often removed post-assembly *via* thermal or chemical annealing.[1] This reveals a porous film architecture, or framework, which we define as being an ordered arrangement of both matter and empty space,[2] with mesoporous materials containing pores between 2 and 50 nm in diameter, wall thicknesses from 2 to 35 nm, and crystallite sizes typically up to the dimensions of the walls.[3-11] These nanostructured architectures are of especially great interest for applications such as solar cells, batteries, capacitors, catalysis, and fuel cells.[3,5,7–8,10–11]

With a BCP as the template, well-developed polymerization chemistries give access to a high degree of tunability of the template's physical dimensions; this results in control over the primary length scale of the pores in the final framework. One can imagine the challenges arising in determining the design rules for combining chemically disparate components such as organic-based BCPs and inorganic or metallic NCs. These materials could be different shapes (e.g., a hard sphere with a flexible coiled chain) but could also be different sizes, with the possibility of either component having the larger scale. The degree to which it is possible to assemble ordered framework architectures, rather than disordered porous materials, from various components depends critically on their interactions, namely between the NC with the BCP template. In this regard, both entropic and enthalpic factors contribute to assembly outcomes. Entropically, it would be necessary to determine how to overcome the energetic penalty resulting from accommodating NCs within the deformed polymer domain. Enthalpically, factors contributing to enhancing the interactions between framework components would need to be established to allow for the formation of stable assemblies.

3.1 Assemblies with surface-ligand functionalized nanoparticles

The seminal work in this area from Wiesner and coworkers in 2008 described the fabrication of a porous Pt nanoparticle (NP) framework, prepared from Pt NPs assembled with an amphiphilic BCP, polyisoprene-*block*-poly(dimethylaminoethyl methacrylate (PI-*b*-PDMAEMA).[12] A complicated synthesis produced a thiol-terminated surface ligand (*N,N*-di-2-propoxyethyl-*N*-3-mercaptopropyl-*N*-methylammonium chloride) designed to coordinate to the surface of the Pt NP through a thiol linkage, with a lengthy aging process required to render the functionalized Pt NP hydrophobic enough for it to segregate into the PDMAEMA block (Figure 3.1). Evaporation-induced self-assembly, in a mixed solvent system of chloroform (good solvent) and methanol (non-solvent for PI block), produced the mesostructured film, as depicted in 3.1d. A two-step process was used to remove the BCP template: first, polymer decomposition *via* pyrolysis, followed by removal of carbon with Argon-oxygen (Ar-O) plasma. A graphic highlighting the inverse-hexagonal morphology is shown (Figure 3.1e) as well as a bright-field TEM image of the final structure (Figure 3.1f).

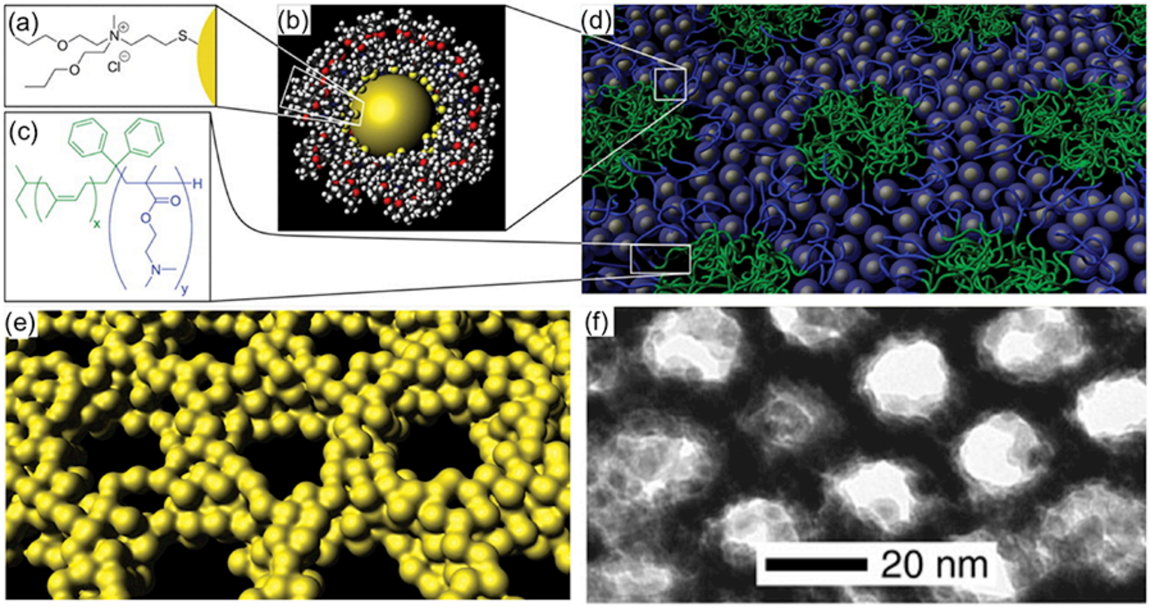

Figure 3.1. Description of components and their assembly trajectory for a Pt NP-based porous framework: (a) chemical structure of *N,N*-di-2-propoxyethyl-*N*-3-mercaptopropyl-*N*-methylammonium chloride; (b) a true-scale model of a NP with a 1.8 nm diameter metal core and 1.4 nm ligand shell; (c) Chemical structure of PI-*b*-PDMAEMA; PI is green and PDMAEMA is blue; (d) self-assembly of Pt NPs with block copolymer followed by annealing afforded a hybrid with a regularly ordered structure, such as the inverse hexagonal morphology; (e) illustration of ordered mesoporous Pt framework; (f) bright-field (BF) TEM image of ordered mesoporous Pt framework. Images adapted from reference 12.

As a means of demonstrating functionality of the framework for device-oriented applications, electrical conductivity of the Pt NP–polymer assembly was measured before and after pyrolysis. It was noted that the NP–polymer hybrid, despite the presence of carbon, showed the highest electrical conductivity (2.5 mS cm^{-1}) ever measured for ordered mesoporous materials derived from block copolymers; the conductivity increased to 400 S cm^{-1} for carbon-free framework, following pyrolysis.[12]

Though this example proved that ordered assemblies between chemically disparate components was possible, broad applicability was not demonstrated as assemblies from one type of NP and only one type and size of BCP were described. Additionally the lengthy and complicated synthesis for both organic-based materials would render this process difficult for a large-scale application. Additionally, the authors demonstrated that a two-step process was required to fully remove the BCP templating agent, noting collapse of the microstructure when attempting annealing in a single process.

3.2 Assemblies with nanocrystals with polar surfaces

The following year Tolbert and coworkers[13] devised a method to prepare mesoporous films from either sol–gel derived or pre-formed TiO_2 anatase NCs templated with poly(ethylene-*co*-butylene)-*block*-poly(ethylene oxide), a class of amphiphilic BCPs known as ‘KLE’ (Figure 3.2a). A concise review on sol–gel chemistry is provided in reference 14. With the chemistry used in the preparation of the pre-formed TiO_2 component,[15] free –OH bonds were presented on the material’s surface (Figure 3.2a). This motif was designed such that surface –OH groups could interact with the PEO block *via* hydrogen bonding, promoting the association of the assembly components through enthalpic interactions. Dip-coating was used to prepare films, which were then thermally annealed to remove the BCP template, leaving a mesoporous NC film (Figure 3.2b).

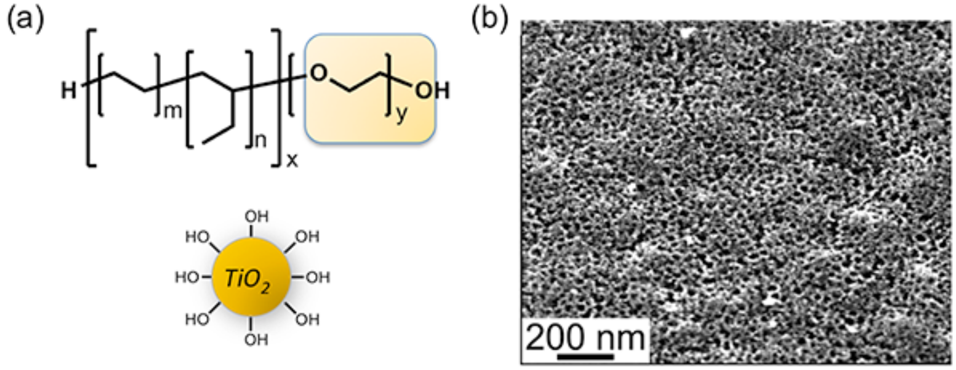

Figure 3.2. (a) Chemical structure of KLE-23 (top) and depiction of –OH functionalized TiO_2 NCs (bottom). (b) Scanning electron microscopy image of mesoporous film resulting from the assembly of KLE-23 and preformed TiO_2 NCs. Scanning electron micrograph adapted from reference 13.

Though mesoporosity was demonstrated, the poor balance of interactions between components did not allow for an ordered arrangement of the pores. Additionally, as polar functionality was required on the NC surface, this method lacked applicability to other classes of NCs. However, the use of the mesoporous TiO_2 film as a capacitor was shown to outperform devices prepared from either the sol-gel derived or an untemplated TiO_2 NC film.[13] More importantly, these results showed that improved charge storage was attributed to the introduction of interconnected porosity accessible only through the BCP templated TiO_2 NC film. Electrochemical charge/discharge properties were enhanced by not only minimizing solid-state diffusion path lengths but also facilitating mass transport of ions and solvent to the electrochemically active sites.[13]

3.3 Assemblies with ligand-stripped nanocrystals

Further work from Tolbert and coworkers[16] made use of ligand-stripping chemistry[17] described in Chapter 2 to prepare assemblies from a variety of metal oxide NCs with poly(ethylene-*alt*-propylene)-*block*-poly(ethylene oxide), PEP-*b*-PEO BCP (Figure 3.3a). Samples were prepared by dip-coating a 9:1 *v*/*v* EtOH–DMF dispersion of BCP and ligand-stripped NCs, with the polymer reported to form micelles in this solvent system.[16] Upon evaporation of the solvent following coating, the micelles co-assembled with the preformed nanocrystals and both components self-organized into a mesostructured organic–inorganic composite.[16] Full removal of the BCP templating agent was realized upon thermal annealing. Figure 3.3b shows top-down SEM images of three templated films prepared from assemblies of PEP-*b*-PEO with ligand-stripped NCs.

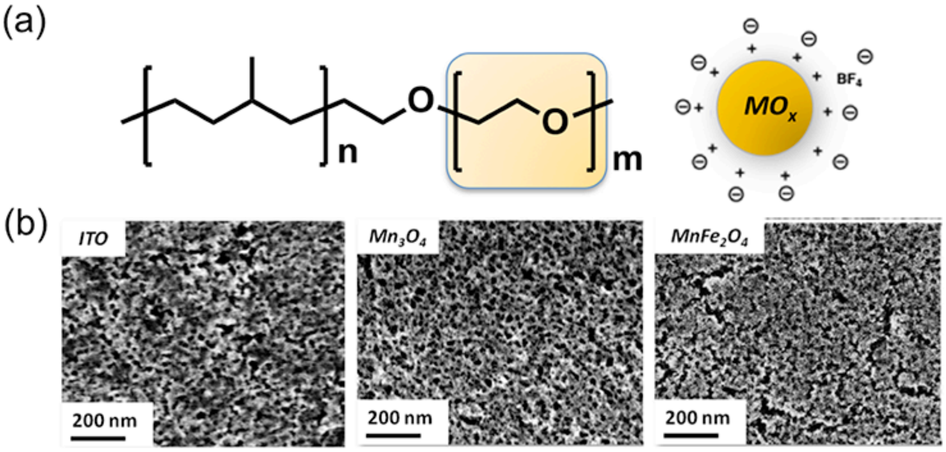

Figure 3.3. (a) Chemical structure of PEP-*b*-PEO (left) and depiction of ligand-stripped metal oxide (MO_x) NCs (right). (b) Scanning electron microscopy images of mesoporous film resulting from the assembly of PEP-*b*-PEO with (l–r) tin-doped indium oxide (ITO), manganese oxide (Mn_3O_4), and manganese iron oxide ($MnFe_2O_4$) NCs. Scanning electron micrographs adapted from reference 16.

The applicability of the assembly technique was also demonstrated for two other PEO-based BCPs: poly(butadiene(1,2-addition))-*block*-poly-(ethylene oxide), PB-*b*-PEO, and poly(butylene oxide)-*block*-poly(ethylene oxide), PBO-*b*-PEO. Different solution-phase film deposition techniques (i.e., drop casting and spin coating) were investigated as well, with top-down SEM micrographs showing the resulting film structures.

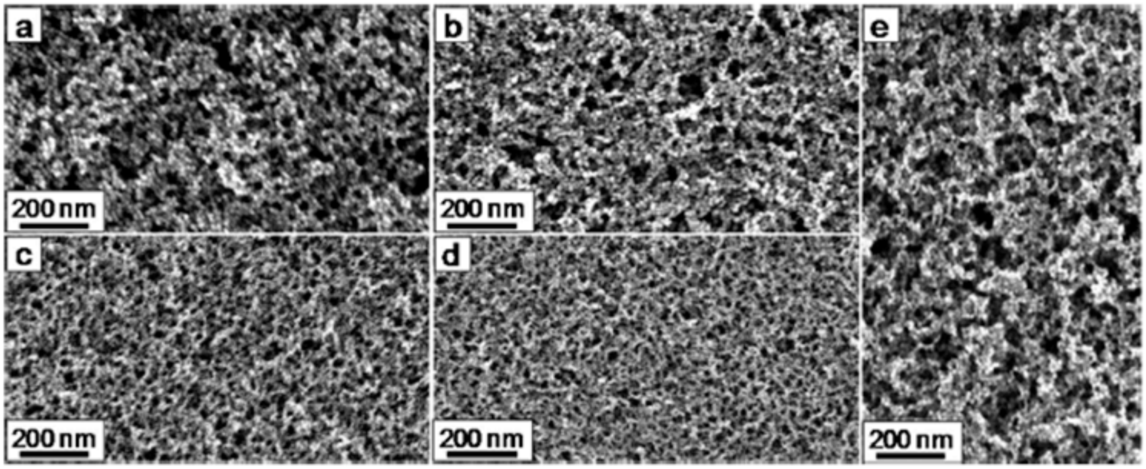

Figure 3.4. Scanning electron microscopy images of templated nanocrystal-based porous films demonstrating variability of the template and coating method: (a) dip-coated and (b) spin-coated ITO NCs templated with PB-*b*-PEO; (c) dip-coated and (d) spin-coated Mn_3O_4 NCs templated with PBO-*b*-PEO; (e) drop casted ITO NCs templated with PEP-*b*-PEO. Image adapted from reference 16.

The authors reported that, once again, disordered but homogeneous mesoporosity resulted from their technique (shown qualitatively by SEM in Figures 3.3 and 3.4), though porosity could be tuned through the choice of template (i.e., block sizes and types). The technique also produced films that showed significant microporosity, formed by the agglomerated nanocrystals, which could also be tuned, based on the nanocrystal size.[16]

3.4 Tuning the interaction potential between framework components

Taking a step back and examining assembly between two components from a broader landscape could provide clues as to how best to leverage individual component functionalities into ordered framework architectures; a review by Grzybowski and coworkers[18] on self-assembly provides the closer look needed. Self-assembly is described here to occur when molecules interact with one another through a balance of attractive interactions and entropic penalties, with the main challenge being the ability to 'program' the properties of the individual pieces such that they organize into a desired structure.[18]

This work makes two distinctions regarding assemblies between discrete materials. The first is the thermodynamic description to forming stable equilibrium structures, which are characterized by a maximum (local or global) in the system's entropy and no systematic energy flows.[18] The second refers to forming ordered, non-equilibrium structures, which are maintained far from equilibrium by a supply and subsequent dissipation (e.g., into heat) of useful energy.[18] As these types of systems are free from the constraints of entropy maximization, they can exist in lower entropy states often characterized by complex spatial or coherent spatio-temporal organization.[18] Further details of these descriptions as well as additional fundamentals governing self assembly can be found in reference 18.

Looking closer at the context of describing the interactions between amphiphilic BCPs and colloidal NCs, four types of interactions at the nanoscale driving assembly outcomes are identified (Figure 3.5): van der Waals, hydrogen bonding, electrostatics, and ionic.[2] For BCP–NC assemblies relying solely on weak, van der Waals-type interactions, typically NC surfaces are functionalized with short (M_n ~ 1300–1500 g mol^{-1}) homopolymer chains.[3,19] Though stable equilibrium structures form through the incorporation of the surface-functionalized NCs into the appropriate polymer block, it is difficult to architecture these components at high NC volume fraction. Two important factors stand out: first, the large increase in particle volume following surface functionalization occupies much greater space than the NC alone, and secondly, the energetic penalties of deforming the polymer chains on both the BCP template and NC surfaces to accommodate a higher volume of solids are too high. This would result in too few NCs available to buttress the framework following removal of the BCP template *via* annealing, leading to an expected collapse of the structure, as described in reference 3. Here, the frameworks are described as being 'fragile' in their final state.[3]

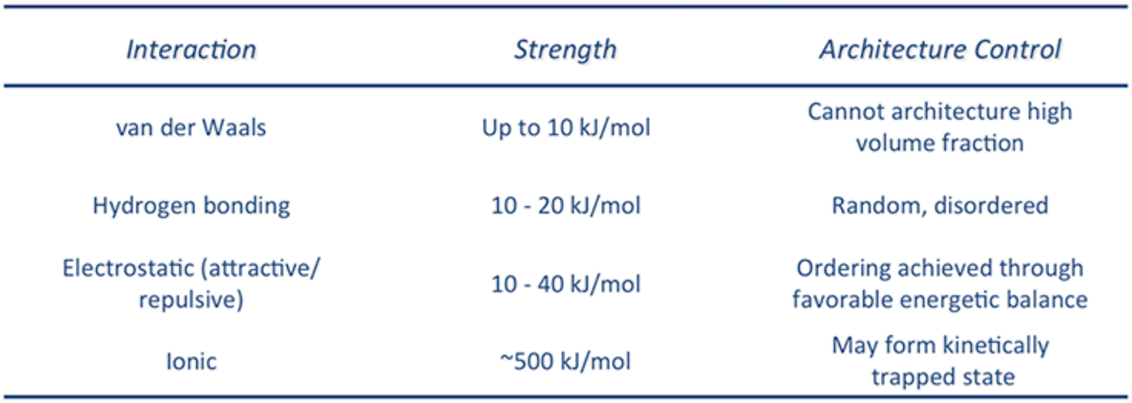

Interaction	*Strength*	*Architecture Control*
van der Waals	Up to 10 kJ/mol	Cannot architecture high volume fraction
Hydrogen bonding	10 - 20 kJ/mol	Random, disordered
Electrostatic (attractive/ repulsive)	10 - 40 kJ/mol	Ordering achieved through favorable energetic balance
Ionic	~500 kJ/mol	May form kinetically trapped state

Figure 3.5. Interactions between particles and surfaces for equilibrium self-assembly (ESA). Adapted from reference 18.

Interactions involving interfacial hydrogen bonding do provide a degree of enhanced strength between BCP–NC components, thereby allowing for an increased loading of NC solids and providing stability to the final framework following thermal annealing.[16] The higher loading is due in part to the decrease in overall volume for a particle bearing –OH functionality in its surface rather than oligomer/polymer surface ligands. Though this method makes an attempt at tuning interaction potentials between

BCP–NC components to access ordered, non-equilibrium structures, despite these efforts the final frameworks, as described in section 3.3, exhibited disordered, randomly organized pore structures due to a poor balance of interactions.

Using electrostatics to tune the attractive properties of BCP–NC components could allow for the greatest opportunity to form the desirable ordered framework architectures, though success will likely lie in the choice and combination of materials. Access to a cationic NC surfaces via ligand-stripping chemistries[17] factors strongly into this scenario, though it was shown, unfortunately, that typical PEO-based amphiphilic BCPs were unable to form strong enough interactions with these cationic surfaces to achieve an ordered arrangement of pores.[16] Again, the assembly process described was evaporation-induced in order to drive the NCs into the PEO corona of the preformed micelle, rather than one driven by a strong enthalpic interaction between the components.

In the scientific output to follow I investigate the use of polymeric materials designed and specifically tailored to interact with the surfaces of a wide variety of ligand-stripped NCs. The first goal is to determine how to impart enhanced functionality to single particles and render them water-soluble without losing their original properties (e.g., semiconducting, electronic). Applying this knowledge to systems of larger assemblies of NCs I investigate the use of a new class of amphiphilic BCPs designed to take advantage of electrostatic interactions between the NC-tethering domain of the BCP and the cationic surface of ligand-stripped NCs. From the well-ordered, tunable mesoporous frameworks that result from the ability to exert control over the assembly trajectory, I am able to explore not only quantitative, and novel, characterization techniques but also the use of the frameworks in device-oriented applications.

3.5 References

1. Wan, Y.; Zhao, D. “On the Controllable Soft-Templating Approach to Mesoporous Silicates” *Chem. Rev*. **2007**, *107*, 2821−2860.
2. Helms, B. A.; Williams, T. E.; Buonsanti, R.; Milliron, D. J. “Colloidal Nanocrystal Frameworks” *Adv. Mater.* **2015**, *27,* 5820–5829.
3. Orillal, M. C.; Wiesner, U. “Block copolymer based composition and morphology control in nanostructured hybrid materials for energy conversion and storage: solar cells, batteries, and fuel cells” *Chem. Soc. Rev*. **2011**, *40*, 520–535.
4. Sanchez, C.; Boissière, C.; Grosso, D.; Laberty, C.; Nicole, L. “Design, Synthesis, and Properties of Inorganic and Hybrid Thin Films Having Periodically Organized Nanoporosity” *Chem. Mater*. **2008**, *20*, 682–737.
5. Nedelcu, M.; Lee, J.; Crossland, E. J. W.; Warren, S. C.; Orilall, M. C.; Guldin, S.; Hüttner, S.; Ducati, C.; Eder, D.; Wiesner, U.; Steiner, U.; Snaith, H. J. “Block copolymer directed synthesis of mesoporous TiO_2 for dye-sensitized solar cells” *Soft Matter* **2009**, *5*, 134–139.
6. Yang, P.; Zhao, D.; Margolese, D. I.; Chmelka, B. F.; Stucky, G. D. “Generalized syntheses of large-pore mesoporous metal oxides with semicrystalline frameworks” *Nature* **1998**, *396*, 152–155.
7. Brezesinski, T.; Wang, J.; Senter, R.; Brezesinski, K.; Dunn, B.; Tolbert, S. H. “On the Correlation between Mechanical Flexibility, Nanoscale Structure, and Charge Storage in Periodic Mesoporous CeO_2 Thin Films” *ACS Nano* **2010**, *4*, 967–977.
8. Brezesinski, T.; Wang, J.; Tolbert, S. H.; Dunn, B. “Ordered mesoporous α-MoO_3 with iso-oriented nanocrystalline walls for thin-film pseudocapacitors” *Nat. Mater*. **2010**, *9*, 146–151.
9. Ortel, E.; Fischer, A.; Chuenchom, L.; Polte, J.; Emmerling, F.; Smarsly, B. M.; Kraehnert, R. “New Triblock Copolymer Templates, PEO-PB-PEO, for the Synthesis of Titania Films with Controlled Mesopore Size, Wall Thickness, and Bimodal Porosity” *Small* **2012**, *8*, 298–309.
10. Hartmann, P.; Lee, D.-K.; Smarsly, B. M.; Janek, J. “Mesoporous TiO_2: Comparison of Classical Sol−Gel and Nanoparticle Based Photoelectrodes for the Water Splitting Reaction” *ACS Nano* **2010**, *4*, 3147–3154.
11. Ren, Y.; Hardwick, L. J.; Bruce, P. G. “Lithium Intercalation into Mesoporous Anatase with an Ordered 3–D Pore Structure” *Angew. Chem., Int. Ed*. **2010**, *49*, 2570–2574.
12. Warren, S. C.; Messina, L. C.; Slaughter, L. S.; Kamperman, M.; Zhou, Q.; Gruner, S. M.; DiSalvo, F. J.; Wiesner, U. “Ordered mesoporous materials from metal nanoparticle–block copolymer self-assembly. *Science*, **2008**, *320*, 1748–1752.
13. Brezesinski, T.; Wang, J.; Polleux, J.; Dunn, B.; Tolbert, S. H. “Templated Nanocrystal-Based Porous TiO_2 Films for Next-Generation Electrochemical Capacitors” *J. Am. Chem. Soc*. **2009**, *131*, 1802–1809.
14. Lakshmi, B. B.; Patrissi, C. J.; Martin, C. R. “Sol−gel template synthesis of semiconductor oxide micro- and nanostructures” *Chem. Mater.* **1997**, *9*, 2544–2550.

15. Wang, J.; Polleux, J.; Lim, J.; Dunn, B. “Pseudocapacitive Contributions to Electrochemical Energy Storage in TiO_2 (Anatase) Nanoparticles” *J. Phys. Chem. C* **2007**, *111*, 14925–14931.
16. Rauda, I. E.; Buonsanti, R.; Saldarriaga-Lopez, L. C.; Benjauthrit, K.; Schelhas, L. T.; Stefik, M.; Augustyn, V.; Ko, J.; Dunn, B.; Milliron, D. J.; Tolbert, S. H. “General method for the synthesis of hierarchical nanocrystal-based mesoporous materials” *ACS Nano* **2012**, *6*, 6386–6399.
17. Dong, A.; Ye, X.; Chen, J.; Kang, Y.; Gordon, T.; Kikkawa, J. M.; Murray, C. B. “A Generalized Ligand-Exchange Strategy Enabling Sequential Surface Functionalization of Colloidal Nanocrystals” *J. Am. Chem. Soc.* **2011**, *133*, 998–1006.
18. Grzybowski, B. A.; Wilmer, C. E.; Kim, J.; Browne, K. P.; Bishop, K. J. “Self-assembly: from crystals to cells” *Soft Matter* **2009**, *5*, 1110–1128.
19. Chiu, J. J.; Kim, B. J.; Kramer, E. J.; Pine, D. J. “Control of nanoparticle location in block copolymers” *J. Am. Chem. Soc.* **2005**, *127*, 5036–5037.

Chapter 4

Instrumentation and characterization techniques

4.1 Imaging with electrons and X-rays

Electron and X-ray imaging are powerful tools and ubiquitous in the structural and chemical characterization of individual nanoscale components (NCs and polymeric materials), as well as their assemblies and resulting mesoporous frameworks.

4.1.1. Scanning electron microscopy (SEM)

This technique employs a focused electron beam to scan over a surface, generating information about the surface topography and sample composition. A schematic of a typical instrument is shown in Figure 4.1a. The sample interacts with the electrons in the beam to produce various signals, such as secondary electrons, backscattered electrons, and characteristic X-rays (Figure 4.1b). The electron beam, depending on the accelerating voltage and sample density, penetrates the sample up to a few microns in depth.[1] One or more detectors collect the signals and are used to form the images that are displayed on the computer screen. The resolution of the instrument, d, is related to the Abbe equation ($d = 0.61\lambda/n \sin \alpha$), with λ derived from the de Broglie equation ($\lambda = h/mv$); $n \sin \alpha$ is referred to as the numerical aperture, h is Planck's constant, m is electron particle mass, and v is electron particle velocity.[2] Resolution is typically ~10 nm for an instrument operating at 5 kV. A complete description of SEM can be found in reference 1. For the experiments in this dissertation a Zeiss Gemini Ultra-55 Analytical Scanning Electron Microscope was operated at an accelerating voltage of 5 kV using an In-Lens detector. The backscattered electron signal was collected to provide top-down and cross-sectional images of colloidal nanocrystal frameworks supported on either glass or Si substrates. For the experiments described in Chapter 7 an accelerating voltage of 3 kV was used due to the insulating nature of the thin film polymer–NC samples. Energy-Dispersive X-ray spectroscopy (EDS) experiments collected the characteristic X-ray signals of nanocrystal frameworks using an in-built EDAX detector operating at an accelerating voltage of 10 kV. Data was analyzed with Genesis software to obtain atomic percentages of each element of interest with 1–2% accuracy.

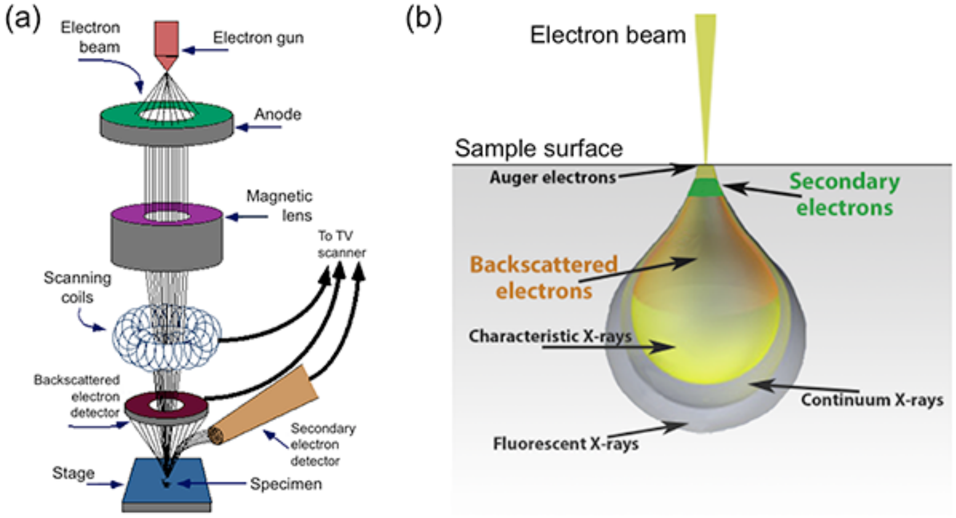

Figure 4.1. Scanning electron microscopy: (a) instrument schematic; (b) signals produced from the electron beam interacting with the sample. Images adapted from Nanoscience Instruments.

4.1.2. Transmission electron microscopy (TEM)

Transmission electron microscopy (Energy-Dispersive X-ray spectroscopy) uses a beam of high-energy (80–200 kV) electrons to transmit through a thin (~100 nm) sample, with the interactions between the electron beam and atoms in the sample providing a wealth of structural and chemical information. As shown in Figure 4.2a, the instrument can be operated in either diffraction mode or imaging mode and is dependent upon the inclusion of the selected-area diffraction (SAD) or objective apertures. Imaging mode, the technique used in this work, utilizes the objective aperture and the contrast seen in the image is due to diffraction/scattering contrast and mass–thickness contrast. The most common imaging mode of operation for a TEM is the bright field (BF), in which image contrast results from scattering and absorption of electrons in the sample.[2] This is why the field is 'bright'; in these areas there is no sample in the beam path. As with SEM, multiple signals are produced from the beam interacting with the sample and include backscattered electrons, secondary electrons, and characteristic X-rays but also elastically and inelastically scattered electrons (Figure 4.2b); each of these signals can be collected depending on the sample information of interest. The resolution of the instrument in 'amplitude contrast' mode is similarly related to the Abbe equation, as described in 4.1.1 for SEM. However, TEM resolution is much higher as a result from higher energy electrons used in the beam giving shorter wavelengths, leading to resolution ~0.1–1 nm, depending on the sample and instrument, further enhanced by employing a 'phase contrast' imaging mode. For a more complete overview of TEM see reference 2. A JEOL-2100F FETEM operating at an accelerating voltage of 200 kV was used to record BF-TEM images of NC dispersions, BCP–NC dispersions, and mesoporous NC frameworks. For some of the experiments described in Chapter 7, a Zeiss Libra 120 TEM operating at an accelerating voltage of 120 kV was used. Samples were prepared by dropping a dilute sample dispersion onto an ultrathin carbon film supported by a lacey carbon film on a 400 mesh copper grid (Ted Pella, 01824), unless otherwise described.

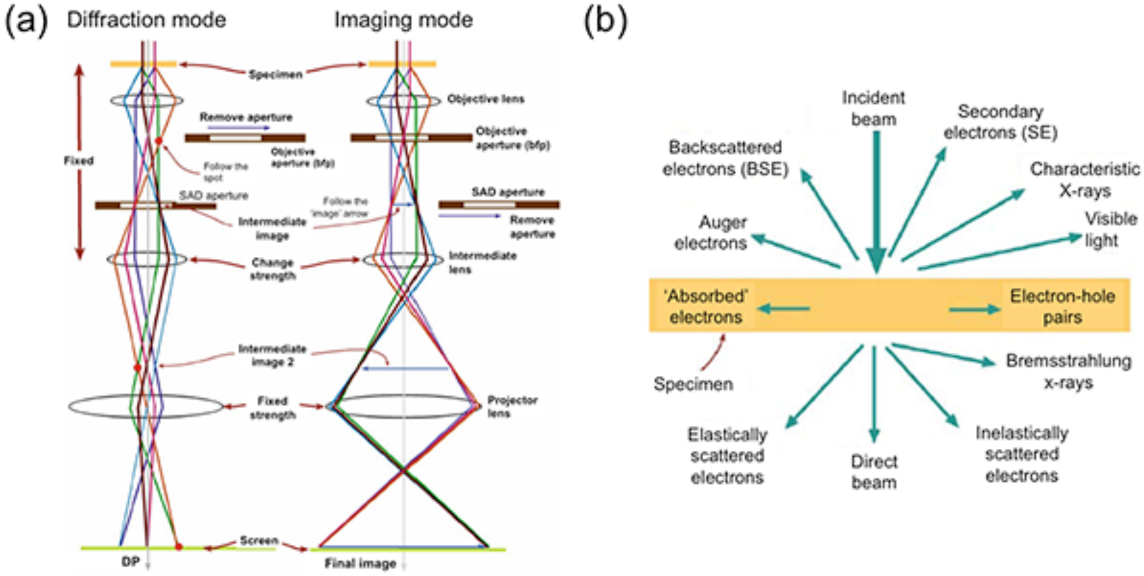

Figure 4.2. Transmission electron microscopy: (a) schematic of optics showing diffraction mode (left) and imaging mode (right); (b) signals produced from the beam interacting with the sample. Images adapted from reference 2.

4.1.3. X-ray diffraction (XRD)

X-ray diffraction (XRD) is defined as the constructive and destructive interference of X-rays by the regularly spaced atoms of a crystal and is used to study their interatomic distances, which typically range from ~0.15–0.5 nm.[3] Diffraction occurs only when Bragg's law ($n\lambda = 2d\sin\theta$) for constructive interference is satisfied, for crystal planes with spacing = d, at incident angle = θ, and X-ray wavelength = λ.[3] The technique is non-destructive and the apparatus is composed of a source of X-rays, a goniometer, the sample stage, and detector. In powder X-ray diffraction, the technique used in this dissertation, the goniometer rotates the monochromatic source and detector through a range of θ–2θ during the experiment. This enables the collection of diffraction from as many crystal planes as possible, which are randomly oriented in the powder sample. Data is presented as a plot of intensity *vs*. collection angle, with the Bragg equation used to convert θ to d. A collection of standard patterns for thousands of crystal structures is available as a searchable database by the International Center for Diffraction Data–Powder Diffraction File (ICDD–PDF) to verify experimental data. Further detailed information about this technique can be found in reference 3. A Bruker Gadds-8 diffractometer with a Cu-Kα source operating at 40 keV and 20 mA equipped and HI-STAR 2D detector was used for diffraction experiments. For the experiments described in Chapter 11, XRD was acquired on a Rigaku R-axis Rapid II diffractometer with Cu-

Kα source operating at 40 kV and 20 mA. Samples were prepared by drop casting a concentrated dispersion of NCs onto a glass substrate.

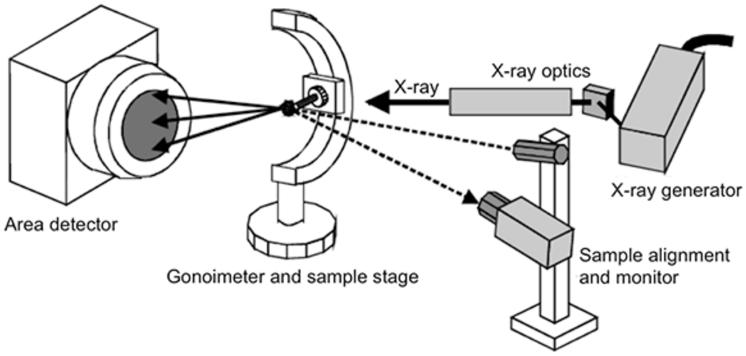

Figure 4.3. Schematic of X-ray diffraction apparatus. Image taken from www.icdd.com.

4.1.4. Grazing-incidence small angle X-ray scattering (GISAXS)

Grazing-incidence small angle X-ray scattering (GISAXS) is used for the characterization of micro- and nano-scale density correlations and shape analysis of objects at surfaces or as buried interfaces for various classes of materials.[4] As shown in Figure 4.4, a monochromatic X-ray beam, typically from a synchrotron source, with the wavevector k_i is directed on a sample surface with a very small incident angle α_i with respect to the surface. The z-axis is perpendicular to the sample plane; the x-axis is the direction along the surface parallel to the beam with the y-axis perpendicular to it. The X-rays are scattered along k_f in the direction ($2\theta_\mathrm{f}$, α_f) by any type of electron density fluctuations at the illuminated portion of the surface. A 2-D detector records the scattered intensity. Data analysis consists of using software applications to transform the 2-D data to 1-D in order to plot signal intensity vs. q (i.e., reciprocal space). Reciprocal space values (q) are converted to real space values (d) using the Bragg equation ($d = 2\pi/q$).[4] While GISAXS experiments are carried out in reflection geometry, solution phase small angle X-ray scattering (SAXS) experiments are instead performed in transmission mode. A complete description of GISAXS can be found in reference 4. For a concise review on using GISAXS for the analysis of nanoparticle-based self-assembly see reference 5. Measurements were performed at beamline 7.3.3 at the Advanced Light Source, Lawrence Berkeley National Laboratory, using an approximately 0.5 mm wide, 10 keV X-ray beam. An ADSC Quantum 4R detector was used with the detector distance set at 3 m. The image processing was carried out in IgorPro using SAS 2D program. For the solution phase SAXS experiments described in Chapter 7, sample dispersions in toluene (NCs) or 2:8 *v/v* DMF:EtOH (micelles) were enclosed in glass capillaries (Charles-Supper Company, Boron Rich, 1.5 mm diameter, 0.01 mm wall thickness). For these experiments data extraction and fitting was carried out using IgorPro Nika and Irena tool suite for modeling and analysis of small angle X-ray scattering data.[6-10]

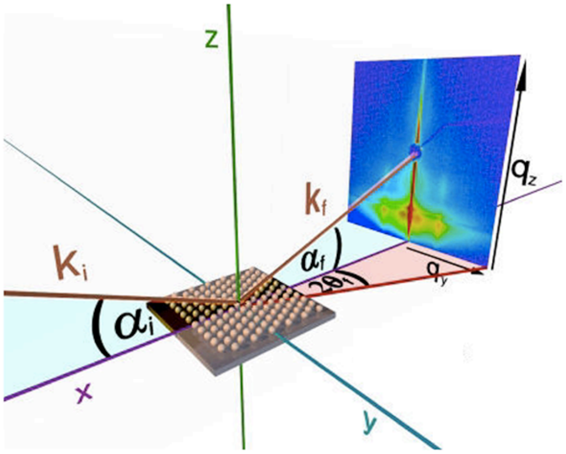

Figure 4.4. Schematic showing GISAXS experimental set up. Image adapted from www.gisaxs.de.

4.2 Spectroscopy

Spectroscopy is defined as the branch of science concerned with the investigation and measurement of the energy dispersion produced when matter interacts with or emits electromagnetic radiation. When quantitative assessment is performed, the technique is more accurately described as ‘spectrometry’. The techniques are typically classified by the wavelength region of the spectrum (e.g., infrared, visible, ultraviolet) and are categorized by absorption, emission, or scattering.

4.2.1 Nuclear magnetic resonance (NMR)

Nuclear magnetic resonance (NMR) spectroscopy studies the absorption of radiofrequency radiation by nuclei in a magnetic field, most commonly ^{1}H and ^{13}C, and is used for the determination/characterization of organic structures. Any nuclei with an odd mass or odd atomic number, having a nuclear spin $l = ½$, can be analyzed. The magnetic field generated from nuclei either aligns itself with (lower energy), or against (higher energy), the instrument’s applied magnetic field. When radio waves are applied, nuclei in the lower energy state can absorb the energy and jump to the higher energy state. Either the absorption of energy, or the subsequent release of energy as the nucleus relaxes back to the lower energy state, can be observed. An NMR spectrum is a plot of the radio frequency applied against absorption. Sample preparation involves dissolving the material of interest in a deuterated solvent in order to avoid spectra dominated by the solvent signal. Reference 11 should be consulted for a thorough description of this technique and its application for organic materials. For the experiments included in this dissertation, proton (^{1}H) and carbon (^{13}C) NMR are used to characterize the different types and numbers of these atoms present in the sample. A 500 MHz Bruker Biospin spectrometer is used in the study.

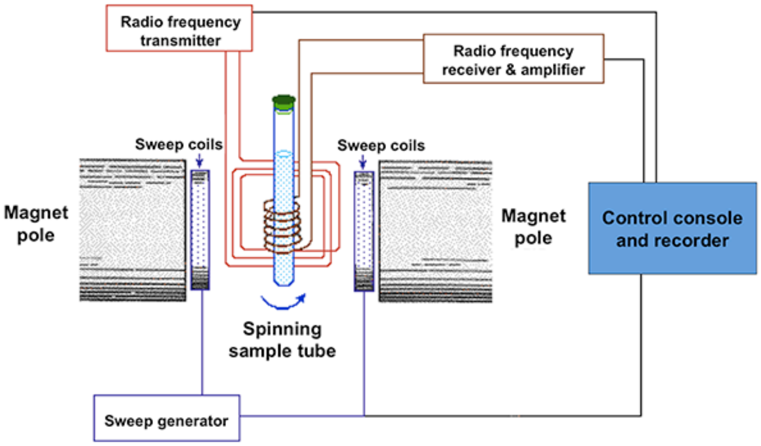

Figure 4.5. Schematic showing NMR experimental apparatus. Image adapted from https://www2.chemistry.msu.edu.

4.2.2 Fourier transform infrared spectroscopy (FT-IR)

In Fourier transform infrared spectroscopy (FT-IR) IR radiation is passed through a sample; some radiation is absorbed and some is transmitted. The absorbed radiation of specific wavelengths causes the change in the dipole moment of sample molecules due to stretching, bending, or twisting of chemical bonds.[12] Therefore, the vibrational energy levels of sample molecules transfer from ground state to excited state, with the frequency of the absorption peak determined by the vibrational energy gap.[12] Experiments are carried out by first collecting an interferogram of a sample signal using an interferometer, and then performing a Fourier Transform (FT) on the interferogram to obtain the spectrum, generating a plot of % transmission vs. wavenumbers. FT-IR is used to determine the spectral fingerprint of a sample, is highly sensitive to certain function groups in a molecule, and can also be used for compound identification. A complete description of FT-IR can be found in reference 12. A Perkin-Elmer Spectrum One Spectrometer equipped with a ZnSe prism using a Horizontal Attenuated Total Reflectance (HATR) sampling accessory is used for the experiments in this dissertation.

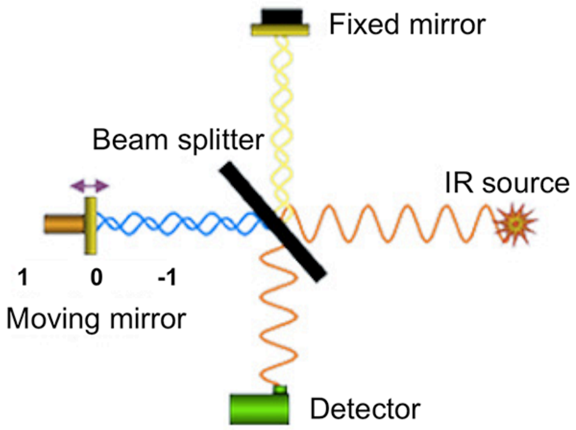

Figure 4.6. Schematic showing FT-IR apparatus. Image adapted from ThermoFisher Scientific.

4.2.3 Dynamic light scattering (DLS)

Dynamic light scattering (DLS) measures the Brownian motion of a particle and uses it to determine the particle's size. When suspended in solution, microscopic particles are constantly in random motion; this motion scatters light, transmitting through the sample, in all directions and can be detected as a function of intensity fluctuation vs. time.[13] This result is used to determine the diffusion coefficient, D_t. The relationship between the size of a particle and its speed due to Brownian motion is defined in the Stokes-Einstein equation, $D_h = k_B T/3\pi\eta D_t$.[14] Here, D_h is the particle size, or hydrodynamic radius, k_B is Boltzmann's constant, T is experiment temperature, η is viscosity. A complete description of Brownian motion can be found in reference 13. For further details of DLS, see reference 14. Dynamic light scattering (DLS) experiments were carried out using a Malvern Nano Series Zetasizer in order to determine sizes of individual framework components as well as their assemblies.

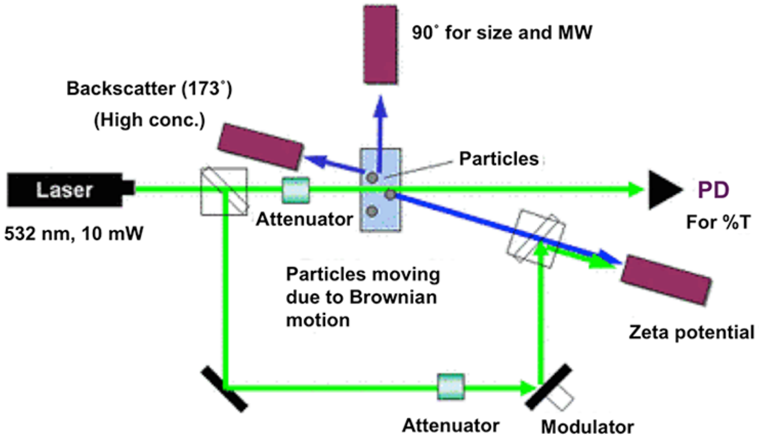

Figure 4.7. Schematic of DLS apparatus. Image adapted from Horiba Instruments.

4.2.4 Ultraviolet-Visible Near-infrared (UV-Vis-NIR) spectroscopy

Ultraviolet-Visible Near-infrared (UV-Vis-NIR) spectroscopy is a technique used to quantify the light that is absorbed and scattered by a sample, covering a range of wavelengths from 250–2500 nm. The sum of absorbed and scattered light defined as extinction.[15] Absorbance, A, is determined by Beer's Law ($A = ebc$): b is the path length of the beam, c is the sample concentration, e is the molar extinction coefficient. A thorough description of Beer's Law can be found in reference 15. As shown in the schematic below (Figure 4.8), the sample is placed between a light source (lamp) and detector (diode array). The UV-Vis-NIR beam passes through the sample and the intensity is measured before and after passing. A molecule absorbs radiation at different wavelengths, which corresponds to the excitation of outer shell electrons that are promoted from their ground state to an excited state. This characterization method provides information about electronic structure, types of bonds, and sample concentration, among others. For a concise review on using NIR spectroscopy for the analysis of plasmonic nanocrystals, consult reference 16. An Agilent–Cary 5000 spectrophotometer (beam path length = 1 cm) was used for most UV-Vis-NIR experiments, with some samples analyzed using an ASD LabSpec Pro Vis-NIR spectrophotometer.

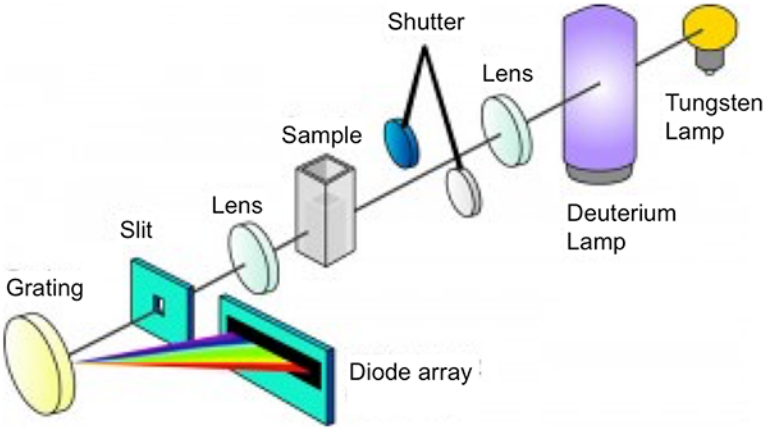

Figure 4.8. Schematic of UV-Vis-NIR apparatus. Image adapted from Nanocomposix.

4.2.5 Fluorescence spectroscopy

Fluorometry is a technique that measures the amount of light absorbed (excitation) or emitted (emission) by a sample upon radiation with light. To record an excitation spectrum, the emission monochromator is set at the desired wavelength and the excitation monochromator is scanned. Setting the excitation wavelength and scanning wavelength with the emission monochromator record an emission spectrum. At room temperature most molecules occupy the lowest vibrational level of the ground electronic state, and on absorption of light they are elevated to produce excited states.[17] Very shortly after excitation, within nanoseconds, the sample emits a photon of a longer wavelength and relaxes back to the ground state; this is called fluorescence.[17] Samples typically absorb in the UV or Vis range, and emit in the Vis or NIR range. A complete description of fluoresence spectroscopy can be found in reference 17. For a concise review of quantum yield as related to colloidal nanocrystals, see reference 18. Photoluminescence spectra and absolute quantum yield experiments were carried out using a Horiba Jobin Yvon Fluorolog-3 Spectrofluorometer equipped with an integrating sphere.

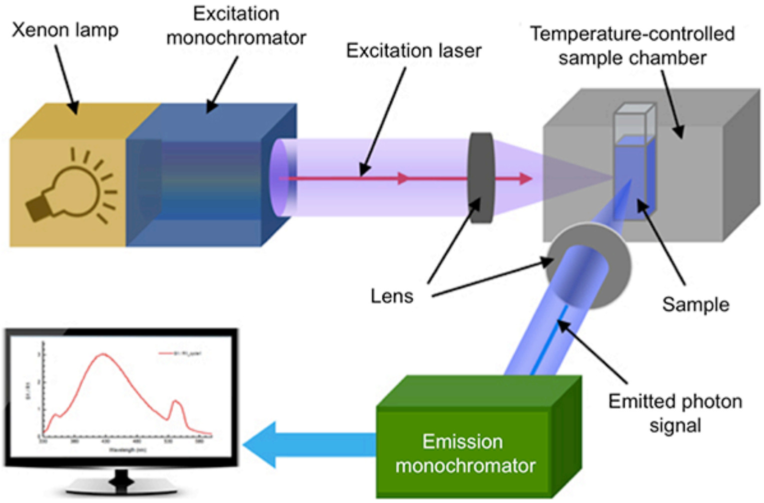

Figure 4.9. Schematic of fluorescence spectrometer. Image adapted from reference 19.

4.2.6 Inductively coupled plasma–optical emission spectroscopy (ICP–OES)

Inductively coupled plasma–optical emission spectroscopy (ICP–OES) is an analytical technique used for the detection of trace metals in the ppb and ppm range.[20] The instrument is composed of two parts: ICP and OES (Figure 4.10). For ICP, Argon gas is typically used to generate the plasma. Upon introduction, the sample (aqueous mist) collides with the electrons and charged ions in the plasma to produce excited atoms and ions that emit electromagnetic radiation at wavelengths characteristic of a particular element are generated. In the OES optical chamber the light emitted from the sample is separated into different wavelengths and the light intensity is measured for the specific wavelength of each element involved. A set of standards of known concentrations is run for each element of interest to create a calibration curve with interpolation along the calibration line determining the concentration of each element of interest. Reference 20 provides a more complete description of the technique. Within the context of this dissertation, ICP-OES was used to determine the ratio of elements for colloidally-synthesized doped nanocrystals. Analysis was carried out on a Varian 720 Series ICP–OES. Nanocrystal samples were digested in concentrated hydrochloric acid prior to analysis.

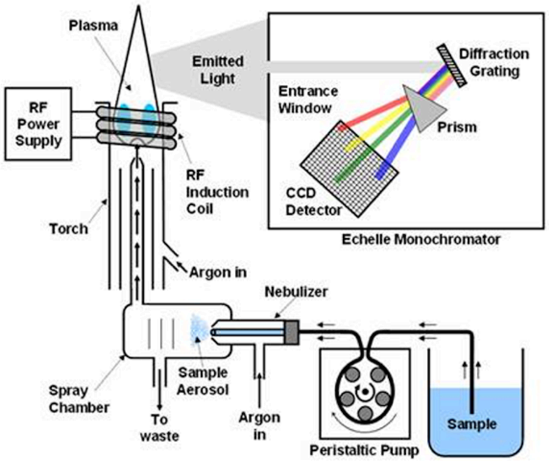

Figure 4.10. Schematic of inductively coupled plasma–optical emission spectroscopy instrument. Image adapted from U.S. Geological Survey.

4.3 Thin film preparation and characterization

4.3.1 Solution deposition of block copolymer-nanocrystal films

Thin films solid substrates (e.g., glass or Si) can be prepared from a variety of solution-processable techniques. The simplest of which is drop-casting, where a sample droplet is pipetted onto the substrate and allowed to dry. In dip-coating the substrate is dipped and withdrawn from the desired solution at a controlled rate and often in a controlled environment (relative humidity) (Figure 4.11a). Film thickness is controlled by the concentration of sample dispersion as well as the withdrawal rate, and the film coats both sides of the substrate. In spin coating, a droplet of viscous solution is placed onto the surface of the substrate followed by the subsequent spinning of the substrate holder at high angular speed (800–3000 rpm) (Figure 4.11b). The sample spreads and coats the substrate due to centripetal forces. Film thickness is controlled by the concentration of the sample dispersion as well as the spin speed. A more complete description of these techniques can be found in reference 20. Each of these film deposition techniques was used in this dissertation to prepare samples from dispersions of nanocrystals, polymers, and their assemblies, with details provided on conditions where appropriate.

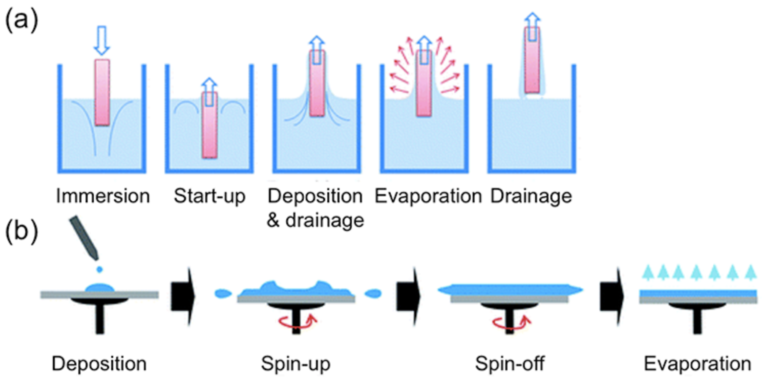

Figure 4.11. Solution processable film preparation for BCP-NC films: schematics of (a) spin-coating and (b) dip-coating. Images adapted from reference 20.

4.3.2 Profilometry

Profilometry is a technique used to measure surface topography of a sample of interest using either a contact (stylus) or non-contact (optical) method. In contact profilometry, which is the technique used in this dissertation, a diamond stylus moves laterally across the sample at a specified contact force while also moving vertically in response to the surface. Features ranging in height from 10 nm to 1 mm are typically measured; this technique can therefore be used to measure film thickness for thin films cast onto glass or Si. As it scans, the height position of the stylus records an analog signal that is converted into a digital signal, then stored, analyzed, and displayed. The resolution depends on the radius of the stylus tip, as shown in Figure 4.12, as well as the scan speed and data signal sampling rate. Reference 22 provides a concise description of this technique to measure film thickness. A Veeco Dektak 150+ Profiler was used to measure film thickness following scratching the surface of the film with a clean razor blade.

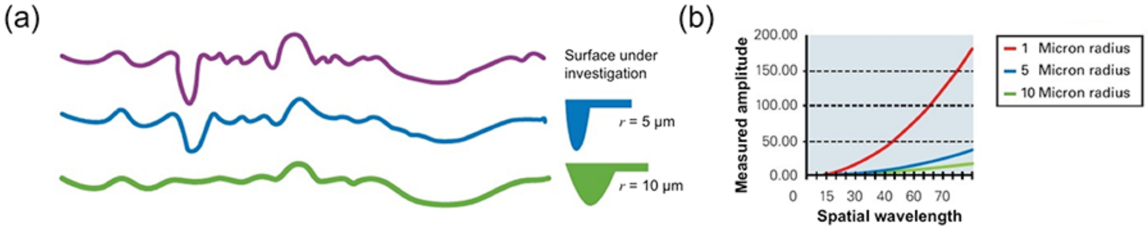

Figure 4.12. Description of contact mode analysis and resolution as related to stylus radius. Image adapted from AZO Materials.

4.3.3 Ellipsometric porosimetry (EP)

Ellipsometric porosimetry (EP) is a technique to determine thickness, porosity, and pore structure of thin films by measuring the change in the incoming, polarized spectral light reflected as solvent (e.g, toluene) vapor is adsorbed/desorbed within the pores of the film (Figure 4.13a). A spectrum is collected at each point of the cycle for relative solvent pressure, p/p_0, until reaching saturation. The known optical properties of the sample, namely the refractive index, n, and extinction coefficient, k, are used to extract the data. The Lorentz-Lorenz equation is used to transform refractive index (Figure 4.13b) to volume absorbed. The modified Kelvin equation is used to transform volume absorbed to pore size. The amplitude ratio, Ψ, and the phase difference, Δ, are also directly measured as a function of wavelength. Reference 23 provides a complete description on using EP for the determination of pore size distribution. Data was acquired on a SEMILAB PS-1100R and analyzed with the accompanied Spectroscopic Ellipsometry Analysis (SEA) software.

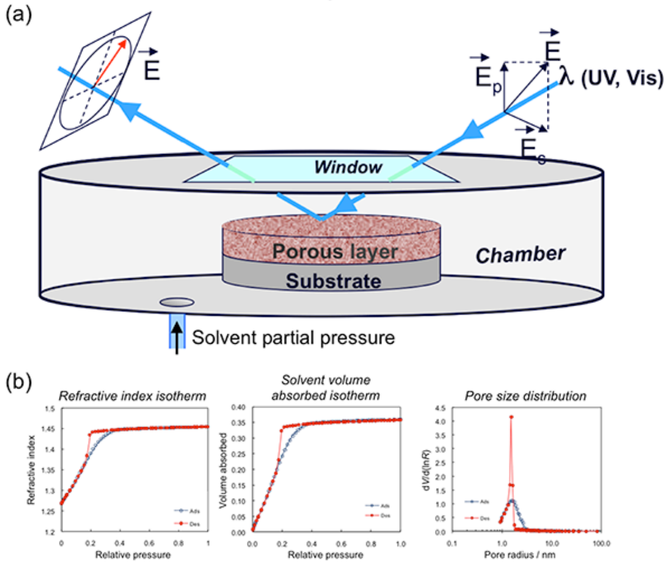

Figure 4.13. Ellipsometric porosimetry: (a) instrument schematic; (b) examples of plots for extracted data. Images adapted from SEMILAB.

4.3.4 Rutherford Backscattering (RBS)

In Rutherford Backscattering (RBS) a beam of high-energy (2 MeV) helium ions is directed at a thin film sample; those ions elastically scattered by nuclei in the sample are detected. Discrimination between atoms in the sample is determined by the energy of the backscattered ion, as atoms with higher masses produce scattered ions with higher energies.[24] The detector is placed at an angle of 170° from the sample to collect the backscattered ions (Figure 4.14). Hydrogen is the only atom that cannot be detected as backscattering occurs only from atoms that are heavier than the projectile ion.[24] An advantage of RBS is that it yields the amount of atoms present quantitatively without the need for any calibration standard. Reference 24 can be consulted for a complete description of the theory behind this technique. RBS was used in the context of this dissertation as a method for determining the volume fraction of solids (f_{NC}) in mesoporous, nanocrystal-based films on a Si. Data was collected using a 5SDH Pelletron tandem accelerator (National Electrostatics Corporation). Samples were analyzed using SIMNRA software.

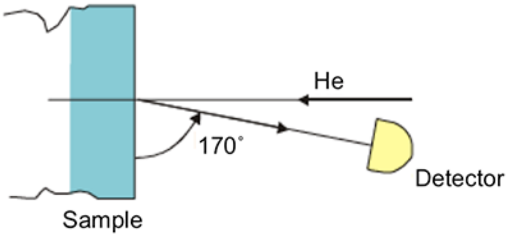

Figure 4.14. Schematic of Rutherford backscattering experiment. Image adapted from Philips Innovation labs.

4.4 Characterization of physical properties of individual framework components

4.4.1 Size exclusion chromatography (SEC)

Size exclusion chromatography (SEC) separates particles based upon their size and is useful for the analysis of the molecular weight distribution of a polymer. The instrument is made up of a mobile phase (solvent), injector, pump, column(s), and detector(s), as shown in Figure 4.15a. The sample is loaded onto the column, carried by the mobile phase, and, due to the microporous nature of the gel packing material, smaller particles, or shorter polymer chains, are retained and larger particles, or longer polymer chains, are excluded (Figure 4.15b). Detectors (e.g., light scattering, refractive index, viscometer) collect the signal of the eluted material and use the information to plot signal intensity *vs*. time. The system is calibrated with a known standard of narrow polydispersity. Though several important parameters are determined, often the most valuable are number average molecular weight (M_n), weight average molecular weight (M_w), and polydispersity index (PDI = M_w/M_n). For a concise overview of the theory and methods used in this study, see reference 25. In this dissertation, SEC employing tetrahydrofuran (THF) as the mobile phase was carried out on a Malvern Viscotek TDA 302 system operating at a temperature of 35 ˚C and equipped with refractive index, light scattering, and viscometer detectors. The system was calibrated against a narrow polystyrene standard of 99,000 g mol^{-1}. For SEC using *N,N*-dimethylformamide (DMF) (containing 0.2% *w/v* lithium bromide, LiBr) as the mobile phase, a home built system was used and consisted of a Shimadzu LC-20AD pump, Viscotek VE 3580 refractive index detector, and two mixed bed columns connected in series (Viscotek GMHHR-M). The system was operated at a temperature of 70 ˚C. Calibration on the system was performed with narrow polymethylmethacrylate standards (Polymer Laboratories) ranging from 620 g mol^{-1} to 910,500 g mol^{-1}.

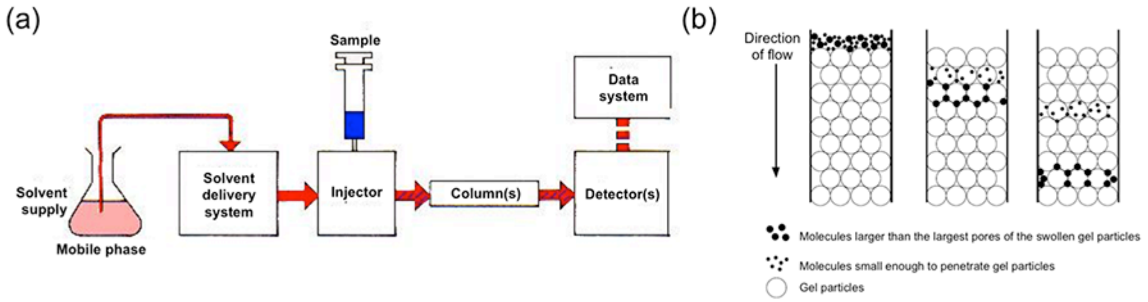

Figure 4.15. Size exclusion chromatography: (a) schematic of instrumentation and (b) description of method of separation. Images adapted from Waters Corporation.

4.4.2 Thermogravimetric analysis (TGA)

Thermogravimetric analysis (TGA) is a technique in which the mass of a substance is monitored as a function of temperature or time as the sample specimen is subjected to a controlled temperature program in a controlled atmosphere. As a result, depending on its properties, the weight of the sample will either increase or decrease. TGA main components are a sample pan, supported by a precision balance, which resides in a furnace that is heated (or cooled) during the experiment (Figure 4.16). The mass of the sample is monitored during the experiment and an inert sample purge gas controls the sample environment. For the experiments described in this dissertation TGA was useful for revealing the decomposition temperature for organic polymeric materials and also to determine the concentration of nanocrystals in a dispersion of organic solvent. A TA Instruments Q5000IR TGA-mass spectrometer (MS) was used to collect the data.

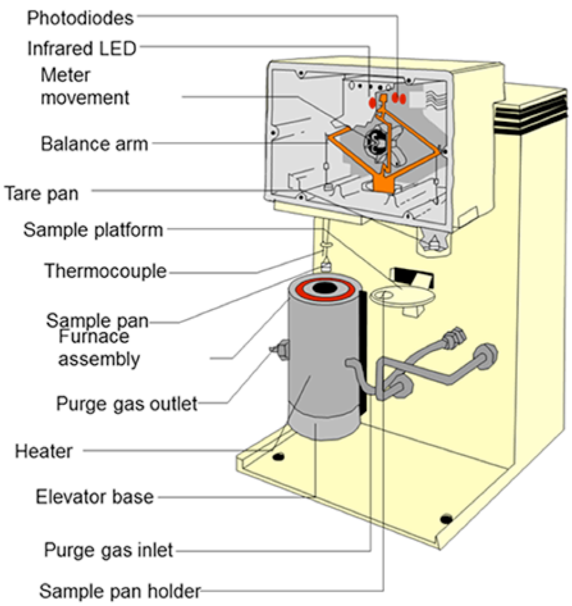

Figure 4.16. Schematic of thermogravimetric analytical instrumentation. Image adapted from TA Instruments.

4.5 Electrochemical experiments

Electrochemistry is based on the study of oxidation–reduction reactions. All electrochemical measurements were performed in an argon glove box, maintained below 1 ppm of water and oxygen, with a Bio-logic VSP potentiostat, and spectroscopy performed using an ASD Quality Spec Pro VIS–NIR spectrometer in a home-built spectroelectrochemical apparatus.

4.5.1 Cyclic voltammetry (CV)

Cyclic voltammetry (CV) is an electrochemical technique that measures redox events. It can be used to study the electrochemical behavior of species diffusing to an electrode surface, interfacial phenomena at an electrode surface, and bulk properties of materials in or on electrodes.[26] The experiment is carried out by cycling the potential of a working electrode and measuring the resulting current. The apparatus typically consists of a three-electrode cell containing a working electrode, counter electrode, and reference electrode, immersed in an electrolyte and connected to a potentiostat, which controls the voltage difference between the working electrode and reference electrode (Figure 4.17a). The potential of the working electrode is measured against a reference electrode that maintains a constant potential, and the resulting applied potential produces an excitation signal, or the ‘input waveform’.[26] This is a plot of potential *vs*. reference electrode (E) as a function of time; the peak indicates the switching potential, or the point where the voltage is sufficient enough to cause an oxidation or reduction event (Figure 4.17a). The slope of the trace indicates the scan rate. Figure 4.17b shows a cyclic voltammogram, obtained by measuring the current at the working electrode during the potential scans. The single peak in the cathodic and anodic scans indicates a single electron oxidation–reduction process, as described by: $\mathrm{Metal}^{+} + e^{-} \rightleftarrows \mathrm{Metal}$. Reference 26 provides a complete description of the fundamentals of CV.

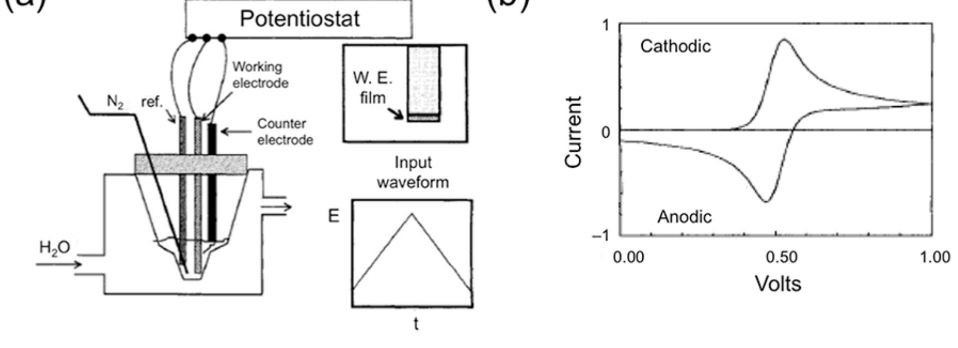

Figure 4.17. Cyclic voltammetry: (a) schematic of apparatus; (b) example of cyclic voltammogram. Image adapted from reference 26.

4.5.2 Chronoamperometry

Chronoamperometry is the measurement of current at a fixed potential over time, using a similar apparatus to CV. The experiment is unstirred, so mass transport to the electrode is by diffusion.[27] Figure 4.18 shows two data plots generated by the experiment. In 4.18a, the potential is held steady at E_1 then after a period of time reduced to E_2. The impact on measured current is shown in Figure 4.18b, where the current first increases as a response to the potential until it levels off; when the potential is reduced the current increases then again decays.[27] This phenomenon is described by the Cottrell equation, $nFAc_j^0\sqrt{D_j}/\sqrt{\pi t}$). Here, i is current, n is number of electrons, F is Faraday constant, A is planar area of the electrode, c_j^0 is the initial concentration of analyte, D_j is diffusion coefficient, t is time. Only t is measured, the rest are constants. This technique is used to measure the amount of active material on a working electrode. A review of the fundamentals of the technique can be found in reference 27.

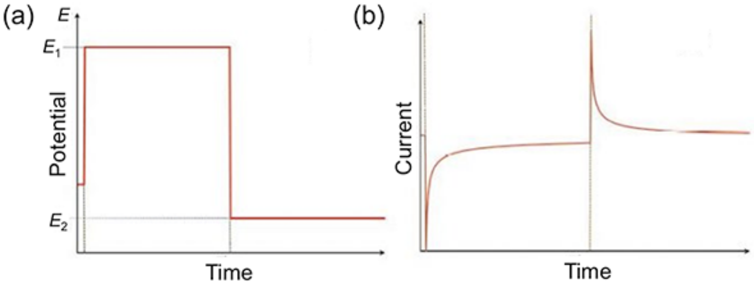

Figure 4.18. Examples of chronoamperometric curves: (a) potential *vs*. time; (b) resulting current *vs*. time. Image adapted from Gamry Instruments.

4.5.3 Spectroelectrochemistry

Spectroelectrochemistry is a technique that combines the investigation of electrochemical and optical processes simultaneously to study single and multiple electron-transfer processes and redox reactions.[28] Spectroscopic methods can include absorption in the UV, Vis, NIR, or IR. As seen in the schematic in 4.19, light passes through the cell, which is coupled to both a potentiostat and spectrometer. The spectrometer's detector converts photocurrent from light into electric current, with the output depending mainly on the intensity of light that passes through the sample cell. Three parameters are determined: light intensity, I, is the amount of light passing through the sample; transmittance, T, the ratio of light passing through the sample; and absorbance, A, or $-\log(T)$. Reference 28 provides a full description of the theory supporting this technique. For the experiments in this dissertation, potential was held at a set value to determine transmittance through the sample as a function of wavelength.

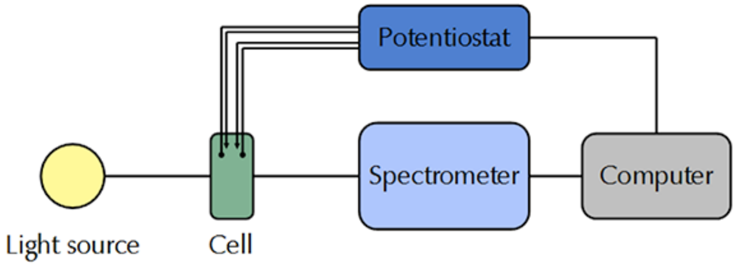

Figure 4.19. Schematic of spectroelectrochemistry apparatus. Image adapted from Gamry Instruments.

4.6 References

1. Reimer, L. *Scanning Electron Microscopy: Physics of Image Formation and Microanalysis, 2nd Edition*. New York: Springer, 1998. Print.
2. Williams, D. B.; Carter, C. B. *Transmission Electron Microscopy, 2nd Edition*. New York: Springer, 2009. Print.
3. Fultz, B.; Howe, J. M. *Transmission Electron Microscopy and Diffractometry of Materials, 3rd Edition*. New York: Springer, 2008. Print.
4. Müller-Buschbaum, P. "A Basic Introduction to Grazing Incidence Small-Angle X-ray Scattering." Applications of Synchrotron Light to Scattering and Diffraction in Materials and Life Sciences. Berlin: Springer, 2009. 61–89. Print.
5. Corricelli, M.; Altamura, D.; Curri, M. L.; Sibillano, T.; Siliqi, D.; Mazzone, A.; Depalo, N. Fanizza, E.; Zanchet, D.; Giannini C.; Striccoli M. "GISAXS and GIWAXS study on self-assembling processes of nanoparticle based superlattices" *CrystEngComm*. **2014**, 1*6*, 9482–9492.
6. Ilavsky J.; Jemian; P. R. "Irena: tool suite for modeling and analysis of small-angle scattering" *J. Appl. Cryst*. **2009**, *42*, 347–353.
7. Zhang, F.; Ilavsky, J.; Long, G. G.; Quintana, J. P. G.; Allen, A. J.; Jemian, P.; *Metall. Mater. Trans. A* **2009**, *41*, 1151–1158.
8. Nelson A. "Co-refinement of multiple-contrast neutron/X-ray reflectivity data using MOTOFIT" *J. Appl. Cryst.* **2006**, *39*, 273–276.
9. Beaucage, G. "Approximations Leading to a Unified Exponential/Power-Law Approach to Small-Angle Scattering" *J. Appl. Cryst.* **1995**, *28*, 717–728.
10. Ilavsky, J. "Nika: software for two-dimensional data reduction" *J. Appl. Cryst*. **2012**, *45*, 324–328.
11. Jackman, L. M.; Sternhell, S. *Application of Nuclear Magnetic Resonance Spectroscopy in Organic Chemistry, 2nd Edition*. New York: Pergamon Press, 1969. Print.
12. Smith, B. C. *Fourier Transform Infrared Spectroscopy, 2nd edition*. New York: CRC Press, 2011. Print.
13. Uhlenbeck, G. E.; Ornstein L. S. "On the theory of the Brownian motion" *Phys. Rev.* **1930**, *36*, 823–841.
14. Goldburg, W. I. "Dynamic light scattering" *Am. J. Phys*. **1999**, *67*, 1152–1160.
15. Swinehart, D. F. "The Beer-Lambert Law" *J. Chem. Educ.* **1962**, 3*9*, 333–335.
16. Lounis, S. D.; Runnerstrom, E. L.; Llordés, A.; Milliron, D. J. "Defect Chemistry and Plasmon Physics of Colloidal Metal Oxide Nanocrystals" *J. Phys. Chem. Lett.* **2014**, *5*, 1564−1574.
17. Lakowicz, J. R. *Principles of Fluorescence Spectroscopy, 3rd Edition*. New York: Springer, 2006. Print.
18. Grabolle, M.; Spieles, M.; Lesnyak, V.; Gaponik, N.; Eychmüller, A.; Resch-Genger, U. "Determination of the Fluorescence Quantum Yield of Quantum Dots: Suitable Procedures and Achievable Uncertainties" *Anal. Chem.* **2009**, *81*, 6285–6294.
19. Li, C.; Yue, Y. "Fluorescence spectroscopy of graphene quantum dots: temperature effect at different excitation wavelengths" *Nanotech*. **2014**, *25*, 435703–435710.

20. Montaser, A.; Golightly, D.W. *Inductively Coupled Plasmas in Analytical Atomic Spectrometry, 2^{nd} Edition*. New York: VCH, 1992. Print.
21. Raut, H. K.; Ganesh, V. A.; Nairb, A. S.; Ramakrishna, S. "Anti-reflective coatings: A critical, in-depth review" *Energy Environ. Sci.* **2011**, *4*, 3779–3804.
22. Wood, J. W.; Redin, R. D. "A simple profilometer for film thickness measurement" *Rev. Sci. Instrum*. **1993**, *64*, 2405–2406.
23. Baklanova, M. R.; Mogilnikov, K. P.; Polovinkin, V. G.; Dultsev, F. N. "Determination of pore size distribution in thin films by ellipsometric porosimetry" *J. Vac. Sci. Technol. B* **2000**, *18*, 1385–1391.
24. Chu, W.-K.; Mayer, J. W.; Nicolet, M.-A. *Backscattering Spectrometry*. New York: Academic Press, 1978. Print.
25. Moore, J. C.; Hendrickson, J. G. "Gel permeation chromatography. II. The nature of the separation" *J. Poly. Sci. Part C: Polymer Symposia*, **1965**, *8*, 233–241.
26. Rusling, J. F., Suib, S. L. "Characterizing Materials with Cyclic Voltammetry" *Adv. Mater*. **1994**, *6*, 922–930.
27. Henstridge, M. C.; Compton, R. G. "Mass transport to Micro- and Nanoelectrodes and their arrays: A review" *Chem. Rec*. **2012**, *12*, 63–71.
28. Kaim, W.; Fiedler, J. "Spectroelectrochemistry: the best of two worlds" *Chem Soc. Rev.* **2009**, *38*, 3373–3382.
29. Orazem, M. E.; Tribollet, B. *Electrochemical Impedance Spectroscopy*. Hoboken: Wiley, 2008. Print.

Understanding the local environment of nanocrystal surfaces

Chapter 5

Efficient polymer passivation of ligand-stripped nanocrystal surfaces

Adapted from:

Jennifer T. Duong, Mark J. Bailey, Teresa E. Pick,[1] Patrick M. McBride, Evelyn L. Rosen, Raffaella Buonsanti, Delia J. Milliron, Brett A. Helms. “Efficient polymer passivation of ligand-stripped nanocrystal surfaces” *Journal of Polymer Science Part A: Polymer Chemistry* **2012**, *50*, 3719–3727.

5.1 Introduction

Colloidal nanocrystals (NCs) are well suited for a variety of important biomedical applications, such as drug delivery,[1] bioimaging,[2,3] bioassays,[4–6] and (bio)chemical remediation.[7,8] As such, aqueous dispersibility is required for their incorporation into such applications. The hydrophobicity of their native ligand shell, however, is a significant barrier to their aqueous transfer as single particles. [9,10] Ligand exchange with hydrophilic small molecules or, alternatively, wrapping over native ligands with amphiphilic polymers is widely employed for aqueous transfer; however, purification can be quite cumbersome. [11–13] Alternatively, native hydrophobic ligands can be displaced from the nanocrystal surface by exchanging with small molecules that contain chemical functionality directed toward metal adatoms at the nanocrystal surface.[14–19] The generality of this approach is less straightforward, as the adsorption enthalpies vary widely between various nanocrystal compositions and ligand types (anionic, dative, multivalent, etc.). In most cases, because driving the ligand exchange involves mass action,[20–27] often at high temperatures,[28–31] or non-equilibrium control via phase transfer,[32–37] the exchange efficiency is typically low. Inefficient exchange protocols may also cause undesirable nanocrystal aggregation,[38,39] in particular for biphasic procedures, and often results in irreversible adatom desorption from the nanocrystal surface or irreversible precipitation. A more attractive approach would involve the removal of hydrophobic ligands to reveal a bare, pristine nanocrystal surface for subsequent repassivation. This has been difficult to achieve without degradation of the nanocrystal, and hence has not been previously explored.

In this chapter I investigate how bare nanocrystal surfaces generated using trialkyloxonium salts, with metal adatoms intact, are readily passivated by a variety of functional polymers based on the synthetically-accessible polyacrylic acid (PAA) platform. The two-step strategy is highly general, and is highlighted here for dispersions of metal oxide, metal chalcogenide, and inorganic nanocrystals. The PAA scaffold is especially desirable because of the simplicity in which it can be functionalized with various end groups or side chains of differing composition or grafting density. Several new polymer coatings based on PAA are synthesized here using, for example, reversible addition–fragmentation chain transfer (RAFT) polymerization[40,41] which affords excellent control over the polymer’s molecular weight and polydispersity and is amenable to end-group modification.[42] The resulting polymer–nanocrystal hybrids exhibit remarkable stability over extended periods, are easy to purify, and in contrast to some previously explored methods, do not suffer from aggregation or precipitation. The

---

[1] This work was published under my former name, Teresa E. Pick.

protocol reported herein for preparing functional polymer–inorganic hybrid nanomaterials from bare nanocrystal dispersions dramatically simplifies their synthesis toward greater commercial scalability. Furthermore, with the ability to use a variety of polymers one can tailor the interactions of nanocrystal surfaces with biological systems to, for example, minimize toxicity thereby allowing their use in clinical setting.

5.2 Experimental

MATERIALS. All reagents were of the highest commercial grade possible and used as received unless otherwise stated. Monomers were distilled over calcium hydride prior to use. 2,2′-Azodiisobutyronitrile (AIBN) was recrystallized from ethanol. Anhydrous solvents were obtained at the highest possible purity. All buffers were prepared from biochemical grade salts and MilliQ water, and sterile filtered prior to use.

NANOCRYSTALS. Octadecylphosphonate (ODPA)-passivated CdSe nanocrystals (*d* ~ 4.1 nm) and ODPA/OAM-passivated CdSe/CdS quantum dot-quantum rods (QD–QRs) were prepared using an automated nanocrystal synthesis robot, WANDA, as reported previously.[18,43–45] Oleate passivated α-Fe_2O_3 (*d* ~ 8 nm) were synthesized via a microwave-assisted hydrothermal route, while I synthesized upconverting β-$NaYF_4$ doped with 20 mol% Yb(III) and 2 mol% Th(III) (*d* ~ 17 nm) using a high-temperature synthesis in an organic medium.[46] Nanocrystal size was determined by using ImageJ software to measure a distribution of particles from bright-field transmission electron microscopy (BF-TEM) images.

POLYMERS. Starting from polyacrylic acid (PAA, MW ~1800 g mol^{-1}), two functionalized PAA analogs were prepared: methoxy-terminated, polyethylene oxide-grafted PAA (PAA-$mPEO_4$) and fluorescein-terminated PAA (PAA-FITC). PAA-$mPEO_4$ was prepared from PAA which had been grafted with four methoxy-terminated, polyethylene oxides *via* amide linkages using *N,N*′-dicyclohexylcarbodiimide (DCC)-mediated coupling, according to a previously published procedure.[47] The synthesis of PAA-FITC is described in Scheme 5.1. The dodecylsulfanylthiocarbonylsulfanyl-2-methylpropionic acid (DMP) chain transfer agent (CTA) **1** was prepared as previously reported.[48] Purification of small molecule precursors **1** and **2** was carried out *via* automated flash chromatography on a Biotage SP1 system using high performance liquid chromatography (HPLC)-grade solvents.

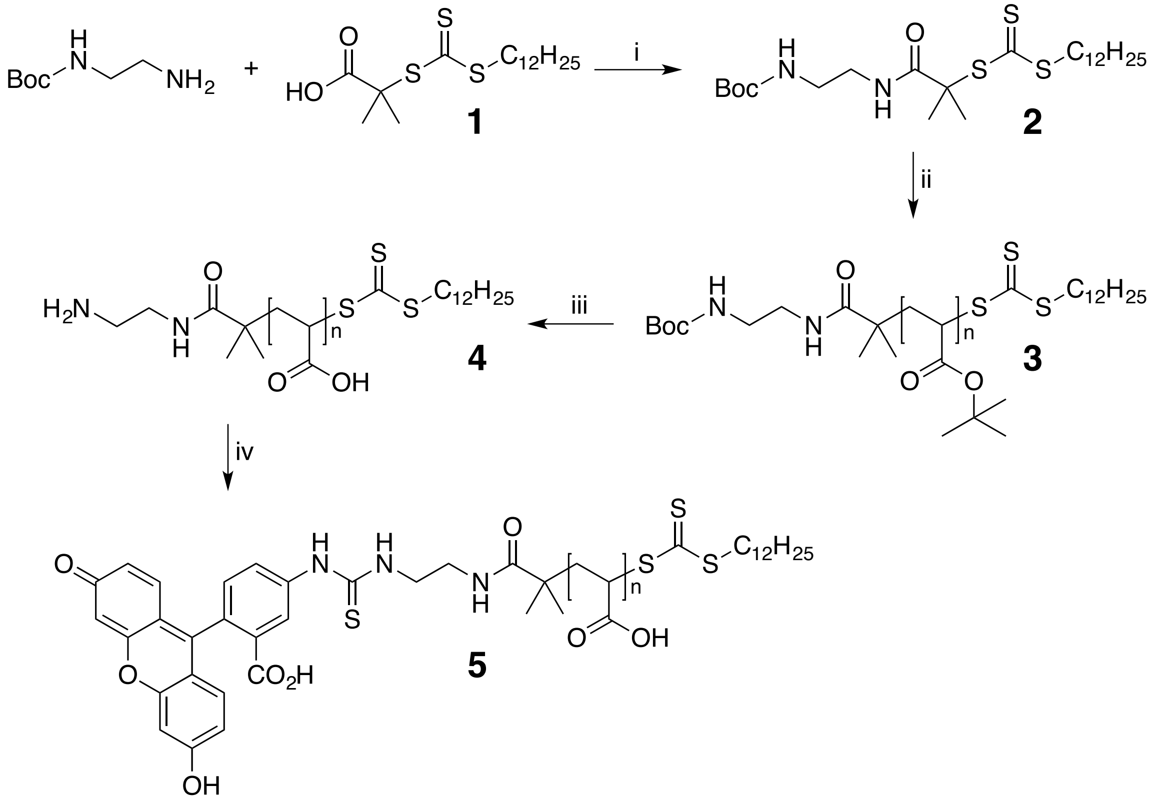

Scheme 5.1. Chemical synthesis of PAA-FITC (**5**) for passivating the surfaces of bare nanocrystals. Reagents: (i) HCTU, DIPEA, DMF; (ii) *t*Bu-Acrylate, AIBN; (iii) DCM, TFA; (iv) FITC, borate buffer, pH 9.0.

Synthesis of *tert*-Butyl 2-(2-(dodecylthiocarbonothioylthio)-2-methylpropanamido) ethylcarbamate Chain Transfer Agent (**2**). To an ice-cold solution of 2-(dodecylthiocarbonothioylthio)-2-methylpropanoic acid **1** (3.65 g, 10 mmol) in dimethylformamide (DMF) (45 mL) was added 2-(6-chloro-1*H*-benzotriazole-1-yl)-1,1,3,3-tetramethylaminium hexafluorophosphate (HCTU) (4.55 g, 11 mmol) portion-wise, followed by *N,N*-diisopropylethylamine (DIPEA) (4.52 g, 35 mmol) in one portion and then mono Boc-protected ethylene diamine (1.60 g, 10 mmol) in DMF (5 mL). After 12 h, the reaction mixture was concentrated *in vacuo*, and the residue dissolved in diethyl ether (200 mL). The ethereal layer was washed successively with saturated aqueous potassium chloride (3 x 50 mL), saturated aqueous sodium bicarbonate (3 x 50 mL), deionized water (3 x 50 mL), and then brine (1 x 50 mL) prior to purification by flash chromatography using a gradient elution of 4:1 to 1:4 hexanes:DCM. The product **2** was isolated as a bright yellow solid (3.30 g, 65%). ^{1}H NMR (500 MHz, $CDCl_3$): δ = 6.91 (t, 1H), 4.82 (t, 1H), 3.4–3.3 (m, 6H), 1.71 (s, 6H), 1.68 (m, 2H), 1.46 (s, 9H), 1.40 (m, 2H), 1.32–1.27 (m, 16H), 0.88 (t, 3H) ppm. ^{13}C NMR (125 MHz, $CDCl_3$): δ = 173.1, 156.4, 79.5, 57.1, 41.0, 37.1, 31.9, 29.6, 29.5, 29.4, 29.3, 29.1, 29.0, 27.7, 25.8, 22.7, 14.1 ppm. FT-IR: ν = 3350 (w), 2960 (s), 2927 (m), 2855 (m), 1698 (m), 1662 (m), 1528 (m), 1496 (s), 1392 (s), 1366 (m), 1278 (m), 1255 (m), 1175 (m), 1146 (m), and 815 (m) cm^{-1}.

Anal. Calc'd for ($C_{24}H_{46}N_2O_3S_3$): C, 56.87; H, 9.15; N, 5.53; S, 18.98. Found: C, 56.84; H, 9.20; N, 5.51; S, 18.93.

Synthesis of Boc-NH-CH_2CH_2-Poly(*tert*-Butyl Acrylate)-Trithiocarbonate (**3**). A solution containing chain transfer agent (CTA) **2** (253 mg, 0.50 mmol), *tert*-butyl acrylate (1.60 g, 12.5 mmol), and AIBN (8.0 mg, 0.05 mmol) was charged into a 50 mL Schlenk tube and degassed using four cycles of a freeze-pump-thaw sequence. The polymerization was carried out at 70 °C for 1 h. The polymer was precipitated three times in 1:3 MeOH:H_2O from acetone, and the residue dissolved in DCM before drying over anhydrous magnesium sulfate, filtering and concentrating to give the final polymer **3** as a viscous yellow product (1.40 g, 76%). Monomer conversion was determined to be 80% by ^{1}H NMR. ^{1}H NMR (500 MHz, $CDCl_3$): δ = 3.4–3.2 (m, 4H), 2.3–2.1 (m, 30H) 1.9–0.7 (m, 380H) ppm. FTIR: ν = 2979 (m), 2936 (m), 2894 (s), 1729 (m), 1529 (s), 1482 (s), 1458 (m), 1373 (m), 1368 (m), 1355 (s), 1152 (m), 1044 (s), 925 (s), 847 (m), and 755 (s) cm^{-1}. Anal. Calc'd for ($C_{164}H_{286}N_2O_{43}S_3$): C, 64.16; H, 9.39; N, 0.91; S, 3.13. Found: C, 64.10; H, 9.50; N, 0.92; S, 3.08. THF-SEC: M_n = 2,750 g mol^{-1}; M_w = 2,840 g mol^{-1}; PDI = 1.03.

Synthesis of H_2N-CH_2CH_2-Poly(acrylic acid)-Trithiocarbonate (**4**). Polymer **3** (1.0 g, mmol) was dissolved in DCM (10 mL) prior to the addition of an equivolume of trifluoroacetic acid (TFA). The reaction mixture was stirred for 24 h before concentrating *in vacuo* to yield the final product **4** as a yellow foam (615 mg, 100%). ^{1}H NMR (500 MHz, CD_3OD): δ = 2.5–2.3 (s, 32H), 2.0–0.9 (m, 72H) ppm. FT-IR: ν = 3500 (m), 3120 (m), 2941 (m), 2878 (s), 2600 (m), 1716 (m), 1457 (m), 1264 (m), 1207 (m), and 820 (s) cm^{-1}. Anal. Calc'd for ($C_{79}H_{118}N_2O_{41}S_3$): C, 51.35; H, 6.44; N, 1.52; S, 5.21. Found: C, 51.30; H, 6.48; N, 1.53; S, 5.14.

Synthesis of FITC-NH-CH_2-CH_2-Poly(acrylic acid)-Trithiocarbonate (**5**). Polymer **4** (92 mg, 0.05 mmol) was dissolved in 50 mM borate buffer at pH 9.0 (2 mL) (and the pH adjusted with 5 N sodium hydroxide until a pH of 9.0 was achieved) and the solution cooled in an ice bath prior to the addition of fluorescein isothiocyanate (96 mg, 0.25 mmol) as an aliquot in dry dimethyl sulfoxide (DMSO) (300 μL). The reaction was placed on a rotating carousel in a cold room maintained at 4 °C for 6 h before passing through a PD10 Size Exclusion Column (GE Healthcare), equilibrated to MilliQ water, to remove unreacted dye. The fraction containing FITC-labeled polymer was acidified with 1 N hydrochloric acid (HCl) until a pH of 2–3 was obtained prior to lyophilization. The crude product **5** i.e., containing some residual NaCl salts was isolated as a yellow–orange solid and used without further purification. ^{1}H NMR (500 MHz, CD_3OD): δ = 8.1–6.5 (m, 9H), 2.4–2.3 (s, 39H) 2.0–0.9 (m, 94H) ppm. FT-IR: ν = 3475 (m), 2956 (m), 2596 (s), 1724 (m), 1457 (s), 1424 (s), 1267 (m), and 828 (s) cm^{-1}. Anal. Calc'd for ($C_{100}H_{129}N_3O_{46}S_4$): C, 53.68; H, 5.81; N, 1.88; S, 5.73. Found: 50.75; H, 5.25; N, 1.80; S, 5.36. Note: the deviation in the elemental analysis from the calculated is consistent with the incomplete reprotonation of all of the sodium acrylates following the work-up. On average, this is ~6 sodium acrylates per polymer. The solubility of **5**, compared to pristine PAA, was also noted—where some portion of water (up to 10% *w/w*) was preferred when attempting to dissolve into polar aprotic solvents like DMF for the NC passivation.

PREPARATION OF LIGAND-STRIPPED NANOCRYSTAL DISPERSIONS. Ligand-stripping reactions were performed in a nitrogen glove box. Equal volumes of nanocrystals in hexanes (1–20 mg mL^{-1}) and Meerwein's salt or, alternatively, Me_3OBF_4 dissolved in acetonitrile (ACN) (1–10 mM) containing DMF (0–10 eq. with respect to the trialkylammonium salt) were combined, resulting in a biphasic solution (Scheme 5.2a). Upon gentle agitation, a precipitate consisting of bare nanocrystals was observed. Chloroform (2 mL) was added to the reaction and the bare nanocrystals were pelleted by centrifugation at 2500 rpm for 1–3 min. The supernatant was discarded and the pellet was washed with additional chloroform (4 mL) and pelleted (2x) before redispersing in DMF (1 mL). The resulting dispersions were transparent and stable for months. In the case of QD–QRs, the preferred method involved direct transfer to DMF containing Me_3OBF_4 (10 mM). Quenching of the excess alkylating agent, if necessary, could be carried out via addition of *N,N*-diisopropyl-2-ethanolamine. Here, the alcohol served as a sacrificial nucleophile, whereas the internal non-nucleophilic, tertiary amine served to quantitatively neutralize the *in situ*-formed fluoroboric acid (HBF_4) upon alkylation of the alcohol.

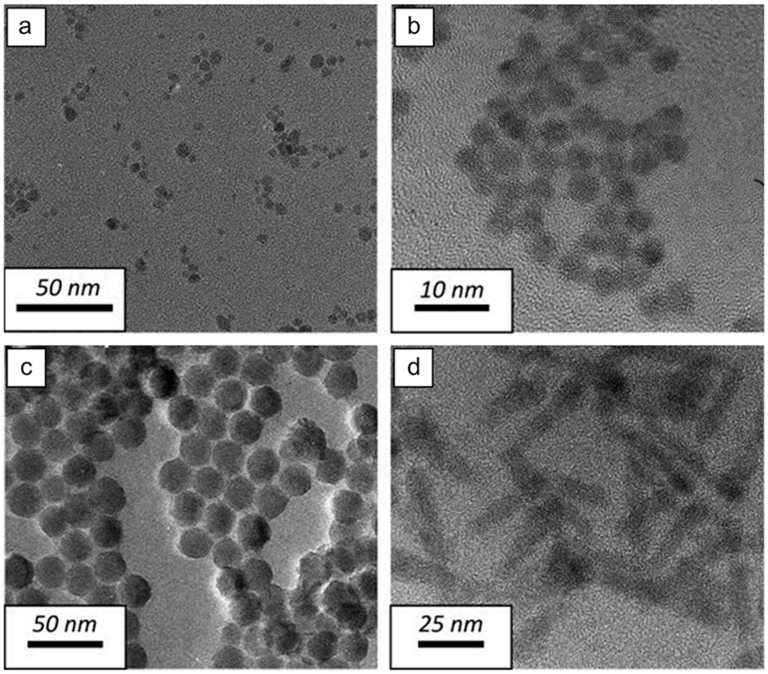

Figure 5.1. Bright-field transmission electron microscopy images of ligand-stripped nanocrystals: (a) α-Fe_2O_3; (b) CdSe; (c) β-$NaYF_4$:Yb/Tm; (d) CdSe/CdS QD–QRs. The removal of native ligands is concomitant with nanocrystal clustering.

PREPARATION OF POLYMER-WRAPPED NANOCYRSTALS. A dispersion of bare nanocrystals in DMF (25–100 mL) was added to 1 mL of DMF containing the PAA-derived polymer coating of interest (10 mg mL^{-1}); either PAA, PAA-mPEO$_4$, or PAA-FITC (Scheme 5.2b). An additional volume of water was required to dissolve PAA-FITC into DMF, most likely owing to the presence of residual salt. In all cases, then, the reaction mixture was sonicated for 1–2 h before adding dropwise into 50 mM borate buffer at pH 9 (20 mL). After stirring (30 min or 24 h, depending on the sample), the solution was purified and concentrated to a final volume ~1 mL via spin dialysis (MWCO = 10, 30, or 50 kDa depending on the size of the nanocrystal and molecular weight of the polymer coating, Millipore Amicon Ultra).

PREPARATION OF CITRATE-PASSIVATED NANOCYRSTALS**.** A similar procedure was carried out for the passivation by small molecules. In this case, citric acid in DMF (up to 100 mg mL^{-1}) was employed.

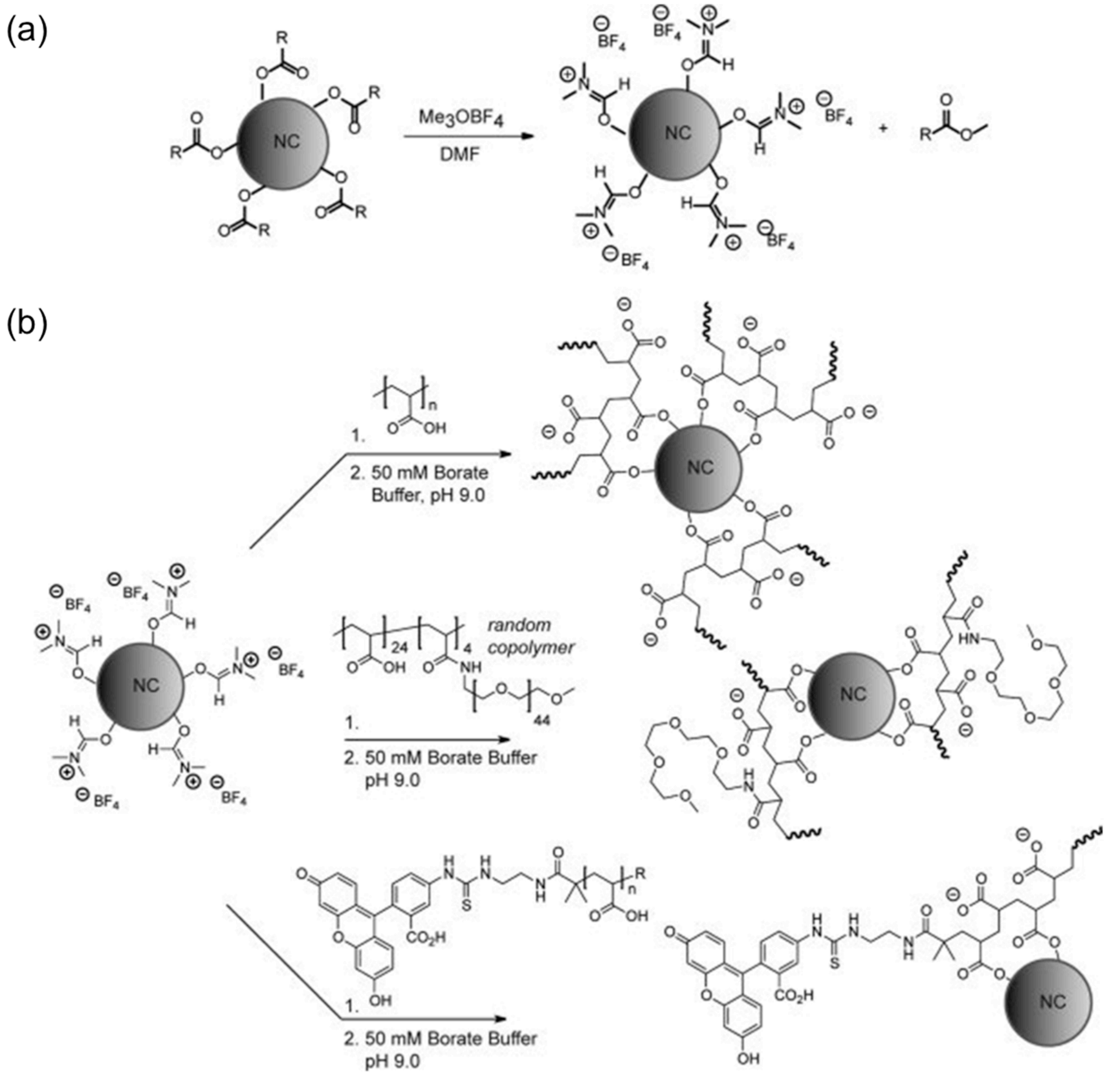

Scheme 5.2. Preparation of ligand-stripped nanocrystals and their polymer-wrapped assemblies: (a) Reactive ligand stripping of nanocrystals using trimethyloxonium tetrafluoroborate and redispersion in DMF: NC = α-Fe_2O_3, CdSe, β-$NaYF_4$:Yb/Tm, or CdSe/CdS QD–QRs; (b) Passivation of bare NCs surfaces with poly(acrylic acid)-derived polymers (e.g., PAA, PAA-$mPEO_4$, PAA-FITC) and subsequent transfer into aqueous buffers.

5.3 Results and Discussion

As described in Chapter 2, ligand-stripped nanocrystals can be redispersed in polar solvents that engage in dative coordination to their cationic adatoms (e.g., DMF or HMPA).[46] Indeed, FT-IR of dried nanocrystal films–either CdSe, CdSe/CdS, α-Fe_2O_3, or upconverting β-$NaYF_4$:Yb/Tm, treated first with Me_3OBF_4 in ACN, precipitated, and redispersed in DMF–showed characteristic stretches in the carbonyl region consistent with DMF-adsorbates to surface adatoms. No etching of the nanocrystals was observed by BF-TEM (Figure 5.1).

The dynamic, dative coordination sphere of DMF ligands is shown here to be readily displaced in favor of stronger-coordinating anionic carboxylate functionality present on polymer side chains (Scheme 5.2b). We selected PAA as a platform for passivating nanocrystals with functional polymers both based on its coordination potential to adatoms at the nanocrystal surface, as well as its straightforward synthesis from commercially available materials or via controlled radical polymerization. In addition to low-molecular weight PAA polymer adsorbates, a series of functional polymer coatings were prepared to assess the generality of the method. For example, PAA grafted with 2000 Da methoxy-terminated polyethylene oxides[49–52] (PAA-$mPEO_4$) was useful for preparing nanocrystals with PEGylated peripheries. Additionally, a fluorescein (FITC)-terminated PAA **5** was prepared using RAFT polymerization, following the sequence shown in Scheme 5.1. To verify the robustness of a polymer passivation approach for coating bare nanocrystals over a small molecule with a similar coordination motif, citrate was also investigated.

The rapid attachment of PAA-derived polymers to bare nanocrystal surfaces was accomplished by combining polymers dissolved in DMF (10 mg mL^{-1}) to DMF dispersions of bare nanocrystals (25–100 mL). The resulting dispersions were sonicated briefly and then transferred dropwise into basic aqueous buffer (50 mM borate buffer, pH 9.0). Polymer-wrapped nanocrystals were readily purified by spin dialysis. In that all the polymer coatings used here were low molecular weight and did not self-assemble into supramolecular aggregates, the purification of excess materials from the wrapped nanocrystals was significantly improved (i.e., did not require extensive purification by size exclusion chromatography, as is a standard practice to yield single nanocrystals). These dispersions were significantly more stable (i.e., no precipitation) than those with citrate as a ligand; unequivocal precipitation occurred for citrate-coated nanocrystals within a few hours post-aqueous transfer (Figure 5.2b). Furthermore, control experiments where, for example, oleate-passivated α-Fe_2O_3 nanocrystals could exchange their surface passivation with PAA-$mPEO_4$ at room temperature and in THF did not produce aqueous dispersible materials, highlighting the importance of first stripping the hydrophobic native ligands prior to passivation with functional PAA-based coatings.

To verify the size distribution and quality of the wrapping procedure, we used DLS to measure the hydrodynamic diameters of both bare nanocrystals dispersed in DMF as well as their wrapped counterparts. Nanocrystals passivated with unmodified PAA coatings exhibited the smallest size increase relative to the bare nanocrystal precursor. For example, α-Fe_2O_3 nanocrystals initially 7–8 nm in diameter, once wrapped with PAA, gave a hydrodynamic diameter of 9 nm. In contrast, for coatings based on PAA-mPEO$_4$, a hydrodynamic diameter of 12 nm was observed. The larger size associated with the PAA-mPEO$_4$ wrapping can be attributed to the polyethylene oxide grafts extending from the nanocrystal surface. For α-Fe_2O_3 passivated with citrate, however, a hydrodynamic diameter of 33 nm indicated significant aggregation even at this early stage of repassivation. The robustness of the polymer-passivated approach was confirmed by images of α-Fe_2O_3 nanocrystals succeeding aqueous transfer. Those nanocrystals possessing the PAA-derived polymer coat were non-aggregated, exhibiting stable uniform dispersions and an overall retention of nanocrystal quality. In contrast, the citrate wrapping of α-Fe_2O_3 was inefficient, resulting in aggregation of nanocrystals (Figure 5.2a).

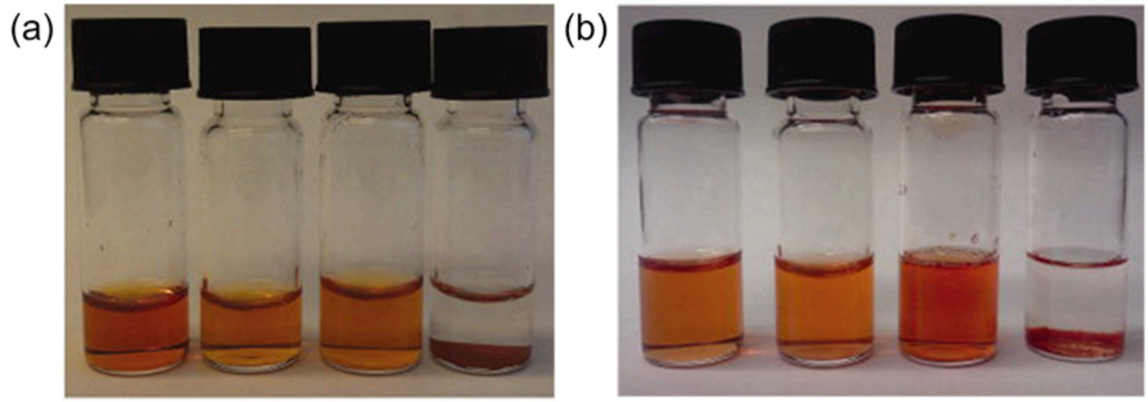

Figure 5.2. Aqueous dispersions of: (a) repassivated α-Fe_2O_3 nanocrystals: PAA, PAA-mPEO$_4$, PAA-FITC, or citrate-coated nanocrystals (left to right); (b) repassivated CdSe nanocrystals: PAA, PAA-mPEO$_4$, PAA-FITC, citrate-coated nanocrystals (left to right).

A similar trend was noted for the wrapping of bare, upconverting β-$NaYF_4$:Yb/Tm. In this case, similar hydrodynamic diameters 18–20 nm were observed for both the PAA and the PAA-mPEO$_4$-wrapped nanocrystals, respectively, where the bare nanocrystals were ~17 nm. For citrate-capped nanocrystals, however, the diameter was measured at 28 nm consistent with significant aggregation using this procedure. Metal chalcogenide nanocrystals were also efficiently transferred to water with direct binding of metal adatoms to polymer-bound carboxylates. Thus, for ~4.1 nm CdSe nanocrystals, hydrodynamic diameters of 6 and 9 nm for CdSe wrapped with PAA and PAA-mPEO$_4$, respectively, were observed. CdSe nanocrystals, passivated by PAA-derived polymers, exhibited non-aggregated, uniform dispersions over extended periods of time (Figure 5.2b). By contrast, a citrate coating was so poor at stabilizing dispersions of CdSe that the sample resulted in precipitation shortly after the aqueous transfer; the hydrodynamic diameter was, therefore, not measurable.

We determined that this strategy was also successful in manipulating the surface of nanocrystals with more elaborate polymer coatings. For example, FITC-PAA polymer **5** derived from RAFT polymerization was readily placed at the surface of otherwise colorless dispersions of bare, upconverting β-$NaYF_4$:Yb/Tm nanocrystals. Upconverting nanocrystals based on these materials offer photostable luminescence ideal for single particle imaging, sharp emission bandwidths, and large anti-Stokes shifts. Previously reported syntheses of aqueous dispersible, upconverting nanocrystals typically require heating for extended periods of time to displace native coordinating ligands with polymeric ligands. This process is known to slowly degrade the lattice over time at the high temperatures required for exchange.[53] Loss of ions from the nanocrystal lattice both reduces the number of sensitizing/emitting species and affects phonon coupling and energy transfer efficiency in the nanocrystal owing to differences in interfacial strain for particles of different sizes. This is completely avoided using the strategy reported here. The mildness of this two-step procedure could retain both the luminescence of the appended dyes now localized to the nanocrystal surface as well as dimensions and crystal phase of the $NaYF_4$ lattice that is necessary to maintain high-photon upconversion efficiency. The FITC dye was readily detected both in the presence and in the absence of UV light, tinting colorless β-$NaYF_4$:Yb/Tm with a readily observable yellow hue (Figure 5.3).

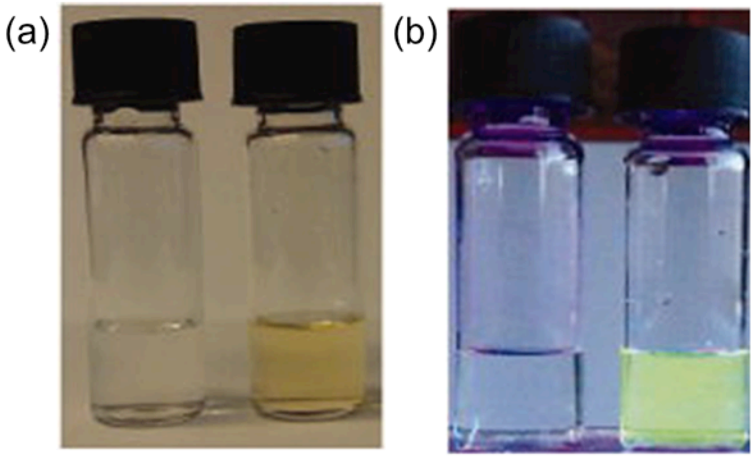

Figure 5.3. Characterization of polymer-passivated upconverting β-$NaYF_4$:Yb/Tm nanocrystals: (a) aqueous dispersions of β-$NaYF_4$:Yb/Tm nanocrystals (left) and those passivated by PAA-FITC (right) in ambient light; (b) same two samples illuminated from below with UV light.

The dispersions were uniform and stable (i.e., no precipitation). I collected and analyzed an XRD pattern of β-$NaYF_4$:Yb/Tm, which showed the expected highly emissive β-phase and its power-dependent emission profile upon excitation at λ_{ex} = 980 nm was taken to confirm its crystal structure and upconverted luminescence (Figure 5.4). Chromogenic tags for these otherwise colorless nanocrystals may also be useful in performing further manipulations (e.g., labeling with proteins or other biomolecules) using standard purification and detection apparatus found in most laboratories engaged in synthetic chemistry or chemical biology.

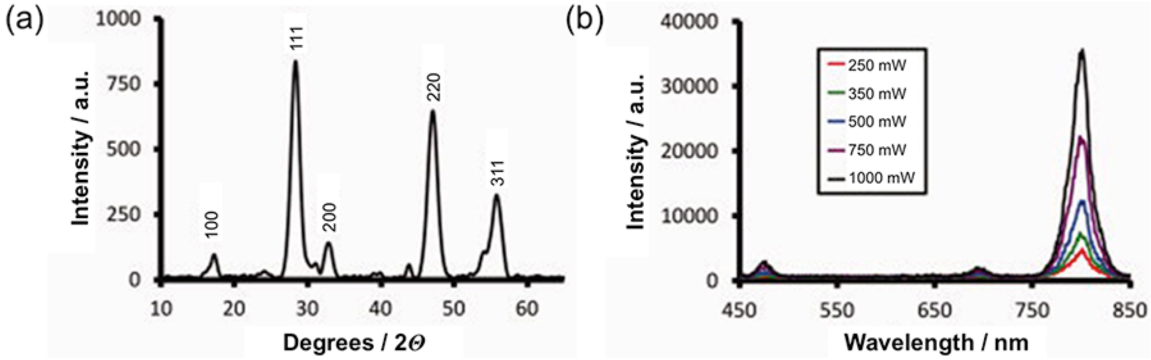

Figure 5.4. (a) X-ray diffraction pattern of β-NaYF$_4$:Yb/Tm nanocrystals showing characteristic peaks for the highly emissive hexagonal phase; (b) Power-dependent upconverted emission from β-NaYF$_4$:Yb/Tm excited at λ_{ex} = 980 nm.

We were also interested in characterizing the limitations, if any, of using a PAA-platform as a stabilization strategy for luminescent metal chalcogenide nanocrystals, as these have not been explored previously. To that end, a detailed investigated of the effects on the photophysical properties upon sequential manipulation of CdSe/CdS QD–QRs surfaces was carried out, from their native ligand coordination sphere of ODPA and OAM to stripping and repassivation with either PAA or PAA-mPEO$_4$ (Figure 5.5).

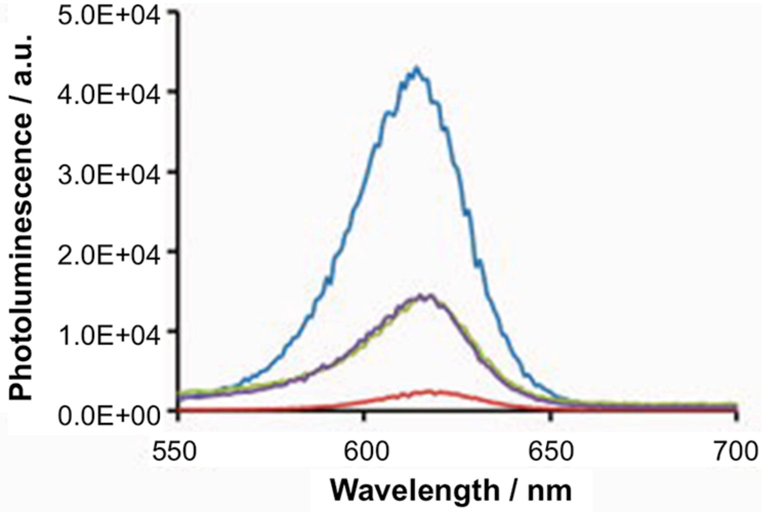

Figure 5.5. Photoluminescence spectra of CdSe/CdS quantum dot-quantum rod nanocrystal heterostructures at the same optical density: ODPA/OAM coated (blue), ligand stripped (red), PAA coated (green), and PAA-mPEO$_4$ coated (purple).

The QD–QRs initially had a photoluminescence quantum yield (PLQY) of 43%, measured in hexanes using a fluorometer equipped with an integrating sphere. The emission maximum was λ_{ex} = 614 nm. Upon stripping and dispersing into DMF, the PLQY decreased to 2.4% and the emission maximum red-shifted to λ_{ex} = 620 nm. The emission at longer wavelengths for stripped QD–QRs confirms that reactive ligand stripping is exceptionally mild (i.e., does not etch, which would shift the emission to shorter wavelengths owing to confinement effects[54]) and suggests that the presence of DMF at dative coordination sites at the nanocrystal surface has the effect of modulating the energetics of the exciton's relaxation, most likely owing to effects on the nanocrystal's phonon modes. As with the CdSe nanocrystals, repassivation was successfully realized for both PAA and PAA-mPEO$_4$. QD–QRs wrapped with either of these coatings shared nearly identical photophysics: both had PLQY values between 14–15%, thus recovering favorably from the losses incurred upon stripping, and both had an emission maximum at λ_{ex} = 617 nm. These data collectively suggest that recovery of photoluminescence to 33% of the original QD–QRs with their native ligands intact is directly related to carboxylate vs. DMF binding at the nanocrystal surface. The extent of photoluminescence recovery is also like that observed for the displacement of native ligands by small molecules.[18] Thus, it was inferred that the extent to which PAA-derived macromolecules are able to conform and passivate trap sites at the nanocrystal surface is competitive with that for small-molecule ligands. In that, grafting additional functionality along the PAA backbone, in this case mPEO chains, does not adversely affect this recovery points more generally to opportunities in future schemes to deliberately engineer the topological display of different chemical functionalities using these coatings. PAA-derived coatings should offer a more reliable platform in that regard than might otherwise be carried out using, for example, amphiphilic polymers where functionalization can be upset in the balance of amphiphilicity required to efficiently wrap the nanocrystal and to ensure its aqueous solubility as required for purification.

5.4 Conclusions

I demonstrated a general, two-step strategy for generating polymer-wrapped nanocrystals from dispersions of bare nanocrystals and hydrophilic polymers. Metal oxide, metal chalcogenide, and inorganic nanocrystals and heterostructures are amenable to repassivation, as shown here, with PAA-based polymer ligands for use in aqueous media. The method is exceptionally mild, minimizing damage to nanocrystals surfaces, and was observed to provide a more robust coating, long term, compared to small molecules like citrate. In carrying out this approach, the use of amphiphilic polymers is completely avoided, which dramatically simplifies the purification of the hybrids. As colloidal dispersions, these new aqueous nanocrystal compositions remained stable for months. The approach should broadly apply to other functional polymer coatings specifically tailored for biological and chemical applications.

5.5 References

1. Kim, J.; Kim, H.-S.; Lee, N.; Kim, T.; Kim, H.; Yu, T.; Song, I.-C.; Moon, W.-K.; Hyeon, T. "Multifunctional uniform nanoparticles composed of a magnetite nanocrystal core and a mesoporous silica shell for magnetic resonance and fluorescence imaging and for drug delivery" *Angew. Chem. Int. Ed.* **2008**, *47*, 8438–8441.
2. Liu, G. L.; Yin, Y.; Kunchakarra, S.; Mukherjee, B.; Gerion, D.; Jett, S. D.; Bear, D. G.; Gray, J. W.; Alivisatos, A. P.; Lee, L. P.; Chen, F. F. "A nanoplasmonic molecular ruler for measuring nuclease activity and DNA footprinting" *Nat. Nanotechnol.* **2006**, *1*, 47–52.
3. Norris, D. J.; Efros, A. L.; Erwin, S. C. "Doped nanocrystals" *Science* **2008**, *319*, 1776–1779.
4. Mattoussi, H.; Mauro, J. M.; Goldman, E. R.; Anderson, G. P.; Sundar, V. C.; Mikulec, F. V.; Bawendi, M. G. "Self-Assembly of CdSe−ZnS Quantum Dot Bioconjugates Using an Engineered Recombinant Protein" *J. Am. Chem. Soc.* **2000**, *122*, 12142–12150.
5. Han, M.; Gao, X.; Su, J. Z.; Nie, S. "Quantum-dot-tagged microbeads for multiplexed optical coding of biomolecules" *Nat. Biotechnol.* **2001**, *19*, 631–635.
6. Zhao, X.; Hilliard, L. R.; Mechery, S. J.; Wang, Y.; Bagwe, R. P.; Jin, S.; Tan, W. "A rapid bioassay for single bacterial cell quantitation using bioconjugated nanoparticles" *Proc. Natl. Acad. Sci. USA* **2004**, *101*, 15027–15032.
7. Dagan, G.; Sampath, S.; Lev, O. "Preparation and Utilization of Organically Modified Silica–Titania Photocatalysts for Decontamination of Aquatic Environments" *Chem. Mater.* **1995**, *7*, 446–453.
8. Nagappa, B.; Chandrappa, G. T. "Mesoporous nanocrystalline magnesium oxide for environmental remediation" *Micropor. Mesopor. Mater.* **2007**, *106*, 212–218.
9. Park, J.; Joo, J.; Kwan, S. G.; Jang, Y.; Hyeon. T. "Synthesis of Monodisperse Spherical Nanocrystals" *Angew. Chem. Int. Ed.* **2007**, *46*, 4630–4660.
10. Murray, C. B.; Norris, D. J.; Bawendi, M. G. "Synthesis and characterization of nearly monodisperse CdE (E = sulfur, selenium, tellurium) semiconductor nanocrystallites" *J. Am. Chem. Soc.* **1993**, *115*, 8706–8715.
11. Pellegrino, T.; Manna, L.; Kudera, S.; Liedl, T.; Koktysh, D.; Rogach, A. L.; Keller, S.; Radler, J.; Natile, G.; Parak, W. J. "Hydrophobic Nanocrystals Coated with an Amphiphilic Polymer Shell: A General Route to Water Soluble Nanocrystals" *Nano Lett.* **2004**, *4*, 703–707.
12. Petruska, M. A.; Bartko, A. P.; Klimov, V. I. "An Amphiphilic Approach to Nanocrystal Quantum Dot−Titania Nanocomposites" *J. Am. Chem. Soc.* **2004**, *126*, 714–715.
13. Lees, E. E.; Nguyen, T.-L.; Clayton, A. H. A.; Mulvaney, P. "The Preparation of Colloidally Stable, Water-Soluble, Biocompatible, Semiconductor Nanocrystals with a Small Hydrodynamic Diameter" *ACS Nano* **2009**, *3*, 1121–1128.
14. Zhang, T.; Ge, J.; Hu, Y.; Yin, Y. "A General Approach for Transferring Hydrophobic Nanocrystals into Water" *Nano Lett.* **2007**, *7*, 3203–3207.
15. Gittins, D. I.; Caruso, F. "Spontaneous Phase Transfer of Nanoparticulate Metals from Organic to Aqueous Media" *Angew. Chem. Int. Ed.* **2001**, *40*, 3001–3004.

16. De Palma, R.; Peeters, S.; Van Bael, M. J.; Van den Rul, H.; Bonroy, K.; Laureyn, W.; Mullens, J.; Borghs, G.; Maes, G. "Silane Ligand Exchange to Make Hydrophobic Superparamagnetic Nanoparticles Water-Dispersible" *Chem. Mater.* **2007**, *19*, 1821–1831.
17. Mei, B. C.; Susumu, K.; Medintz, I. L.; Mattoussi, H. "Polyethylene glycol-based bidentate ligands to enhance quantum dot and gold nanoparticle stability in biological media" *Nat. Protoc.* **2009**, *4*, 412–423.
18. Caldwell, M. A.; Albers, A. E.; Levy, S. C.; Pick, T. E.; Cohen, B. E.; Helms, B. A.; Milliron, D. J. "Driving oxygen coordinated ligand exchange at nanocrystal surfaces using trialkylsilylated chalcogenides" *Chem. Commun.* **2011**, *47*, 556–558.
19. Llordes, A.; Hammack, A. T.; Buonsanti, R.; Tangirala, R.; Aloni, S.; Helms, B. A.; Milliron, D. J. "Polyoxometalates and colloidal nanocrystals as building blocks for metal oxide nanocomposite films" *J. Mater. Chem.* **2011**, *21*, 11631–11638.
20. Gaponik, N.; Talapin, D. V.; Rogach, A. L.; Eychmuller, A.; Weller, H. "Efficient Phase Transfer of Luminescent Thiol-Capped Nanocrystals: From Water to Nonpolar Organic Solvents" *Nano Lett.* **2002**, *2*, 803–806.
21. Dubois, F.; Mahler, B.; Dubertret, B.; Doris, E.; Mioskowski, C. "A Versatile Strategy for Quantum Dot Ligand Exchange" *J. Am. Chem. Soc.* **2007**, *129*, 482–483.
22. Mitchell, G. P.; Mirkin, C. A.; Letsinger, R. L. "Programmed Assembly of DNA Functionalized Quantum Dots" *J. Am. Chem. Soc.* **1999**, *121*, 8122–8123.
23. Mattoussi, H.; Mauro, J. M.; Goldman, E. R.; Anderson, G. P.; Sundar, V. C.; Mikulec, F. V.; Bawendi, M. G. "Self-Assembly of CdSe−ZnS Quantum Dot Bioconjugates Using an Engineered Recombinant Protein" *J. Am. Chem. Soc.* **2000**, *122*, 12142–12150.
24. Chan, W. C.; Nie, S. "Quantum dot bioconjugates for ultrasensitive nonisotopic detection" *Science* **1998**, *281*, 2016–2018.
25. Hermanson, G. T. *Bioconjugate Techniques*. Academic Press: San Diego, 2008. Print.
26. Talapin, D. V.; Murray, C. B. "PbSe nanocrystal solids for n- and p-channel thin film field-effect transistors" *Science* **2005**, *310*, 86–89.
27. Kovalenko, M. V.; Scheele, M.; Talapin, D. V. "Colloidal nanocrystals with molecular metal chalcogenide surface ligands" *Science* **2009**, *324*, 1417–1420.
28. Millstone, J. E.; Hurst, S. J.; Metraux, G. S.; Cutler, J. I.; Mirkin, C. A. "Colloidal Gold and Silver Triangular Nanoprisms" *Small* **2009**, *5*, 646–664.
29. Lokteva, I.; Radychev, N.; Witt, F.; Borchert, H.; Parisi, J.; Kolyny-Olesiak, J. "Surface Treatment of CdSe Nanoparticles for Application in Hybrid Solar Cells: The Effect of Multiple Ligand Exchange with Pyridine" *J. Phys. Chem. C* **2010**, *114*, 12784–12791.
30. Peng, X.; Schlamp, M. C.; Kadavanich, A. V.; Alivisatos, A. P. "Epitaxial Growth of Highly Luminescent CdSe/CdS Core/Shell Nanocrystals with Photostability and Electronic Accessibility" *J. Am. Chem. Soc.* **1997**, *119*, 7019–7029.

31. Wang, Y.; Zeiri, O.; Neyman, A.; Stellacci, F.; Weinstock, I. A. "Nucleation and Island Growth of Alkanethiolate Ligand Domains on Gold Nanoparticles" *ACS Nano* **2012**, *6*, 629–640.
32. Liu, D.; Snee, P. T. "Water-Soluble Semiconductor Nanocrystals Cap Exchanged with Metalated Ligands" *ACS Nano* **2011**, *5*, 546–550.
33. Yu, W. W.; Chang, E.; Sayes, C. M.; Drezek, R.; Colvin, V. L. "Aqueous dispersion of monodisperse magnetic iron oxide nanocrystals through phase transfer" *Nanotechnology* **2006**, *17*, 4483–4487.
34. Pong, B.-K.; Trout, B. L.; Lee, J.-Y. "Modified Ligand-Exchange for Efficient Solubilization of CdSe/ZnS Quantum Dots in Water: A Procedure Guided by Computational Studies" *Langmuir* **2008**, *24*, 5270–5276.
35. Jiang, W.; Mardyani, S.; Fischer, H.; Chan, W. C. W. "Design and Characterization of Lysine Cross-Linked Mercapto-Acid Biocompatible Quantum Dots" *Chem. Mater.* **2006**, *18*, 872–878.
36. Smith, A. M.; Duan, H.; Rhyner, M. N.; Ruan, G.; Nie, S. "A systematic examination of surface coatings on the optical and chemical properties of semiconductor quantum dots" *Phys. Chem. Chem. Phys.* **2006**, *8*, 3895–3903.
37. Aldana, J.; Wang, Y. A.; Peng, X. "Photochemical Instability of CdSe Nanocrystals Coated by Hydrophilic Thiols" *J. Am. Chem. Soc.* **2001**, *123*, 8844–8850.
38. Potapova, I.; Mruk, R.; Prehl, S.; Zentel, R.; Basché, T.; Mews, A. "Semiconductor Nanocrystals with Multifunctional Polymer Ligands" *J. Am. Chem. Soc.* **2003**, *125*, 320–321.
39. Andala, D. M.; Shin, S. H. R.; Lee, H.-Y.; Bishop, K. J. M. "Templated Synthesis of Amphiphilic Nanoparticles at the Liquid–Liquid Interface" *ACS Nano* **2012**, *6*, 1044–1050.
40. Chiefari, J.; Chong, Y. K.; Ercole, F.; Krstina, J.; Jeffery, J.; Le, T. P. T.; Mayadunne, R. T. A.; Meijs, G. F.; Moad, C. L.; Moad, G.; Rizzardo, E.; Thang, S. H. "Living Free-Radical Polymerization by Reversible Addition−Fragmentation Chain Transfer: The RAFT Process" *Macromolecules* **1998**, *31*, 5559–5562.
41. Loiseau, J.; Doeerr, N.; Suau, J. M.; Egraz, J. B.; Llauro, M. F.; Ladaviere, C.; Claverie, J. "Synthesis and Characterization of Poly(acrylic acid) Produced by RAFT Polymerization. Application as a Very Efficient Dispersant of $CaCO_3$, Kaolin, and TiO_2" *Macromolecules* **2003**, *36*, 3066–3077.
42. Llauro, M.-F.; Loiseau, J.; Boisson, F.; Delolme, F.; Ladavière, C.; Claverie, J. "Unexpected end-groups of poly(acrylic acid) prepared by RAFT polymerization" *J. Polym. Sci. Part A: Polym. Chem.* **2004**, *42*, 5439–5462.
43. Albers, A. E.; Chan, E. M.; McBride, P. M.; Ajo-Franklin, C. M.; Cohen, B. E.; Helms, B. A. "Dual-Emitting Quantum Dot/Quantum Rod-Based Nanothermometers with Enhanced Response and Sensitivity in Live Cells" *J. Am. Chem. Soc.* **2012**, *134*, 9565–9568.
44. Carbone, L.; Nobile, C.; De Giorgi, M.; Della Sala, F.; Morello, G.; Pompa, P.; Hytch, M.; Snoeck, E.; Fiore, A.; Franchini, I. R.; Nadasan, M.; Silvestre, A. F.; Chiodo, L.; Kudera, S.; Cingolani, R.; Krahne, R.; Manna, L. "Synthesis and

Micrometer-Scale Assembly of Colloidal CdSe/CdS Nanorods Prepared by a Seeded Growth Approach” *Nano Lett.* **2007**, *7*, 2942–2950.

45. Talapin, D. V.; Rogach, A. L.; Kornowski, A.; Haase, M.; Weller, H.; “Highly Luminescent Monodisperse CdSe and CdSe/ZnS Nanocrystals Synthesized in a Hexadecylamine−Trioctylphosphine Oxide−Trioctylphospine Mixture” *Nano Lett.* **2001**, *1*, 207–211.
46. Rosen, E. L.; Buonsanti, R.; Llordes, A.; Sawvel, A. M.; Milliron, D. J.; Helms, B. A. “Exceptionally Mild Reactive Stripping of Native Ligands from Nanocrystal Surfaces by Using Meerwein’s Salt” *Angew. Chem. Int. Ed.* **2012**, *51*, 684–689.
47. Bailey, M. J.; van der Weegen, R.; Klemm, P. J.; Baker, S. L.; Helms, B. A. “Stealth Rare Earth Oxide Nanodiscs for Magnetic Resonance Imaging” *Adv. Healthcare Mater.* **2012**, *1*, 437-442.
48. Lai, J. T.; Filla, D.; Shea, R. “Functional Polymers from Novel Carboxyl-Terminated Trithiocarbonates as Highly Efficient RAFT Agents” *Macromolecules* **2002**, *35*, 6754–6756.
49. Na, B. H.; Palui, G.; Rosenberg, J. T.; Ji, X.; Grant, S. C.; Mattoussi, H. “Multidentate Catechol-Based Polyethylene Glycol Oligomers Provide Enhanced Stability and Biocompatibility to Iron Oxide Nanoparticles” *ACS Nano* **2012**, *6*, 389–399.
50. Walkey, C. D.; Olsen, J. B.; Guo, H.; Emili, A.; Chan, W. C. W. “Nanoparticle Size and Surface Chemistry Determine Serum Protein Adsorption and Macrophage Uptake” *J. Am. Chem. Soc.* **2012**, *134*, 2139–2147.
51. Song, H.-T.; Choi, J.-S.; Huh, Y.-M.; Kim, S.; Jun, Y.-W.; Suh, J.-S.; Cheon, J. “Surface Modulation of Magnetic Nanocrystals in the Development of Highly Efficient Magnetic Resonance Probes for Intracellular Labeling” *J. Am. Chem. Soc.* **2005**, *127*, 9992–9993.
52. Harris, J. M. “Laboratory synthesis of polyethylene glycol derivatives” *J. Macromol. Sci. Rev. Polym. Chem Phys.* **1985**, *25*, 325–373.
53. Naccache, R.; Vetrone, F.; Mahalingam, V.; Cuccia, L. A.; Capobianco, J. A. “Controlled Synthesis and Water Dispersibility of Hexagonal Phase $NaGdF_4:Ho^{3+}/Yb^{3+}$ Nanoparticles” *Chem. Mater.* **2009**, *21*, 717–723.
54. Lin, W.; Fritz, K.; Guerin, G.; Bardajee, G. R.; Hinds, S.; Sukhovatkin, V.; Sargent, E. H.; Scholes, G. D.; Winnik, M. A. “Highly Luminescent Lead Sulfide Nanocrystals in Organic Solvents and Water through Ligand Exchange with Poly(acrylic acid)” *Langmuir* **2008**, *24*, 8215–8219.

Chapter 6

Assembly of ligand-stripped nanocrystals into precisely controlled mesoporous architectures

Adapted from:

Raffaella Buonsanti, Teresa E. Pick,[2] Natacha Krins, Thomas J. Richardson, Brett A. Helms, Delia J. Milliron. “Assembly of Ligand-Stripped Nanocrystals into Precisely Controlled Mesoporous Architectures” *Nano Letters* **2012**, *12*, 3872–3877.

6.1 Introduction

Research on mesoporous materials (2 nm < *d* < 50 nm) has generally focused on tuning one structural parameter: either pore size, wall thickness, or crystallite size, with no reports demonstrating control over all of them and no synthetic strategies for controlling the crystallite shape.[1−9] In this chapter I investigate the use of ligand-stripped nanocrystals (NCs)[10,11] to produce mesoporous materials where all of these parameters are controlled to give architectures with a high degree of local ordering and regularity. The key to success is a new class of block copolymer (BCP) architecture-directing agents (ADAs) that I synthesized, which are designed to enhance the enthalpy of adsorption to the bare surfaces of ligand-stripped NCs. This combination allows the assembly of NCs with an unprecedented diversity of compositions. The metrics (pore size and wall thickness) of mesoporous ITO frameworks are varied, such that the length scale of ordering changes from 33 to 46 nm, for each crystallite size of 4.5, 6, and 8 nm. Spherical and, for the first time, rod-shaped crystallites are assembled using the same strategy to give mesoporous TiO_2 architectures with even larger structural features of 54 nm. We demonstrate that these nanorod-based mesoporous TiO_2 films exhibit outstanding durability, > 1000 cycles) under electrochemical cycling, performance highly sought after in energy storage materials.

6.2 Experimental

MATERIALS. *N,N*-Dimethylacrylamide (DMA) and styrene were purchased from Sigma-Aldrich and distilled under reduced pressure from calcium hydride. 1,4-dioxane was purchased from Sigma-Aldrich and distilled under N_2 from calcium hydride. Azobisisobutyronitrile (AIBN) was purchased from Sigma-Aldrich and recrystallized from ethanol. Titanium tetraisopropoxide ($Ti(OPr)_4$ or TTIP, 97%), trimethylamine *N*-oxide dihydrate ($(CH_3)_3NO\bullet 2H_2O$ or TMAO, 98%), oleic acid ($C_{17}H_{33}CO_2H$ or OLAC, 90%) indium acetylacetonate ($In(acac)_3$, 99.99%), tin bis(acetylacetonate) dichloride ($Sn(acac)_2Cl_2$, 98%), tin acetate ($Sn(Ac)_4$, 99.99%), myristic acid (MA, ≥ 98%), 1-octadecene (ODE, 90%), cerium(IV)ammonium nitrate ($(NH_4)_2Ce(NO_3)_6$), titanium(IV) butoxide ($Ti(OBu)_4$, 95%), Yttrium(III) chloride (anhydrous powder, 99.99%), ytterbium(III) chloride (anhydrous powder, 99.99%), erbium(III) chloride (anhydrous powder, 99.9%), platinum(II)acetylacetonate (99.99%), iron(II) acetylacetonate (99.99%), triethyloxonium tetrafluoroborate (Et_3OBF_4, 1M in dichloromethane), nitrosyl tetrafluoroborate ($NOBF_4$, 95%), *N,N*-dimethylformamide (DMF, anhydrous 98.8%),

---

[2] This work was published under my former name, Teresa E. Pick.

ethanol (EtOH, 200 proof, anhydrous, ≥ 99.5%), were purchased from Aldrich and used without further purification. Oleylamine (OLAM, 90%) was obtained from Acros. Sodium oleate (Pfaltz and Bauer, 97%) was purchased from VWR. All other solvents were purchased from EMD and used without further purification. PEO_{53k}-*b*-PS_{40k} was obtained from Polymer Source.

NANOCRYSTALS. Literature protocols were followed for the synthesis of ITO NCs,[12,13] TiO_2 nanorods[14] and nanospheres,[15] CeO_2 NCs,[16] Yb,Er-doped $NaYF_4$ NCs,[17] and FePt NCs.[18]

POLYMERS. I performed the synthesis of PDMA-*b*-PS block copolymer architecture directing agents *via* RAFT polymerization of HO_2C-PDMA-TTC macro-chain transfer agent with styrene (Scheme 6.1). I prepared the dodecylsulfanylthiocarbonylsulfanyl-2-methylpropionic acid chain transfer agent (DMP-CTA) as previously reported.[19]

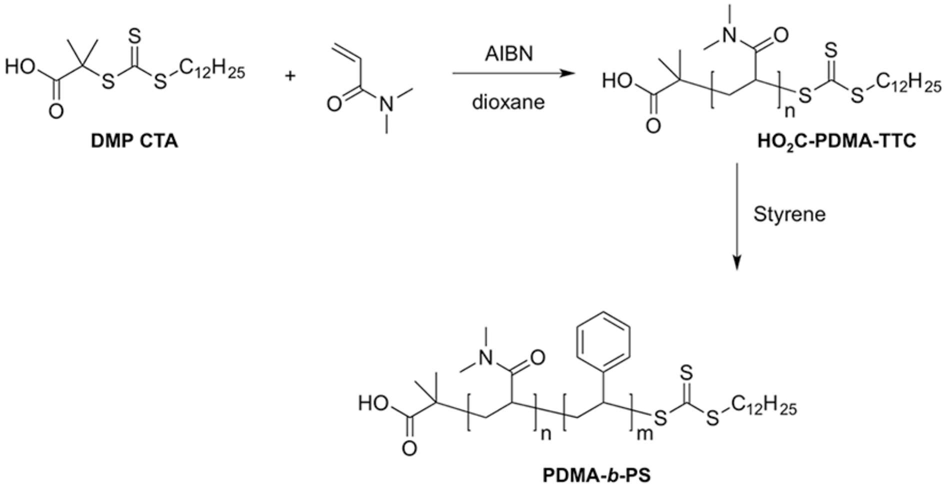

Scheme 6.1. Synthetic scheme for preparation of PDMA-*b*-PS block copolymers.

Representative Polymerization of HO_2C-PDMA-TTC *via* RAFT. A solution of DMA (2.00 g, 20.2 mmol), DMP (36.8 mg, 0.101 mmol), AIBN (1.66 mg, 0.010 mmol) and 1,4-dioxane (2.00 g) was charged to an oven dried, 25 mL Schlenk tube. The mixture was degassed by three freeze-pump-thaw cycles, sealed under nitrogen and heated at 70 ˚C for 40 min. After quenching with liquid N_2 the viscous polymerization mixture was dissolved in acetone (5 mL) and precipitated three times into cold hexanes (500 mL). The pale yellow flocculate solid was filtered, and then dried *in vacuo*. Yield: 98%.

$PDMA_{10k}$: ^1H NMR ($CDCl_3$): δ 3.42–2.91 (m; N-(CH_3)$_2$, SCH_2- CTA), 2.64–2.13 (m, -*CH*- backbone), 1.76–1.21 (m; -CH_2- backbone, SC(CH_3)$_2$- CTA, -CH_2- CTA), 0.99 (-CH_3 CTA) ppm. FT-IR ($CHCl_3$): ν 3518, 2990, 2930, 2470, 1631, 1496, 1457, 1428, 1414, 1400, 1356, 1256, 1215, 1139, 1096, 1057, 926, 748, 665 cm^{-1}.

$PDMA_{20k}$: ^{1}H NMR ($CDCl_3$): δ 3.42–2.91 (m; N-(CH_3)$_2$, SCH_2- CTA), 2.86–2.67 (m, -CH- backbone), 1.78–1.30 (m; -CH_2- backbone, SC(CH_3)$_2$- CTA, -CH_2- CTA),), 0.99 (-CH_3 CTA) ppm. FT-IR ($CHCl_3$): ν 3500, 2986, 2928, 2471, 1628, 1495, 1457, 1428, 1413, 1399, 1355, 1256, 1214, 1138, 1095, 1057, 941, 924, 787, 747, 664 cm^{-1}.

PS_{50k}: ^{1}H NMR ($CDCl_3$): δ 7.12–6.49 (m, Ar-H), 3.42 (m, SCH_2- CTA), 2.23–1.75 (m; -CH- backbone, SC(CH_3)$_2$- CTA), 1.47–1.19 (m; -CH_2- backbone, -CH_2- CTA), 0.99 (-CH_3 CTA) ppm. FT-IR ($CHCl_3$): ν 3082, 3060, 3025, 3001, 2924, 2849, 2246, 1944, 1871, 1803, 1746, 1601, 1583, 1543, 1492, 1452, 1372, 1328, 1312, 1219, 1181, 1154, 1068, 1028, 980, 965, 942, 908, 842, 770, 732, 697 cm^{-1}.

Representative Block Copolymerization of HO_2C-PDMA-TTC with Styrene. A solution of HO_2C-PDMA-TTC macro-CTA (200 mg, M_w = 19,790) and styrene (1.41 g) was charged to an oven dried, 25 mL Schlenk tube. The mixture was degassed by three freeze-pump-thaw cycles, sealed under nitrogen and heated at 110 ˚C for 18 h. After quenching with liquid N_2 the viscous reaction mixture was dissolved in acetone (3 mL) and precipitated three times into cold hexanes (250 mL). The pale yellow flocculate solid was filtered, and then dried *in vacuo*. Yield: 85%.

$PDMA_{10k}$-*b*-PS_{60k}: ^{1}H NMR ($CDCl_3$): δ 7.09–6.45 (m, Ar-H), 3.42–2.91 (m; N-(CH_3)$_2$, SCH_2- CTA), 2.70–2.05 (m, -CH- backbone), 1.87–1.27 (m; -CH_2- backbone, SC(CH_3)$_2$- CTA, -CH_2- CTA), 0.99 (-CH_3 CTA) ppm. FT-IR ($CHCl_3$): ν 3503, 3082, 3060, 3025, 3002, 2924, 2850, 1943, 1871, 1803, 1746, 1639, 1601, 1492, 1452, 1399, 1358, 1256, 1218, 1181, 1152, 1141, 1096, 1067, 1028, 942, 907, 842, 755, 697, 666 cm^{-1}.

$PDMA_{20k}$-*b*-PS_{20k}: ^{1}H NMR ($CDCl_3$): δ 7.11–6.48 (m, Ar-H), 3.42–2.88 (m; N-(CH_3)$_2$, SCH_2- CTA), 2.72–2.07 (m, -CH- backbone), 1.86–1.27 (m; -CH_2- backbone, SC(CH_3)$_2$- CTA, -CH_2- CTA), 0.99 (-CH_3 CTA) ppm. FT-IR ($CHCl_3$): ν 3485, 3082, 3060, 3025, 2924, 2853, 1943, 1871, 1803, 1718, 1634, 1492, 1452, 1399, 1355, 1256, 1139, 1096, 1058, 1028, 941, 907, 842, 748, 698, 665 cm^{-1}.

$PDMA_{20k}$-*b*-PS_{60k}: ^{1}H NMR ($CDCl_3$): δ 7.12–6.48 (m, Ar-H), 3.42–2.91 (m, N-(CH_3)$_2$, SCH_2- CTA), 2.74–2.10 (m, -CH - backbone), 1.86–1.29 (m, -CH_2- backbone, SC(CH_3)$_2$- CTA, -CH_2- CTA), 0.99 (-CH_3 CTA) ppm. FT-IR ($CHCl_3$): ν 3478, 3082, 3060, 3026, 2924, 2851, 1943, 1869, 1803, 1640, 1493, 1452, 1400, 1357, 1258, 1219, 1142, 1028, 909, 843, 770, 734, 698, 667 cm^{-1}.

$PDMA_{60k}$-*b*-PS_{50k}: ^{1}H NMR ($CDCl_3$): δ 7.11–6.48 (m, Ar-H), 3.42–2.91 (m, N-(CH_3)$_2$,SCH_2- CTA), 2.72–2.08 (m, -CH- backbone), 1.79–1.33 (m, -CH_2- backbone, SC(CH_3)$_2$-CTA, -CH_2- CTA), 0.99 (-CH_3 CTA) ppm. FT-IR ($CHCl_3$): ν 3496, 3082, 3060, 3026, 3000, 2925, 2852, 2237, 1944, 1873, 1805, 1634, 1492, 1452, 1399, 1356, 1257, 1219, 1139, 1095, 1058, 1028, 911, 843, 770, 729, 697 cm^{-1}.

Table 6.1. Number average (M_n) and weight average (M_w) molecular weights and polydispersity indices (PDI = M_w/M_n) for all homopolymers and block copolymers synthesized via RAFT polymerization, as determined by DMF-SEC.

Polymer	M_n	M_w	PDI
$PDMA_{10k}$	8,410	9,440	1.12
$PDMA_{20k}$	17,040	19,790	1.16
PS_{50k}	52,360	57,100	1.09
$PDMA_{10k}$-*b*-PS_{60k}	58,560	70,590	1.2
$PDMA_{20k}$-*b*-PS_{20k}	32,810	43,530	1.3
$PDMA_{20k}$-*b*-PS_{60k}	63,460	82,500	1.3
PS_{50k}-*b*-$PDMA_{60k}$	64,540	87,510	1.36

PREPARATION OF LIGAND-STRIPPED NANOCRYSTAL DISPERSIONS. Ligand-stripping reactions were performed in a nitrogen glovebox, using previously reported procedures[10,11]: $NOBF_4$ was used to strip ITO, TiO_2, FePt and Yb,Er-doped $NaYF_4$ NCs and EtO_3BF_4 was used to strip CeO_2 NCs. Highly concentrated (120 mg mL^{-1} by ICP-AES) NC solutions were obtained following dispersion of ligand-stripped NCs in DMF. Nanocrystal size was determined by using ImageJ software to measure a distribution of particles from bright-field transmission electron microscopy (BF-TEM) images.

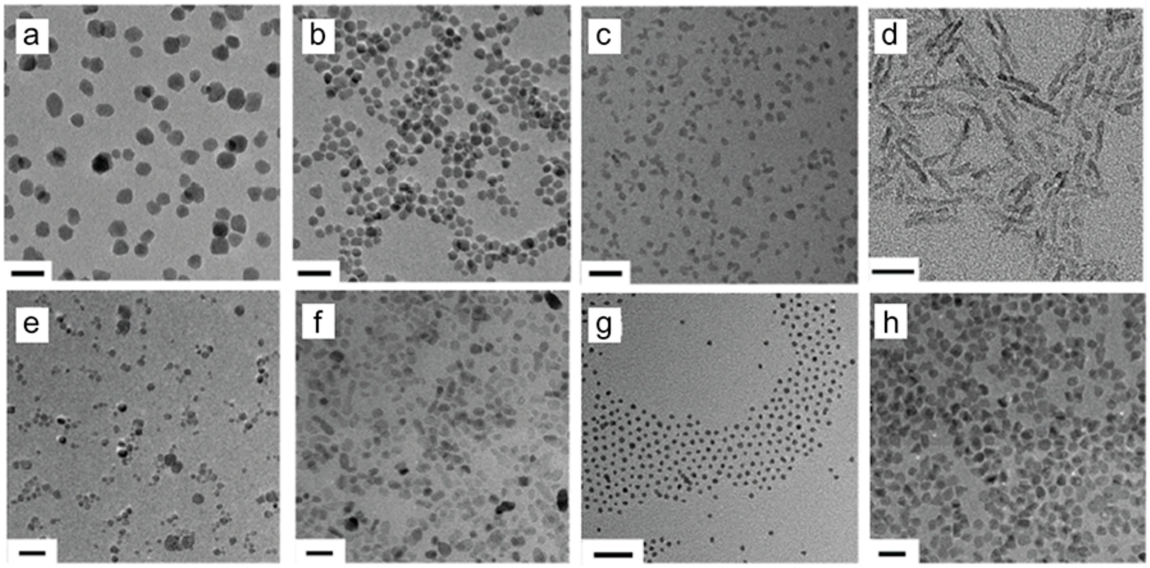

Figure 6.1. Bright-field TEM images of ligand stripped nanocrystals: (a) 8 ± 2 nm ITO; (b) 6 ± 1 nm ITO; (c) 4.5 ± 0.6 nm ITO; (d) 3 x 20 nm TiO_2 rods; (e) CeO_2; (f) TiO_2 nanospheres; (g) FePt NCs; (h) Yb,Er-doped $NaYF_4$. Scale bar = 20 nm.

PREPARATION OF MESOPOROUS NANAOCRYSTAL FRAMEWORKS. I prepared micellar dispersions of PDMA-*b*-PS (5–30 mg mL^{-1} final concentration) in 20% *v/v* DMF in EtOH by dissolving the BCPs in DMF first then adding EtOH in a slow drop-wise stream. After stirring for 24 h, the NCs (10–45 mg) were added and the BCP–NC solution was left stirring for an additional 24 h. The BCP–NC solutions were deposited on different substrates (silicon, quartz, FTO, NaCl) both by dip-coating (150 mm min^{-1} withdrawal speed at 30% relative humidity) and spin-coating (600 rpm to 3000 rpm). Film thickness was controlled by changing the spinning rate and/or increasing BCP–NC solution concentration. For example, a 70 nm thick mesoporous film on 2x2 cm^2 FTO glass was obtained by spinning at 1000 rpm 60 μL of a solution containing 10 mg mL^{-1} $PDMA_{10k}$-*b*-PS_{60k} and 15 mg mL^{-1} TiO_2 rods; 200 nm thick mesoporous films on 2x2 cm^2 FTO glass were obtained by spinning at 1000 rpm 60 μL of a solution containing 30 mg mL^{-1} $PDMA_{10k}$-*b*-PS_{60k} and 45 mg mL^{-1} TiO_2 rods. Multilayer deposition was used to further increase the film thickness. Thermal annealing was performed in air in a quartz tube furnace using a 2 h ramp to 550 ˚C, followed by holding at that temperature for 1 h and 30 min, then cooling to rt, which fully removed the BCP templating agent. Faster heating rates (up to 150 ˚C min^{-1}) as well as annealing temperature as low as 400 ˚C (corresponding to the BCP decomposition temperature as determined by thermogravimetric analysis) with a 4 h hold at that temperature were found to succeed in preserving the mesostructured framework while removing the templating agent as well. Samples for TEM analysis of mesoporous NC frameworks were prepared by spin-coating the BCP–NC dispersion on a NaCl substrate. After annealing in air to fully remove the BCP template, film lift-off was accomplished by a slow immersion of the NaCl in water; a 100 mesh Cu grid collected the floating film.

ELECTROCHEMICAL METHODS. Electrochemical measurements were carried out using a conventional 3-electrode cell in an argon-filled glove box. The electrolyte solution was 1 M $LiPF_6$ in ethylene carbonate/propylene carbonate (EC:PC, 1:1 *v/v*). Two Li foils were used as counter and reference electrodes; the working electrode consisted of 200 and 600 nm thick films deposited by spin coating BCP–NC solutions on 2x2 cm^2 FTO/glass substrates, then annealed in air to remove the BCP ADA. Charge/discharge experiments and cyclic voltammograms were performed using an Arbin Instrument potentiostat. All the measurements were performed in the 1–2.8 V *vs.* Li^+/Li voltage range.

6.3 Results and Discussion

The BCPs contain a NC-tethering domain consisting of poly(*N,N*-dimethylacrylamide) (PDMA), which was chosen to mimic the dynamic adsorption interactions of dimethylformamide (DMF) at bare NC surfaces,[10,11] alongside a porogenic polystyrene (PS) domain. To tune the mesoscale architectures, I synthesized and characterized several PDMA-*b*-PS BCP architecture-directing agents (ADAs) with different molecular weights and block ratios by reversible addition-fragmentation chain transfer (RAFT) polymerization (Scheme 6.1 and Table 6.1).

In polar solvents, I observed that these amphiphilic BCPs formed micelles with a PDMA corona; the ligand-stripped NCs decorate the periphery when added to a solution of preformed micelles (Scheme 6.2).

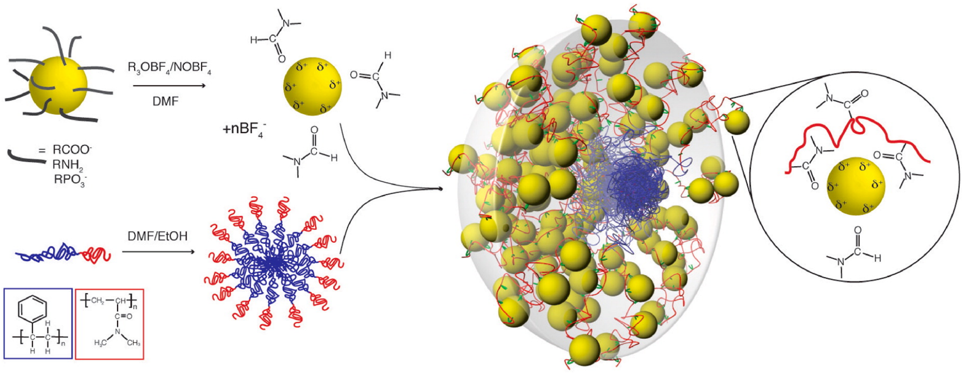

Scheme 6.2. Assembly of Ligand-Stripped Nanocrystals with PDMA-*b*-PS Micelles

We investigated the co-assembly of BCP micelles with ligand-stripped NCs by BF-TEM and quantified their assembly using dynamic light scattering (DLS), as shown in Figure 6.2 for 6 nm ITO NCs assembled with each of the four BCP ADAs.

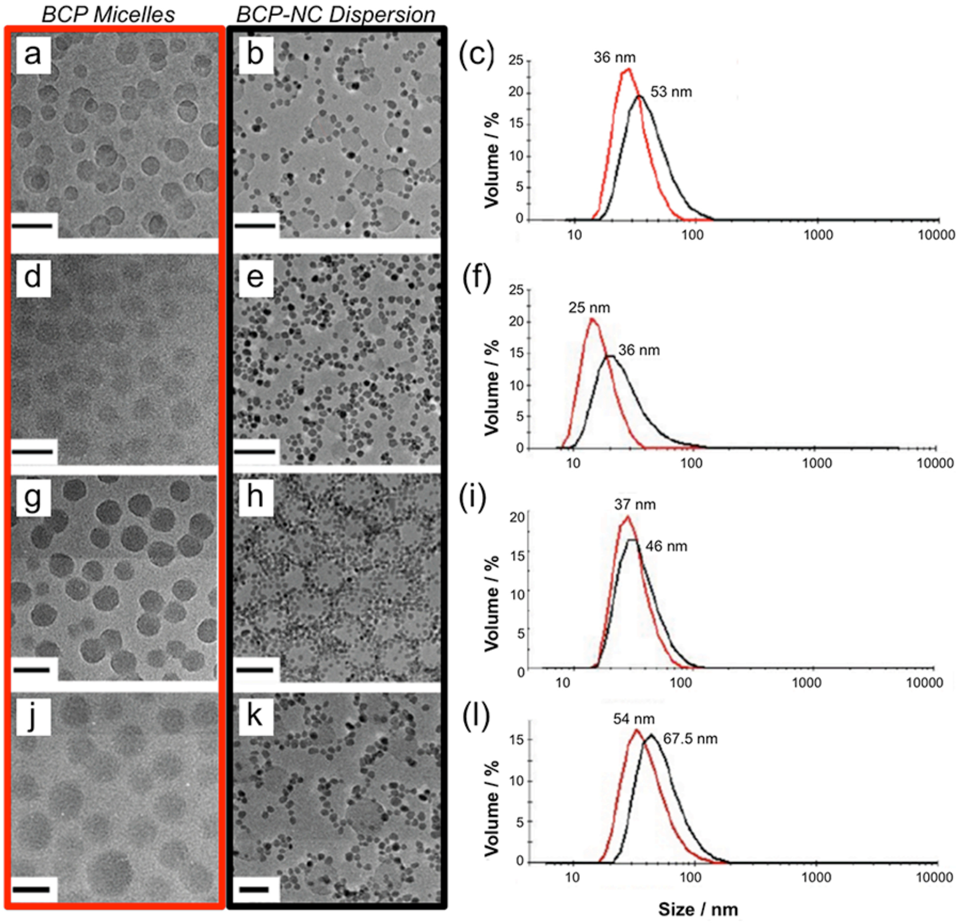

Figure 6.2. Bright-field TEM images (left columns) and DLS analysis (right column) of

BCP micelles (red trace) and BCP–NC dispersions (black trace) for assemblies prepared from 6 nm ITO NCs with BCP ADAs: (a–c) PDMA$_{20k}$-*b*-PS$_{60k}$; (d–f) PDMA$_{20k}$-*b*-PS$_{20k}$; (g–i) PDMA$_{10k}$-*b*-PS$_{60k}$; (j–l) PDMA$_{60k}$-*b*-PS$_{50k}$. Scale bar = 50 nm.

Notably, while bare NCs are also compatible with traditional PEO-based BCPs, a weak interaction between PEO and NC surfaces was observed, and it was determined that NCs do not decorate micelles of these polymers (Figure 6.3). When the traditional architecture-directing agent PEO-*b*-PS was used in a solvent mixture of 20% DMF *v/v* in ethanol, no hydrodynamic size increase was observed when NCs were added to the micelle solution. Rather, a peak corresponding to the NC diameter appeared (Figure 6.3d). The NC segregation was confirmed also by TEM analysis (Figure 6.3b). Only after the addition of toluene to the NC–BCP solution did I observe NC-decorated micelles (Figure 6.3c) and the hydrodynamic size of the PEO-*b*-PS micelles increased (Figure 6.3d). No size change occurred when toluene was added to a solution of PEO-*b*-PS micelles alone. This evidence allowed me to exclude the possibility of any swelling of the micelles induced by toluene. Because the PEO–NC interactions are much weaker than the DMF–NC interactions, the NC dispersion in DMF was more energetically favorable, making it unfavorable for the NCs to decorate the PEO corona. Therefore, it was necessary to destabilize both the PEO corona and the NC surface by the addition of toluene to drive the NCs to the PEO block. The strikingly different behavior of PDMA-*b*-PS (Figure 6.2) supports the existence of a substantial affinity between the NC surface and the PDMA block that is then reflected in the regular ordering in the mesoporous architectures when PDMA-*b*-PS acts as an architecture-directing agent. Assemblies formed from PEO-based polymers, by comparison, lack significant ordering.[20]

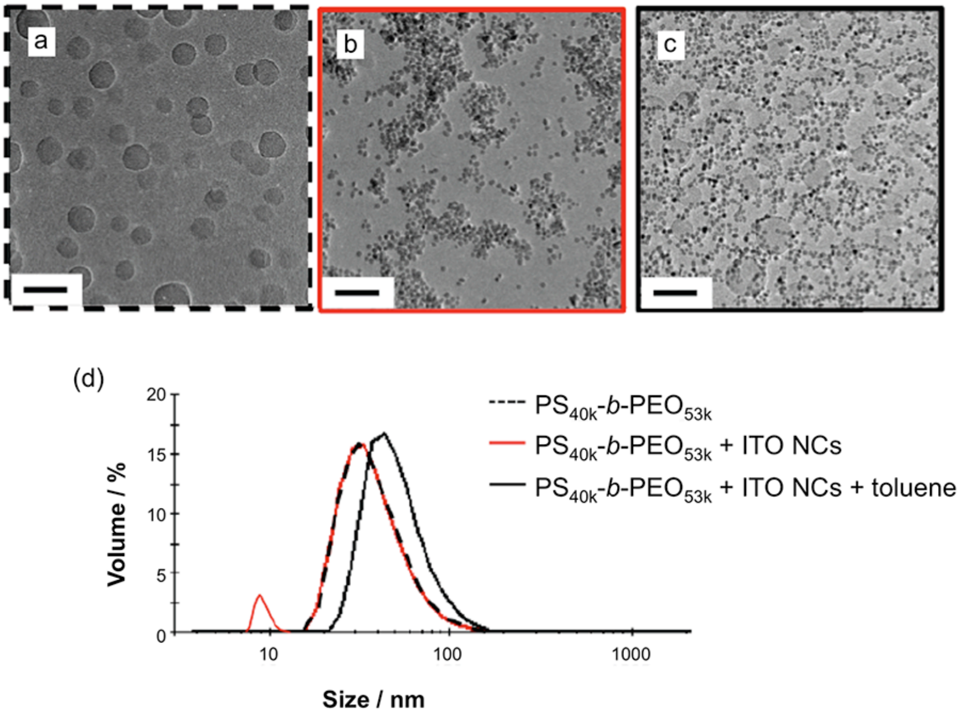

Figure 6.3. Bright-field TEM images and DLS analysis of PS-*b*-PEO–ITO dispersions. TEM images of PS-*b*-PEO micelles: (a) alone; (b) after the addition of 6 nm ITO NCs; (c) after the addition of 200 μL of toluene to the PS-*b*-PEO + ITO NC dispersion; (d) DLS analysis of each sample. Scale bar = 50 nm.

When DMF was included in the solvent mixture (e.g., 20% DMF in ethanol), the NC-decorated PDMA-*b*-PS micelles remained stably suspended, and uniform films could be deposited by spin- or dip-coating. Mesoporous NC framework architectures were realized by annealing the film in air to remove the BCP architecture-directing agent. The assembly process was applicable to NCs of diverse size, shape, and composition; oxides (TiO_2, CeO_2, and ITO) are readily assembled into mesoporous frameworks, as are nanophosphors (Yb, Er-doped $NaYF_4$) and metal alloys (FePt) (Figure 6.4) while, when DMF is substituted by a non-polar solvent, such as toluene, precipitation of macroscopic assemblies occurs (Figure 6.4i).

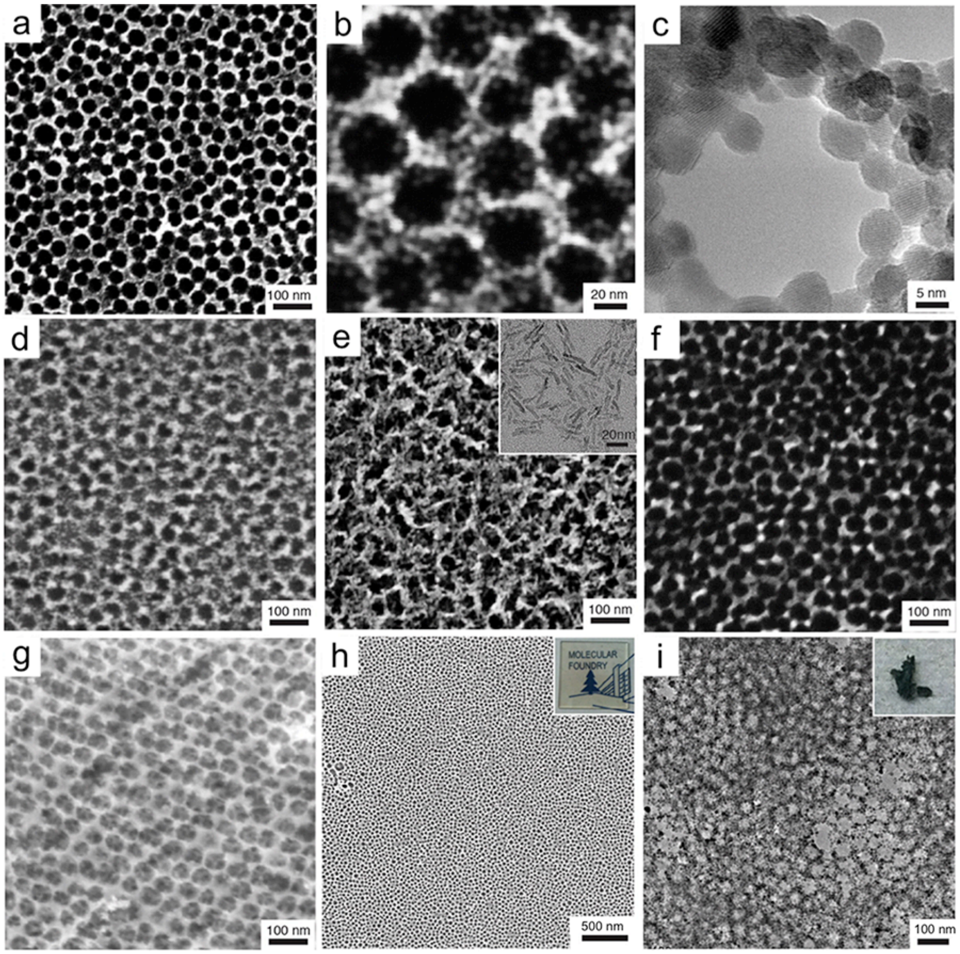

Figure 6.4. Compositional diversity among mesoporous frameworks based on NCs assembled with $PDMA_{10k}$-*b*-PS_{60k}. (a) Top-down SEM image of a framework derived

from 4.5 nm ITO NCs; (b) high-resolution SEM and (c) bright-field TEM images of the same. Scanning electron microscopy images of mesoporous frameworks: (d) 5 nm CeO_2 NCs; (e) 3 by 20 nm TiO_2 nanorods (inset: BF-TEM of the nanorods alone); (f) 8 nm Yb,Er-doped $NaYF_4$; and (g) 3 nm FePt NCs. (h) Low-resolution SEM of an ITO NC mesoporous framework shows long-range uniformity. Inset: photo of a mesoporous framework where the homogeneity is evident by the high transparency and absence of scattering. (i) Bright-field TEM image of a mesoporous ITO powder of 8 nm ITO NCs (inset: photo of the original assembly).

As a way to investigate the frameworks' structural dimensions for assemblies generated from a single NC size (i.e., 4.5 nm ITO NCs) with BCPs of different PDMA and PS block sizes, we generated a series of frameworks with $PDMA_{20k}$-*b*-PS_{20k}, $PDMA_{20k}$-*b*-PS_{60k}, and $PDMA_{10k}$-*b*-PS_{60k} ADAs by dip-coating and annealing to reveal the mesoporosity, as shown by top-down SEM images in Figure 6.6a–c. The resulting framework architectures were highly ordered at the meso length scale, though they did not generally exhibit long-range translational symmetry. Their well-defined periodicity over large areas was quantified by grazing-incidence small-angle X-ray scattering (GISAXS) (Figure 6.5d). The metrics of these films are reported in Table 6.2.

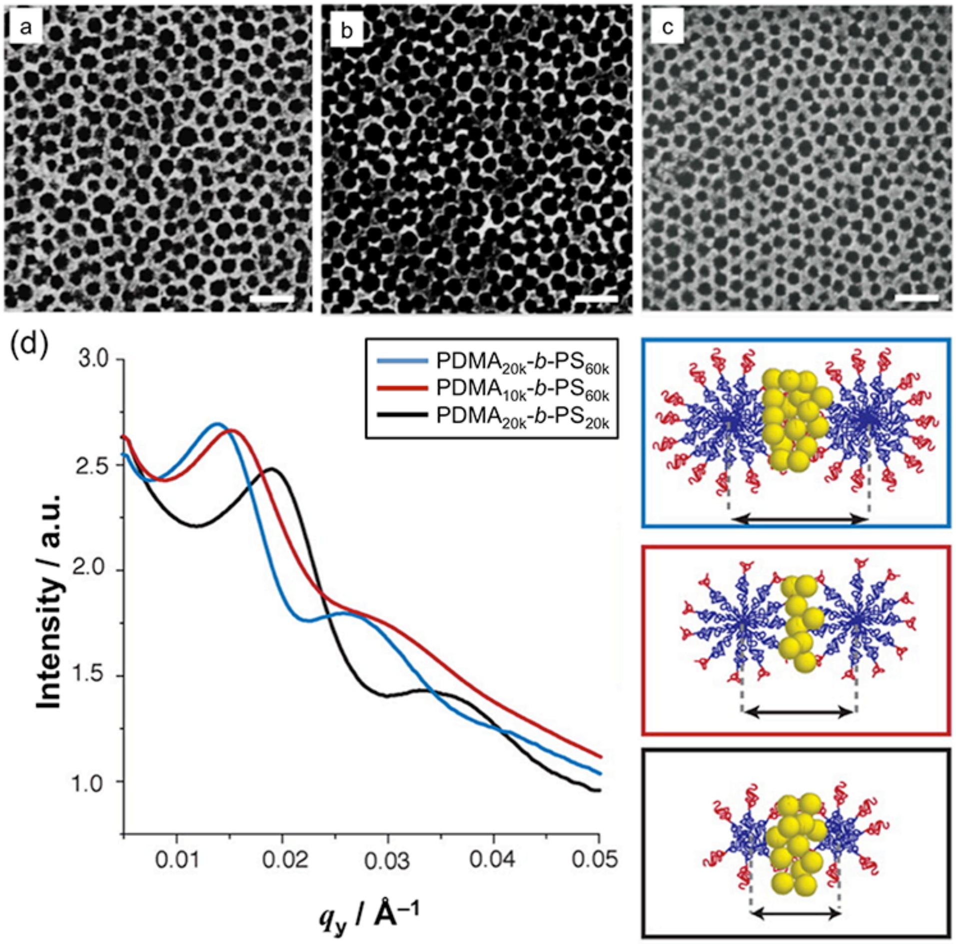

Figure 6.5. Analysis of the structural dimensions of mesoporous ITO NC frameworks. Top-down SEM images of 4.5 nm ITO NC frameworks derived from architecture-directing agents: (a) $\mathrm{PDMA_{20k}}$-*b*-$\mathrm{PS_{60k}}$; b) $\mathrm{PDMA_{10k}}$-*b*-$\mathrm{PS_{60k}}$; (c) $\mathrm{PDMA_{20k}}$-*b*-$\mathrm{PS_{20k}}$. Scale bar = 100 nm. (d) Grazing-incidence SAXS line profiles along the in-plane scattering axis of the same mesoporous frameworks.

Table 6.2: Metrics variation in mesoporous ITO frameworks assembled from 4.5 nm ITO nanocrystals.[a]

BCP ADA	Periodicity (nm)	Pore size (nm)	Wall Thickness (nm)
$\mathrm{PDMA_{20k}}$-*b*-$\mathrm{PS_{60k}}$	46	34 ± 5	14 ± 3
$\mathrm{PDMA_{10k}}$-*b*-$\mathrm{PS_{60k}}$	42	33 ± 5	10 ± 3
$\mathrm{PDMA_{20k}}$-*b*-$\mathrm{PS_{20k}}$	33	23 ± 3	13 ± 3

[a] Periodicity was derived from GISAXS line scans (Figure 6.5d). Pore size and wall thickness were determined by collecting statistics using ImageJ software on SEM images (Figure 6.5a–c).

A similar comparison was made for the investigation of frameworks generated from different sizes of ITO NCs (i.e., 4.5 nm, 6 nm, and 8 nm), which were similarly assembled with $\mathrm{PDMA_{20k}}$-*b*-$\mathrm{PS_{20k}}$, $\mathrm{PDMA_{20k}}$-*b*-$\mathrm{PS_{60k}}$, and $\mathrm{PDMA_{10k}}$-*b*-$\mathrm{PS_{60k}}$ ADAs by dip-coating and annealing to reveal the mesoporous framework (Figure 6.6). The loss of order, qualitatively appreciated by SEM images, while increasing the NC size or increasing the BCP molecular weight, is confirmed by GISAXS showing an intensity decrease of the second order reflections. See Figure 6.5a–c for SEM images of mesoporous frameworks generated from 4.5 nm ITO NCs with the same three ADAs.

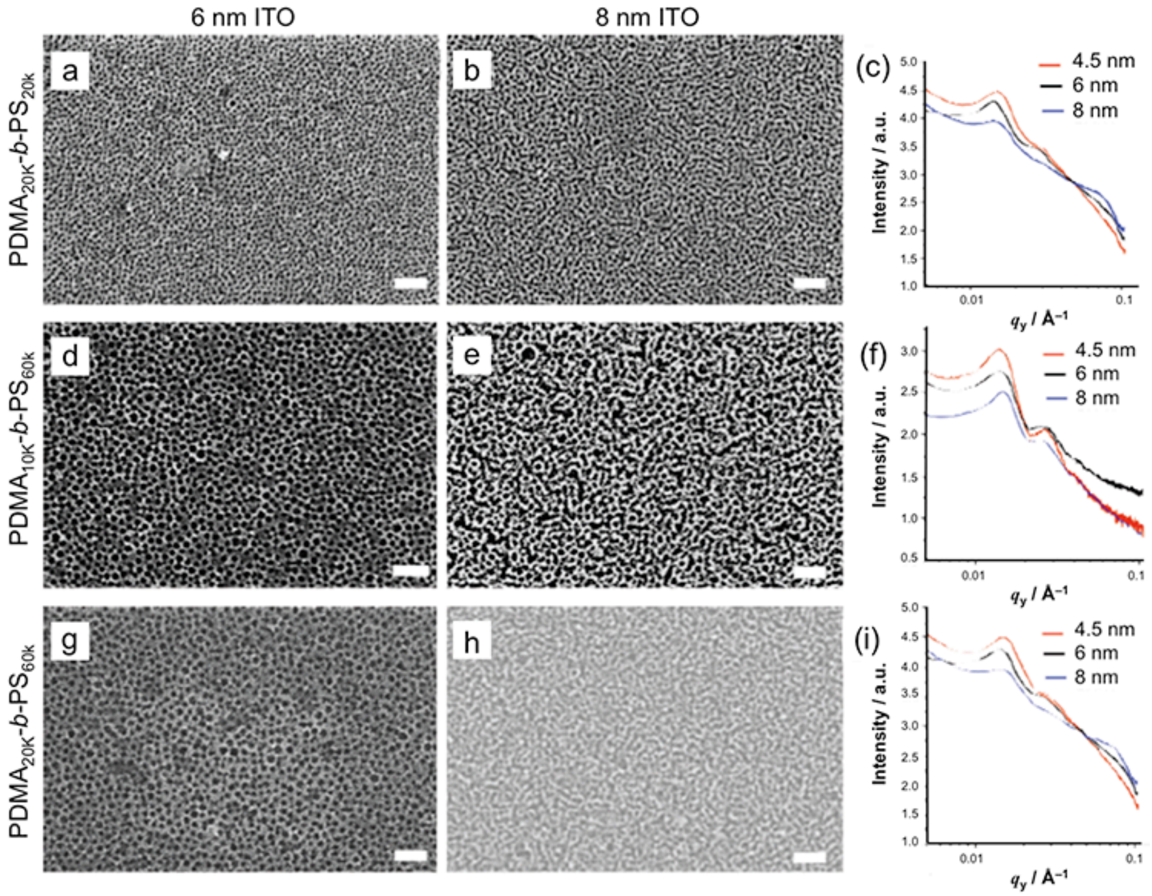

Figure 6.6. Mesoporous frameworks based on different sizes of ITO NCs and PDMA-*b*-PS BCPs. Left and center panels are top-down SEM images of mesoporous frameworks generated from 6 nm (left panel) and 8 nm (center panel) ITO NCs. Right panel are GISAXS line profiles along the in-plane scattering axis for 4.5 nm (red trace), 6 nm (black trace), 8 nm (blue trace) ITO NCs. Frameworks were generated by: (a–c) PDMA$_{20K}$-*b*-PS$_{20k}$; (d–f) PDMA$_{10K}$-*b*-PS$_{60k}$; (g–i) PDMA$_{20K}$-*b*-PS$_{60k}$. Scale bar = 100 nm.

Additionally, the role that NC loading played in the regularity of the framework metrics was investigated. A series of frameworks was prepared, generated from assemblies of PDMA$_{10K}$-*b*-PS$_{60k}$ (10 mg mL^{-1}) with 6 nm ITO NCs (loadings ranging from 15–30 mg mL^{-1}). By analyzing both top-down SEM and GISAXS data, we observed regularity of architectural ordering from assemblies prepared at intermediate BCP–NC ratios, with high NC loading resulting in loss of periodicity and low NC loading resulting in a worm-like morphology (Figure 6.7). To quantify these results we used the position of the primary scattering peak in the GISAXS data to show that the *d*-spacing increased as NC loading increased for the lowest three loadings as more NCs were incorporated into the framework (e.g., 45 nm, 50 nm, and 56 nm, for loadings of 15, 20, and 25 mg mL^{-1}, respectively) (Figure 6.7e). At the highest loading, 30 mg mL^{-1}, the *d*-spacing decreased to 53 nm along with a decrease in the scattering intensity and a broadening of the peak corresponding poorer ordering. Based upon these observations, 20 ± 5 mg mL^{-1} was chosen as the optimal NC loading.

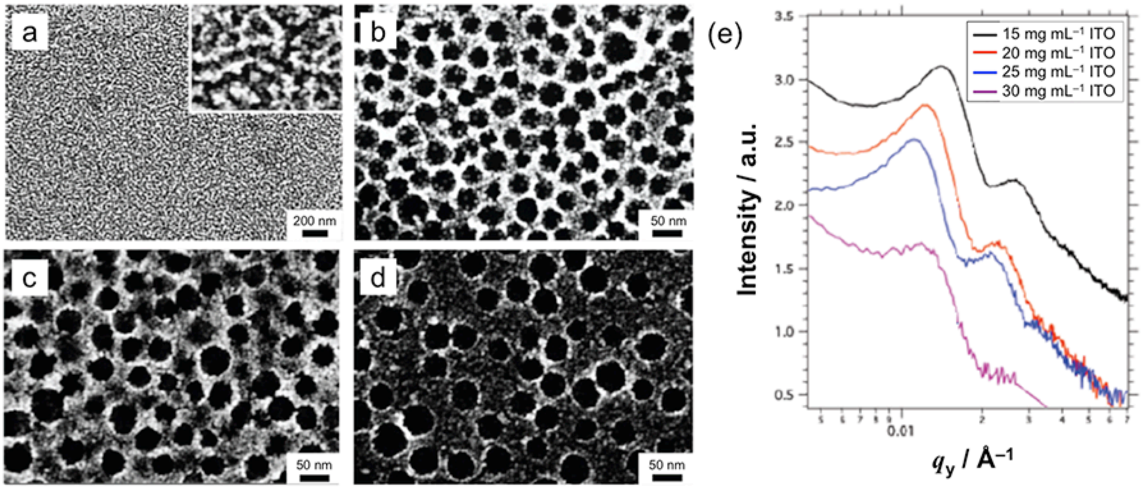

Figure 6.7. Evolution of mesoporous frameworks architectures as related to BCP–NC weight ratio. Top-down SEM images of frameworks generated from assemblies of 6 nm ITO with PDMA$_{10K}$-*b*-PS$_{60k}$ at ITO concentrations of: (a) 15 mg mL^{-1}; (b) 20 mg mL^{-1}; (c) 25 mg mL^{-1}; (d) 30 mg mL^{-1}. (e) GISAXS line profiles along the in-plane scattering axis (q_y) for ITO NC loading series.

These results showed that all of the critical dimensions in the mesoporous framework architectures were controlled through the selection of building blocks. Varying the M_w of the BCP domains systematically changed the periodicity; the M_w of the PDMA block tuned the wall thickness, while the M_w of the PS block tuned the mesopore dimensions (Figure 6.6, Table 6.2). In general, the NC size and shape, established through colloidal synthesis, persisted through assembly and annealing; investigating frameworks before and after the final thermal processing step provided proof. Here, for frameworks derived from 8 nm ITO NCs and PDMA$_{20k}$-*b*-PS$_{60k}$ ADA, wide-angle X-ray diffraction (XRD) was used to show that the pattern remained unchanged after annealing, indicating a lack of crystallite grain growth (Figure 6.8a). Analysis of the GISAXS line profiles, which are offset for clarity, of the same frameworks shows the persistent periodicity by the position of the primary scattering peak (Figure 6.8b). SEM images, both top-down and cross-sectional show little change in film morphology or thickness following the removal of the ADA

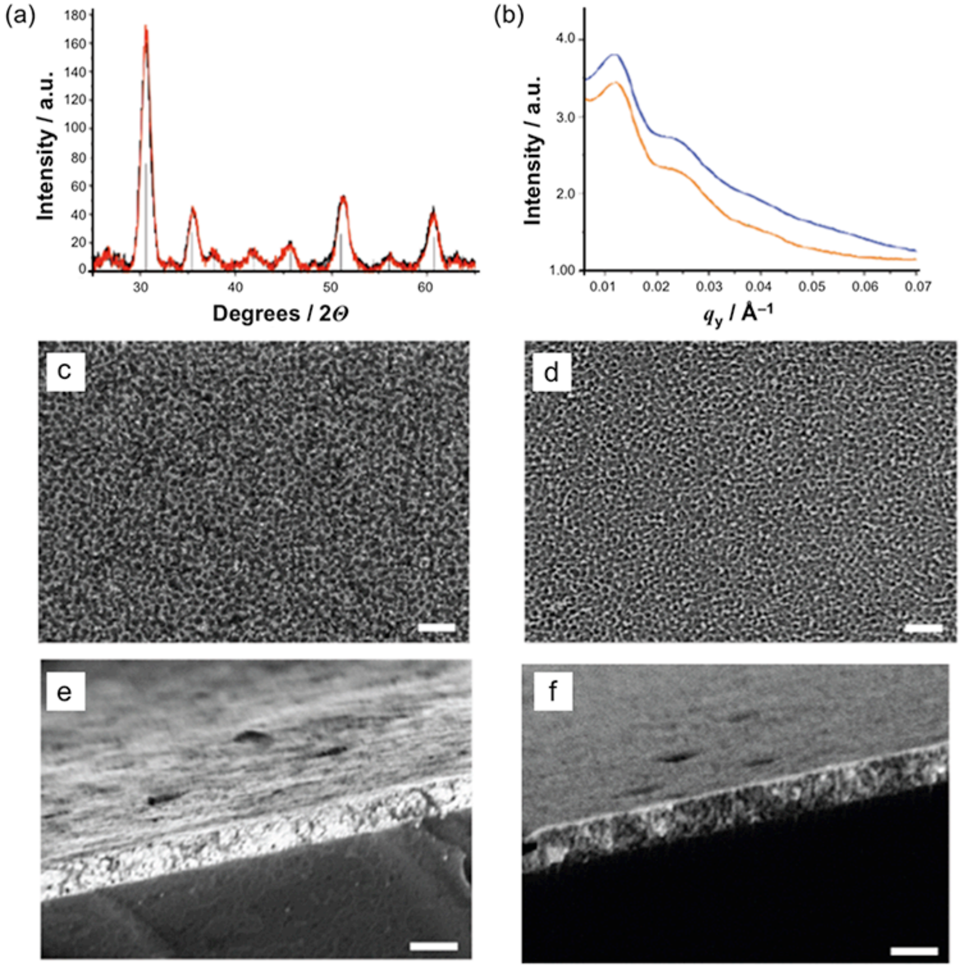

Figure 6.8. Analysis of mesoporous frameworks before and after annealing: (a) Wide-angle XRD patterns before (red trace) and after (black trace) annealing; (b) GISAXS line profiles along the in-plane scattering axis before (orange trace) and after (blue trace) annealing; top-down and cross-sectional SEM images (c,e) before and (d,f) after annealing. Scale bar = 100 nm for (c,d) and 250 nm for (e,f).

Controlling the coassembly of BCPs with NCs relied on the balance between enthalpic gain, due to BCP–NC chemical interactions ($\Delta H_{\text{BCP–NC}}$), and entropic penalty, which is due primarily to the loss of conformational entropy of polymeric chains when stretching to incorporate NCs (ΔS_{BCP}).[21−23] ΔS_{BCP} has been demonstrated in both theoretical and experimental results to depend on the ratio of NC diameter (d) to the size of the polymer domain with which the NCs interact, specifically its root-mean-squared end-to-end distance (R_0).[21−23] At larger d / R_0, the entropic cost of coassembly increases due to more severe conformational restriction of the polymer chains. Hence, based on entropic trends, poorer ordering was expected as $R_{0,\text{PDMA}}$ became smaller, keeping the NC size fixed. Contrary to this expectation, we observed improved ordering for shorter PDMA chains, an effect which is most apparent for larger NCs (e.g., 6 or 8 nm ITO, Figure 6.6). This suggested that a strong enthalpic driving force deriving from the adsorption of PDMA on the naked NC surfaces ($\Delta H_{\mathrm{BCP\text{-}NC}}$) was dominating the assembly process.

An investigation into PDMA adsorption revealed a variable shift in the frequency of the carbonyl stretching vibration using attenuated total reflectance Fourier transform infrared spectroscopy (ATR-FTIR) (Figure 6.9). When NCs were introduced to a dispersion of BCP micelles, we observed that the position of the carbonyl peak (on the PDMA backbone) shifted systematically to a higher frequency, eventually reaching a stable value around the same BCP–NC weight ratios that yielded long-range ordering (Figure 6.9a). Data shown here are for assemblies generated from PDMA_{10k}-*b*-PS_{60k} with increasing content of 3 nm TiO_2 spheres. This was interpreted as the saturation of NC loading in the micelles' coronas, which is a useful indicator to identify the optimum weight fraction of NCs needed to create an ordered architecture using any given BCP. Furthermore, because there was no additional shift at higher BCP–NC ratio, this peak position is characteristic of a given combination of BCP and NC.

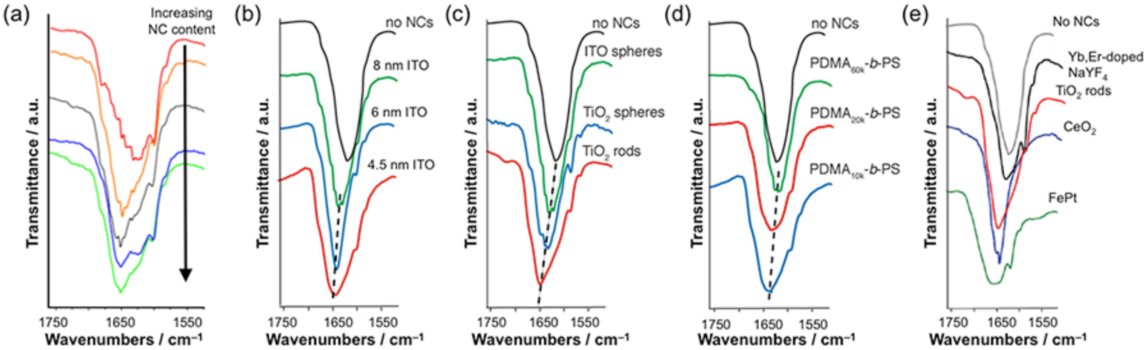

Figure 6.9. Spectroscopic study of BCP–NC interactions underlying enthalpy-driven assembly: (a) films assembled with increasing content of 3 nm TiO_2 spheres; (b) films assembled from different sizes of ITO NCs; (c) films assembled from ITO versus TiO_2 NCs of a similar size (8 nm) or TiO_2 nanorods (3 x 20 nm) of larger specific surface area; (d) films assembled from different BCP ADAs with the same ITO NCs (4.5 nm); (e) films assembled with different composition NCs (see Figure 6.1 for corresponding BF-TEM images).

This shift of the carbonyl resonance was also interpreted as indicating the extent of PDMA adsorption at NC surfaces, which was correlated with $\Delta H_{\mathrm{BCP\text{-}NC}}$. For instance, a bigger shift and a broader peak were found for higher NC surface area, that is, smaller NCs (Figure 6.9b), since more adsorption sites were available to coordinate with the PDMA amide groups. We also investigated small diameter TiO_2 nanorods (3 by 20 nm) that presented a larger specific surface area than TiO_2 spheres (8 nm), which similarly results in a larger peak shift (Figure 6.9c). Shorter PDMA chains likewise resulted in larger peak shifts (Figure 6.9d), in agreement with a higher fraction of PDMA monomers being tethered to NC surfaces. The shift of the carbonyl resonance is therefore a sensitive probe of the enthalpic driving force for coassembly. Keeping NC size and BCP M_w fixed, apparent differences in adsorption enthalpy emerged for different NC compositions. For example, the higher frequency resonance for TiO_2 versus ITO suggested a larger adsorption enthalpy for the former (Figure 6.9c), while small (3 nm) FePt NCs resulted in the highest observed carbonyl stretching frequency (Figure 6.9e). In general, I determined that larger peak shifts correlated with improved ordering (e.g., FePt in Figure 6.4g), consistent with enthalpy-driven assembly. Indeed, highly ordered mesoporous materials derived from sol−gel precursors rely on strong enthalpic interactions between the precursors and structure-directing agents as well.[2]

Finally, compared to the assembly of isotropic particles, nanorod assembly posed additional challenges since rod−rod interactions and changes in orientational entropy can create further thermodynamic opposition to achieving the high volume fractions required to stabilize a mesostructured architecture during template removal.[24−26] Here we demonstrated fabricating, for the first time, mesoporous frameworks derived from nanorods of TiO_2 assembled with $PDMA_{10k}$-*b*-PS_{60k}, which was led by the strong enthalpic driving force of PDMA adsorption at the nanorod surfaces (Figure 6.10a). This framework was compared to one derived similarly from TiO_2 nanospheres and determined that framework periodicity was invariant, with *d*-spacing in each corresponding to 54 nm.

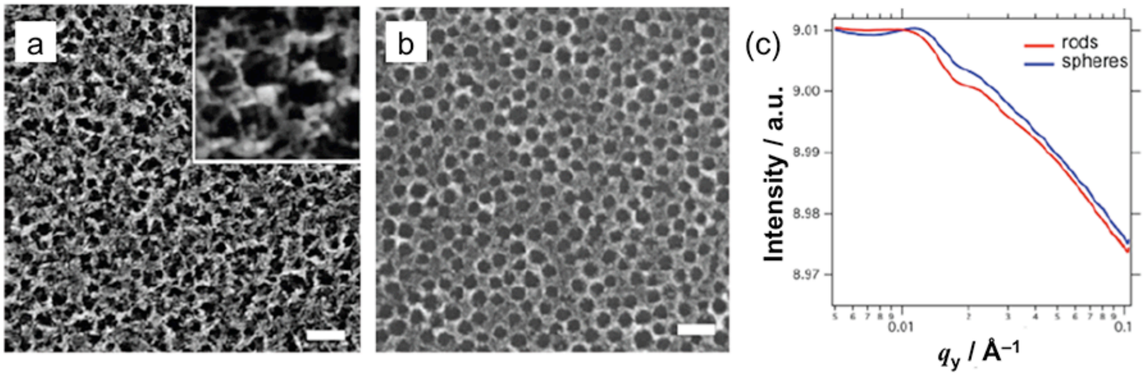

Figure 6.10. Analysis of TiO_2-based mesoporous frameworks: SEM images of (a) TiO_2 nanorods and (b) TiO_2 nanospheres; (c) GISAXS line profiles along the in-plane scattering axis showing frameworks derived from TiO_2 nanorods (red trace) and TiO_2 nanospheres (blue race). Scale bar = 100 nm.

TiO_2 is a prototypical material for both electrochemical storage[1,2,9,27,28] and dye-sensitized solar cells.[1−3,29,30] For both applications, mesoporous TiO_2 has shown enhanced performance, and, separately, crystallite shape has been suggested to have a strong influence on properties.[1−3,9,27−29,30−32] However, the lack of a generally applicable approach to assemble colloidal NCs of various shapes into ordered mesoporous materials has left open questions about the interplay between porosity and crystallite morphology in determining functional properties.

Having assembled mesoporous architectures of anatase TiO_2 nanorods, their electrochemical cycling performance versus a Li metal counter electrode was studied.

The frameworks exhibited exceptional capacity retention (Figure 6.11a) at both high (100C) and more moderate (5C) charge–discharge rates (C = 50 mA g^{-1}).

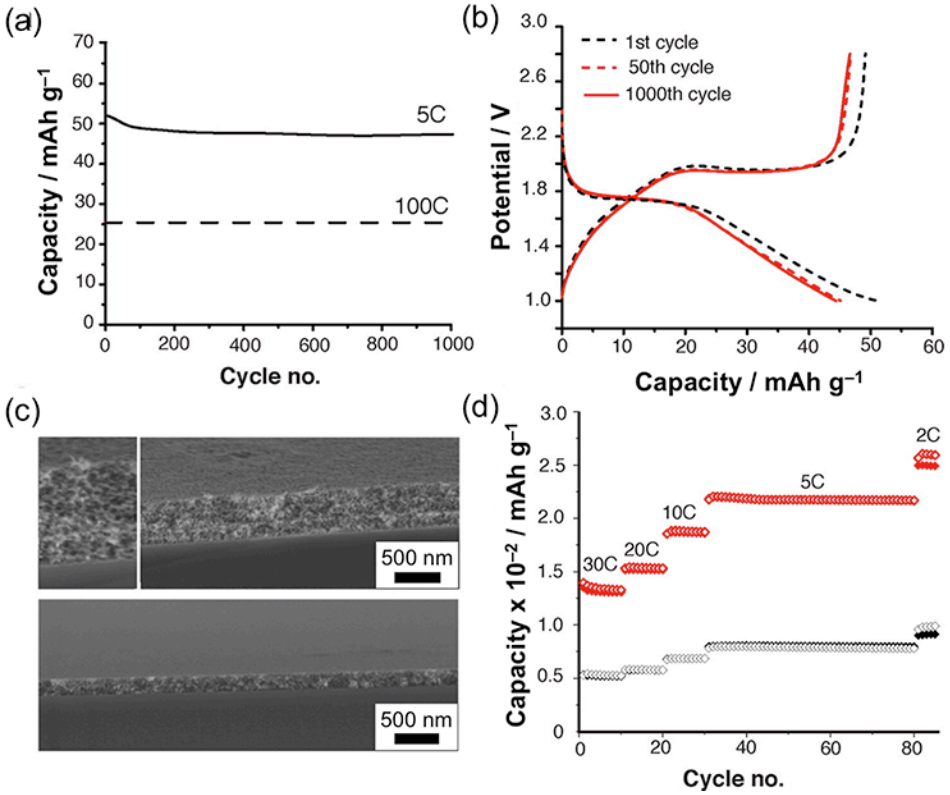

Figure 6.11. Electrochemical performance of TiO_2 nanorod-based mesoporous frameworks. (a) Discharge gravimetric capacity retention over 1000 cycles at different rates (C = 50 mA g^{-1}) and (b) corresponding loading curves at 5C. (c) Cross-sectional SEM of 200 nm (bottom) and 600 nm thick (top) frameworks and (d) their capacity variation with the charge–discharge rate (black and red symbols correspond to the 200 and 600 nm thick films, respectively, with open circles indicating charge and filled circles indicating discharge).

This is in contrast to mesoporous frameworks derived from the assembly of $PDMA_{10k}$-*b*-PS_{60k} with TiO_2 nanospheres (Figure 6.12), which experienced substantial capacity fade upon cycling at a moderate rate (5C).

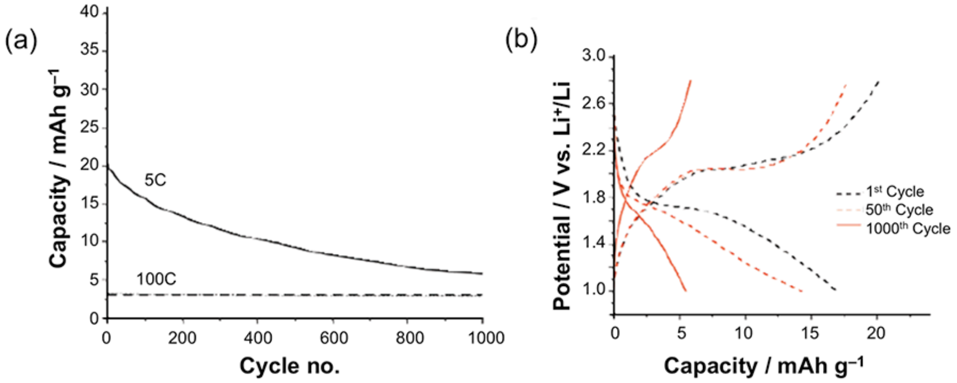

Figure 6.12. Electrochemical cycling performance of TiO_2 nanosphere-based mesoporous frameworks. (a) Discharge gravimetric capacity retention over 1000 cycles at different rates; (b) corresponding loading curves at 5C (C = 50 mA g^{-1}).

Although introducing mesoporosity was previously reported to enhance the capacity of TiO_2 nanosphere films, their stability over long cycling was not discussed.[27,28] One possible explanation for the stability of the TiO_2 nanorod frameworks at a high rate might could be attributed to the fact that charge storage becomes largely capacitive in this limit, with ion transport facilitated by the network of mesopores. However, at a moderate rate, a plateau in the loading curves (Figures 6.11b) clearly indicated that the TiO_2 underwent a phase transition.[9] Hence, despite the strain accompanying insertion–deinsertion of lithium ions, the mesoporous nanorod films did not degrade with cycling but instead maintained their architectural integrity as seen by top-down SEM (Figure 6.13). Furthermore, we also investigated thicker mesoporous films of nanorods (up to 600 nm) by depositing multiple layers (Figure 6.11c). The capacity scaled approximately with film thickness over a range of charge–discharge rates, indicating that the electrolyte can access the mesoporous network throughout the film thickness (Figure 6.11d).

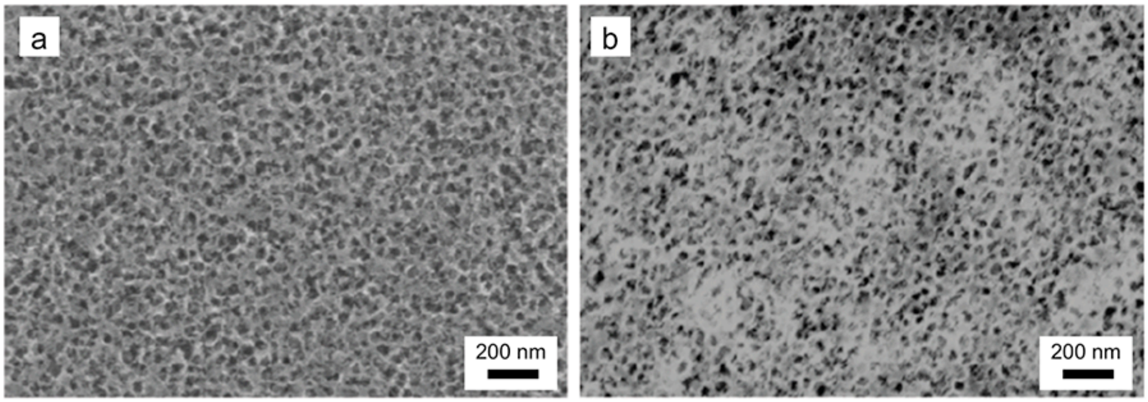

Figure 6.13. Top-down SEM images of TiO_2 nanorod-based mesoporous framework (a) before and (b) after 1000 cycles at 5C.

6.4 Conclusions

Our assembly approach offers unprecedented simultaneous control of structure on multiple length scales within mesoporous architectures driven by the use of a new class of block copolymer architecture-directing agent, PDMA-*b*-PS. The use of organic-phase synthesized nanocrystals as building units lends exceptional control over the size and shape of the crystallites. Meanwhile, the pore size ranges between about 20 and 50 nm, which is larger than that accessible in conventional surfactant templated (sol−gel) methods, wherein molecules such as sodium dodecyl sulfate (SDS) create pores around 2−10 nm.[2,29] At the same time, mesopores in my frameworks are smaller than those achievable by templating inverse opals using assemblies of colloidal polymeric beads, which are difficult to synthesize with good uniformity below about 100 nm, resulting in pore sizes in the same range or larger.[33] Hence, the architectures offer an excellent opportunity to backfill pores with larger molecules to create more complex materials and devices. Because of the tunability of the architectures in this distinctive range of pore and crystallite dimensions, I expect that further systematic variations will afford a comprehensive understanding of the key parameters controlling energy storage performance. The same approach can be used to rationalize the roles of porosity and crystallite size/shape on the performance of dye-sensitized solar cells,[1−3,29,30] photoelectrochemical cells,[8] electrochromic devices,[34] or catalytic systems[35,36] based on mesoporous materials. Finally, since PDMA can adsorb to all varieties of ligand-stripped NCs, my enthalpy-driven assembly approach offers a universal strategy that can be used to understand the performance of mesoporous materials across an even wider range of applications.

6.5 References

1. Orillal, M. C.; Wiesner, U. "Block copolymer based composition and morphology control in nanostructured hybrid materials for energy conversion and storage: solar cells, batteries, and fuel cells" *Chem. Soc. Rev.* **2011**, *40*, 520–535.
2. Sanchez, C.; Boissière, C.; Grosso, D.; Laberty, C.; Nicole, L. "Design, Synthesis, and Properties of Inorganic and Hybrid Thin Films Having Periodically Organized Nanoporosity" *Chem. Mater.* **2008**, *20*, 682–737.
3. Nedelcu, M.; Lee, J.; Crossland, E. J. W.; Warren, S. C.; Orilall, M. C.; Guldin, S.; Hüttner, S.; Ducati, C.; Eder, D.; Wiesner, U.; Steiner, U.; Snaith, H. J. "Block copolymer directed synthesis of mesoporous TiO_2 for dye-sensitized solar cells" *Soft Matter* **2009**, *5*, 134–139.
4. Yang, P.; Zhao, D.; Margolese, D. I.; Chmelka, B. F.; Stucky, G. D. "Generalized syntheses of large-pore mesoporous metal oxides with semicrystalline frameworks" *Nature* **1998**, *396*, 152–155.
5. Brezesinski, T.; Wang, J.; Senter, R.; Brezesinski, K.; Dunn, B.; Tolbert, S. H. "On the Correlation between Mechanical Flexibility, Nanoscale Structure, and Charge Storage in Periodic Mesoporous CeO_2 Thin Films" *ACS Nano* **2010**, *4*, 967–977.
6. Brezesinski, T.; Wang, J.; Tolbert, S. H.; Dunn, B. "Ordered mesoporous α-MoO_3 with iso-oriented nanocrystalline walls for thin-film pseudocapacitors" *Nat. Mater*. **2010**, *9*, 146–151.
7. Ortel, E.; Fischer, A.; Chuenchom, L.; Polte, J.; Emmerling, F.; Smarsly, B. M.; Kraehnert, R. "New Triblock Copolymer Templates, PEO-PB-PEO, for the Synthesis of Titania Films with Controlled Mesopore Size, Wall Thickness, and Bimodal Porosity" *Small* **2012**, *8*, 298–309.
8. Hartmann, P.; Lee, D.-K.; Smarsly, B. M.; Janek, J. "Mesoporous TiO_2: Comparison of Classical Sol−Gel and Nanoparticle Based Photoelectrodes for the Water Splitting Reaction" *ACS Nano* **2010**, *4*, 3147–3154.
9. Ren, Y.; Hardwick, L. J.; Bruce, P. G. "Lithium Intercalation into Mesoporous Anatase with an Ordered 3–D Pore Structure" *Angew. Chem. Int. Ed*. **2010**, *49*, 2570–2574.
10. Dong, A.; Ye, X.; Chen, J.; Kang, Y.; Gordon, T.; Kikkawa, J. M.; Murray, C. B. "A Generalized Ligand-Exchange Strategy Enabling Sequential Surface Functionalization of Colloidal Nanocrystals" *J. Am. Chem. Soc.* **2011**, *133*, 998–1006.
11. Rosen, E. L.; Buonsanti, R.; Llordes, A.; Sawvel, A. M.; Milliron, D. J.; Helms, B. A. "Exceptionally Mild Reactive Stripping of Native Ligands from Nanocrystal Surfaces by Using Meerwein's Salt" *Angew. Chem. Int. Ed.* **2012**, *51*, 684–689.
12. Gilstrap Jr., R. A.; Capozzi, C. J.; Carson, C. G.; Gerhardt, R. A.; Summers, C. J. "Synthesis of a Nonagglomerated Indium Tin Oxide Nanoparticle Dispersion" *Adv. Mater.* **2008**, *20*, 4163–4166.
13. Choi, S.; Nam, K. M.; Park, B. K.; Seo, W. S.; Park, J. T. "Preparation and Optical Properties of Colloidal, Monodisperse, and Highly Crystalline ITO Nanoparticles" *Chem. Mater.* **2008**, *20*, 2609–2611.

14. Cozzoli, P. D.; Kornowski, A.; Weller, H. "Low-Temperature Synthesis of Soluble and Processable Organic-Capped Anatase TiO_2 Nanorods" *J. Am. Chem. Soc*. **2003**, *125*, 14539–14548.
15. Dinh, C.-T.; Nguyen, T.-D.; Kleitz, F.; Do, T.-O. "Shape-Controlled Synthesis of Highly Crystalline Titania Nanocrystals" *ACS Nano* **2009**, *3*, 3737–3743.
16. Liu, Y.; He, S.; Maeda, H. "Wet Chemical Preparation of Well-dispersed Colloidal Cerium Oxide Nanocrystals" *Chem. Lett.* **2007**, *36*, 764–765.
17. Ostrowski, A. D.; Chan, E. M.; Gargas, D. J.; Katz, E. M.; Han, G.; Schuck, P.J.; Milliron, D. J.; Cohen, B. E. "Controlled Synthesis and Single-Particle Imaging of Bright, Sub-10 nm Lanthanide-Doped Upconverting Nanocrystals" *ACS Nano* **2012**, *6*, 2686–2692.
18. Liu, C.; Wu, X.; Klemmer, T.; Shukla, N.; Yang, X.; Weller, D.; Roy, A. G.; Tanase, M.; Laughlin, D. "Polyol Process Synthesis of Monodispersed FePt Nanoparticles" *J. Phys. Chem. B* **2004**, *108*, 6121–6123.
19. Lai, J. T.; Filla, D.; Shea, R. "Functional Polymers from Novel Carboxyl-Terminated Trithiocarbonates as Highly Efficient RAFT Agents" *Macromolecules* **2002**, *35*, 6754–6756.
20. Rauda, I. E.; Buonsanti, R.; Saldarriaga-Lopez, L. C.; Benjauthrit, K.; Schelhas, L. T.; Stefik, M. M.; Augustyn, V.; Ko, J.; Dunn, B.; Wiesner, U.; Milliron, D. J.; Tolbert, S. H. "General Method for the Synthesis of Hierarchical Nanocrystal-Based Mesoporous Materials" *ACS Nano* **2012**, *6*, 6386–6399.
21. Thompson, R. B.; Ginzburg, V. V.; Matsen, M. W.; Balazs, A. C. "Predicting the mesophases of copolymer-nanoparticle composites" *Science* **2001**, *292*, 2469−2472.
22. Warren, S. C.; Disalvo, F. J; Wiesner, U. "Nanoparticle-tuned assembly and disassembly of mesostructured silica hybrids" *Nat. Mater*. **2007**, *6*, 156–161.
23. Huh, J.; Ginzburg, V. V.; Balazs, A. C. "Thermodynamic Behavior of Particle/Diblock Copolymer Mixtures: Simulation and Theory" *Macromolecules* **2000**, *33*, 8085–8096.
24. Thorkelsson, K.; Mastroianni, A. J.; Ercius, P.; Xu, T. "Direct Nanorod Assembly Using Block Copolymer-Based Supramolecules" *Nano Lett*. **2012**, *12*, 498–504.
25. Kao, J.; Bai, P.; Chuang, V. P.; Jiang, Z.; Ercius, P.; Xu, T. "Nanoparticle Assemblies in Thin Films of Supramolecular Nanocomposites" *Nano Lett*. **2012**, *12*, 2610–2618.
26. Tang, Q.-Y.; Ma, Y.-Q. "Self-Assembly of Rod-Shaped Particles in Diblock-Copolymer Templates" *J. Phys. Chem. B* **2009**, *113*, 10117–10120.
27. Brezesinski, T.; Wang, J.; Polleux, J.; Dunn, B.; Tolbert, S. H "Templated Nanocrystal-Based Porous TiO_2 Films for Next-Generation Electrochemical Capacitors" *J. Am. Chem. Soc.* **2009**, *131*, 1802–1809.
28. Szeifert, J. M.; Feckl, J. M.; Fattakhova-Rohlfing, D.; Liu, Y.; Kalousek, V.; Rathousky, J.; Bein, T. "Ultrasmall Titania Nanocrystals and Their Direct Assembly into Mesoporous Structures Showing Fast Lithium Insertion" *J. Am. Chem. Soc*. **2010**, *132*, 12605–12611.
29. Szeifert, J. M.; Fattakhova-Rohlfing, D.; Rathouský, J.; Bein, T. "Multilayered High Surface Area "Brick and Mortar" Mesoporous Titania Films as Efficient Anodes in Dye-Sensitized Solar Cells" *Chem. Mater*. **2012**, *24*, 659–663.

30. De Marco, L.; Manca, M.; Buonsanti, R.; Giannuzzi, R.; Malara, F.; Pareo, P.; Martiradonna, L.; Giancaspro, N. M.; Cozzoli, P. D.; Gigli, G. “High-quality photoelectrodes based on shape-tailored TiO_2 nanocrystals for dye-sensitized solar cells” *J. Mater. Chem*. **2011**, *21*, 13371–13379.
31. Sun, C. H.; Yang, X. H.; Chen, J. S.; Li, Z.; Lou, X. W.; Li, C.; Smith, S. C.; Luc, G. Q.; Yang, H. G. “Higher charge/discharge rates of lithium-ions across engineered TiO_2 surfaces leads to enhanced battery performance” *Chem. Commun*. **2010**, *46*, 6129–6131.
32. Hengerer, R.; Kavan, L.; Ktril, P.; Grätzel, M. “Orientation Dependence of Charge–Transfer Processes on TiO_2 (Anatase) Single Crystals” *J. Electrochem. Soc*. **2000**, *147*, 1467–1472.
33. Stein, A.; Li, F.; Denny, N. R. “Morphological Control in Colloidal Crystal Templating of Inverse Opals, Hierarchical Structures, and Shaped Particles” *Chem. Mater*. **2008**, *20*, 649–666.
34. Garcia, G.; Buonsanti, R.; Runnerstrom, E. L.; Mendelsberg, R. J.; Llordes, A.; Anders, A.; Richardson, T. J.; Milliron, D. J. “Dynamically Modulating the Surface Plasmon Resonance of Doped Semiconductor Nanocrystals” *Nano Lett*. **2011**, *11*, 4415–4420.
35. Torvatelli, A., editor. *Catalysis by Ceria and Related Materials*. Imperial College Press: London, 2002.
36. Stamenkovic, V. R.; Mun, B. S.; Arenz, M.; Mayrhofer, K. J. J.; Lucas, C. A.; Wang, G.; Ross, P. N.; Markovic, N. M. “Trends in electrocatalysis on extended and nanoscale Pt-bimetallic alloy surfaces” *Nat. Mater*. **2007**, *6*, 241–247.

Characterization and quantitative analysis of block copolymer–nanocrystal assemblies

Chapter 7

Ordering in polymer micelle-directed assemblies of colloidal nanocrystals

Adapted from:

Gary K. Ong, Teresa E. Williams, Ajay Singh, Eric Schaible, Brett A. Helms, Delia J. Milliron. "Ordering in Polymer Micelle-Directed Assemblies of Colloidal Nanocrystals" *Nano Letters* **2015**, *15*, 8240–8244.

7.1 Introduction

Design rules for coassembly of two or even three nanocrystal (NC) components into ordered architectures have been gleaned by evaluating assembly outcomes while systematically varying the nanocrystal sizes and relative volume fractions. When block copolymers, in the dilute limit, are used to direct the assembly of preformed nanocrystals such assemblies follow principles established for thermodynamically driven block copolymer (BCP) self-assembly, with the low volume fraction of nanocrystals acting as a perturbation. However, these design rules fail at high nanocrystal volume fractions, where in fact the realization of thermodynamically directed ordering may be rendered kinetically infeasible.[1] As such, the development of clear principles to predict the emergence of ordering in BCP-NC co-assemblies at high loading fraction is needed. In this chapter I investigate how NC size and volume fraction impact the potential to create ordered mesostructured composite films by micelle-directed assembly of nanocrystals. Though the ability to template nanocrystals in this way opens up new opportunities for fabricating functional materials from the vast library of already-developed colloidal nanocrystals, the loss of configurational entropy upon mixing nanocrystals with polymers makes it challenging to assemble nanocrystals whose diameter, d, may be comparable to the mean end-to-end distance, R_0, of the polymer segments.[2,3] The model system to test my hypothesis consists of poly(*N,N*-dimethylacrylamide)-*b*-polystyrene (PDMA-*b*-PS) micelles and monodisperse, colloidally synthesized iron oxide nanocrystals,[4,5] stripped of their native surface ligands and ranging in size from 3 to 16 nm in diameter.[6] Thin films (~100 nm) that result after spin coating from a single dispersion containing these two components consist of nanocrystals incorporated between close packed micelles. X-ray scattering techniques are employed to quantify the resulting films.

7.2 Experimental Procedures

MATERIALS. Iron chloride hexahydrate ($FeCl_3 \bullet 6H_2O$, 98%), oleic acid (90%), oleyl alcohol (85%), dioctyl ether (99%), diphenyl ether (> 99%), toluene (≥ 99.5%), *n*-hexanes (≥ 95%), *N,N*-dimethyl formamide (DMF, ≥ 99%), reagent alcohol (ACS grade), nitrosyl tetrafluoroborate ($NOBF_4$, 95%), ethanol (EtOH, 200 proof, anhydrous, ≥ 99.5%), chloroform ($CHCl_3$, 99.5%), acetone (99.9%), and isopropanol (iPrOH, 99.7%) were purchased from Aldrich. Sodium oleate (95%) was purchased from TCI. Silicon wafers (University Wafers, 0-100 ohm cm, P type) were cleaved to 1x1 cm^2 substrates and cleaned using stepwise sonication for 10 minutes each in $CHCl_3$, acetone, and iPrOH, then treated with UV–ozone for 10 minutes.

NANOCRYSTALS. Iron oxide synthesis was carried out using the decomposition of iron oleate, following literature procedures.[4,5] Nanocrystal sizes determined by SAXS (Figure 7.1; see also TEM images in Figure 7.2) were rounded to the closest nanometer for clarity, with a tabulation of the nanocrystal diameters and dispersities provided in Table 7.1.

Table 7.1. Compilation of the nanocrystal sizes obtained from fitting the nanocrystal form factor assuming a Gaussian size distribution. Fits to sample data made by varying three parameters of nanocrystal size, dispersity and sphere aspect ratio. The leftmost column is the abbreviated nanocrystal sized referenced in the main text while the second column contains the corresponding true nanocrystal sizes.

NC size label (*d*; nm)	**NC size (SAXS; nm)**	**NC size dispersity standard deviation (nm)**	**NC shape dispersity**
3	3.41	0.42	1.7
4	4.49	0.56	1.54
5	4.60	0.25	1
7	7.14	0.65	1
8	7.76	0.46	1
9	9.15	0.68	1
12	11.7	0.66	1
14	14.3	0.82	1
16	15.9	0.72	1

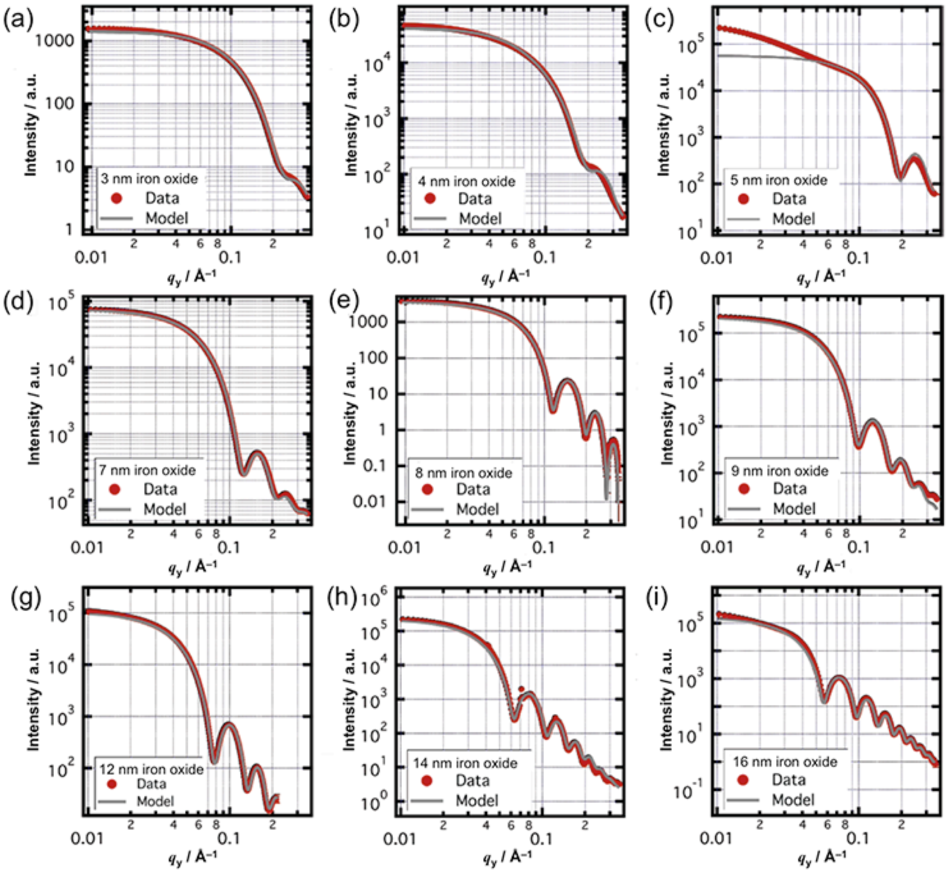

Figure 7.1. Form factor plots showing data (red circles) and model (black line) to determine nanocrystal size, dispersity and circularity for: (a) 3 nm; (b) 4 nm; (c) 5 nm; (d) 7 nm; (e) 8 nm; (f) 9 nm; (g) 12 nm; (h) 14 nm; (i) 16 nm iron oxide.

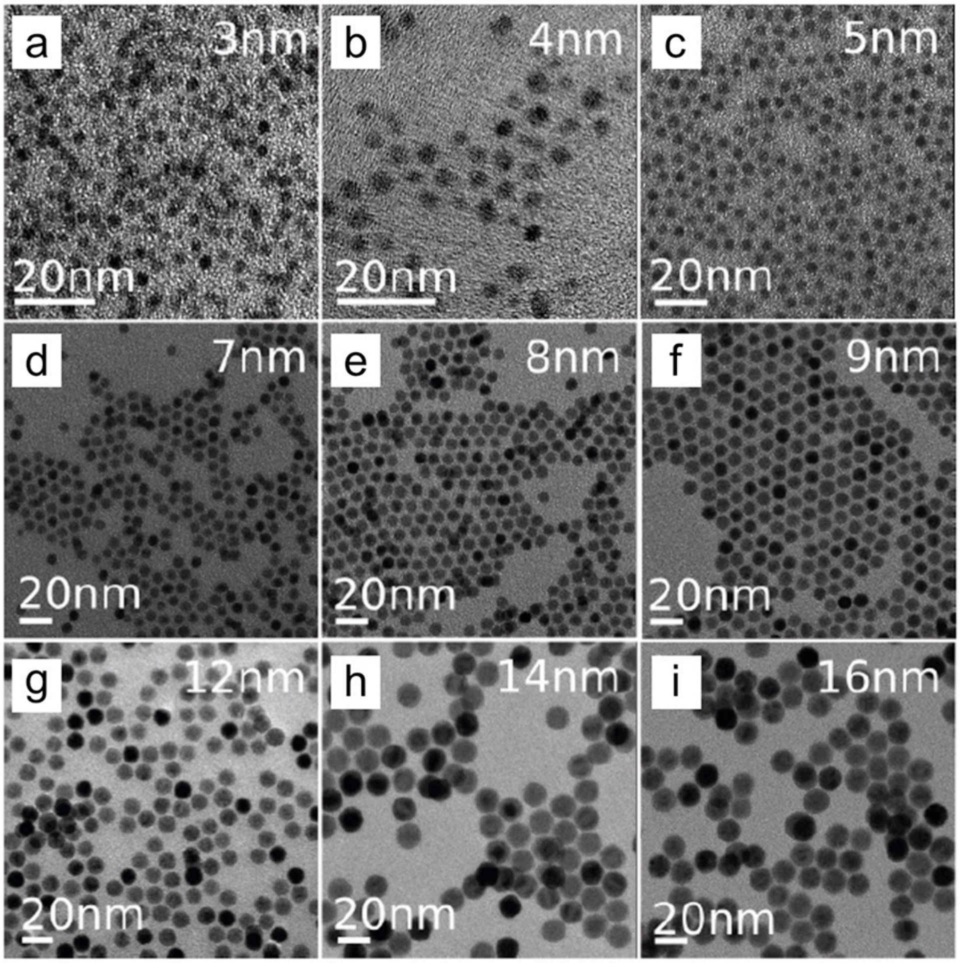

Figure 7.2. Bright-field TEM images of iron oxide nanocrystal dispersions: (a) 3 nm; (b) 4 nm; (c) 5 nm; (d) 7 nm; (e) 8 nm; (f) 9 nm; (g) 12 nm; (h) 14 nm; (i) 16 nm.

PREPARATION OF LIGAND-STRIPPED NANOCRYSTAL DISPERSIONS. In a typical ligand stripping procedure,[7] a dispersion of NCs in hexanes (~20 mg mL^{-1}) was added into an equivalent volume of *N,N*-dimethylformamide (DMF) to form a two phase mixture. The stripping agent, $NOBF_4$, equivalent to half the approximated weight of nanocrystal in solution, was added into the mixture, and the mixture was agitated to promote ligand stripping. Phase transfer of the ligand-stripped NCs from hexane to DMF indicated completion of ligand stripping and occurred within ten min. The phases were separated and the NCs are washed three times using a DMF/toluene combination for suspension and precipitation, and filtered through a 0.5 μm PTFE membrane.

PREPARATION OF BCP MICELLE–NC ASSEMBLIES. I prepared $PDMA_{10k}$-*b*-PS_{60k} BCP as previously described.[8] In a typical preparation of block copolymer micelles, 10 mg of BCP was dissolved in 100 μL of DMF and added dropwise into 800 μL of EtOH under constant stirring at 350 rpm and maintained for 18 h. 180 μL of micelles was transferred to a separate vial and combined with 20 μL of ligand-stripped NCs in DMF.

For a typical assembly consisting of 1:1.5 BCP to NC weight ratio, this corresponded to 2 mg of polymer and 3 mg of NCs in 200 μL of 2:8 *v/v* DMF:EtOH. The dispersion stirred for 16 h. Samples for TEM, for micelles and BCP–NC assemblies, were prepared by spin-coating the dispersion onto a TEM grid by first placing the grid at the center of a silicon substrate followed by spin-coating 15 μL of dispersion at 2000 rpm.

Table 7.2. Compilation of PDMA$_{10k}$-PS$_{60k}$ and iron oxide weights in solution and their conversion to reported nanocrystal weight and volume fractions. Conversions from nanocrystal and polymer weight fractions to volume fractions were made assuming a bulk density of PDMA-*b*-PS of 1.1 g cm^{-3} and an average bulk density of 5.07 g cm^{-3} for iron oxide.

PDMA-*b*-PS (mg)	**Iron Oxide (mg)**	**NC weight fraction**	**NC volume fraction**
1	0.5	0.33	0.10
1	1.5	0.6	0.25
1	3	0.75	0.39
1	4	0.80	0.46

FILM PREPARATION. Assemblies of BCP–NC (15 μL) were spin-coated with a 1 s ramp to 1250 rpm, and held for 1 min; 2–3 coatings were used to achieve desired film thicknesses.

7.3 Results and Discussion

To investigate the influence of nanocrystal size on mesoscale ordering, building units (PDMA$_{10k}$-PS$_{60k}$ micelles and iron oxide NCs) of highly uniform size and shape were synthesized and characterized by transmission electron microscopy (TEM) and small-angle X-ray scattering (SAXS) (Figure 7.3). The SAXS data showed that the form factors, which describe the scattering from a single particle and strongly depend on its size and shape, exhibited periodic undulations characteristic of monodisperse, uniform particles with different distinctive sizes.

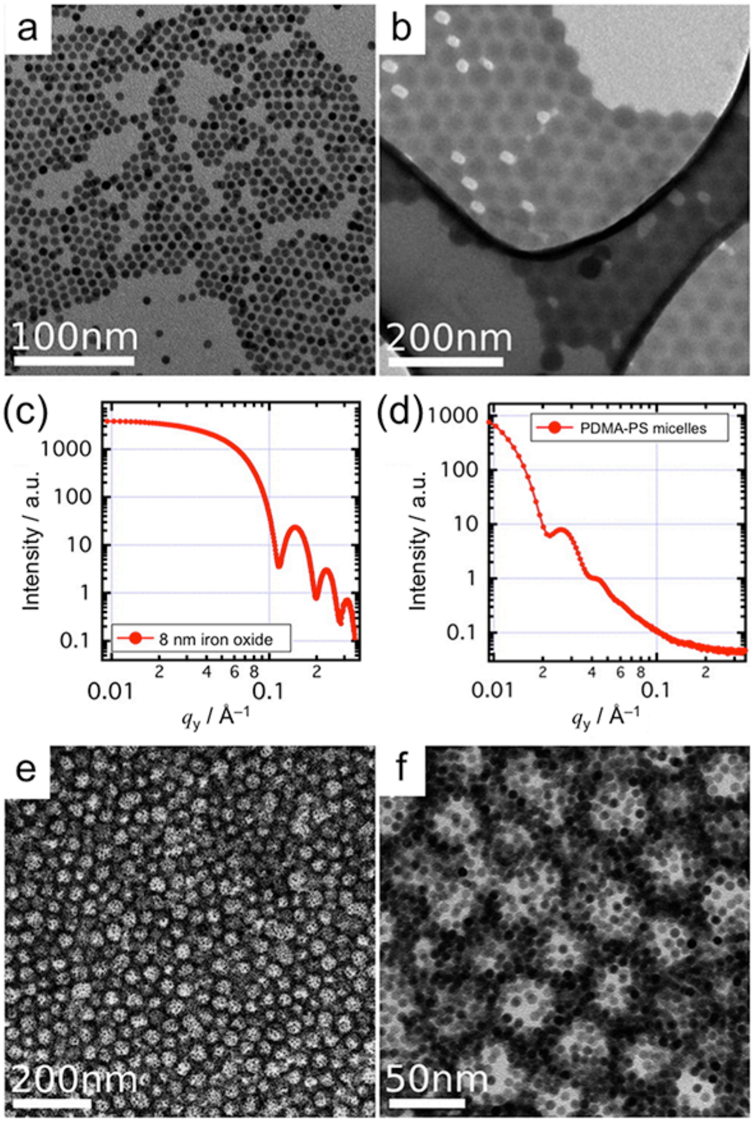

Figure 7.3. Characterization of individual components (micelles, nanocrystals) and their assembly. Bright-field TEM images of: (a) 8 nm diameter iron oxide NCs and (b) PDMA$_{10k}$-PS$_{60k}$ BCP micelles. Solution phase SAXS (c–d) of the same building blocks; (e–f) Bright-field TEM of the resulting BCP–NC assembly at two magnifications.

Because the PDMA corona adsorbs to the nanocrystal's surface during assembly, we hypothesized that the relative sizes of the nanocrystals and PDMA corona would significantly influence assembly outcomes. The PDMA coronal width was assessed by fitting the block copolymer micelle SAXS form factor with a core–shell model;[9] the fit results indicated a micelle with a 23.6 nm diameter core, derived from PS, and 8.7 nm shell, derived from PDMA (Figure 7.4a), for a total diameter of d = 41 nm. A fit with a regular spheroid model[10] was also made as a comparison giving a micelle diameter of d = 40.4 nm, in good agreement (Figure 7.4b).

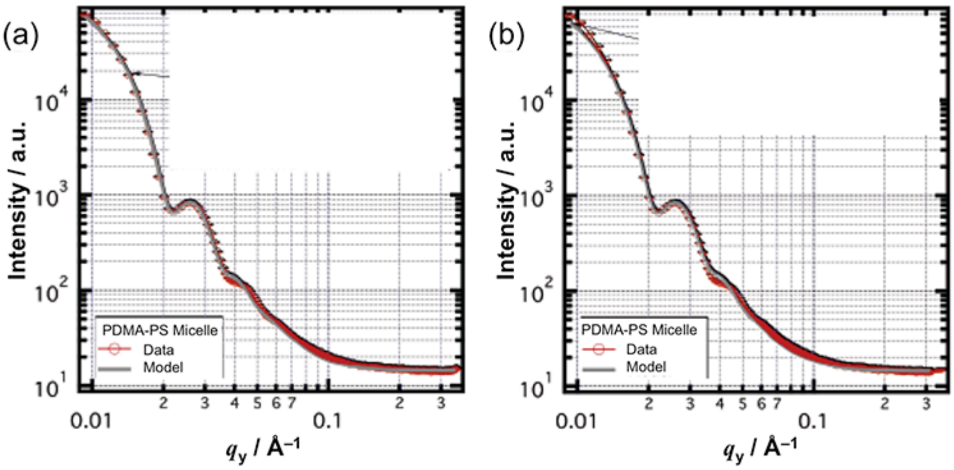

Figure 7.4. $PDMA_{10k}$-PS_{60k} micelle form factor fitted to: (a) core-shell model; (b) regular spheroid.

The micelle coronal width, l_0, was also estimated by using SAXS to determine R_0, the root mean square end-to-end distance, for PDMA homopolymer;[10] data were collected for three polymer concentrations, 1, 2, and 3 wt% (Table 7.3 and Figure 7.5). These curves are characterized by two main features: the Guinier region and the Porod region, with standard linear plots available to fit the data and obtain a radius of gyration, R_g.[10] R_0 was approximated to be 6.9 nm assuming the freely jointed chain model with $R_0 = \sqrt{6}R_g$. As the actual solution concentration used for micelle assembly was ~1 wt%, this value was used as the reference point. Thus, the coronal width, l_0, was ~7–9 nm, with the nanocrystal diameters ranging from about 0.5 to 2 times this dimension.

Table 7.3. Tabulation of R_g, P, and R_0 for the fitting results of free $PDMA_{10k}$ chains. Sample data are presented in Figure 7.5.

	1 wt% PDMA	**3 wt% PDMA**	**5 wt% PDMA**
R_g (Å)	27.9	25.8	20.7
P	1.99	2.15	2.26
R_0 (Å)	68.5	63.1	50.7

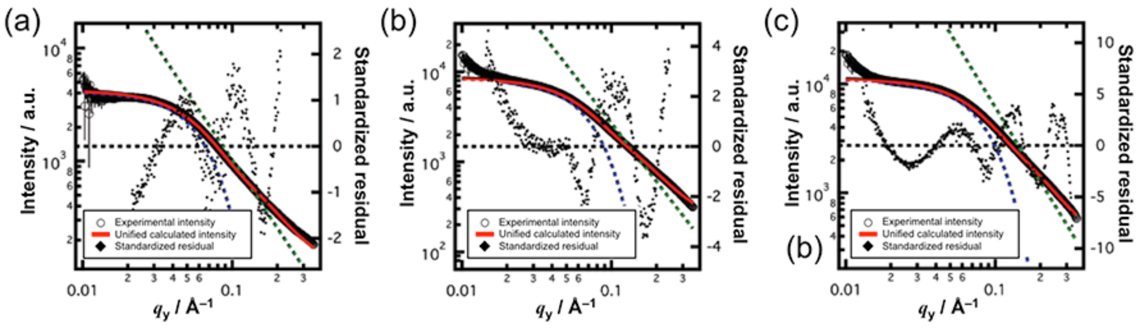

Figure 7.5. Guinier–Porod fitting of free PDMA_{10k} chains in 2:8 *v/v* DMF:EtOH at polymer concentrations of: (a) 1 wt%; (b) 3 wt%; and (c) 5 wt%.

The degree of ordering in BCP–NC composite films was investigated using grazing-incidence SAXS (GISAXS) while interpreting the data in the context of local structure by electron microscopy. Samples were prepared at a BCP–NC loading of 1:1.5 *w*/*w*, an empirically determined lower limit of nanocrystal content that yielded a freestanding structure when the polymer was removed by post-assembly thermal processing.[6] The NCs ranged in size from $3 < d < 16$ nm. We investigated the influence of nanocrystal size on assembly by varying the nanocrystal diameter, d, hypothesizing that the assembled structure would exhibit marked degradation of order for $d > l_0$, the micelle coronal width. This weight ratio corresponded to around 25 vol% of iron oxide, assuming bulk densities (Table 7.2). An average density was used because as-synthesized iron oxide nanocrystal are known to be a mixed phase material of Fe_2O_3 and Fe_3O_4. Bright-field TEM images of the composite films (Figure 7.3e–f) typically revealed structures with hexatic ordering on the mesoscale (i.e., local close-packing of nanocrystal-covered micelles without long-range translational order). As these films measured ~100 nm, or two micelles, in thickness and did not exhibit out of plane ordering, one-dimensional line-cuts across the horizon were analyzed. A typical line-cut exhibited two sets of peaks: the first three peaks at low q, $0.01\ Å^{-1} < q < 0.05\ Å^{-1}$, were characteristic of local structure among micelles, whereas additional peaks at $q > 0.05\ Å^{-1}$ were characteristic of order on the nanocrystal length scale, i.e., close-packing of nanocrystals in the interstitial spaces between micelles (Figure 7.6a). Ordering at the length scale of the micelles was qualitatively determined by observing changes of peak width and peak height of the primary peak at $q = 0.015\ Å^{-1}$ as nanocrystal diameter was varied (Figure 7.6a). As a quantitative measure of structural order, the peak height ratio of the primary (lowest q) and secondary SAXS peaks were calculated (Figure 7.6b), after removal of the form factor background, using a log-cubic fit (see '7.5 Appendix' and Figure 7.12 for an example calculation). Ordering was apparent for the smallest nanocrystals and improved slightly with increasing nanocrystal size up to $d \simeq l_0$ after which marked degradation of order occurred (Figure 7.6b).

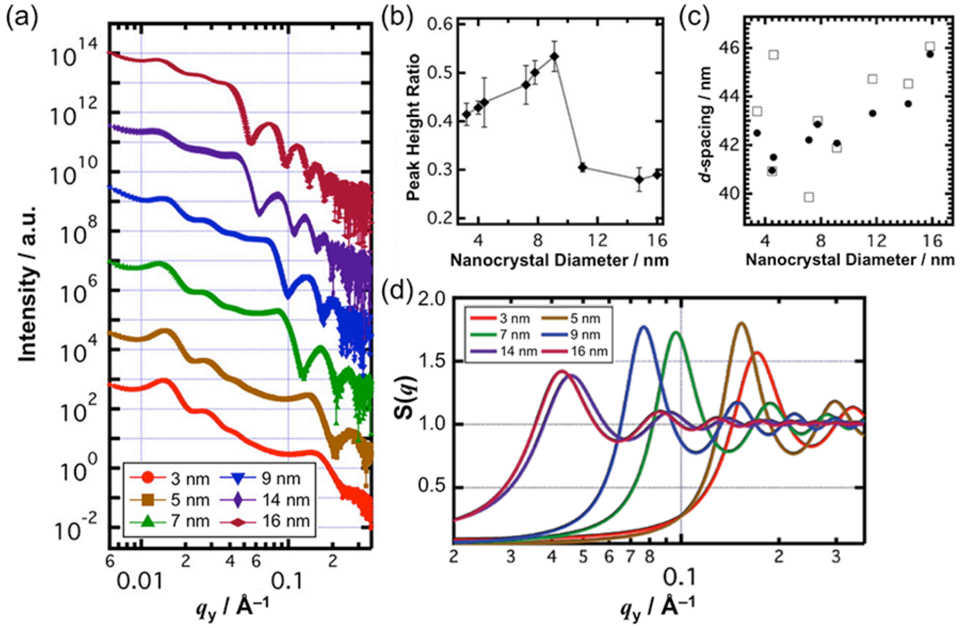

Figure 7.6. Scattering analysis of BCP micelle-NC films for different NC sizes: (a) one-dimensional GISAXS line-cuts with the data vertically offset for clarity; (b) ratio of low *q* GISAXS peak heights as a function of nanocrystal size; (c) change in *d*-spacing between micelles, derived from the *q* value of the primary scattering peak, with filled and unfilled points from two independent sets of samples; (d) fits with the Percus–Yevick structure factor in the higher *q* range.

From these experiments we determined that poorer mesoscale ordering for larger ($d > 8$ nm) nanocrystals was consistent with expectations based on theoretical models that considered the entropic cost of incorporating nanocrystals within the coronal region. Previous studies that contemplated BCP–NC assembly in the dilute limit highlighted the constraint on polymer chain configuration imposed by nanoparticles with increasing diameters, approaching and exceeding R_0.[2,11,12] The associated increase in free energy tended to exclude nanoparticles or confine them at the block center, with polymer chains demixing from the nanoparticle domain. Through the inclusion of favorable enthalpy of PDMA polymer adsorption, such segregation effects were avoided here; nonetheless, the entropic penalty remained and explained the poorer ordering observed for larger nanocrystals. For somewhat reduced ordering noted below an optimum nanocrystal size of ∼8 nm (similar to l_0), these results were associated to the extensive interaction between PDMA and the large surface area of these small nanocrystals.

Analysis of the scattering vectors, that is, *q* values for the peaks, suggested that these same considerations of size-dependent enthalpic and entropic terms caused nanocrystals of different diameters to locate at variable distances from the micelle cores. Specifically, we noted that the intermicelle spacing (*d*-spacing) decreased with diminishing nanocrystal size (Figure 7.6c), suggesting a more compact assembly in which small nanocrystals were well embedded in the corona. Conversely, larger nanocrystals remained at the micelle's periphery, thus moderating the entropic cost of assembly. Segregation of smaller nanocrystals toward a BCP interface was similarly observed in low-loading assemblies of nanoparticles with BCPs driven by equilibrium microphase separation.[11,13]

Besides influencing structural ordering at the micellar length scale, nanocrystal size impacted the structural ordering at the nanocrystal scale. Most of the composites exhibited a second length scale of ordering attributed to ordering within the nanocrystal domains. This phenomenon was qualitatively observable in GISAXS as the appearance of interference peaks at the shoulder of the nanocrystal form factors, with higher order peaks convoluted with form factor oscillations at higher q. To extract the structure factor representative of ordering at the nanocrystal length scale, the scattering data were fit using a combination of the nanocrystal form factor and a simple Percus–Yevick structure factor, S(q) (see '7.5 Appendix' and Figure 7.13 for an example calculation).[14–16] The structure factor was pronounced for nanocrystals with $d < l_0$, indicating regular nanocrystal packing (Figure 7.6d). The intensity of the structure factor was significantly diminished for nanocrystals $d > l_0$.

For larger ($d > l_0$) nanocrystals, we hypothesized that ordering at the nanocrystal length scale could be improved at sufficiently high loading, as it was observed in theoretical simulations that nanocrystal ordering became more pronounced at higher nanocrystal volume fractions.[15,16] For a NC loading series of assemblies prepared from 7 nm iron oxide, results from GISAXS offered proof of the same trend (Figure 7.7c).

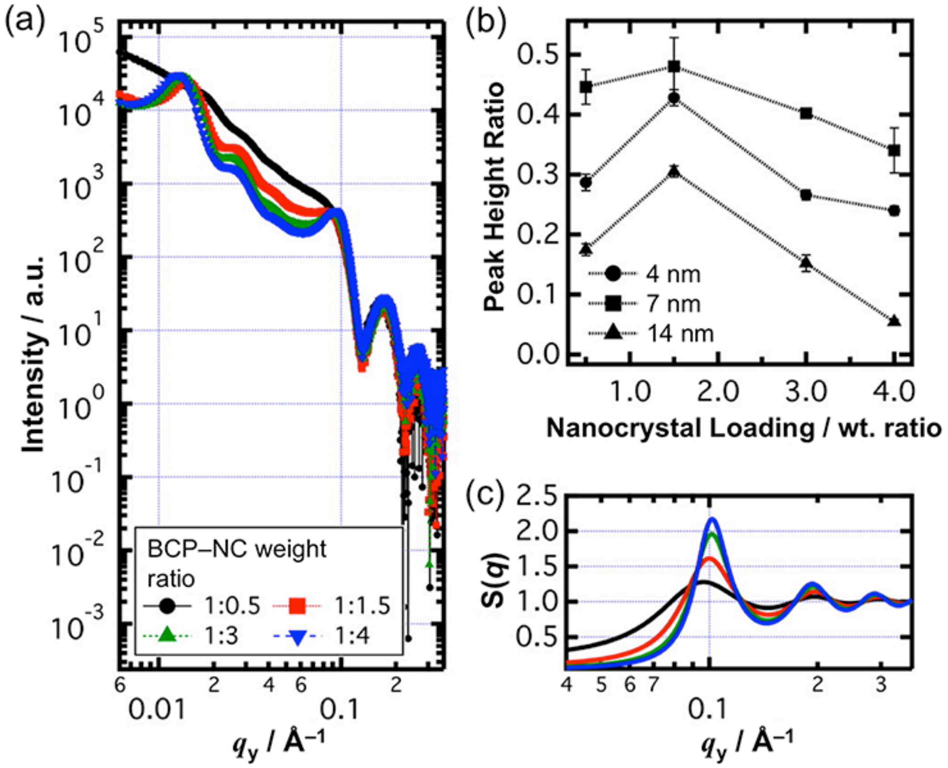

Figure 7.7. (a) One-dimensional GISAXS line-cuts for BCP–NC assemblies at different loadings of 7 nm iron oxide nanocrystals, expressed in weight ratio; (b) peak height ratio

of low q scattering peaks as a function of nanocrystal loading for three NC diameters; (c) structure factors, extracted by fitting, in the range of q corresponding to the NC length scale at different loading of 7 nm NCs. The legend applies to (a) and (c).

As the loading of 7 nm diameter nanocrystals increased, the structure expanded to accommodate well-packed domains of nanocrystals between the micelles. This was shown by the systematic shift of the primary micellar scattering peak at q = 0.015 Å^{-1} toward lower q (Figures 7.7a and 7.8b) and was most prominent for nanocrystal sizes smaller than the estimated coronal width (d = 4 nm). These results demonstrated a general increase in intermicelle spacing with nanocrystal loading.

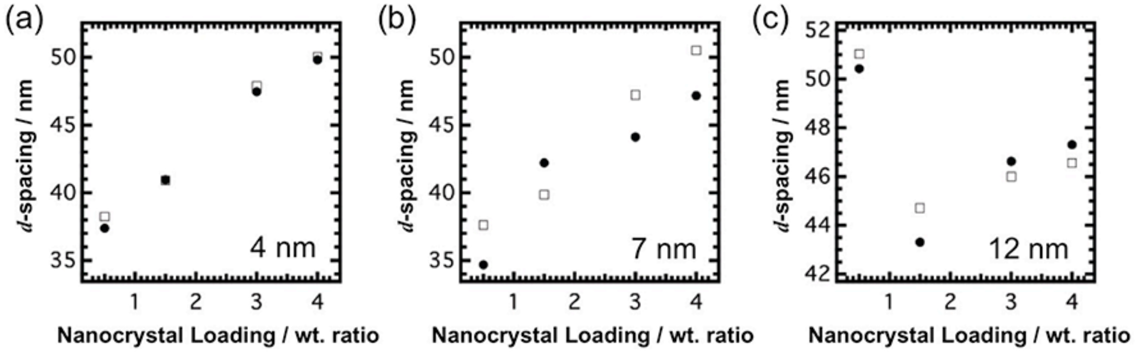

Figure 7.8. Compilation of the change in d-spacing between micelles derived from the q value of the primary scattering peak, converted using $d = 2\pi/q$, and plotted against nanocrystal loading for nanocrystal sizes: (a) 4 nm; (b) 7 nm; (c) 12 nm. The filled and unfilled data points are from two independent sets of samples.

However, nanocrystals larger than l_0 failed to incorporate homogeneously at higher loading, as the shown in Figure 7.8c, which appeared to asymptote. Though we observed the enhancement of nanocrystal order in the structure factor (Figure 7.9c,d), intermicelle spacing stopped increasing with further nanocrystal addition (Figure 7.8c), suggesting saturation and phase separation of additional nanocrystals out of the intermicellar domain.

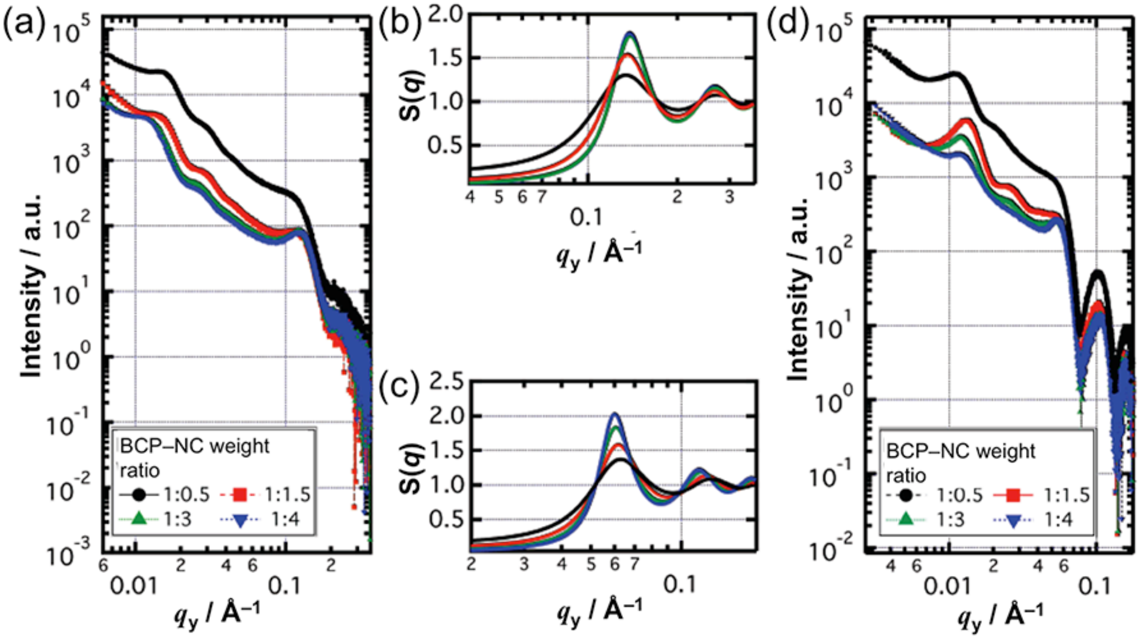

Figure 7.9. (a,b) Grazing-incidence SAXS 1-D line-cuts for the loading series made with 4 nm iron oxide nanocrystals with the corresponding structure factor for nanocrystal ordering. (c,d) Structure factor analysis for nanocrystal ordering and GISAXS 1-D line-cuts for the loading series made with 12 nm iron oxide nanocrystals.

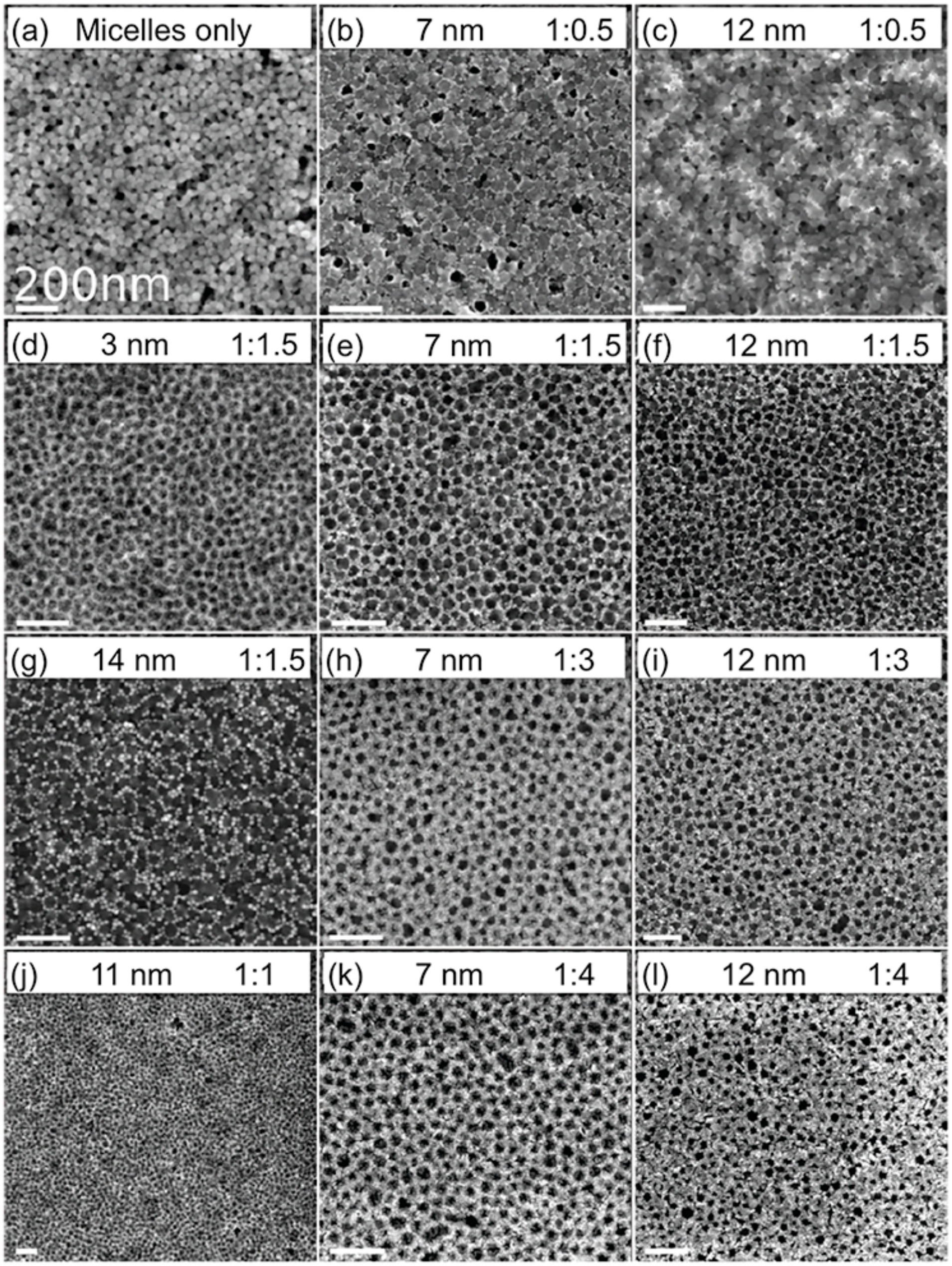

Figure 7.10. Scanning electron microscopy images of BCP micelle–NC assemblies for nanocrystal sizes and loadings: (a,d,g) SEM image of assemblies prepared from no NCs, 3 nm, and 14 nm NCs, respectively; (d) lower magnification SEM image of area highlighted in Figure 7.14a; (b,e,h,k) SEM images of assemblies prepared from 7 nm NCs used in the loading series studies; (c,f,i,l) SEM images of assemblies prepared from 12 nm NCs used in the loading series studies. Scale bar = 200 nm.

Examining the trends in ordering at the micellar length scale, there emerged a nanocrystal loading at which micellar ordering was optimal, independent of nanocrystal size. Peak height ratios of the first and second order peaks at low *q* were once again used as a metric of ordering (Figure 7.7b). The ordering was greatest at a 1:1.5 weight ratio of polymer micelles to nanocrystals, corresponding to 25 vol% nanocrystals. At higher loading (up to 1:4 or 46 vol%), ordering diminished for all nanocrystal sizes, though most severely for large nanocrystals, consistent with the phase segregation observed under these conditions (Figure 7.10l).

Collectively, these trends in micellar and nanocrystal ordering could be understood by considering the nanocrystal-binding PDMA corona of the polymer micelles exhibited a constant width (l_0) that could be compared to nanocrystal size to differentiate assembly regimes (Figure 7.11a). For all nanocrystal sizes less than or equal to this coronal width, the most ordered composite architectures were realized at a size-independent optimal nanocrystal loading achieved when the micelle corona was completely populated by nanocrystals. Beyond this loading limit, additional nanocrystals could be incorporated but the regularity on the micellar length scale declined. When nanocrystals larger than the coronal width were assembled, they were positioned further from the PDMA–PS interface (Figure 7.11). One or two layers of large nanocrystals could thus be stabilized between adjacent micelles, though micellar ordering was limited when assembling these large nanocrystals and ordering at the nanocrystal length scale was absent. See Figure 7.10 for larger area images.

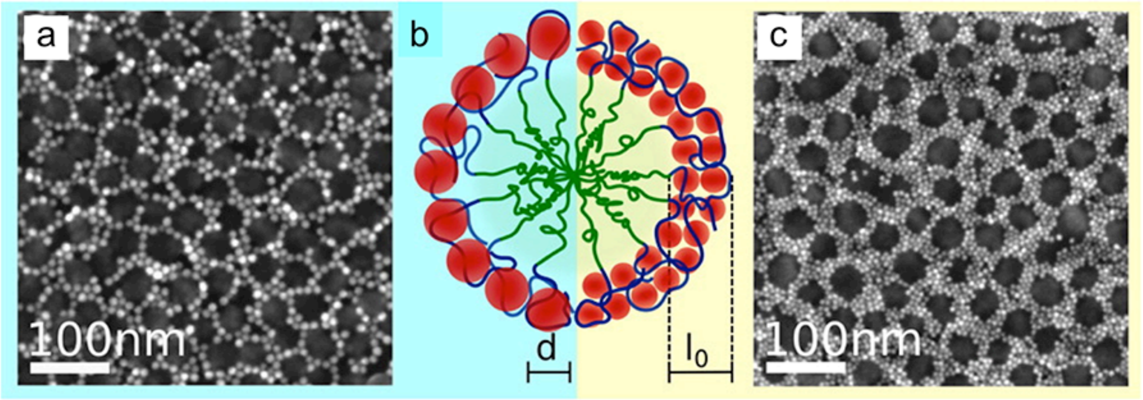

Figure 7.11. Graphic depicting assembly for a persistent PDMA corona (l_0) with different sizes of NCs: SEM of (a) a single nanocrystal network structure made with large 12 nm nanocrystals and (c) of an assembly with two length scales of order made with small 7 nm nanocrystals; (b) Schematic of the two extreme limits of assembly: green PS chain core, blue PDMA coronal chains, and red nanocrystals.

In fact, the structure on the nanocrystal length scale, and its dependence on nanocrystal size, was consistent with thermodynamic predictions. Especially when a favorable enthalpy of interaction existed between nanoparticles and one polymer component, it was expected that smaller particles would be accommodated within that polymer block; meanwhile, larger nanoparticles were excluded from the polymer to reduce entropic penalties but could remain in the space between self-assembled polymer domains. Meanwhile, ordering on the micelle length scale was kinetically determined. The micelles packed most regularly when (smaller) nanocrystals were sequestered within the corona, whereas the presence of large nanocrystals between the micelles could disrupt ordering.

7.4. Conclusions

Within this framework of assembly for PDMA-*b*-PS BCP micelles and iron oxide NCs and using X-ray scattering techniques, I identified two structural extremes of interest: dual length scale structures made with high loading of small nanocrystals, and single nanocrystal network structures made with intermediate loading of large nanocrystals, using the micelle coronal width as a reference point for nanocrystal size (Figure 7.11). As mentioned previously, structures with high volume fractions of nanocrystals could often exhibit deep kinetically trapped states that prevented directed assembly of nanocrystals via equilibrium BCP microphase separation. It was likely that micelle templating of nanocrystals also resulted in structures that were kinetically trapped. However, this was leveraged advantageously in the micellar method, which enabled access to the fringe limits of assembly to construct unusual structures such as single nanocrystal networks; in the case of equilibrium BCP microphase separation-driven assembles utilizing linear BCPs, large nanocrystals were commonly driven out of the system toward exposed surfaces, and the use of brush-type BCPs was required for assembly.[17] This kinetic pathway, therefore, enabled realization of a wide range of composite architectures with well-defined local ordering.

7.5 Appendix

Figure 7.12 shows an example of the sample data collected, and fits made, for the determination of peak height ratio of the primary (lowest *q*) and secondary SAXS peaks for the NC size series. The data presented is for assemblies prepared from 7 nm iron oxide NCs. First, spectra were acquired for both the BCP–NC sample and the blank Si substrate (Figure 7.12a,b) with the two halves of the area detector 1–D line-cut on each side of the beam stop normalized by collection time and merged to remove gaps in the data. The blank Si substrate was subtracted from the sample spectrum (Figure 7.12c) and the *y*-axis was converted to log scale (Figure 7.12d). Fitting was done using a log-cubic background and Gaussian peaks in IgorPro multipeak-fitting module, with peak height ratios taken as the height of the first peak divided by the height of the zeroth peak. Results for all six BCP–NC samples are shown in Figure 7.6b.

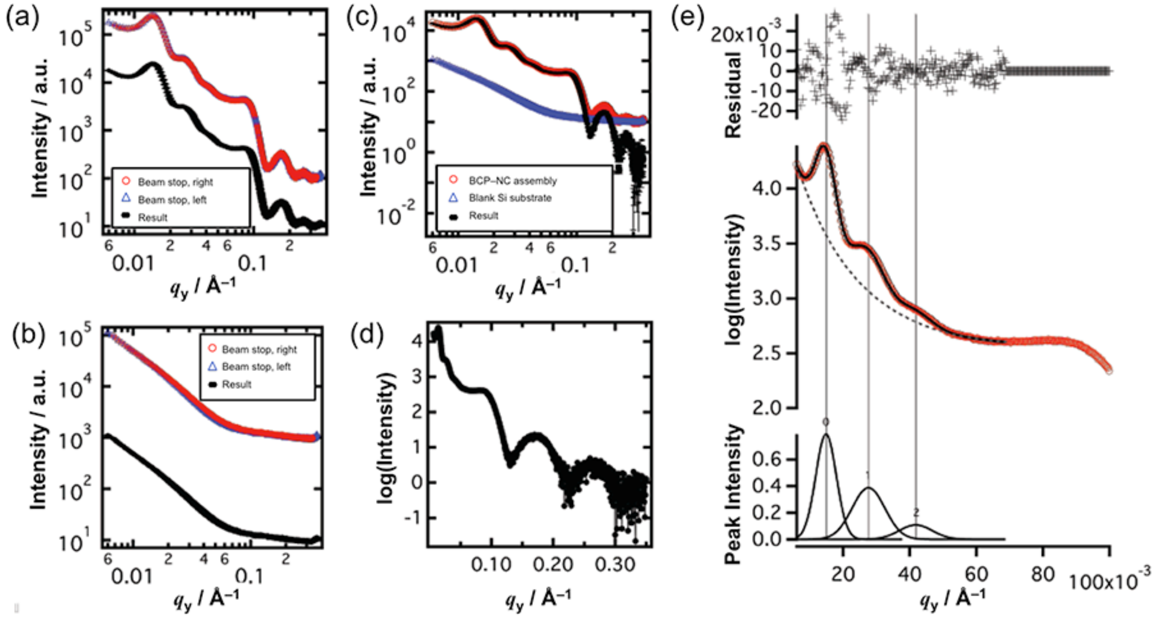

Figure 7.12. Data treatment procedure to obtain peak heights of the low *q* peaks for peak height ratio analysis for 7 nm iron oxide: (a) spectrum of BCP–NC assembly; (b) spectrum of blank Si substrate; (c) spectrum of blank Si substrate subtracted from BCP-NC spectrum; (d) spectrum of background-subtracted BCP–NC sample, with intensity converted to log scale; (e) Results from log-cubic showing BCP–NC sample data (red trace) and resultant fit (black trace).

Figure 7.13 shows an example of the sample data collected, and fitting procedure, to determine the fitting of the higher *q* region of the data with a combination of a spheroid and Percus-Yevick structure factor for the NC loading series. The data presented is for assemblies prepared from 7 nm iron oxide NCs at a 1:1.5 BCP:NC *w*/*w* ratio.

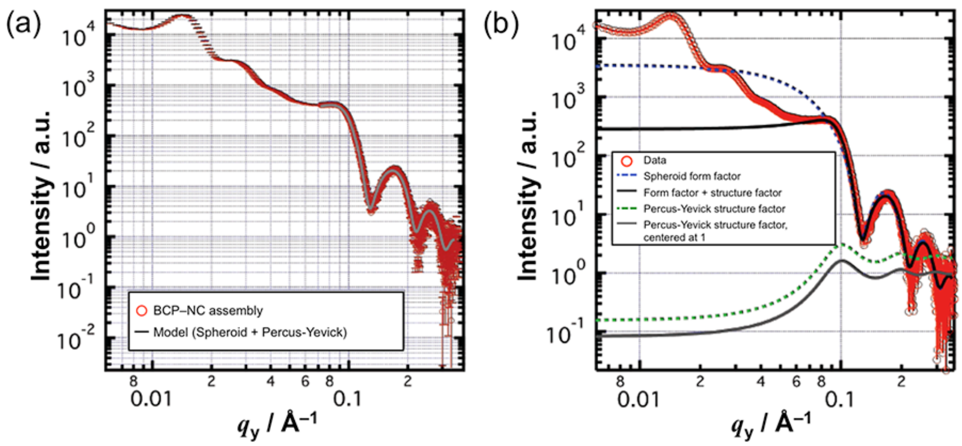

Figure 7.13. (a) Results from GISAXS experiment showing raw data and fitting of the higher *q* region of with a combination of a spheroid and Percus-Yevick structure factor. (b) The separate form factor and structure factor contributions to the model are shown in blue and green, respectively, while the data and corresponding fit are shown in red and black, respectively. The structure factors presented in the main text were set to be centered around S(*q*)=1 under the assumption that the structure factor should converge to S(*q*)=1 for high *q* values.

7.6 References

1. Kao, J.; Xu, T. “Nanoparticle Assemblies in Supramolecular Nanocomposite Thin Films: Concentration Dependence” *J. Am. Chem. Soc.* **2015**, *137*, 6356−6365.
2. Bockstaller, M. R.; Mickiewicz, R. A.; Thomas, E. L. “Block Copolymer Nanocomposites: Perspectives for Tailored Functional Materials” *Adv. Mater.* **2005**, *17*, 1331−1349.
3. Thompson, R. B.; Ginzburg, V. V.; Matsen, M. W.; Balazs, A. C. “Predicting the mesophases of copolymer-nanoparticle composites” *Science* **2001**, *292*, 2469−2472.
4. Kim, B. H.; Lee, N.; Kim, H.; Park, Y. I.; An, K.; Choi, Y.; Shin, K.; Lee, Y.; Kwon, S. G.; Na, H. B.; Park, J. G.; Ahn, T. Y.; Kim, Y. W.; Moon, W. K.; Choi, S. H.; Hyeon, T. “Large-scale synthesis of uniform and extremely small-sized iron oxide nanoparticles for high-resolution T1 magnetic resonance imaging contrast agents” *J. Am. Chem. Soc.* **2011**, *133*, 12624−12631.
5. Park, J.; An, K.; Hwang, Y.; Park, J. G.; Noh, H. J.; Kim, J. Y.; Park, J. H.; Hwang, N. M.; Hyeon, T. “Ultra-large-scale syntheses of monodisperse nanocrystals” *Nat. Mater*. **2004**, *3*, 891−895.
6. Song, D.-P.; Lin, Y.; Gai, Y.; Colella, N. S.; Li, C.; Liu, X.-H.; Gido, S.; Watkins, J. J. “Controlled Supramolecular Self-Assembly of Large Nanoparticles in Amphiphilic Brush Block Copolymers” *J. Am. Chem. Soc*. **2015**, *137*, 3771−3774.
7. Dong, A.; Ye, X.; Chen, J.; Kang, Y.; Gordon, T.; Kikkawa, J. M.; Murray, C. B. “A Generalized Ligand-Exchange Strategy Enabling Sequential Surface Functionalization of Colloidal Nanocrystals” *J. Am. Chem. Soc.* **2011**, *133*, 998–1006.
8. Buonsanti, R.; Pick, T. E.; Krins, N.; Richardson, T. J.; Helms, B. A.; Milliron, D. J. “Assembly of Ligand-Stripped Nanocrystals into Precisely Controlled Mesoporous Architectures” *Nano Lett*. **2012**, *12*, 3872–3877.
9. Guinier, A.; Fournet, G. *Small-Angle Scattering of X-Rays*. New York: John Wiley and Sons, 1955. Print.
10. Hammouda, B. “A new Guinier–Porod model” *J. Appl. Cryst.* **2010**, *43*, 716–719.
11. Thompson, R. B.; Ginzburg, V. V.; Matsen, M. W.; Balazs, A. C. “Predicting the mesophases of copolymer-nanoparticle composites” *Science* **2001**, *292*, 2469−2472.
12. Thompson, R. B.; Ginzburg, V. V.; Matsen, M. W.; Balazs, A. C. “Block Copolymer-Directed Assembly of Nanoparticles: Forming Mesoscopically Ordered Hybrid Materials” *Macromolecules* **2002**, *35*, 1060−1071.
13. Bockstaller, M. R.; Lapetnikov, Y.; Margel, S.; Thomas, E. L. “Size-Selective Organization of Enthalpic Compatibilized Nanocrystals in Ternary Block Copolymer/Particle Mixtures” *J. Am. Chem. Soc*. **2003**, *125*, 5276−5277.
14. Ilavsky, J.; Jemian, P. R. “Irena: tool suite for modeling and analysis of small-angle scattering” *J. Appl. Crystallogr*. **2009**, *42*, 347−353.
15. Ilavsky, J. “Nika: software for two-dimensional data reduction” *J. Appl. Crystallogr*. **2012**, *45*, 324−328.
16. Percus, J. K.; Yevick, G. “Analysis of Classical Statistical Mechanics by Means

of Collective Coordinates" *J. Phys. Rev*. **1958**, *110*, 1−13.

17. Song, D. P.; Lin, Y.; Gai, Y.; Colella, N. S.; Li, C.; Liu, X. H.; Gido, S.; Watkins, J. J. "Controlled Supramolecular Self-Assembly of Large Nanoparticles in Amphiphilic Brush Block Copolymers" *J. Am. Chem. Soc*. **2015**, *137*, 3771−3774.

Chapter 8

Nearest-neighbour nanocrystal bonding dictates framework stability or collapse in colloidal nanocrystal frameworks

Adapted from:

Teresa E. Williams, Daniela Ushizima, Chenhui Zhu, André Anders, Delia J. Milliron, Brett A. Helms. “Nearest-Neighbour Nanocrystal Bonding Dictates Framework Stability or Collapse in Colloidal Nanocrystal Frameworks” *Chemical Communications,* 2017. DOI: 10.1039/x0xx00000x.

8.1 Introduction

Colloidal nanocrystal frameworks (CNFs) are comprised of periodic arrangements of colloidal nanocrystals (NCs) and mesoscopic pores, typically in 3-D or quasi-2-D formats.[1–9] As previously described, the placement of NCs in such periodic arrangements from colloidal dispersions is initially directed by the presence of larger polymer colloids—e.g., block copolymer (BCP) micelles—that typically pack into progenitor lattices with smaller NCs packing in the interstitial voids.[3,6,10–12] Simple thermal or chemical processing of solution-cast BCP–NC composites reveals the intended mesoporosity. During mesopore generation, it is desirable that the CNF retain the high degree of order present in progenitor mesostructured composite;[3,6,11,13-15] furthermore, the CNF should be self-supporting at the end of the procedure. It follows that the fraction of NCs (f_{NC}) in the composite could play a key role in those aspects, in particular since chemical contacts between NC surfaces are required to buttress the framework.[3,6] As a systematic approach to understanding that role quantitatively has been lacking, I developed a strategy to test this hypothesis by preparing a series of seven loadings of NC vs. BCP, using tin-doped indium oxide (ITO) NCs with polystyrene-*block*-poly(*N,N*-dimethylacrylamide (PS-*b*-PDMA) architecture-directing agents.[3] Here I show that the number of nearest-neighbor contacts between NCs in the CNF is deterministic in whether the framework is self-supporting after thermal processing, or rather collapses under its own weight. Concomitant with framework collapse is loss of order, which I observe, and quantify, using top-down and cross-sectional scanning electron microscopy (SEM), and grazing incidence small-angle X-ray scattering (GISAXS). Additionally, I apply image analysis techniques to quantitatively assess an order-disorder transition, pore-size distribution within the framework, and ranges of f_{NC} yielding CNFs rather than disordered mesoporous films. The design rules laid out here indicate self-supporting films assembled from spherical NCs are feasible only when $f_{NC} > 17\%$. Furthermore, CNFs emerge only for $f_{NC} = 30–55\%$.

8.2 Experimental Procedures

MATERIALS. Ethanol (EtOH, anhydrous, ≥ 99.5%), toluene (anhydrous, 99.8%) and *N,N*-dimethylformamide (DMF, anhydrous, 99.8%) were obtained from Sigma-Aldrich and passed through a 0.2 μm PTFE (EtOH, toluene) or PVDF (DMF) syringe-tip filter (Whatman) prior to use. Nitrosyl tetrafluoroborate was obtained from Sigma-Aldrich and used as received. <100> Si wafers (single-sided polished) were obtained from Silicon Quest.

NANOCRYSTAL SYNTHESIS AND STRIPPING. Synthesis of ITO NCs was carried out as described previously.[17] Ligand stripping was carried as described previously[18] in an oxygen- and water-free glove box using $NOBF_4$. Nanocrystals were dispersed in DMF at a concentration of 11.3 wt % (TGA). ImageJ software was used to determine the distribution of nanocrystal size (Figure 8.1) from a series of TEM images.

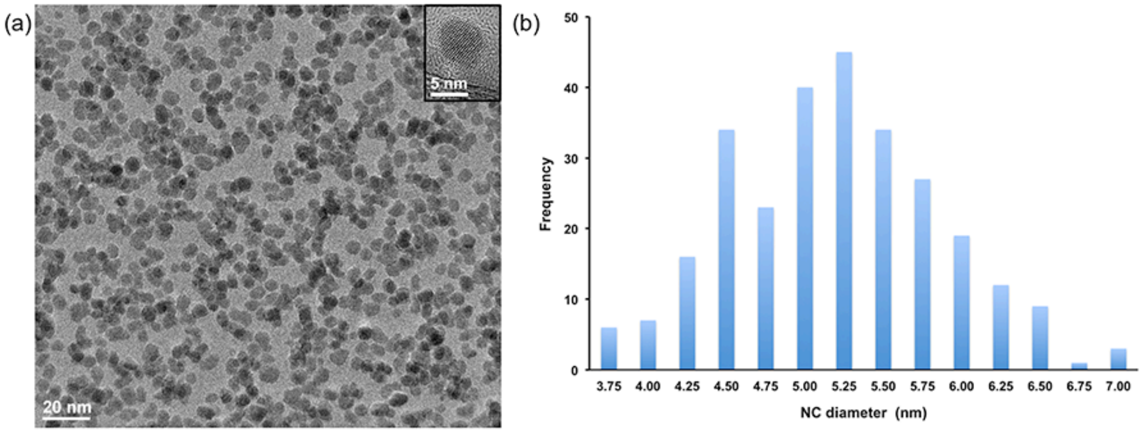

Figure 8.1. Analysis of ligand-stripped ITO nanocrystals: (a) BF-TEM image; (b) histogram for size-distribution analysis ($n = 276$, $d = 5.3$ nm ± 0.7 nm).

Polystyrene-*block*-poly(*N,N*-dimethylacrylamide (PS-*b*-PDMA) BLOCK COPOLYMER MICELLES. The PS-*b*-PDMA copolymers were prepared as described previously.[3] To assemble the micelles, PS-*b*-PDMA was dissolved in DMF, then EtOH was added drop-wise to make a 25 mg mL^{-1} BCP solution in 8:2 *v/v* EtOH/DMF. ImageJ software was used to determine the distribution of micelle sizes from a series of BF-TEM images (Figure 8.2 for PS_{60k}-*b*-$PDMA_{20k}$ and Figure 8.3 for PS_{20k}-*b*-$PDMA_{20k}$).

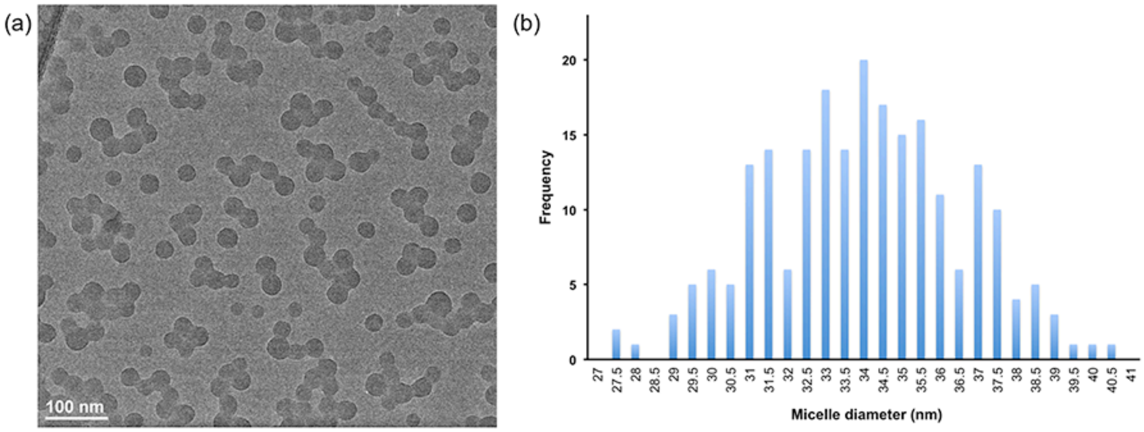

Figure 8.2. Analysis of PS_{60k}-*b*-$PDMA_{20k}$ micelles: (a) BF-TEM image; (b) histogram for size-distribution analysis ($n = 248$, $d = 34.4$ nm ± 2.3 nm).

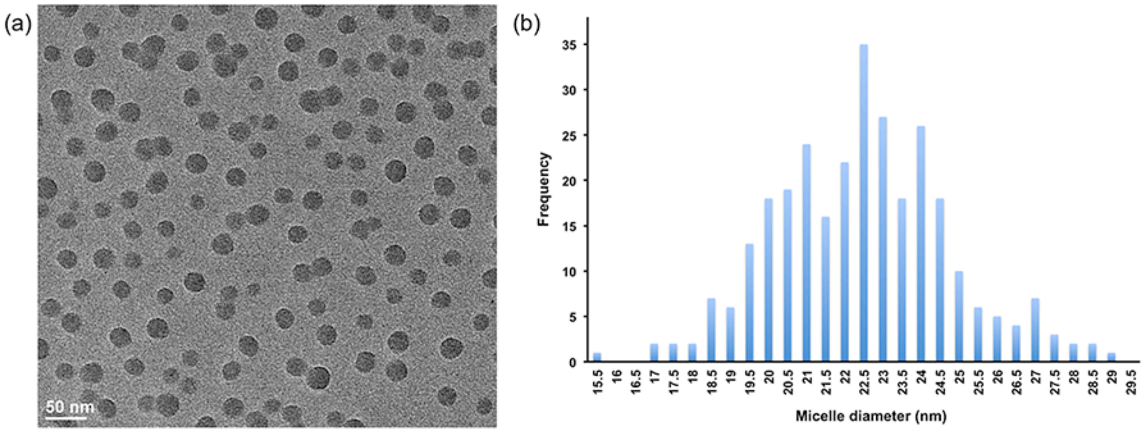

Figure 8.3 Analysis of PS_{20k}-*b*-$PDMA_{20k}$ micelles: (a) BF-TEM image; (b) histogram for size-distribution analysis ($n = 296$, $d = 22.7$ nm ± 2.3 nm).

PREPARATION OF POLYMER MICELLE–NC ASSEMBLIES. Assemblies were prepared by adding the appropriate weight of ITO NC dispersion in DMF to a stirring solution of BCP micelles (Table 8.1). Samples were equilibrated overnight at ambient temperature.

Table 8.1. Ratio of ITO NC and BCP for preparation of binary colloidal assemblies.

Sample	NC wt (mg mL^{-1})	BCP wt (mg mL^{-1})	BCP% *w/w*	NC% *w/w*
1	183.33	25	12	88
2	100.00	25	20	80
3	64.28	25	28	72
4	44.44	25	36	64
5	31.82	25	44	56
6	23.07	25	52	48
7	16.67	25	60	40

MESOPOROUS COLLOIDAL NC FRAMEWORKS. Substrates were prepared by spin coating 50 μL of BCP–NC dispersion onto a 2x2 cm^2 Si wafer with a 3 s ramp to 800 rpm, then holding at 800 rpm for 3 min. Mesoporosity was revealed following annealing in air with a 3 h ramp from rt to 550 ˚C, then holding at 550 ˚C for 1.5 h.

8.3 Results and Discussion

To understand the impact of NC nearest-neighbor contacts on framework stability during thermal processing, I prepared CNFs from BCP–NC composites loaded with variable quantities of NCs. To do so, composite thin films (240–440 nm) were cast onto Si substrates from a dispersion of cationic naked[18–20] tin-doped indium oxide NCs (d_{NC} = 5.3 ± 0.7 nm, Figure 8.1) and BCP micelles that were pre-formed in DMF:EtOH (2:8 *v/v*) from one of two polystyrene-*block*-poly(*N,N*-dimethylacrylamide) architecture directing agents:3,11 PS_{60k}-*b*-PDMA_{20k} (d_{BCP} = 34.4 nm ± 2.3 nm, Figure 8.2) and PS_{20k}-*b*-PDMA_{20k} (d_{BCP} = 22.7 nm ± 2.3 nm, Figure 8.3). Seven loadings were prepared for each architecture-directing agent, with BCP loadings spanning 12–60% *w/w* (Table 8.1). The composite films were thermally annealed in air (550 ˚C, 1.5 h) to sinter the NCs and also reveal the mesopores (Scheme 8.1).

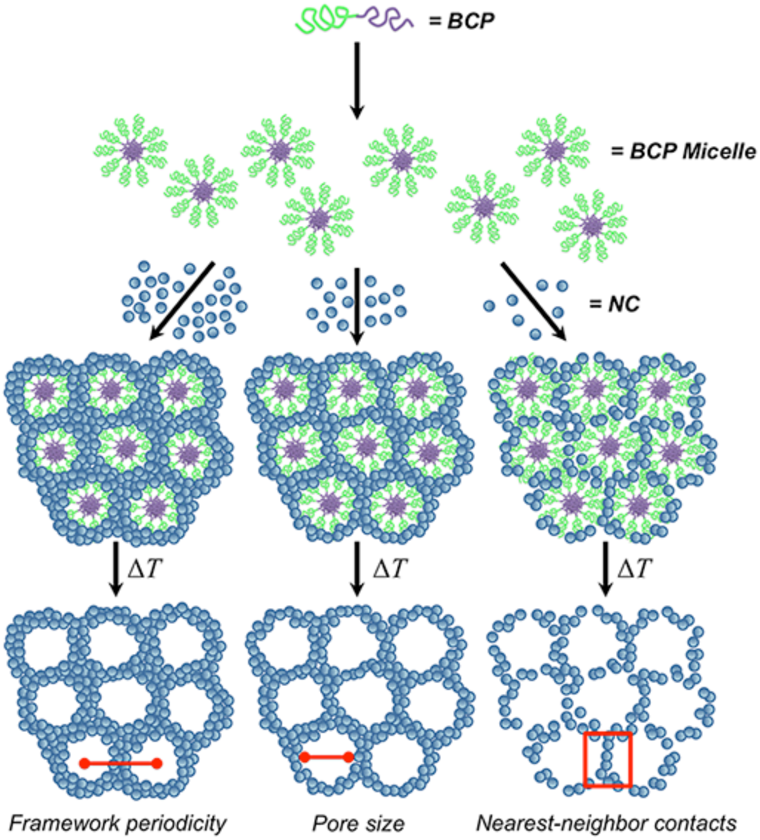

Scheme 8.1. Assembly trajectory for the preparation of mesoporous, colloidal nanocrystal frameworks and their analysis for framework periodicity, pore size, and nearest-neighbor contacts.

Regardless of the size of BCP micelle used as architecture-directing agent, I noted a trend in order to disorder in the CNF as the BCP loading in the initial mesostructured composite was increased. This was evidenced both in the top-down SEM and the associated GISAXS patterns (Figure 8.4 for CNFs assembled with PS_{60k}-*b*-PDMA_{20k} and Figure 8.5 for CNFs assembled with PS_{20k}-*b*-PDMA_{20k}).

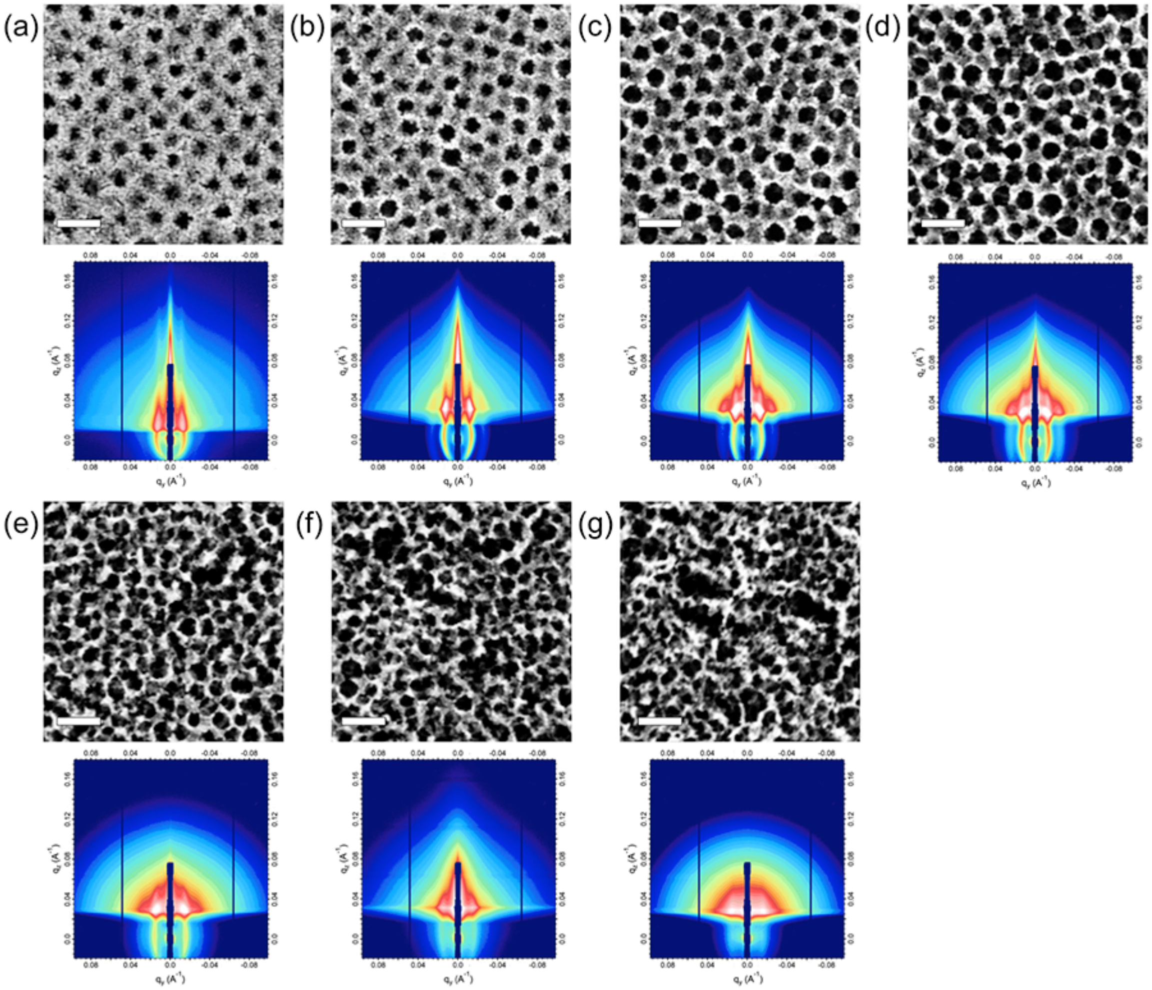

Figure 8.4. Evolution of film architecture as a function of BCP loading, as evidenced by top-down SEM and GISAXS, for PS_{60k}-*b*-$PDMA_{20k}$ at BCP loadings of: (a) 12%; (b) 20%; (c) 28%; (d) 36%; (e) 44%; (f) 52%; (g) 60% w/w. Scale bar = 100 nm.

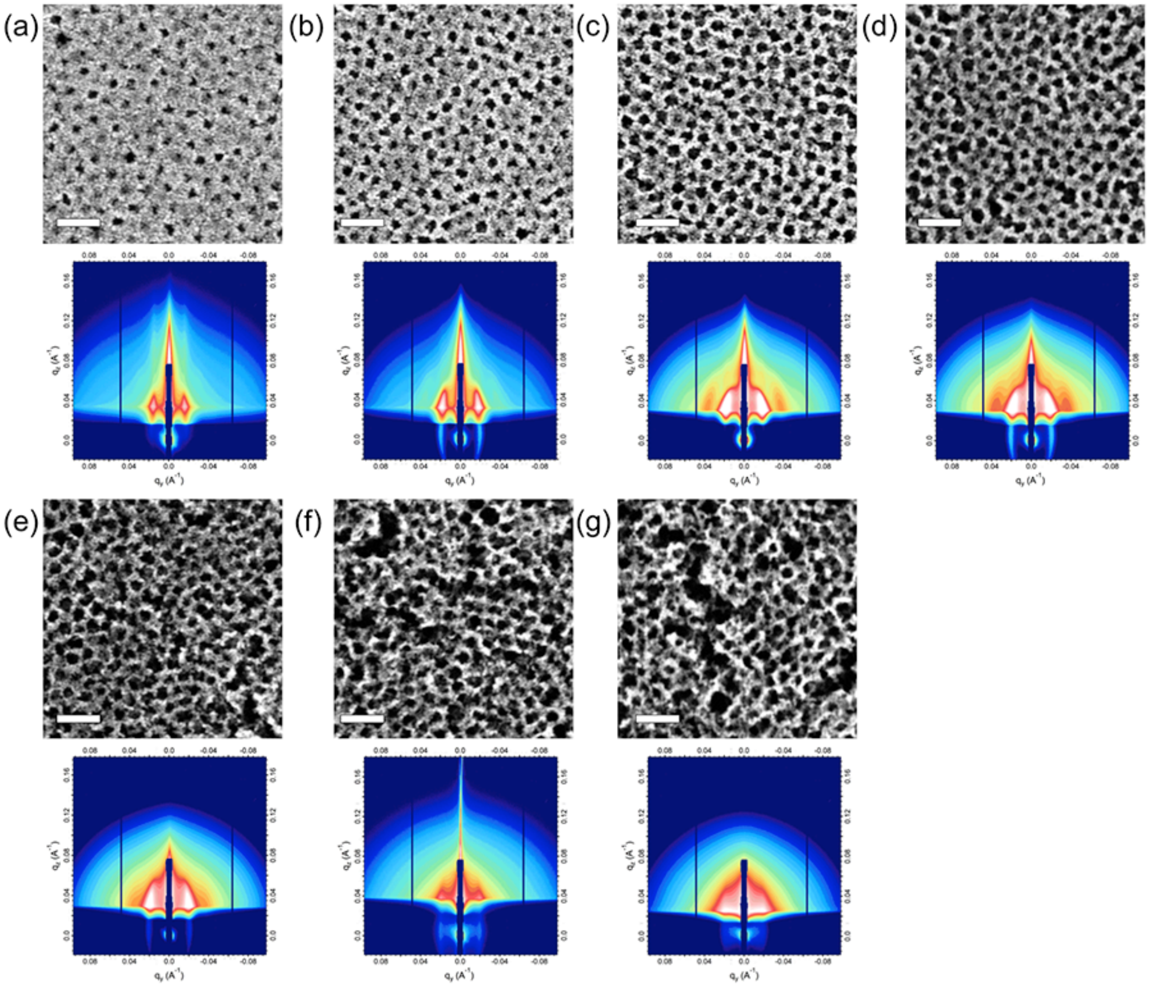

Figure 8.5. Evolution of film architecture as a function of BCP loading, as evidenced by top-down SEM and GISAXS, for PS_{20k}-*b*-$PDMA_{20k}$ at BCP loadings of: (a) 12%; (b) 20%; (c) 28%; (d) 36%; (e) 44%; (f) 52%; (g) 60% w/w. Scale bar = 100 nm.

To quantitatively characterize the CNFs I applied tools from DiameterJ, an open source plugin for ImageJ software developed at NIST (National Institutes of Standards and Technology). It is a validated nanofiber diameter characterization tool.[21] DiameterJ is bundled with OrientationJ, for analysis of 'fiber' orientation within an image, and also the 'analyze particles' function to analyze pore space within scaffolds and produce summary statistics for pores. Though my films consisted of interconnected frameworks comprised of colloidal nanocrystals rather than individual nanofibers, the analyses were made on binary images, which had been segmented for matter (framework) and void spaces (pores); this made the calculations applicable for my desired analyses.

In order to identify the order-disorder transition (ODT), first, top-down SEM images were segmented into binary images, with pores indicated by black regions and NCs by white regions (Figure 8.6 for CNFs assembled with PS_{60k}-*b*-$PDMA_{20k}$ and Figure 8.7 for CNFs assembled with PS_{20k}-*b*-$PDMA_{20k}$). Next, a Voronoi tessellation algorithm was applied to determine the distribution of pixels from one pore centroid to the next, with borders drawn to indicate equal distances between adjacent pores; these borders segmented the image into Voronoi cells. Finally, a frequency diagram was generated for the pore centroid-to-centroid orientation of surrounding Voronoi cells, with peaks indicating an ordered arrangement in the framework. This method was based upon Fourier spectrum analysis, using a Gaussian window of 7 pixels.[21]

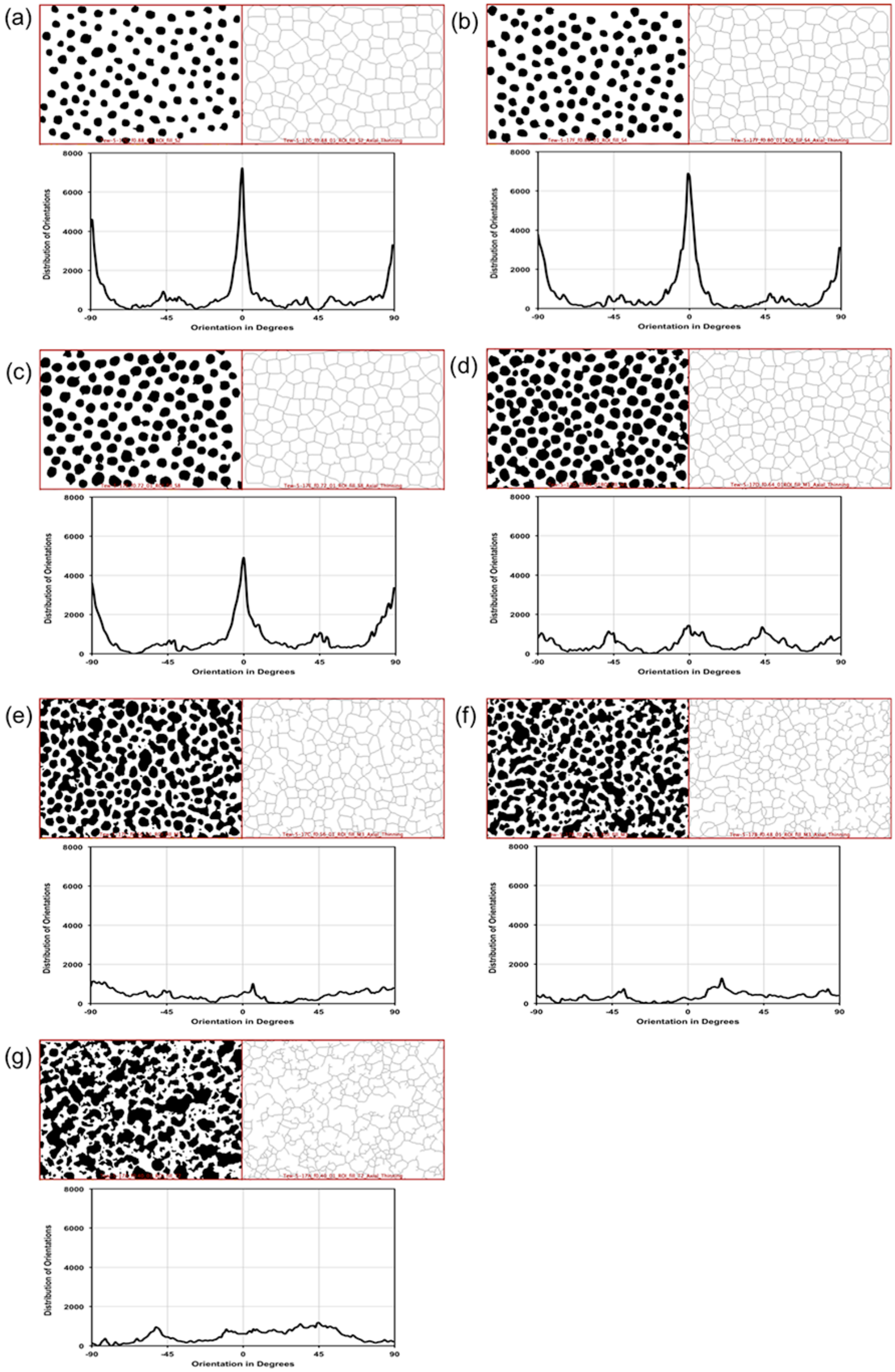

Figure 8.6. Binary segmentation, Voronoi diagram, and orientation analysis for films assembled with PS_{60k}-*b*-PDMA at all BCP loadings: (a) 12%; (b) 20%; (c) 28%; (d) 36%; (e) 44%; (f) 52%; (g) 60% *w/w*.

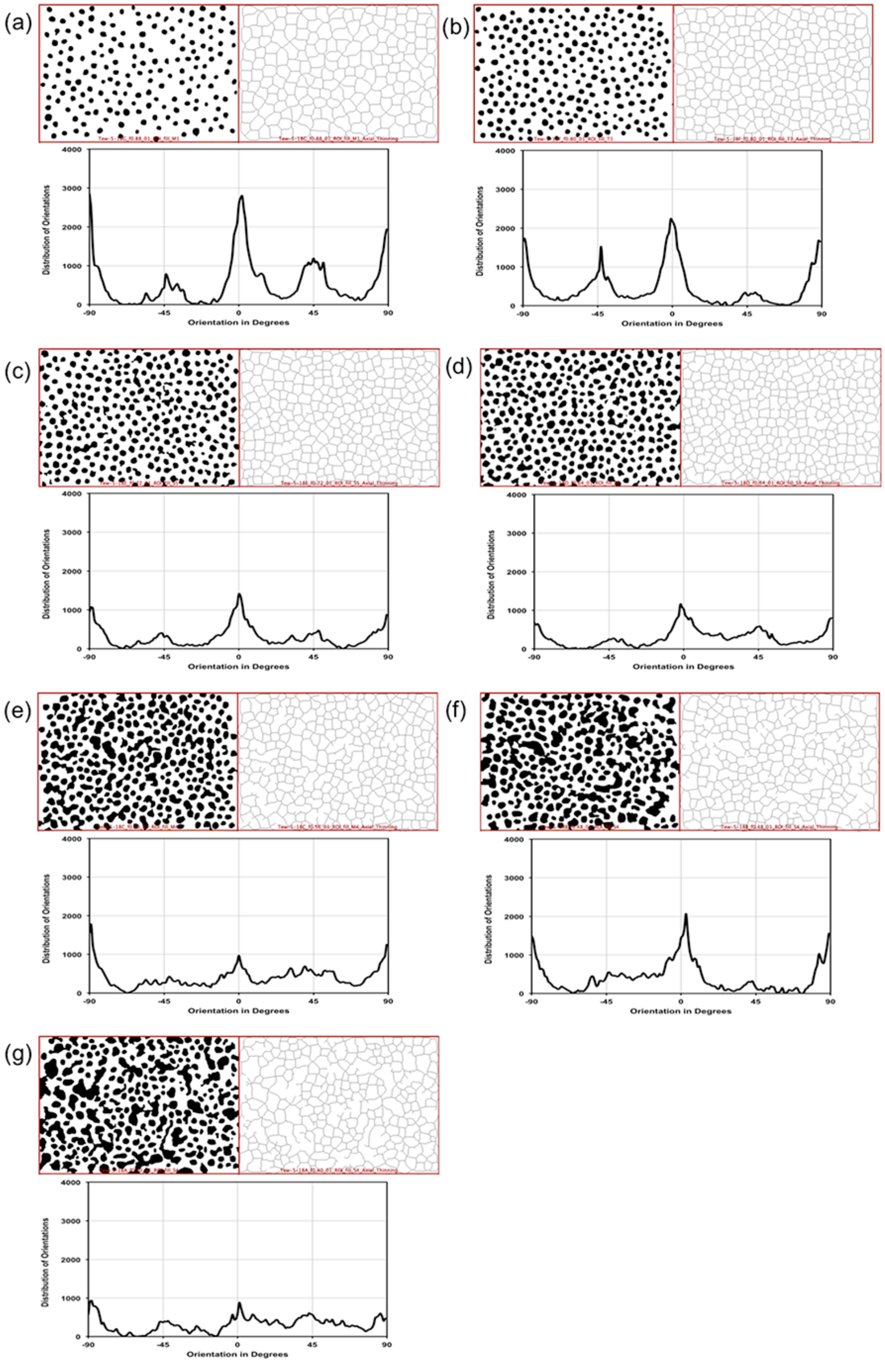

Figure 8.7. Binary segmentation, Voronoi diagram, and orientation analysis for films assembled with PS$_{20k}$-*b*-PDMA at all BCP loadings: (a) 12%; (b) 20%; (c) 28%; (d) 36%; (e) 44%; (f) 52%; (g) 60% *w/w*.

For CNFs prepared from PS_{60k}-*b*-$PDMA_{20k}$ BCP micelles, I found the lowest BCP loadings (12–28% *w/w*) show Voronoi cells of regular size and shape: as BCP loading is increased (particularly for 44–60% *w/w*), the segmented cells became less defined and transform into disordered, irregular shapes. The same trend was seen in the distribution of pore centroid orientations within the Voronoi textures; peaks at –90°, 0°, and 90° significantly decrease in intensity at higher BCP loadings. Less intense peaks at –45° and +45° were indicative of short-range order—likely, mixed orientations of one or more cubic lattices presented at the surface. For CNFs prepared from PS_{60k}-*b*-$PDMA_{20k}$ BCP micelles, the ODT occurred at a BCP loading of 36% *w/w*; for CNFs prepared from PS_{20k}-*b*-$PDMA_{20k}$ BCP micelles, the ODT occurred at a BCP loading of 28% *w/w*.

Having identified the ODT for CNFs assembled with different BCP micelles, I was further interested in understanding how framework periodicity and other architectural metrics such as pore size and regularity varied with NC loading—i.e., either above or below the ODT. To do so, line-traces were taken along the horizontal axis for each of the GISAXS scattering patterns (Figure 8.8 for PS_{60k}-*b*-$PDMA_{20k}$ & Figure 8.9 for PS_{20k}-*b*-$PDMA_{20k}$) for CNFs assembled with either of the BCP architecture-directing agents. For CNFs assembled with PS_{60k}-*b*-$PDMA_{20k}$, I observed an invariant framework periodicity of ~51 nm (within experimental error) for BCP loadings of 12–36% *w/w*, which is consistent with the top-down SEM in Figure 8.4. At these loadings, the frequency distribution of the Voronoi cells indicated this to be the ordered regime typical of CNFs. GISAXS gave further evidence of a higher degree of order in the CNF regime by the emergence of a secondary scattering peak.

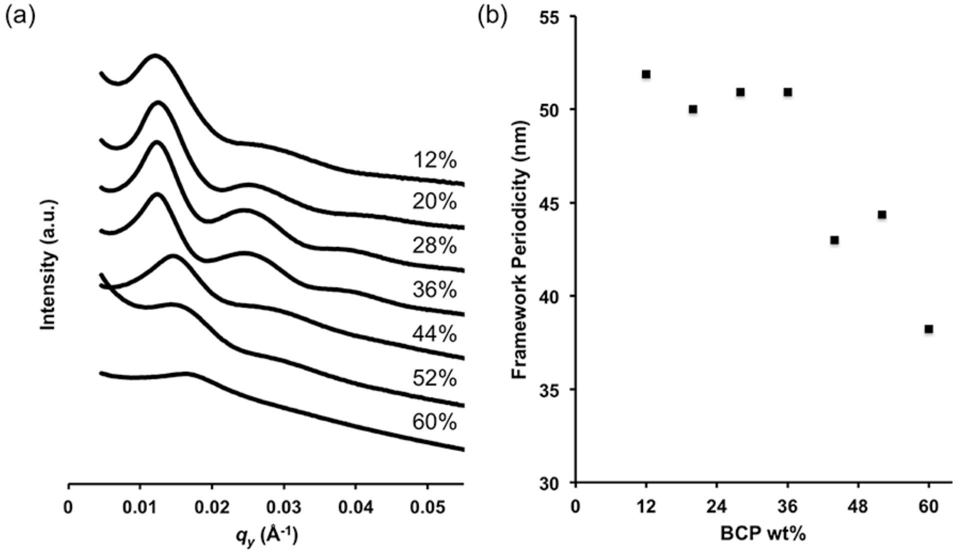

Figure 8.8. GISAXS analysis for CNFs assembled with PS_{60k}-*b*-$PDMA_{20k}$ micelles: (a) horizontal line cuts from GISAXS scattering patterns, with BCP loading indicated on each trace; (b) plot of framework periodicity as a function of BCP loading.

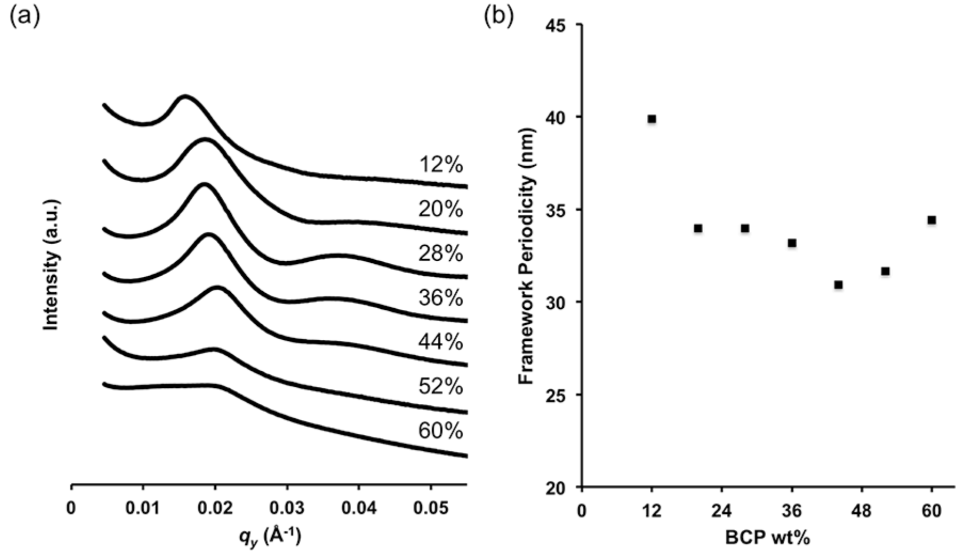

Figure 8.9. GISAXS analysis for CNFs assembled with PS_{20k}-*b*-$PDMA_{20k}$ micelles: (a) horizontal line cuts from GISAXS scattering patterns, with BCP loading indicated on each trace; (b) plot of framework periodicity as a function of BCP loading.

Below the ODT, periodicity held a more tenuous definition for these films, but nevertheless emerged as an observable in the GISAXS. Across these samples, the primary scattering peak broadened significantly and periodicity experienced a steep decline. This was concomitant with other framework irregularities visible by SEM, including disjunctions, where too few NCs are available to form the walls of the framework; mesopore coalescence was also observed in this regime. To distinguish these disordered films from ordered CNFs, I will refer to them simply as mesoporous NC films.

Further analysis of the segmented, binary SEM images gave insight into the pore structure (i.e., pore area and circularity) above and below the ODT (Table 8.2). For pore size analysis, the algorithm looked for discrete clusters of black pixels–which indicate pores in our samples rather than individual particles–and counted the number of pixels in each cluster, and reported their area.[21] Clusters on the edges of the image were excluded. Reports of pore area and standard deviation, and pore circularity and standard deviation, were generated; here, pore circularity is defined as 4π×[Area/(Perimeter)^2], with a value of 1.0 indicating a perfect circle.

Table 8.2. Pore area and circularity, and their standard deviation (SD), from ImageJ analysis on binary, top-down SEM images.

	PS_{60k}-*b*-$PDMA_{20k}$				**PS_{20k}-*b*-$PDMA_{20k}$**			
BCP % *w/w*	**Pore area (nm^2)**	**SD (nm^2)**	**Pore circularity**	**SD**	**Pore area (nm^2)**	**SD (nm^2)**	**Pore circularity**	**SD**
12	677.374	148.845	0.900	0.032	292.868	68.303	0.917	0.022
20	776.238	136.052	0.897	0.030	300.104	77.947	0.920	0.016

28	1058.759	248.455	0.872	0.076	374.571	164.670	0.848	0.121
26	1139.791	601.252	0.838	0.134	416.420	224.492	0.839	0.126
44	1101.71	1176.40	0.76	0.20	624.36	528.63	0.80	0.17
52	941.39	1270.09	0.74	0.22	801.76	1013.23	0.77	0.20
60	919.45	2197.30	0.71	0.24	723.60	913.82	0.78	0.19

These results were most significant within the ordered CNF regime (i.e., BCP loadings 12–36% *w/w*), which showed the narrowest distribution in both pore area and circularity (Figure 8.10a,b).

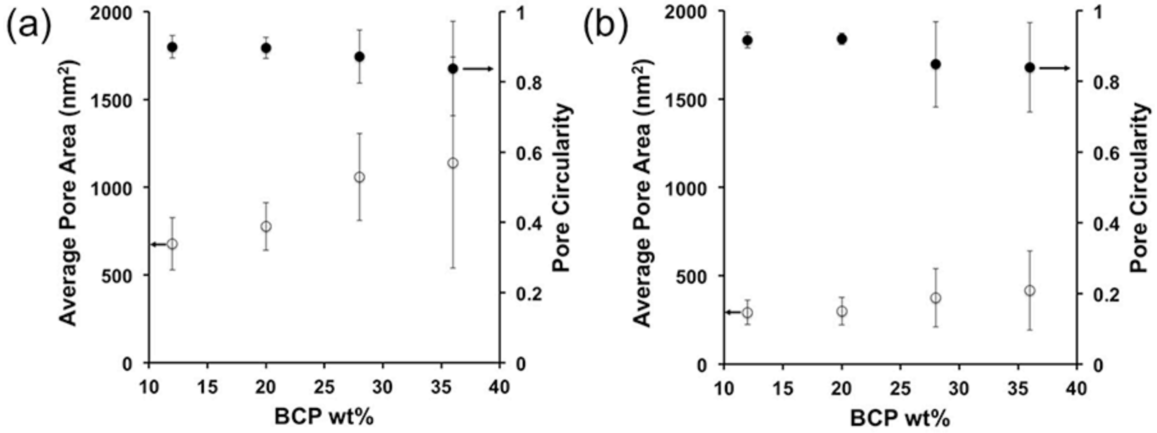

Figure 8.10. Average pore area (open circles) and pore circularity (filled circles) vs. BCP loading for CNFs assembled with (a) PS_{60k}-*b*-$PDMA_{20k}$ or (b) PS_{20k}-*b*-$PDMA_{20k}$. For PS_{60k}-*b*-$PDMA_{20k}$, pore diameters were: 29 nm at 12%, 31 nm at 20%, 36 nm at 28%, and 38 nm at 36% BCP loading *w/w*. For PS_{20k}-*b*-$PDMA_{20k}$, pore diameters were: 19 nm at 12%, 19 nm at 20%, 22 nm at 28%, and 23 nm at 36% BCP loading *w/w*.

I estimated pore diameter from average pore area for these CNFs, and, while framework periodicity remained invariant, pore diameter steadily increased (e.g., from 29 nm at 12% BCP loading *w/w* to 38 nm at 36% BCP loading). This indicated that NCs increasingly penetrate the PDMA corona of the micelle at higher NC loadings. Notably, then, framework periodicity was solely determined by the periodicity in packing of the BCP micelles; in this regard, they were indeed architecture-directing. I noted that salient aspects of the architectural evolution between CNFs and mesoporous NC films—i.e., above and below the ODT—were largely consistent for mesoporous films prepared using the smaller PS_{20k}-*b*-$PDMA_{20k}$ micelles as architecture-directing agent.

In that for disordered mesoporous NC films, there are too few NCs present to constitute a load-bearing segment (or wall) in the structure, it followed such films may also experience a film collapse during the thermal treatment used to rid the composite of the organic BCP micelles. Indeed, I showed that framework collapse at BCP loadings in excess of 52% *w/w* was evident after examining the films in cross-section using SEM (Figure 8.11 for PS_{60k}-*b*-$PDMA_{20k}$ and Figure 8.12 for PS_{20k}-*b*-$PDMA_{20k}$).

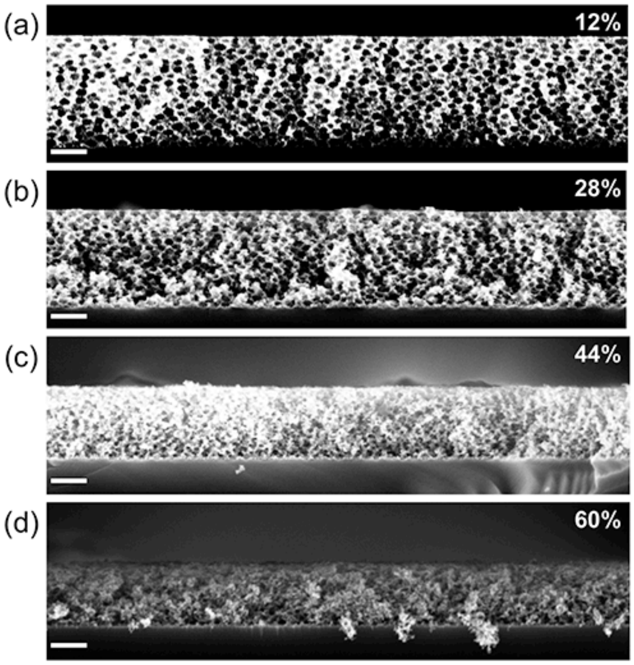

Figure 8.11. Cross-sectional SEM for CNFs or mesoporous NC films assembled with PS_{60k}-*b*-$PDMA_{20k}$ BCPs at a loading of: (a) 12%; (b) 28%; (c) 44%; or (d) 60% *w/w*. Scale bar = 200 nm.

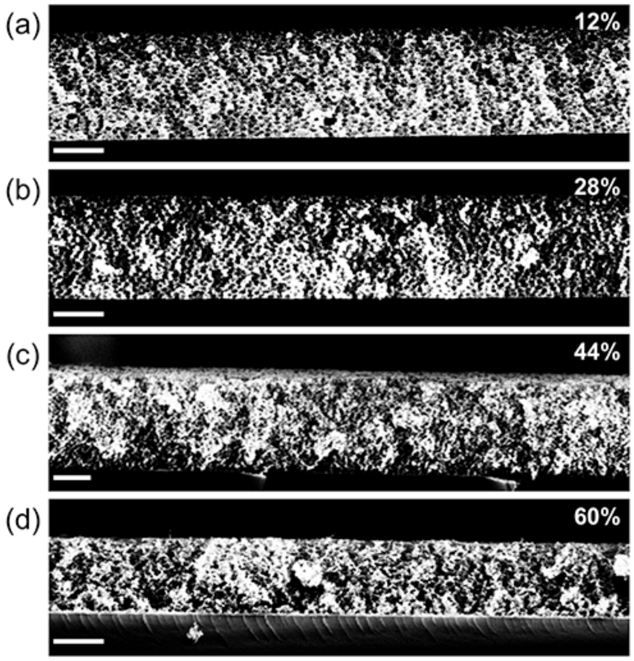

Figure 8.12. Cross-sectional SEM for CNFs or mesoporous NC films assembled with PS_{20k}-*b*-$PDMA_{20k}$ BCPs at a loading of: (a) 12%; (b) 28%; (c) 44%; or (d) 60% *w/w*. Scale bar = 200 nm.

Table 8.3. Film thickness measurements for all samples, as analyzed by ImageJ from cross-sectional SEM images.

	PS_{60k}-*b*-$PDMA_{20k}$		**PS_{20k}-*b*-$PDMA_{20k}$**	
BCP % *w/w*	**Thickness (nm)**	**SD (nm)**	**Thickness (nm)**	**SD (nm)**
12	425.10	5.29	437.26	10.93
20	443.05	4.87	410.48	5.97
28	376.59	8.57	403.20	3.28
26	355.37	5.19	356.31	5.63
44	281.86	3.72	363.06	5.41
52	297.34	8.46	264.33	5.11
60	242.61	4.27	291.02	4.32

I also employed Rutherford Backscattering Spectroscopy (RBS) to determine f_{NC} for each film after thermal annealing; the expected trend would be for f_{NC} to increase with NC loading relative to BCP. However, this is not the case. At the highest BCP loading for both micelle sizes, the observed framework collapse lead to a higher f_{NC} than expected (Table 8.4; also see Figure 8.13 for PS_{60k}-*b*-$PDMA_{20k}$ and Figure 8.14 for PS_{20k}-*b*-$PDMA_{20k}$ for raw data).

Table 8.4. Determination of f_{NC} for all films from fitting RBS data using SIMNRA software.

	PS_{60k}-*b*-$PDMA_{20k}$	**PS_{20k}-*b*-$PDMA_{20k}$**
BCP % *w/w*	**f_{NC}**	**f_{NC}**
12	0.56	0.55
20	0.395	0.455
28	0.38	0.375
26	0.282	0.375
44	0.2685	0.3
52	0.1975	0.17
60	0.265	0.33

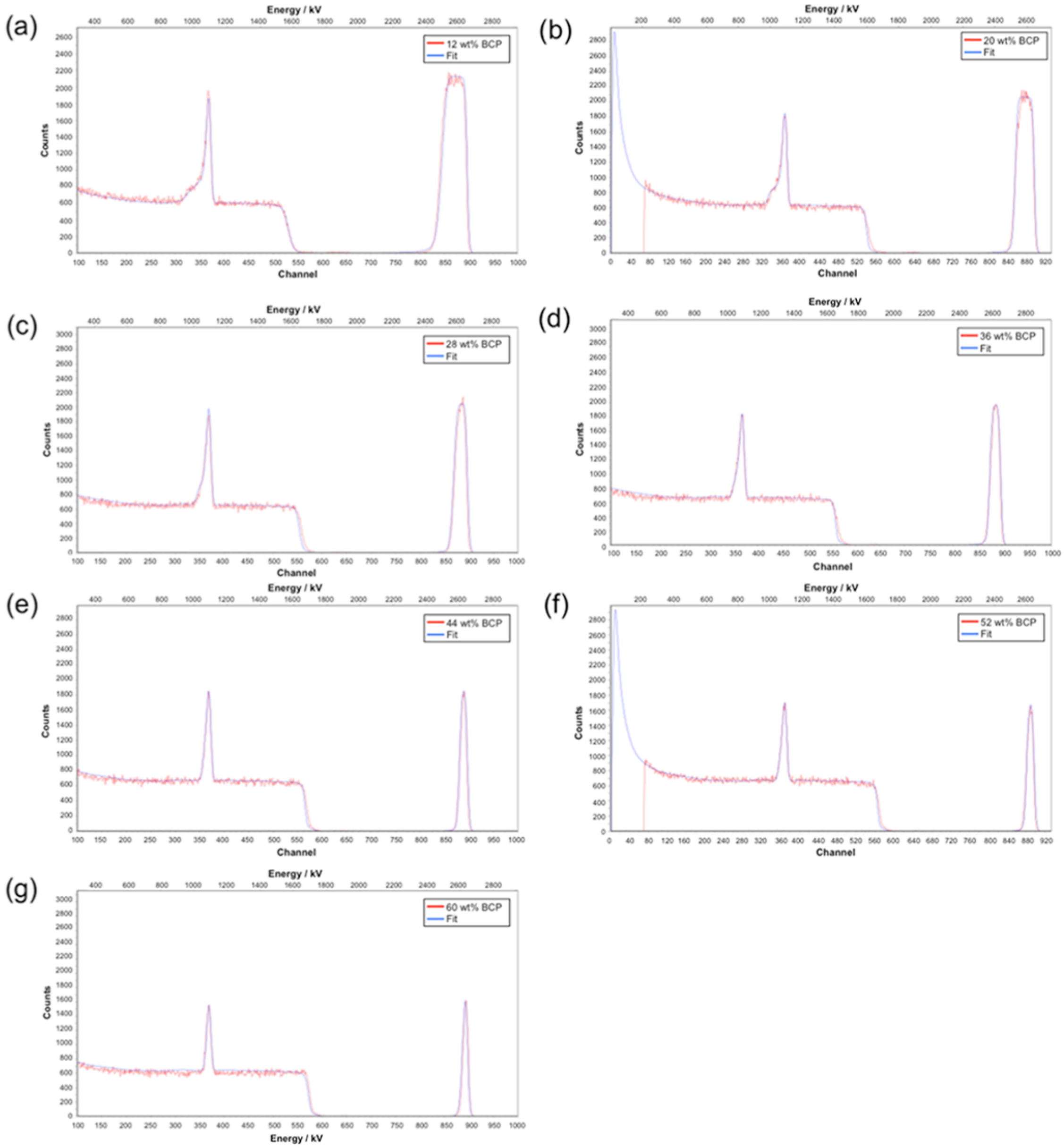

Figure 8.13. Raw data (red trace) and fits (blue trace) from RBS measurements for films assembled using PS_{60k}-*b*-$PDMA_{20k}$ micelles at variable loadings of: (a) 12%; (b) 20%; (c) 28%; (d) 36%; (e) 44%; (f) 52%; (g) 60% *w/w*.

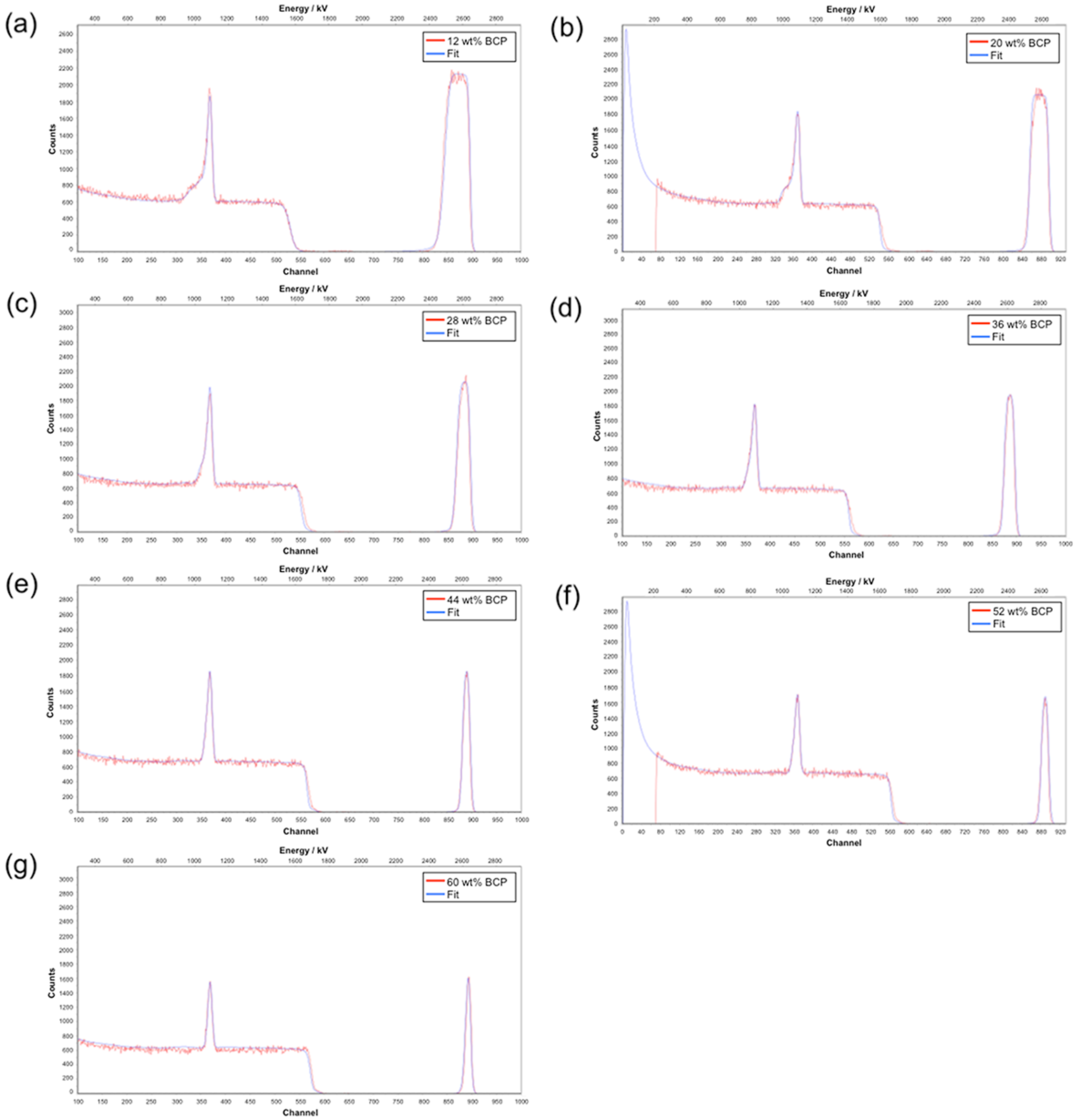

Figure 8.14. Raw data (red trace) and fits (blue trace) from RBS measurements for films assembled using PS_{20k}-*b*-$PDMA_{20k}$ micelles at variable loadings of: (a) 12%; (b) 20%; (c) 28%; (d) 36%; (e) 44%; (f) 52%; (g) 60% *w/w*.

In contrast, for ordered CNFs, cross-sectional analysis of the architecture by SEM confirmed the presence of well-formed, homogeneously-distributed mesopores throughout the films (Figure 8.11 for PS_{60k}-*b*-$PDMA_{20k}$ and Figure 8.12 for PS_{20k}-*b*-$PDMA_{20k}$). Here, film thickness increased proportionally to the loading of NCs while the mass fraction of BCP was kept constant (Figure 8.15).

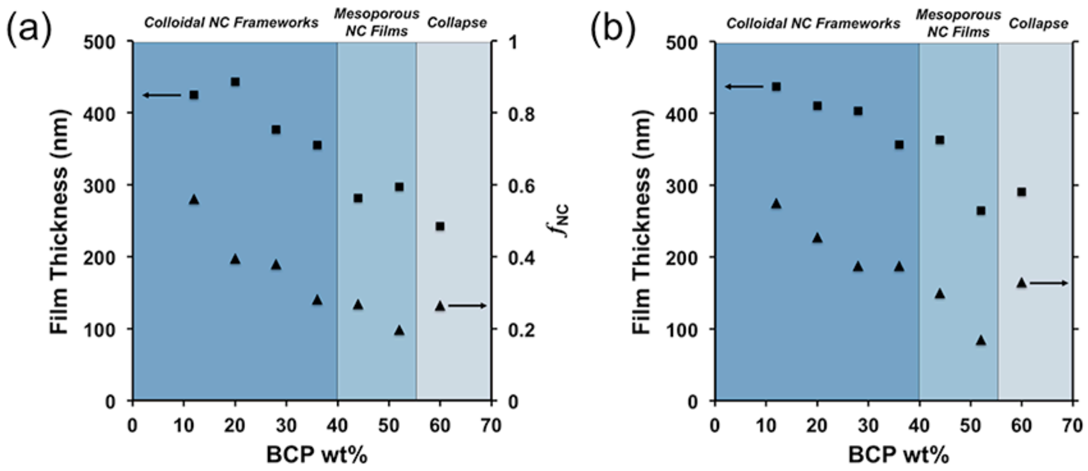

Figure 8.15. Film thickness (squares) & f_{NC} (triangles) vs. BCP loading for films assembled with (a) PS_{60k}-*b*-$PDMA_{20k}$ or (b) PS_{20k}-*b*-$PDMA_{20k}$.

To better understand these outcomes, I quantified the average width of load-bearing segments in each film (Table 8.5; also Figure 8.16 for PS_{60k}-*b*-$PDMA_{20k}$ and Figure 8.17 for PS_{20k}-*b*-$PDMA_{20k}$). For segment width analysis, binary, top-down SEM images were analyzed to find the centerlines of the framework segments, then the width was determined by examining every pixel along the framework's axis to produce a histogram of the framework widths.[21] Included were summary statistics such as mean segment width and standard deviation.

Table 8.5. Load-bearing segment widths from DiameterJ analysis for all films.

	PS_{60k}-*b*-$PDMA_{20k}$		**PS_{20k}-*b*-$PDMA_{20k}$**	
BCP% *w/w*	**Width (nm)**	**SD (nm)**	**Width (nm)**	**SD (nm)**
12	26.04	7.13	22.59	5.60
20	21.89	6.67	17.34	5.08
28	16.18	5.59	14.31	4.28
36	12.82	4.50	12.48	4.00
44	10.57	3.97	11.23	4.15
52	10.09	4.21	10.88	4.08
60	9.58	4.23	11.20	4.56

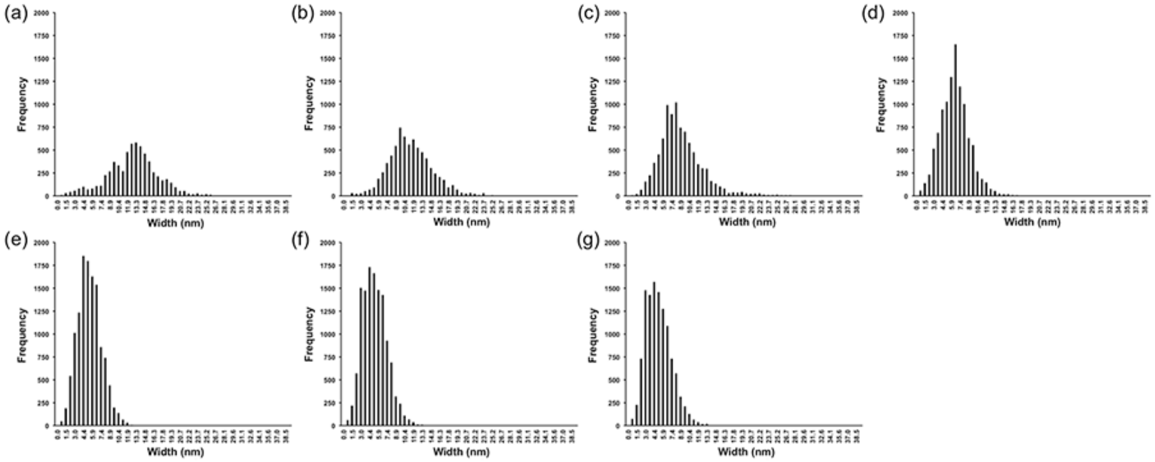

Figure 8.16. Distribution of segment widths for films assembled with PS_{60k}-*b*-$PDMA_{20k}$ micelles at BCP loadings of: (a) 12%; (b) 20%; (c) 28%; (d) 36%; (e) 44%; (f) 52%; (g) 60% *w/w*.

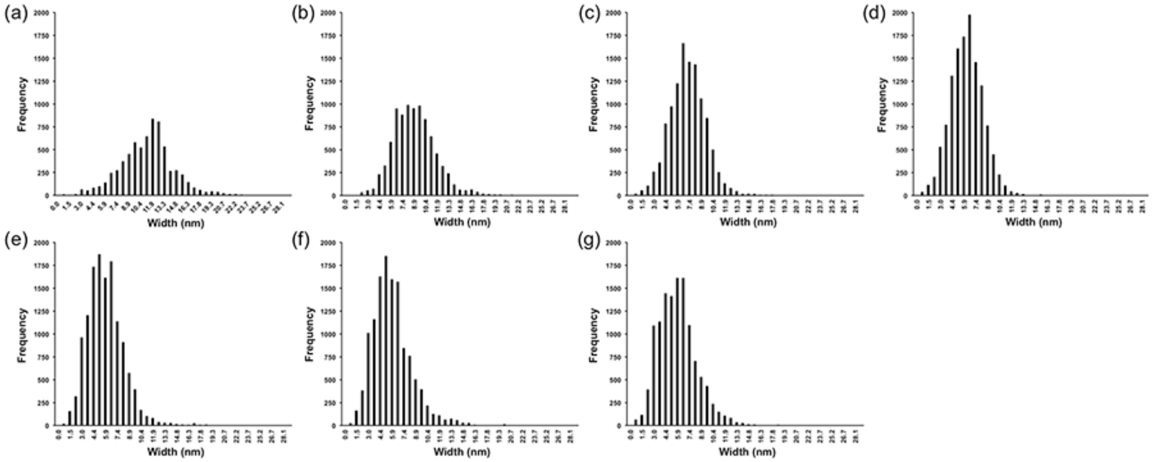

Figure 8.17. Distribution of segment widths for films assembled with PS_{20k}-*b*-$PDMA_{20k}$ micelles at BCP loadings of: (a) 12%; (b) 20%; (c) 28%; (d) 36%; (e) 44%; (f) 52%; (g) 60% *w/w*.

For collapsed structures, i.e., BCP loadings of >52% *w/w*, I found the average width of such segments (d_{seg}) was only 9.6 nm, which is less than the width of two NCs; the number of nearest-neighbors (and nearest-neighbor bonds) for each NC was therefore considerably smaller than for thicker load bearing segments. Specifically, I found film collapse for $d_{seg} / d_{NC} < 2$, stable mesoporous NC films for $2 < d_{seg} / d_{NC} < 3$, and stable CNFs $d_{seg} / d_{NC} > 3$. These relationships may vary by size-commensurability of NC and BCP components as well as their chemical composition and the annealing temperature.

8.4. Conclusions

The perspectives offered here indicated that my investigation and application of image analysis techniques, including matter segmentation and empty space estimation, were needed for more reliable understanding and quantitative analysis of film architecture and differentiation among classes of mesoporous materials based on colloidal NCs. My analysis showed that $d_{seg} / d_{NC} > 2$ was needed in the load-bearing segments to support the pore structure but that $d_{seg} / d_{NC} > 3$ was needed to assemble CNFs from 5.3 nm ITO NCs, offering more definitive insight into architecture than was afforded by reciprocal-space GISAXS analysis. I anticipate that this toolbox will apply to other multi-component, mesoporous materials, and thereby enable more deterministic explorations of meso-phase space than has been possible previously.

8.5 References

1. Warren, S. C.; Messina, L. C.; Slaughter, L. S.; Kamperman, M.; Zhou, Q.; Gruner, S. M.; DiSalvo, F. J.; Wiesner, U. "Ordered mesoporous materials from metal nanoparticle-block copolymer self-assembly" *Science* **2008**, *320*, 1748–1752.
2. Brezesinski, T.; Wang, J.; Polleux, J.; Dunn, B.; Tolbert, S. H. "Templated Nanocrystal-Based Porous TiO_2 Films for Next-Generation Electrochemical Capacitors" *J. Am. Chem. Soc.* **2009**, *131*, 1802–1809.
3. Buonsanti, R.; Pick, T. E.; Krins, N.; Richardson, T. J.; Helms, B. A.; Milliron, D. J. "Assembly of Ligand-Stripped Nanocrystals into Precisely Controlled Mesoporous Architectures" *Nano Lett.* **2012**, *12*, 3872–3877.
4. Rauda, I. E.; Buonsanti, R.; Saldarriaga-Lopez, L. C.; Benjauthrit, K.; Schelhas, L. T.; Stefik, M.; Augustyn, V.; Ko, J.; Dunn, B.; Wiesner, U.; Milliron, D. J.; Tolbert, S. H. "General Method for the Synthesis of Hierarchical Nanocrystal-Based Mesoporous Materials" *ACS Nano* **2012**, *6*, 6386–6399.
5. Liu, Y.; Stefanic, G.; Rathousky, J.; Hayden, O.; Bein, T.; Fattakhova-Rohlfing, D. "Assembly of mesoporous indium tin oxide electrodes from nano-hydroxide building blocks" *Chem. Sci.* **2012**, *3***,** 2367–2374.
6. Rivest, J. B.; Buonsanti, R.; Pick, T. E.; Zhu, L.; Lim, E.; Clavero, C.; Schaible, E.; Helms, B. A.; Milliron, D. J. "Evolution of Ordered Metal Chalcogenide Architectures through Chemical Transformations" *J. Am. Chem. Soc.* **2013**, *135*, 7446–7749.
7. Rauda, I. E.; Saldarriaga-Lopez, L. C.; Helms, B. A.; Schelhas, L. T.; Membreno, D.; Milliron, D. J.; Tolbert, S. H. "Nanoporous Semiconductors Synthesized Through Polymer Templating of Ligand-Stripped CdSe Nanocrystals" *Adv. Mater.* **2013**, *25*, 1315–1322.
8. Milliron, D. J.; Buonsanti, R.; Llordes, A.; Helms, B. A. "Constructing Functional Mesostructured Materials from Colloidal Nanocrystal Building Blocks" *Acc. Chem. Res.* **2014**, *47*, 236–246.
9. Helms, B. A.; Williams, T. E.; Buonsanti, R.; Milliron, D. J. "Colloidal Nanocrystal Frameworks" *Adv. Mater.* **2015**, *27*, 5820–5829.
10. Wills, A. W.; Michalak, D. J.; Ercius, P.; Rosenberg, E. R.; Perciano, T.; Ushizima, D.; Runser, R.; Helms, B. A. "Block Copolymer Packing Limits and Interfacial Reconfigurability in the Assembly of Periodic Mesoporous Organosilicas" *Adv. Funct. Mater.* **2015**, *25*, 4120–4128
11. Ong, G. K.; Williams, T. E.; Singh, A.; Schaible, E.; Helms, B. A.; Milliron, D. J. "Ordering in polymer micelle-directed assemblies of colloidal nanocrystals" *Nano Lett.* **2015**, *15*, 8240–8244.
12. Lokupitiya, H. N.; Jones, A.; Reid, B.; Guldin, S.; Stefik, M. "Ordered Mesoporous to Macroporous Oxides with Tunable Isomorphic Architectures: Solution Criteria for Persistent Micelle Templates" *Chem. Mater.* **2016**, *28*, 1653–1667.

13. Kim, J.; Ong, G. K.; Wang, Y.; LeBlanc, G.; Williams, T. E.; Mattox, T. M.; Helms, B. A.; Milliron, D. J. "Nanocomposite Architecture for Rapid, Spectrally-Selective Electrochromic Modulation of Solar Transmittance" *Nano Lett.* **2015**, *15*, 5574–5579.
14. Lyons, D. M.; Ryan, K. M.; Morris, M. A. "Preparation of ordered mesoporous ceria with enhanced thermal stability" *J. Mater. Chem.* **2002**, *12*, 1207–1212.
15. Wang, S.; Tangvijitsakul, P.; Qiang, Z.; Bhaway, S. M.; Lin, K.; Cavicchi, K. A.; Soucek, M. D.; Vogt, B. D. "Role of Amphiphilic Block Copolymer Composition on Pore Characteristics of Micelle-Templated Mesoporous Cobalt Oxide Films" *Langmuir*, 2016, **32**, 4077–4085.
16. Ilavsky, J. "Nika: software for two-dimensional data reduction" *J. Appl. Cryst.* **2012**, *45*, 324–328.
17. Lounis, S. D.; Runnerstrom, E. L.; Bergerud, A.; Nordlund, D.; Milliron, D. J. "Influence of Dopant Distribution on the Plasmonic Properties of Indium Tin Oxide Nanocrystals" *J. Am. Chem. Soc.* **2014**, *136*, 7110–7116.
18. Dong, A.; Ye, X.; Chen, J.; Kang, Y.; Gordon, T.; Kikkawa, J. M.; Murray, C. B. "A Generalized Ligand-Exchange Strategy Enabling Sequential Surface Functionalization of Colloidal Nanocrystals" *J. Am. Chem. Soc.* **2011**, *133*, 998–1006.
19. Rosen, E. L.; Buonsanti, R.; Llordes, A.; Sawvel, A. M.; Milliron, D. J.; Helms, B. A. "Exceptionally Mild Reactive Stripping of Native Ligands from Nanocrystal Surfaces by Using Meerwein's Salt" *Angew. Chem. Int. Ed.* **2012**, *51*, 684–689.
20. Doris, S. E.; Lynch, J. J.; Li, C.; Wills, A. W.; Urban, J. J.; Helms, B. A. "Mechanistic Insight into the Formation of Cationic Naked Nanocrystals Generated under Equilibrium Control" *J. Am. Chem. Soc*. **2014**, *136*, 15702–15710.
21. Hotaling, N.A.; Bharti, K.; Kriel, H.; Simon, C.G. "DiameterJ: A validated open source nanofiber diameter measurement tool" *Biomater.* **2015**, *61*, 327–338.

Applications of architecture-directed mesoporous nanocrystal frameworks

Chapter 9

Evolution of ordered metal chalcogenide architectures through chemical transformations

Adapted from:

Jessy B. Rivest, Raffaella Buonsanti, Teresa E. Pick,[3] Lina Zhu, Eunhee Lim, Cesar Clavero, Eric Schaible, Brett A. Helms, and Delia J. Milliron. "Evolution of Ordered Metal Chalcogenide Architectures through Chemical Transformations" *Journal of the American Chemical Society* **2013**, *135*, 7746–7749.

9.1 Introduction

Metal chalcogenides, now ubiquitously employed in light harvesting[1] and thermoelectrics,[2] are taking new strides as active materials for electrochemical devices,[3] photocatalysis,[4] and chemical sensing.[5] Key to their further development in these areas has been the introduction of mesoscale porosity into their structure.[6] Increased surface area in mesoporous films allows the semiconductor network to interact chemically with exogenous or infiltrating species, thereby revealing new function. Unfortunately, generating ordered mesoporous architectures of metal chalcogenides in films, and preserving them during chemical transformations, has been a challenge that limits systematic delineation of critical architecture–property relationships in devices.[6–9] In this chapter I investigate how to construct robust metal chalcogenide architectures from colloidal nanocrystal (NC) building units using tailored block copolymer architecture-directing agents (ADAs). By following the thermal process *in situ*, we show that deliberate engineering of NC–ADA interfacial chemistry was deterministic in maintaining mesoscale ordering through the removal of the ADA to generate hierarchical structures (with control of both nanocrystal and mesopore dimensions). We also demonstrate the robustness of my mesoporous metal chalcogenide architectures by chemically transforming them using cation exchange. In this manner, we are able to diversify the composition of the architectures while maintaining the ordered structure of the original film. These results suggest that a rational approach to ADA design, based on interfacial interactions, is a successful strategy for constructing robust mesoscale architectures.

9.2 Experimental

MATERIALS. *N,N*-Dimethylacrylamide (DMA), *tert*-butyl acrylate (*t*BA), and styrene were purchased from Aldrich and distilled under reduced pressure from calcium hydride. 1,4-dioxane was purchased from Aldrich and distilled under N_2 from calcium hydride. Azobisisobutyronitrile (AIBN) was purchased from Aldrich and recrystallized from ethanol. All other solvents were purchased from EMD and used without further purification. Single-sided, polished Si substrates were cleaned by oxygen plasma etch for 5 min prior to film deposition.

---

[3] This work was published under my former name, Teresa E. Pick

NANOCRYSTAL SYNTHESIS AND LIGAND STRIPPING. Cadmium Selenide (CdSe) nanocrystals (d ~ 3.8 nm) were prepared as previously reported.[11] Ligand stripping[12] was carried out in an oxygen- and water-free glove box using EtO_3BF_4 (Figure 9.1).

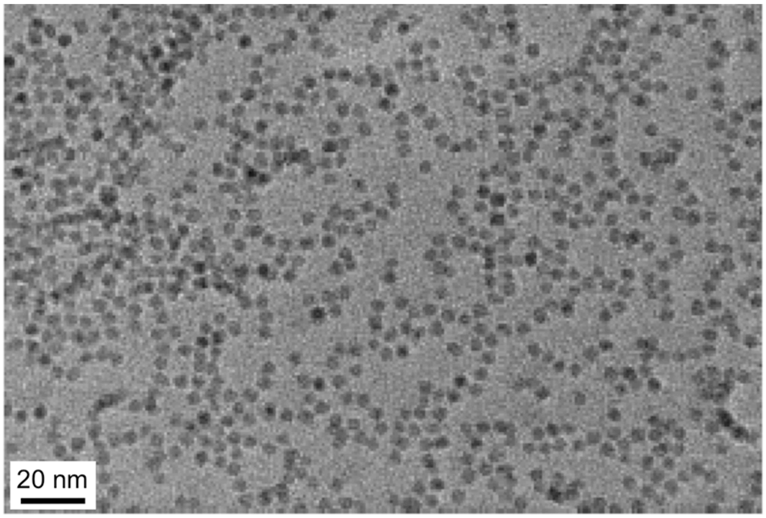

Figure 9.1. Bright-field TEM image of ligand-stripped, CdSe nanocrystals.

BLOCK COPOLYMERS. I prepared poly(*N,N*-dimethylacrylamide)-*block*-polystyrene (PDMA-*b*-PS) copolymers[13] and dodecylsulfanylthiocarbonylsulfanyl-2-methylpropionic acid (DMP) chain transfer agent (CTA) as previously reported.[14]

Polymerization of HO_2C-PDMA-*r*-P*t*BA-TTC *via* RAFT. A solution of DMA 1.80 g, 18.2 mmol), *t*BA (0.20, 1.56 mmol), DMP (73.6 mg, 0.20 mmol), AIBN (3.3 mg, 0.02 mmol) and 1,4-dioxane (2.00 g) was charged to an oven dried, 25 mL Schlenk tube. The mixture was degassed by three freeze-pump-thaw cycles, sealed under nitrogen and heated at 70 ˚C for 2.5 h. After quenching with liquid N_2 the viscous polymerization mixture was dissolved in acetone (5 mL) and precipitated three times into cold diethyl ether (500 mL). The pale yellow flocculate solid was filtered, then dried *in vacuo*, and freeze dried from benzene. ^1H NMR ($CDCl_3$): δ 3.56–3.06 (m; N-(CH_3)$_2$, SCH_2- CTA), 2.89 (s; O-(CH_3)$_3$), 2.63–2.12 (m, -CH- backbone), 1.74–1.25 (m; -CH_2- backbone, SC(CH_3)$_2$- CTA, -CH_2- CTA), 0.89 (-CH_3 CTA) ppm. SEC (DMF): $M_n = 7{,}370$ g mol^{-1}; $M_w = 8{,}510$ g mol^{-1}; PDI = 1.15.

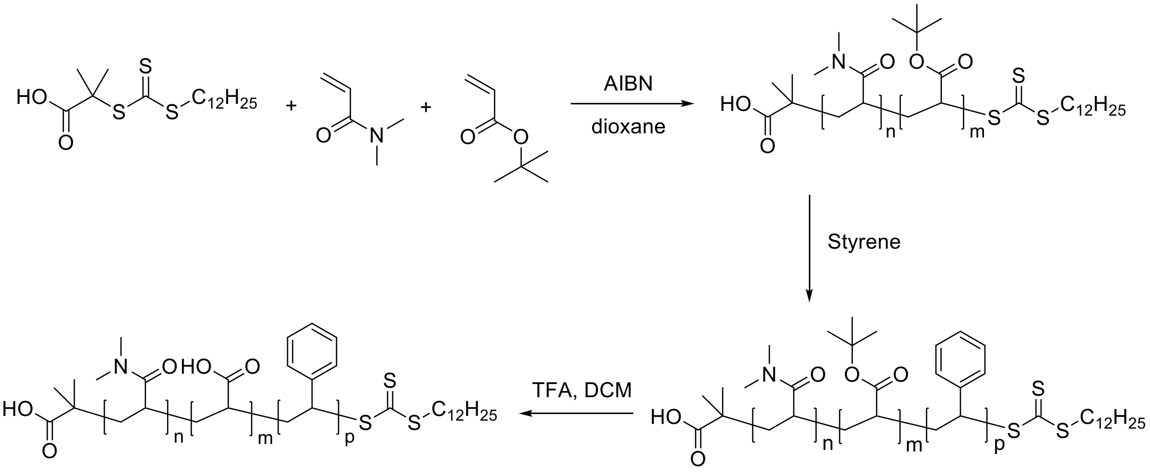

Scheme 9.1. Synthesis of [PDMA-*r*-PAA]-*b*-PS block copolymer structure directing agent via RAFT polymerization of HO_2C-PDMA-*r*-P*t*BA-TTC macro-chain transfer agent with styrene.

Block Copolymerization of HO_2C-PDMA-*r*-P*t*BA-TTC with Styrene. A solution of HO_2C-PDMA-*r*-PAA-TTC macro-CTA (500 mg, M_w = 7,370 g mol^{-1}) and styrene (4.0 g) was charged to an oven dried, 25 mL Schlenk tube. The mixture was degassed by three freeze-pump-thaw cycles, sealed under nitrogen and heated at 110 ˚C for 18 h. After quenching with liquid N_2 the viscous reaction mixture was dissolved in acetone (3 mL) and precipitated three times into cold hexanes (250 mL). The pale yellow flocculate solid was filtered, and then dried *in vacuo*. ^{1}H NMR ($CDCl_3$): δ 7.09–6.45 (m, Ar-*H*), 3.56–3.06 (m; N-(CH_3)$_2$, SCH_2- CTA), 2.89 (s; O-(CH_3)$_3$), 2.63–2.12 (m, -C*H*- backbone), 1.74–1.25 (m; -CH_2- backbone, SC(CH_3)$_2$- CTA, -CH_2- CTA), 0.89 (-CH_3 CTA) ppm. SEC (DMF): M_n = 57,960 g mol^{-1}; M_w = 68,470 g mol^{-1}; PDI = 1.18.

Deprotection of HO_2C-[PDMA-*r*-P*t*BA]-*b*-PS-TTC. HO_2C-[PDMA-*r*-PtBA]-*b*-PS-TTC (1 g) was dissolved in DCM (15 mL). An equal volume of trifluoroacetic acid (TFA) was added and the reaction stirred at rt for 24 h. The crude mixture was concentrated *in vacuo* then dissolved in DCM and precipitated three times into cold hexanes (250 mL). The off-white flocculate solid was filtered, and then dried *in vacuo*. ^{1}H NMR ($CDCl_3$): δ 8.37 (s, -CO_2H), 7.09–6.45 (m, Ar-*H*), 3.56–3.06 (m; N-(CH_3)$_2$, SCH_2- CTA), 2.63–2.12 (m, -C*H*- backbone), 1.74–1.25 (m; -CH_2- backbone, SC(CH_3)$_2$- CTA, -CH_2- CTA), 0.89 (-CH_3 CTA) ppm.

PREPARATION OF MESOPOROUS FILMS. 10 mg of either PDMA-*b*-PS or [PDMA-*r*-PAA]-*b*-PS was combined with an anhydrous mixture of 500 μL *N,N'*-dimethylformamide (DMF) and 350 μL ethanol (EtOH). After stirring for 1 hour at ambient temperature, 150 μL of 0.15 mM ligand-stripped CdSe nanocrystals in DMF was added and the mixture was maintained for 48 h. The ADA–NC dispersion was filtered through a 0.2 μm PVDF filter, and immediately spin-cast or drop-cast onto a 2x2 cm^2 Si wafer. Thermal annealing was performed into a quartz tube furnace under nitrogen or argon flow with an 8 h ramp from ambient to 350 ˚C, then held for 2 h before cooling to rt.

CATION EXCHANGE. Cation exchange was performed by soaking the film in a methanolic solution containing the new cation of interest: Tetrakis(acetonitrile)copper(I) hexafluorophosphate for Cu^+; silver nitrate for Ag^+; lead(II) acetate trihydrate for Pb^{2+}; cadmium nitrate tetrahydrate for Cd^{2+} reverse exchange. Cu^+ and Ag^+ were added in 2x molar excess to what was needed stoichiometrically for full exchange. Pb^{2+} and Cd^{2+} were added in 50x molar excess with trioctylphosphine in a 1:1 molar ratio to the exchanging cations to facilitate the reaction. Substrates were soaked overnight to ensure complete conversion, though the extended reaction time may not have been necessary.

ESTIMATION OF SPECIFIC SURFACE AREA. To estimate the specific surface area of the films, I noted the nanocrystal diameter of d = 3.8 nm and CdSe density of 5.82 g cm^{-3}. This gave an upper bound to the surface area of the films (neglecting nanocrystal sintering) of ~600 m^2 g^{-1}. With nanocrystal sintering (~2 Å), the specific surface area reduced to ~575 m^2 g^{-1}.

9.3. Results and Discussion

In developing the approach for generating metal chalcogenide architectures from colloidal NC building units, we were inspired by my own and other's reported developments for metal oxide architectures.[13,15−16] These reports collectively highlighted the importance of enthalpically-favored, yet dynamic adsorption of the ADA to the NC surface. Such interactions were possible by first removing the nanocrystal's aliphatic surface ligands, which yielded open metal coordination sites at their surface. Complementary functionality on the ADA's NC tethering domain was then key to direct the co-assembly in films without entropy-driven macrophase separation. For ligand-stripped metal oxide NCs, our use of poly(*N,N*-dimethylacrylamide) (PDMA) as a NC tethering domain was found to yield well-ordered architectures.[13] While this polymer was an attractive starting point to direct the arrangement of metal chalcogenide NCs, further enhancement of the adsorptive interactions was ultimately required to maintain order in the architectures constructed from these NCs. I overcome this challenge by synthesizing new ADAs specifically tailored for assembly of ligand-stripped metal chalcogenide NCs, thereby surpassing many of the limitations previously observed in generating porous non-oxide semiconductors using NCs as building blocks[6,17−20] or using sol−gel chemistry.[8,9,21] As a result, architectural uniformity can be leveraged to quantify any mesostructural changes that occur during thermally or chemically triggered transformations. Controlling uniformity simultaneously at the nano- and mesoscale should also, in future schemes, facilitate systematic understanding of the impact of specific architectural metrics on device function.

We found that doping the PDMA block in PDMA-*b*-PS with 10% acrylic acid to make [PDMA-*r*-PAA]-*b*-PS strengthened the ADA–NC interactions[22] while still retaining enough lability to avoid uncontrolled aggregation; polymer–NC co-assemblies were cast onto substrates from stable dispersions to form high-quality films. I synthesized these new [PDMA-*r*-PAA]-*b*-PS ADAs in an iterative manner using RAFT polymerization starting with the NC-tethering domain, followed by the porogenic domain (Scheme 9.1). Meanwhile, for the as-synthesized CdSe NCs, their surfaces were treated with Meerwein's salt (Et_3OBF_4) to remove the native ligands, thereby opening up coordination sites at the NC surface for binding to polymer side-chains.[12] Ordered mesoporous films were formed by mixing either ADA with ligand-stripped CdSe NCs, casting films, and thermally annealing to remove the ADA template, revealing the mesopores and linking the NCs to each other.

Tuning the ADA–NC surface interaction was critical to achieving ordered mesoporosity. This was apparent when comparing films prepared with two ADAs expected to have different strengths of coordination to the cationic adatoms at the NC surface: PDMA-*b*-PS (weaker, dative coordination expected) and [PDMA-*r*-PAA]-*b*-PS (combines dative with stronger, ionic coordination). Bright-field transmission electron microscopy (BF-TEM) of drop-cast ADA–NC dispersions and scanning electron microscopy (SEM) of the resulting mesoporous films qualitatively revealed the strength of the ADA–NC interactions and the mesostructural order, respectively (Figure 9.2). Only when [PDMA-*r*-PAA]-*b*-PS was employed as an ADA was it demonstrated that the polymer micelles were decorated by NCs and good order was yielded in the mesoporous frameworks remaining after template removal.

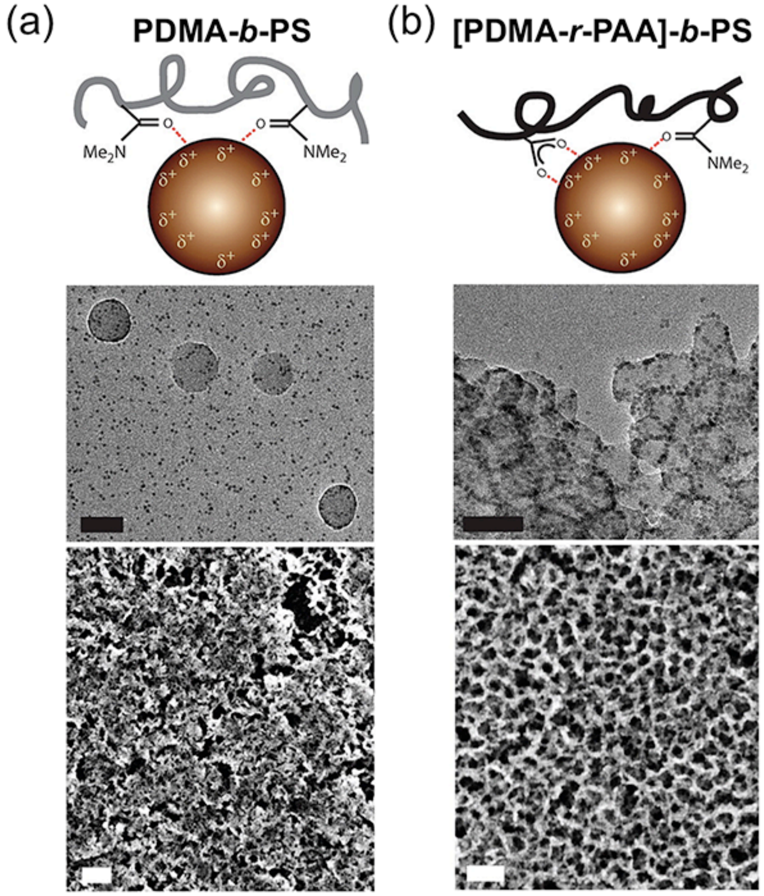

Figure 9.2. Top row: Schematics of sample polymers used in mesostructuring; Middle row: BF-TEM images of ADA–NC solutions (scale bar = 50 nm); Bottom row: SEM images (scale bar = 200 nm) indicating existence of ordered mesoporosity for (a) PDMA-*b*-PS or (b) [PDMA-*r*-PAA]-*b*-PS.

Directly after casting the ADA–NC dispersion, a high degree of order was observed in the ADA–NC films by electron microscopy (Figure 9.2) and GISAXS for either type of ADA (Figure 9.3). Here, six films were prepared–three for each type of ADA–and subjected to one of three annealing conditions: no annealing, a slow ramp (< 0.7 ˚C min^{-1}), or faster ramp (< 3 ˚C min^{-1}) to 350 ˚C under inert atmosphere. Only with very slow temperature ramp could order be largely preserved, and only in the case of [PDMA-*r*-PAA]-*b*-PS; this difference is ascribed to the stabilization of the structure by stronger coordination motif of carboxylates to the NC surfaces than those of datively-coordinated PDMA. Nonetheless, even when using [PDMA-*r*-PAA]-*b*-PS, more rapid annealing resulted in greater loss of order.

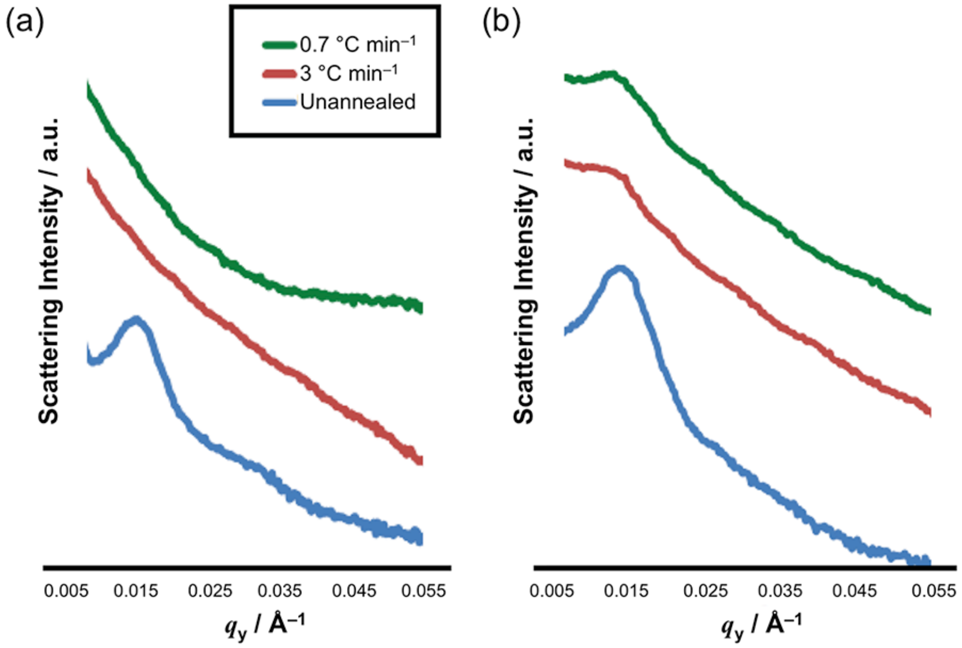

Figure 9.3. GISAXS data comparing annealing conditions for: (a) PDMA-*b*-PS; and (b) [PDMA-*r*-PAA]-*b*-PS templated films.

To better understand the mesostructure evolution during thermal annealing, we combined *in-situ* GISAXS, optical absorption spectroscopy, and TGA. By integrating background-subtracted first-order GISAXS peaks, the degree of order in the films could be rigorously tracked (Figures 9.4). Peaks at 0.013 Å^{-1} corresponded to a spacing of 48 nm, consistent with pore−pore distance observed by SEM. Early in the thermal ramp (Figure 9.4b, Stage I), increase in order was observed that may have be attributed to enhanced mobility of polymer chains. The degree of order plateaued in Stage II until > 300 ˚C when it decreased rapidly without disappearing; order was retained in the final porous film. In Stage I and II, temperature was ramped to 350 ˚C over 8 h. In Stage III, temperature was held at 350 ˚C for 2 h. The *x*-axis intercept with SAXS peak area indicated zero area, or no order.

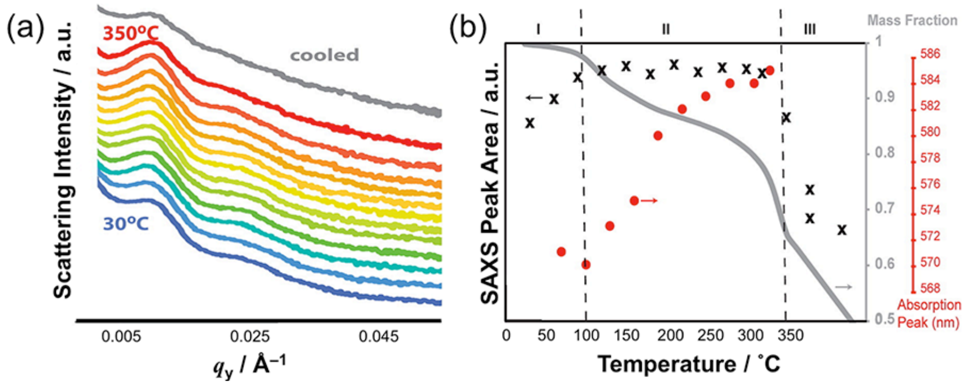

Figure 9.4. Evolution of film order as evolved during thermal annealing: (a) *In-situ* GISAXS data during thermal anneal with temperatures ranging incrementally from 30–350 ˚C. Traces are offset for clarity; (b) Evolution of mesoscopic order (indicated by black X, from data collected in (a)), polymer decomposition by TGA (gray line), and *ex-situ* optical data (red dots) indicative of NC–NC bonding and slight grain growth.

A loss of second-order scattering peaks was observed beyond 330 ˚C (Stage III, in which temperature is held for 2 h at 350 ˚C), further indicating a decline of regularity at high temperature. At this stage, a partial loss of order was correlated with the rapid thermal decomposition of polymer observed by TGA. Note that the TGA data indicated some remaining ADA polymer at 350 ˚C (Figure 9.5).

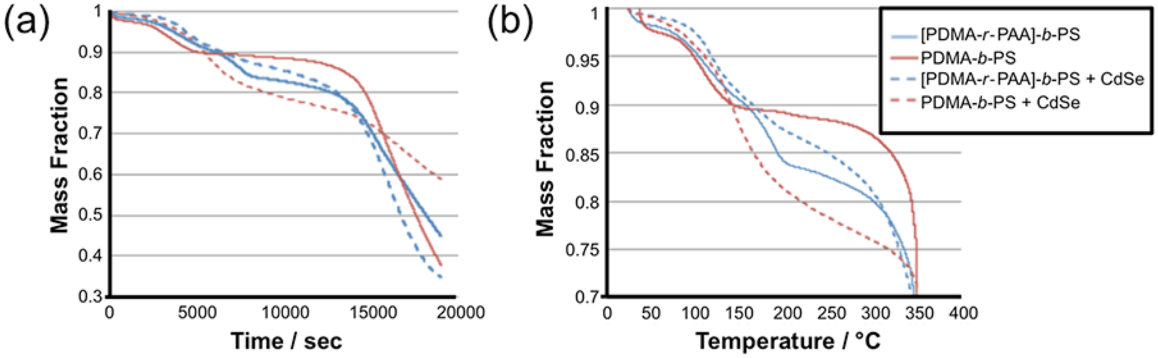

Figure 9.5. Thermogravimetric analysis (TGA) of assembled films composed of either PDMA-*b*-PS and [PDMA-*r*-PAA]-*b*-PS, without and with CdSe NCs. Time profile and temperature profile are shown in panel (a) and (b), respectively.

By increasing the temperature end point to 400 ˚C, at a ramp of 5 ˚C min^{-1}, it was still possible to decompose the polymer (Figure 9.6a), while retaining mesopore order (Figure 9.6b–d).

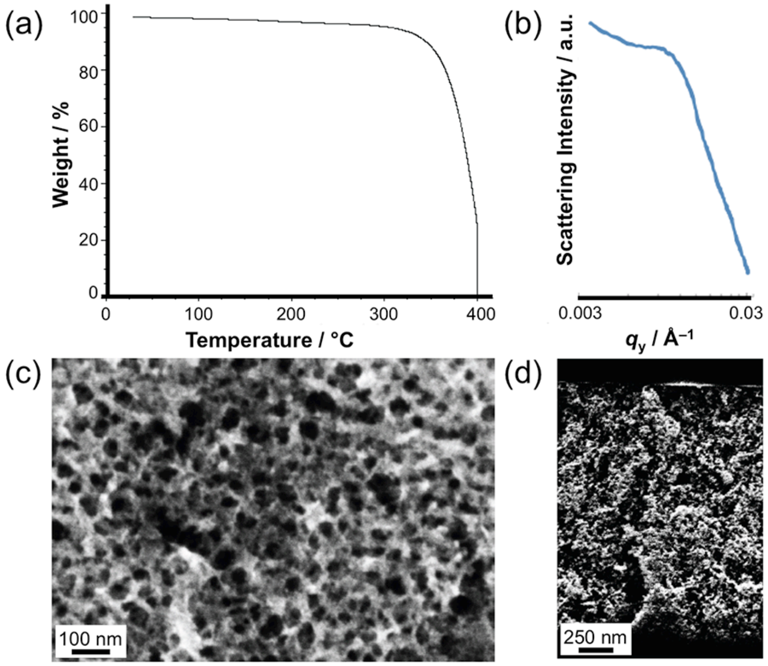

Figure 9.6. Characterization of [PDMA-*r*-PAA]-*b*-PS, annealed at 400 ˚C: (a) TGA results for a [PDMA-*r*-PAA]-*b*-PS film; (b) GISAXS scattering data for mesoporous film assembled from [PDMA-*r*-PAA]-*b*-PS and CdSe NCs; (c) top-down and (d) cross-section SEM images of same film.

It was striking that the films retain order during porogen removal, given the large volume fraction of ADA initially in the films (~70% porous as derived by Rutherford Backscattering; Figure 9.7) and the large pore diameters (~38 nm). RBS results from a simulated spectrum (Figure 9.7a), using SIMNRA software, showed the relative Cd:Se concentration to be Cd = 50 ± 0.1% and Se = 50 ± 0.1%, with a thickness of 35 x 10^{15} atoms cm^{-2}. Using a bulk density for CdSe of 5.82 g cm^{-3}, and a measured film thickness of 30 nm by SEM (Figure 9.7b), the film was ~30% CdSe and ~70% void space. The porosity and pore dimensions were similar to the averages observed in disordered porous networks formed from metal chalcogenide NCs,[6] and were well in excess of pore sizes achievable in mesoporous chalcogenides derived from sol−gel chemistry.[9,21]

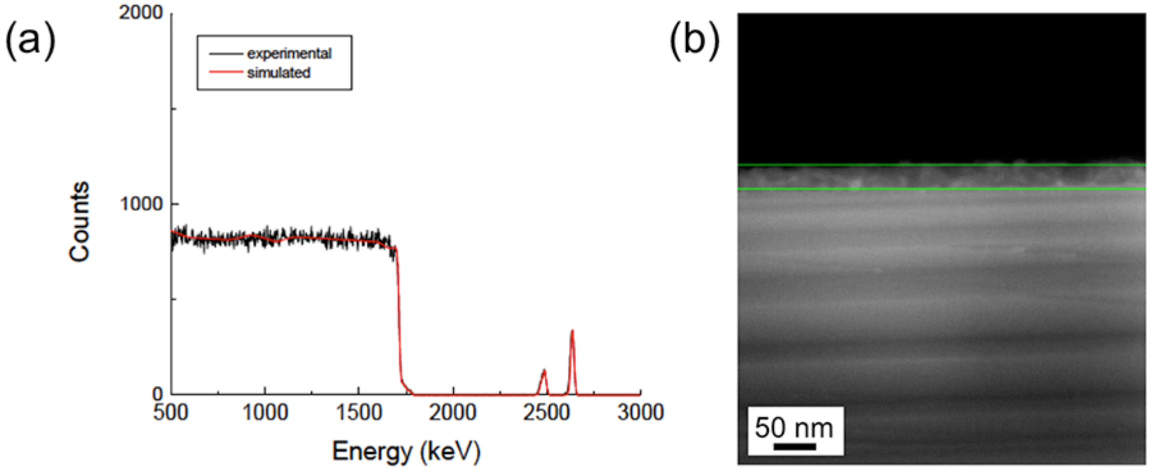

Figure 9.7. (a) Experimental (black trace) and simulated (red trace) RBS spectrum of mesoporous CdSe film; (b) SEM micrograph of cross-section of the same film.

The optical absorption of the NCs provided insight to understand how order was retained even while the ADA thermally depolymerizes: NCs form bonds to one another that preserve order when the ADA eventually decomposes. Starting at 100 ˚C (Stage II; Figure 9.4b), a redshift was observed in the first exciton absorption peak of the NCs, which increased as the thermal treatment proceeds, indicating coupling between NCs, or slight grain growth (i.e., a few Å). This suggested the formation of a covalently bonded NC network that preserved NC shape and size (as shown by XRD, Figure 9.8a) and quantum confinement (Figure 9.8b). This bonded network was likely the key to the architectural integrity observed during subsequent chemical transformations.

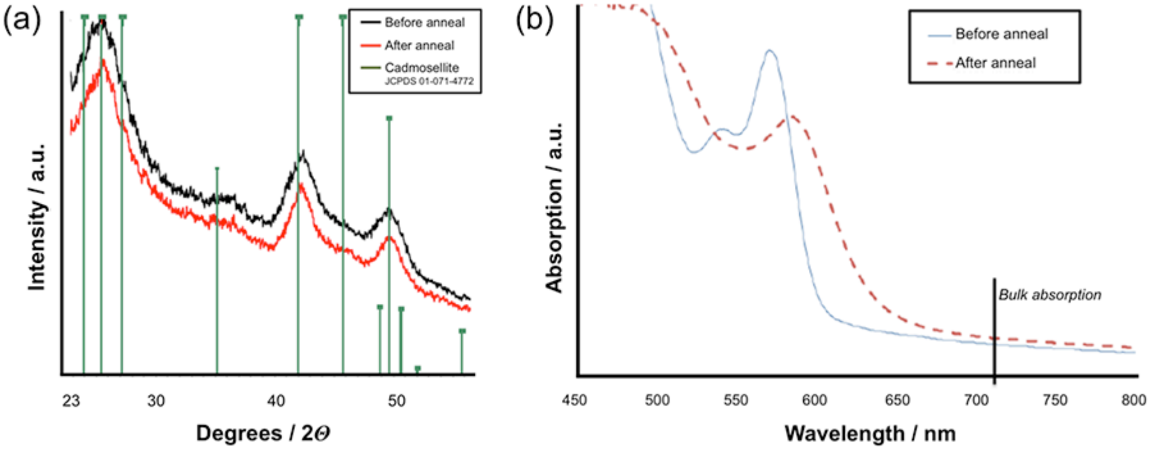

Figure 9.8. (a) XRD of mesoporous CdSe film before & after annealing; (b) optical absorption spectra of mesoporous CdSe nanocrystal film before and after annealing. Vertical line corresponds to bulk absorption peak of CdSe @ ~1.73 eV or ~715 nm.

The achievement of structurally robust, uniform mesoporosity enabled me to follow in detail the evolution of porous architectures during chemical transformations. One such transformation of relevance to this chemical system was cation exchange. In cation exchange, the composition of an ionic crystal is changed by place-exchanging the parent cation for a new cation, while leaving the anionic framework intact. This process has been shown to proceed rapidly and at room temperature in nanoscale systems.[17,19,23,24] Cation exchange was performed on my ordered CdSe mesoporous thin films to achieve compositions of PbSe, Cu_2Se, and Ag_2Se; additionally, a reverse-exchange was carried out on a Cu_2Se film, converting it back to CdSe. Stoichiometry was confirmed by EDS (Figure 9.9) and RBS (Figure 9.10), with results summarized in Table 9.1. Note that RBS data for Ag_2Se was omitted due to poor maintenance of film order upon exchange, which caused difficulty in obtaining the measurement.

Table 9.1. Summary of results by EDS and RBS for stoichiometry of cation-exchanged films.

	EDS		RBS	
PbSe	Pb: 47%	Se: 51%	Pb: 53 ± 2%	Se: 47 ± 2%
Cu_2Se	Cu: 62%	Se: 38%	Cu: 68.5 ± 2%	Se: 31.5 ± 2%
Ag_2Se	Ag: 63%	Se: 37%	n/a	n/a
$CdSe_{(reversed)}$	Cd: 50%	Se: 50%	Cd: 53 ± 2%	Se: 47 ± 2%

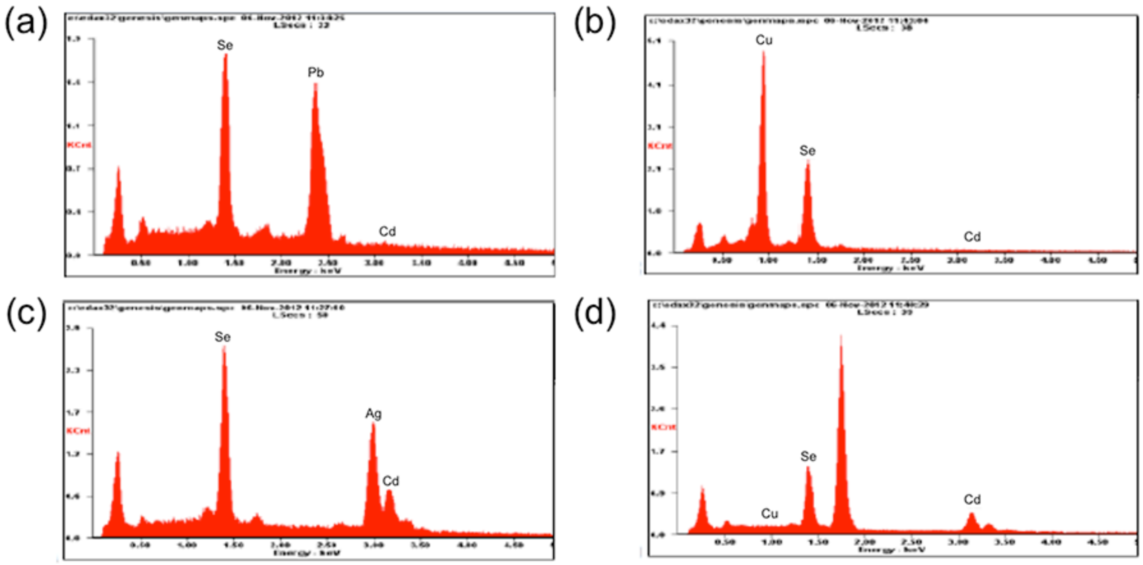

Figure 9.9. EDS spectra and results for exchanged films: (a) exchanged PbSe film from CdSe; (b) exchanged Cu_2Se film from CdSe; (c) exchanged Ag_2Se film from CdSe; (d) reverse-exchanged CdSe film from Cu_2Se

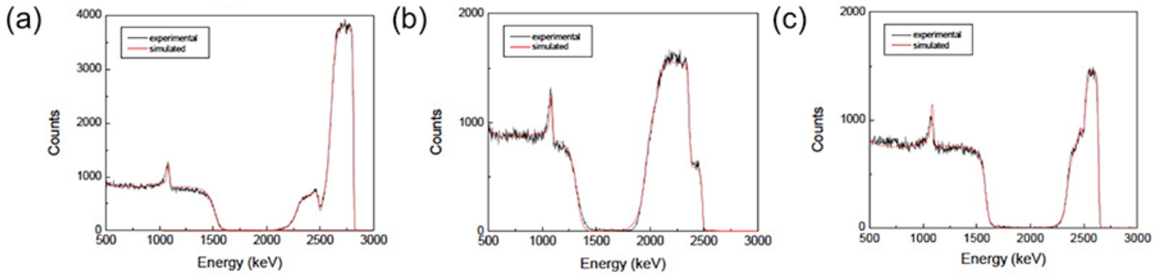

Figure 9.10. Experimental (black trace) and simulated (red trace) Rutherford backscattering spectrum for: (a) exchanged PbSe film from CdSe; (b) exchanged Cu_2Se film from CdSe; (c) reverse-exchanged CdSe film from Cu_2Se.

The new crystallographic phases formed from the parent CdSe NCs were verified by wide-angle XRD (Figure 9.11). Data are not sequential, but from a set of compositions generated from equivalent starting CdSe samples annealed at 350 ˚C for 2 h after an 8 h ramp. PbSe (green trace) and CdSe reversed (black trace) samples were obtained after first exchanging to from CdSe to Cu_2Se. Cu_2Se (red trace) and Ag_2Se (purple trace) films were reached directly from CdSe (gray trace). SEM confirmed qualitatively that the morphology of the porous films remained intact during this chemical transformation, while GISAXS showed that the mesoscale order was maintained throughout the film during cation exchange.

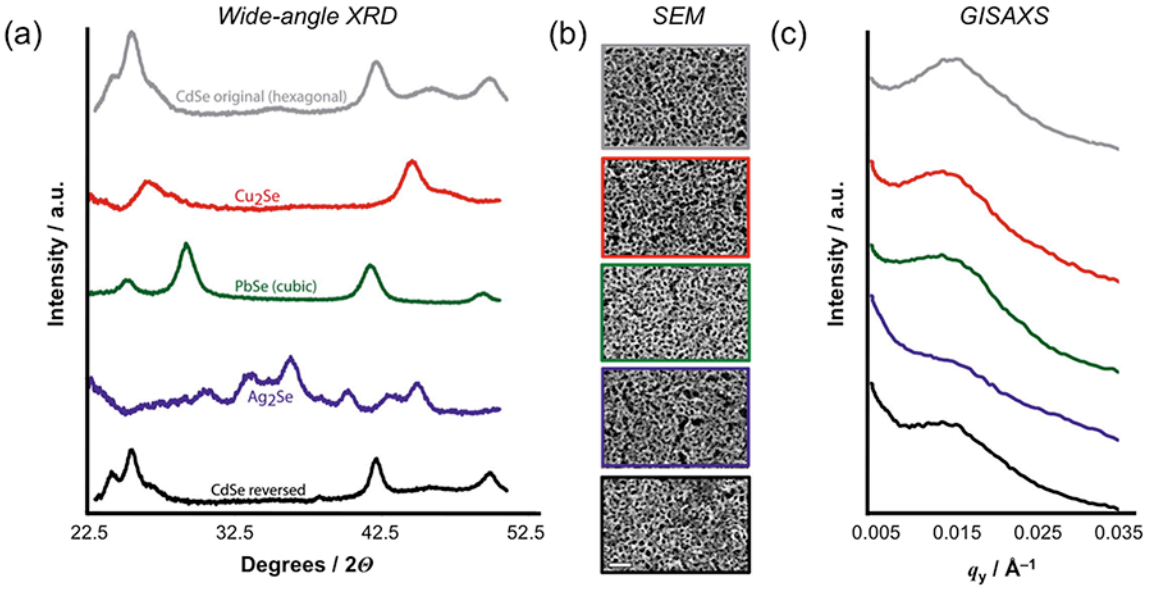

Figure 9.11. Cation exchange in CdSe mesoporous films. (a) Wide-angle XRD patterns for each film, confirming crystallographic identity of the new phase; (b) SEM images and (c) GISAXS scattering data showing that mesoscopic order was maintained post-exchange. Scale bar = 200 nm.

The Ag_2Se exchange was the most detrimental to the pore ordering, perhaps because of the very high mobility of Ag^+ ions that may have enabled crystallographic rearrangement or swelling of the structure. The frameworks were able to return to the original composition (CdSe) after first exchanging to Cu_2Se or Ag_2Se, demonstrating the reversibility of this transformation, while maintaining an ordered mesoporous architecture established by selection of the original CdSe NC and ADA building blocks.

9.4 Conclusions

I showed that the use of a PAA-doped PDMA-*b*-PS BCP, when assembled with ligand-stripped CdSe NCs, was able to preserve ordered mesoporosity throughout chemical transformation. This indicated a number of favorable properties of our original CdSe films. It demonstrated the interconnectivity of the pores, and the access they provided for solvent molecules and ions to interact with the semiconductor network. In this case, the pores remained connected through the entire ~1 μm film thickness. The preservation of order also demonstrated an architectural robustness that is promising for utility in various applications as it suggests electronic connectivity, ionic permeability, and mechanical integrity can be maintained through multiple processing and transformation stages. It may prove useful to perform a partial cation exchange to introduce additional hierarchical control, exchanging the outermost layer of the pore walls while maintaining the original composition within the wall, or creating a laterally graded composition by partial substrate submersion.

The preservation of order after cation exchange enabled us to access a range of new compositions. This obviated the need to identify individualized NC surface treatments and block copolymers capable of templating order in NCs of each new composition. Indeed, adequate surface chemistries for PbSe, Cu_2Se, and Ag_2Se, among others still need to be developed to expose reactive, positively charged, bare NC surfaces while also preserving NC dispersibility. Because of the loss of colloidal stability of many members of the chalcogenide family upon ligand removal,[12] cation exchange of hierarchically ordered mesoporous films was an especially important advance. In effect, I can leverage the synthetic control and understanding of CdSe surface chemistry to generate a far greater diversity of ordered mesoporous architectures. This new degree of control could facilitate a careful investigation of structure−composition−property relationships, which ultimately may fuel the optimization of mesoporous films for application in chemical sensing, nanoionics, and photocatalysis.

9.5 References

1. Reynolds, D.; Leies, G.; Antes, L.; Marburger, R. "Photovoltaic Effect in Cadmium Sulfide" *Phys. Rev*. **1954**, *96*, 533–534.
2. Goldsmid, H. J. *Thermoelectric Refrigeration*. Plenum: New York, 1964. Print
3. Lai, C.-H.; Huang, K.-W.; Cheng, J.-H.; Lee, C.-Y.; Hwang, B.-J.; Chen, L.-J. "Direct growth of high-rate capability and high capacity copper sulfide nanowire array cathodes for lithium-ion batteries" *J. Mater. Chem.* **2010**, *20*, 6638–6645.
4. Kibsgaard, J.; Chen, Z.; Reinecke, B. N.; Jaramillo, T. F. "Engineering the surface structure of MoS_2 to preferentially expose active edge sites for electrocatalysis" *Nat. Mater*. **2012**, *11*, 963–969.
5. Xu, J.; Zhang, W.; Yang, Z.; Ding, S.; Zeng, C.; Chen, L.; Wang, Q.; Yang, S. "Large-Scale Synthesis of Long Crystalline $Cu_{2-x}Se$ Nanowire Bundles by Water-Evaporation-Induced Self-Assembly and Their Application in Gas Sensing" *Adv. Funct. Mater.* **2009**, *19*, 1759–1766.
6. Mohanan, J. L.; Arachchige, I. U.; Brock, S. L. "Porous Semiconductor Chalcogenide Aerogels" *Science* **2005**, *307*, 397–400.
7. Yao, Q.; Brock, S. L. "Porous CdTe Nanocrystal Assemblies: Ligation Effects on the Gelation Process and the Properties of Resultant Aerogels" *Inorg. Chem.* **2011**, *50*, 9985–9992.
8. Gacoin, T.; Malier, L.; Boilot, J.-P. "New Transparent Chalcogenide Materials Using a Sol−Gel Process" *Chem. Mater.* **1997**, *9*, 1502–1504.
9. Fischereder, A.; Martinez-Ricci, M. L.; Wolosiuk, A.; Haas, W.; Hofer, F.; Trimmel, G.; Soler-Illia, G. J. A. A. "Mesoporous ZnS Thin Films Prepared by a Nanocasting Route" *Chem. Mater.* **2012**, *24*, 1837–1845.
10. Ilavsky, J. "Nika: software for two-dimensional data reduction" *J. Appl. Cryst.* **2012**, *45*, 324–328.
11. Chan, E. M.; Xu, C.; Mao, A. W.; Han, G.; Owen, J. S.; Cohen, B. E.; Milliron, D. J. "Reproducible, High-Throughput Synthesis of Colloidal Nanocrystals for Optimization in Multidimensional Parameter Space" *Nano Lett.* **2010**, *10*, 1874–1885.
12. Rosen, E. L.; Buonsanti, R.; Llordes, A.; Sawvel, A. M.; Milliron, D. J.; Helms, B. A. "Exceptionally Mild Reactive Stripping of Native Ligands from Nanocrystal Surfaces by Using Meerwein's Salt" *Angew. Chem. Int. Ed.* **2012**, *51*, 684–689.
13. Buonsanti, R.; Pick, T. E.; Krins, N.; Richardson, T. J.; Helms, B. A.; Milliron, D. J. "Assembly of Ligand-Stripped Nanocrystals into Precisely Controlled Mesoporous Architectures" *Nano Lett*. **2012**, *12*, 3872–3877.
14. Lai, J. T.; Filla, D.; Shea, R. "Functional Polymers from Novel Carboxyl-Terminated Trithiocarbonates as Highly Efficient RAFT Agents" *Macromolecules* **2002**, *35*, 6754–6756.
15. Ortel, E.; Fischer, A.; Chuenchom, L.; Polte, J.; Emmerling, F.; Smarsly, B.; Kraehnert, R. "New triblock copolymer templates, PEO-PB-PEO, for the synthesis of titania films with controlled mesopore size, wall thickness, and bimodal porosity" *Small* **2011**, *8*, 298–309.

16. Quickel, T. E.; Le, V. H.; Brezesinski, T.; Tolbert, S. H. "On the Correlation between Nanoscale Structure and Magnetic Properties in Ordered Mesoporous Cobalt Ferrite ($CoFe_2O_4$) Thin Films" *Nano Lett.* **2010**, *10*, 2982–2988.
17. Lubeck, C. R.; Han, T. Y. J.; Gash, A. E.; Satcher, J. H.; Doyle, F. M. "Synthesis of Mesostructured Copper Sulfide by Cation Exchange and Liquid-Crystal Templating" *Adv. Mater.* **2006**, *18*, 781–784.
18. Bag, S.; Arachchige, I. U.; Kanatzidis, M. G. "Aerogels from metal chalcogenides and their emerging unique properties" *J. Mater. Chem*. **2008**, *18*, 3628–3632.
19. Yao, Q.; Arachchige, I. U.; Brock, S. L. "Expanding the Repertoire of Chalcogenide Nanocrystal Networks: Ag_2Se Gels and Aerogels by Cation Exchange Reactions" *J. Am. Chem. Soc.* **2009**, *131*, 2800–2801.
20. Rauda, I. E.; Saldarriaga-Lopez, L. C.; Helms, B. A.; Schelhas, L. T.; Membreno, D.; Milliron, D. J.; Tolbert, S. H. "Nanoporous Semiconductors Synthesized Through Polymer Templating of Ligand-Stripped CdSe Nanocrystals" *Adv. Mater.* **2013**, *25*, 1315–1322.
21. Braun, P. V.; Osenar, P.; Tohver, V.; Kennedy, S. B.; Stupp, S. I. "Nanostructure Templating in Inorganic Solids with Organic Lyotropic Liquid Crystals" *J. Am. Chem. Soc.* **1999**, *121*, 7302–7309.
22. Duong, J. T.; Bailey, M. J.; Pick, T. E.; McBride, P. M.; Rosen, E. L.; Buonsanti, R.; Milliron, D. J.; Helms, B. A. "Efficient polymer passivation of ligand-stripped nanocrystal surfaces" *J. Polym. Sci. Part A: Polym. Chem.* **2012**, *50*, 3719–3727.
23. Dloczik, L.; Koenenkamp, R. "Nanostructured metal sulfide surfaces by ion exchange processes" *J. Solid State Electrochem*. **2004**, *8*, 142–146.
24. Rivest, J. B.; Jain, P. K. "Cation exchange on the nanoscale: an emerging technique for new material synthesis, device fabrication, and chemical sensing" *Chem. Soc. Rev*. **2013**, *42*, 89–96.

Chapter 10

NIR-selective electrochromic heteromaterial frameworks: a platform to understand mesoscale transport phenomena in solid-state electrochemical devices

Adapted from:

Teresa E. Williams, Christina M. Chang, Evelyn L. Rosen, Guillermo Garcia, Evan L. Runnerstrom, Bradley L. Williams, Bonil Koo, Raffaella Buonsanti, Delia J. Milliron, and Brett A. Helms. "Near IR-selective electrochromic heteromaterial frameworks: a platform to understand mesoscale transport phenomena in solid-state electrochemical devices" *Journal of Materials Chemistry C* **2014**, *2*, 3328−3335.

10.1 Introduction

Near-infrared (NIR)-selective electrochromic devices are an emerging class of smart window technologies[1–3] seeking to improve building energy efficiency by more effectively managing solar heat gain in commercial and residential spaces.[4] The active layer in these devices is a conductive film of doped metal oxide nanocrystals[5–8] (NCs) – e.g., Sn-doped In_2O_3 (ITO),[9] Al-doped ZnO (AZO),[10] or Sb-doped SnO_2 (ATO)[11,12] – or a nanocrystal-in-glass composite.[13,14] Switching from a NIR-blocking state to a NIR-transmissive state is achieved by electrochemically modulating the nanocrystals' state of charge (i.e., carrier concentration), which in turn predictably tunes their plasmon absorption band in the NIR. As described previously,[1,2] the charging mechanism in these electrodes is capacitive; injection of electrons into the conduction band of the nanocrystals is compensated by delivery of cations from the supporting electrolyte to the NC–electrolyte interface. This capacitive switching mechanism was shown to operate effectively in a liquid electrolyte, with transparent NC films having a dynamic transmission range of more than 40 % of solar NIR.[2] Nonetheless, the active material utilization in ITO NC electrodes realized in prior work has been restricted either by poor electrolyte penetration into the microporous NC films or due to charging inefficiencies of the network,[2] which limits the dynamic range of the electrochromic device. Furthermore, these plasmonic electrochromic electrodes have yet to be incorporated into layered, solid-state devices suitable for smart window applications. To realize the same capacitive switching mechanism in a solid-state device, the integration of the NC electrode with a solid electrolyte is paramount and the resulting multiphasic electrodes must facilitate the transport of ions and electrons to the heteromaterial interface. These fundamental transport processes are deterministic in switching speeds and overall coloration efficiency, and thus energy savings potential of a possible dynamic window technology.

Here, I investigate heteromaterial frameworks as a new concept to better understand and ultimately control the charge transport processes necessary to switch NIR-selective electrochromic devices. These heteromaterial frameworks feature separate mesoscale domains for ion and electron transport, reciprocally arranged in space with tunable periodic architectures (Figure 10.1).

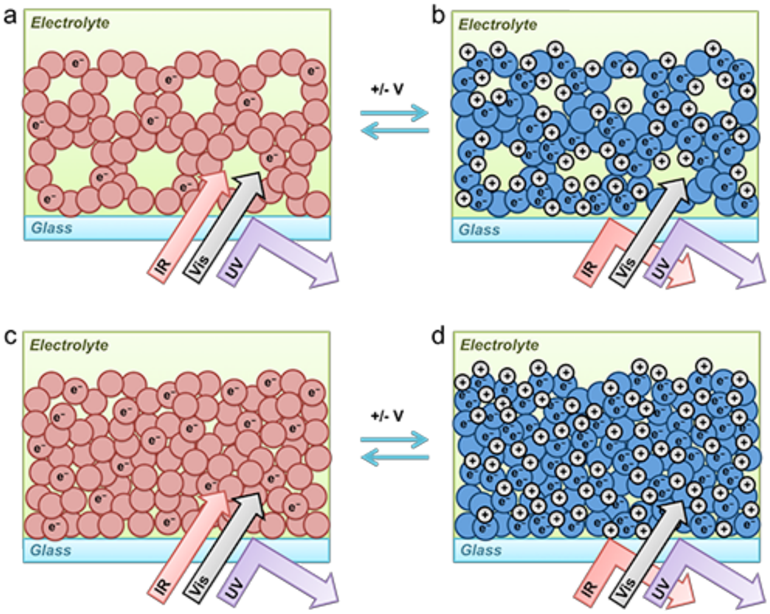

Figure 10.1. NIR-selective electrochromic films based on ligand-stripped ITO nanocrystals arranged in space with hierarchically ordered (a,b), meso- and microporosity; or (c,d) random microporosity Devices are switched by reversing the voltage bias.

First, I generate electronically conductive and NIR-switchable mesoporous ITO frameworks by block copolymer directed assembly[15–19] of ITO nanocrystals stripped of their native organic ligands.[20,21] Through careful selection of the block copolymer architecture-directing agent (ADA), here, poly(*N*,*N*-dimethylacrylamide)-*block*-polystyrene (PDMA-*b*-PS) I show the arrangement of ITO nanocrystals into precise mesoporous architectures with controllable topologies and definable metrics is possible for both pore dimension and wall thickness.[15,19] Next, voids within the ITO framework are subsequently filled with a plasticized polymer electrolyte (PPE), which functions in the device as the ionically conductive framework. Solid-state devices can then be configured using a transparent CeO_2 nanocrystal-based counter electrode[22–24] (Fig. 10.2).

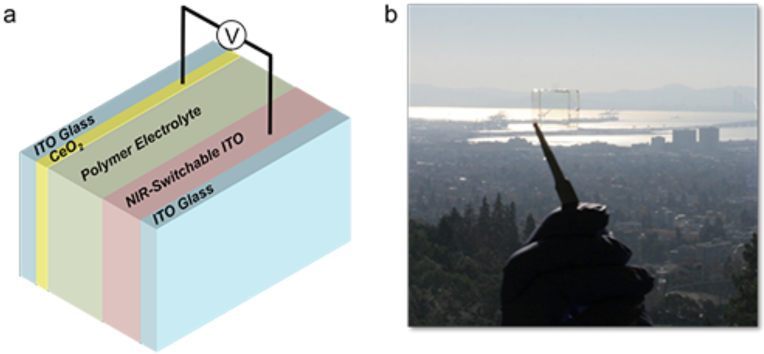

Figure 10.2. Schematic (a) and realization (b) of a solid-state NIR-selective electrochromic device. The Kapton tape spacer has been removed from the device in (b) for clarity.

To understand the relationship between mesoscale structure and the performance of the NIR-selective electrochromic heteromaterial frameworks in solid-state devices, mesoporous ITO frameworks are first studied alongside randomly packed nanocrystal films in half cells using spectroelectrochemical methods in the presence of propylene carbonate–$LiClO_4$ as the supporting electrolyte. We show that electroreversible charging of the active layer proceeds with over two-fold higher specific capacity for the mesoporous ITO frameworks when compared to unarchitectured films, indicating improved active material utilization; enhanced charging kinetics were also demonstrated. We then construct full, solid-state electrochromic devices, infiltrating the porous ITO frameworks with a PPE to create mixed ionic and electronic conducting heteromaterial frameworks. Favorable characteristics of the porous frameworks translate to performance advantages in solid-state devices. The gains in device performance achieved by my NIR-electrochromic heteromaterial frameworks is traced to the mesoscopic ordering of domains responsible for charge transport, which overcomes framework charging inefficiencies associated with overlapping electrical double layers (EDLs) in strictly microporous, unarchitectured nanocrystal films. As such, they are well poised to address practical limitations that might make these devices otherwise difficult to deploy in the marketplace.

10.2 Experimental

MATERIALS. $NOBF_4$ (95%), poly(vinyl butyral) (PVB, M_n ~500–800 kDa), trimethylolpropane propoxylate (PO/OH, M_n ~308 kDa), 1-butanol (BuOH, anhydrous), ethanol (EtOH, anhydrous, ≥ 99.5%), and *N,N*-dimethylformamide (DMF, anhydrous, 98.8%) were purchased from Sigma-Aldrich and used without further purification. Bis(trifluoromethane)sulfonamide, lithium salt (LiTFSI) was purchased from 3M. ITO-coated glass substrates were purchased from Diamond Coatings Limited (20mm x 20mm x 1.1mm, 200 Ω per sq sheet resistance) and were cleaned *via* sonication in a three step process: 15 min deionized water with 2% Hellmanex cleansing solution, 15 min in acetone, followed by 15 min in isopropanol. Three rinses were performed between each sonication step; substrates were then subjected to UV–ozone treatment for 20 min.

NANOCRYSTAL SYNTHESIS AND LIGAND STRIPPING. I synthesized tin-doped indium oxide (ITO) nanocrystals (NCs) according to a previously reported procedure;[25] samples ranged from 17–22 wt% Sn (ICP-OES). I stripped ITO NCs of their organic coordinating surface ligands using $NOBF_4$ and re-dispersed them in DMF prior to use.[20] I determined final NC concentration in DMF was 22 mg mL^{-1} TGA). I used ImageJ software to determine the distribution of nanocrystal size from BF-TEM images (Figure 10.3)

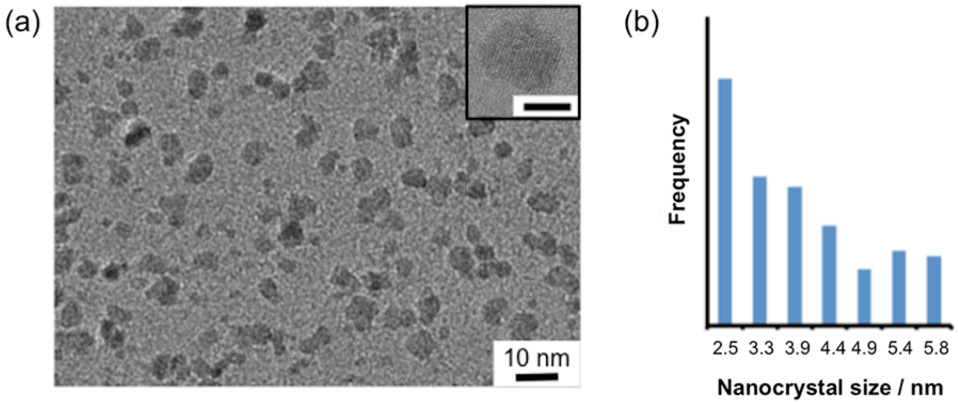

Figure 10.3. Analysis of ligand-stripped ITO nanocrystals: (a) Bright-field TEM image (inset scale bar = 4 nm); (b) histogram for size distribution (n = 539; d = 4.0 nm ± 3.1 nm).

CeO_2 NCs were synthesized using a recently reported method, except that 1-octadecene was eliminated as a solvent[26] and were used as synthesized at a concentration of 57 mg mL^{-1}. ImageJ software was used to determine the distribution of nanocrystal size from BF-TEM images (Figure 10.4).

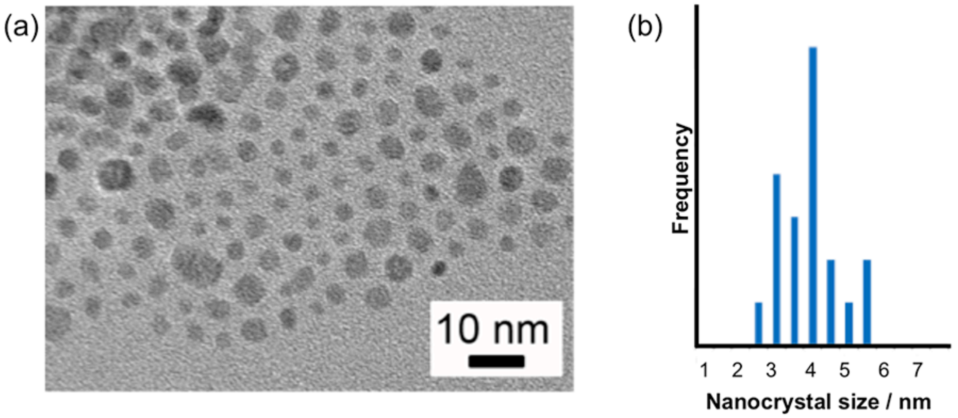

Figure 10.4. Analysis of as-synthesized CeO_2 nanocrystals: (a) Bright-field TEM image; (b) histogram for size-distribution analysis (n = 50; d = 3.6 nm ± 0.8 nm).

PDMA-*b*-PS BLOCK COPOLYMER MICELLES. I prepared PDMA-*b*-PS copolymers as described previously;[15] architecture-directing agents with different overall molecular weights and block ratios were prepared: $PDMA_{20k}$-*b*-PS_{20k}, $PDMA_{10k}$-*b*-PS_{60k}, $PDMA_{20k}$-*b*-PS_{60k}. To assemble the micelles, I first dissolved PDMA-*b*-PS in DMF, and EtOH was added drop-wise to make a 15 mg mL^{-1} BCP solution in 8:2 *v/v* EtOH/DMF. The dispersion stirred for 18 h at ambient temperature.

PREPARATION OF NANOCRYSTAL-BASED ELECTRODES. I prepared the BCP–NC assemblies by adding ligand-stripped ITO NCs to a dispersion of BCP micelles and stirred for 18 h. I used spin coating to generate thin films for both architectured and unarchitectured ITO NC films, as well as CeO_2 NC-based counter electrodes; multilayer deposition was used to increase the film thickness. I thermally annealed both architectured and unarchitectured ITO NC films in air using a 2 h ramp to 550 ˚C, followed by a 1.5 h hold at that temperature before cooling to rt. This process led to full removal of the BCP template and residual organic dispersants.[15] I used cross-sectional SEM was used to determine film thickness for ITO NC-based films using ImageJ software. Average film thicknesses for ITO NC films were: 258 ± 8 nm (unarchitectured, Figure 10.5a); 309 ± 10 nm (derived from $PDMA_{20k}$-*b*-PS_{20k}; Figure 10.5b), 342 ± 32 nm (derived from $PDMA_{10k}$-*b*-PS_{60k}; Figure 10.5c), and 289 ± 64 nm (derived from $PDMA_{20k}$-*b*-PS_{60k}; Figure 10.5d).

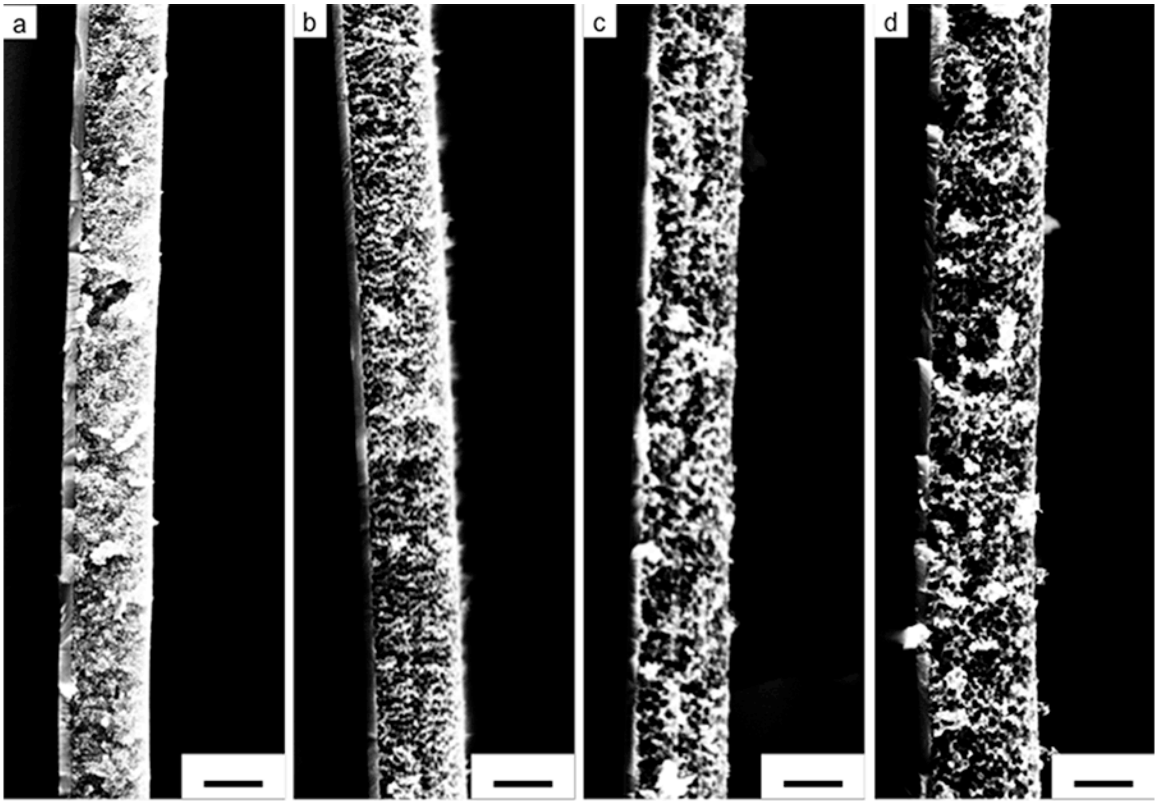

Figure 10.5. Cross-sectional scanning electron microscopy images of ITO nanocrystal films: (a) unarchitectured film; hierarchically porous frameworks assembled using (b) $PDMA_{20k}$-*b*-PS_{20k}, (c) $PDMA_{10k}$-*b*-PS_{60k}, or (d) $PDMA_{10k}$-*b*-PS_{60k} block copolymer as architecture-directing agents. Scale bar = 200 nm.

I prepared CeO_2 NC counter electrodes by spin coating a 1:1 hexane/octane solution of NCs onto a prepared glass substrate, followed by soaking for 5 min in 100 mM solution of formic acid in acetonitrile (ACN) to exchange the native ligands on the NC surface with formate.[1] The film was rinsed three times with 1:1 ACN/chloroform, then annealed in air for 5 min at 320 ˚C. Multilayer deposition was used to increase film thickness. CeO_2 film thickness was ~200 nm after three rounds of NC deposition, ligand exchange, and thermal annealing.

ELECTROCHEMICAL METHODS. For analysis of NIR-switchable ITO films in half-cells, a three electrode configuration was used with ITO-coated substrate as working electrode, lithium metal counter electrode, and lithium metal reference electrode in anhydrous propylene carbonate containing $LiClO_4$ (100 mM). The films were driven at a potential range of 1.8 V to 4 V *vs.* Li/Li^+. In situ optical spectra were taken of the films at various potentials. Coloration efficiency was calculated by taking the ratio of the change in optical density between the positive and negative bias with its associated charge per unit area. Film cycling was performed using cyclic voltammetry (CV) at different scan rates (100, 10, and 1 mV s^{-1}). Chronoamperometry was used to determine the charge capacity with voltage steps of 1.8 or 4.0 V vs. Li/Li^+.

PREPARATION OF SOLID-STATE ELECTROCHROMIC DEVICES. A plasticized polymer electrolyte[27–29] (PPE) stock solution was prepared by dissolving PVB (10.03 g), PO/OH (12.13 g), and LiTFSI (1.97 g) in BuOH (35.35 g). The solution was stirred in a glove box until homogeneous. The ionic conductivity of the PPE was determined by electrochemical impedance spectroscopy (EIS) (Figure 10.6a). The PPE's electrochemical stability window (–1.8 V to +1.8 V) was determined by CV (Figure 10.6b) using a two electrode configuration involving a 50 mm thick PPE film sandwiched between two ITO-coated glass substrates as working and counter electrodes operating over a voltage range of –2 V to +2 V. Solid-state devices were prepared using an ITO NC electrode as the positive electrode and a CeO_2 NC electrode as the negative electrode, which were separated by the PVB-based PPE. A thin layer of Kapton tape was used during device assembly to define the final thickness of the PPE (50 mm). PPE stock solution (300 mL) was deposited directly onto both NC films, and spread gently over the active layer using a plastic applicator. Substrates were then placed on a hot plate and heated at 80 ˚C for 30 min to liberate any volatile organics. One NIR-selective electrochromic ITO electrode and one CeO_2 counter electrode, each coated with the PPE, were then pressed together offset by ~0.5 cm to facilitate electrical contact, leaving an active device area of 2.25 cm^2. The sandwiched device was then laminated using a hot press (40 psi, 80 ˚C, 10 min per side). The device was then tested under ambient conditions.

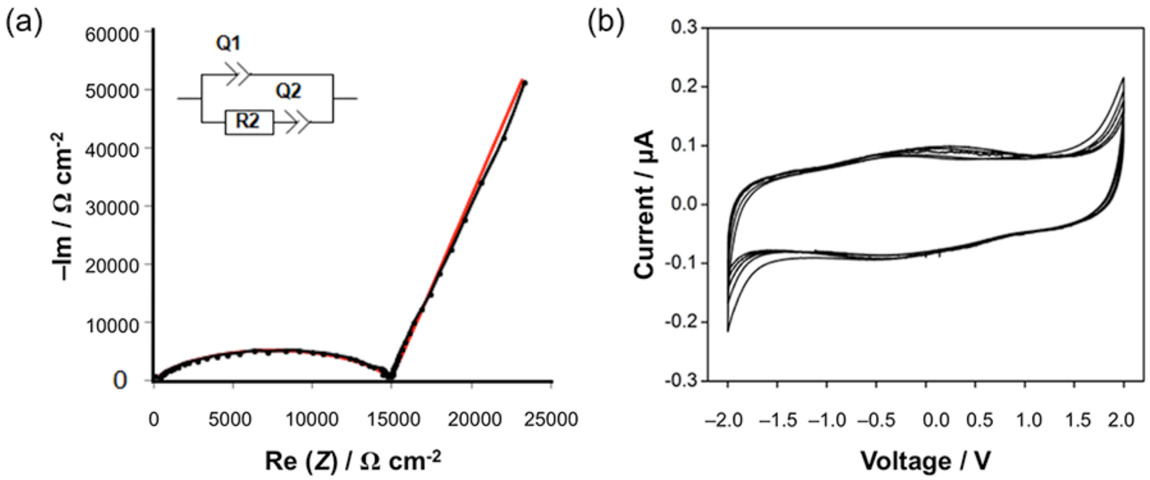

Figure 10.6. Electrochemical characterization of plasticized polymer electrolyte (PPE): (a) Nyquist plot derived from electrochemical impedance spectroscopy for PPE (black trace and data points) and fit (red trace) calculated using the equivalent circuit model shown (inset). Q_1 and Q_2 are constant phase elements, and R_2 is a resistor. To provide a direct comparison to the PPE films used for devices, a dried film of PPE was pressed between two ITO-coated substrates, which functioned as the working and counter electrodes using a two-electrode configuration. A 50 µm spacer defined the electrolyte thickness. Electrochemical impedance spectroscopy was obtained in the frequency range of 1 MHz to 1 Hz with 10 frequency points per logarithmic decade and an oscillation voltage of 10 mV. The Nyquist plot was used to determine the room-temperature ionic conductivity for the PPE, $\sigma = 1.1 \times 10^{-7}$ S cm^{-1}. (b) Cyclic voltammetry for the same PPE film as in Figure 10.4b at 10 mV s^{-1} scan rate in the potential range of –2 to +2 V. The first of 5 cycles has been omitted. The potential stability window for the PPE was taken to be –1.8 to +1.8 V.

ELECTROCHEMICAL EVALUATION OF SOLID-STATE ELECTROCHROMIC DEVICES. A constant potential of –4 V was applied for 6 min to generate charge in the device *via* electrochemical oxidation of the PPE at the CeO_2 negative electrode, most likely at its terminal hydroxyl groups (i.e., proton-coupled electron transfer). As such, no solid-electrolyte interphase is expected. After this “break-in” cycle, the device could be operated and optical switching evaluated in a potential range spanning –1.8 V to +1.8 V. Chronoamperometry was obtained between the potential limits of –1.8 V and +1.8 V for 10 cycles to determine the specific charge capacity. CV was also performed at different scan rates (100, 10, and 1 mV s^{-1}) to obtain the charging capacity per gram of ITO NCs.

10.3 Results and Discussion

Electrochromic devices based on ITO nanocrystal active layers leveraged the ITO's electrochemically tunable plasmonic properties to switch between NIR-transmissive and NIR-blocking states. The intrinsic plasmonic properties of individual ITO nanocrystals were influenced by a number of factors, including Sn-dopant concentration and distribution, NC size, and its local dielectric environment. These dependencies have been delineated in detail from both experimental and theoretical perspectives in previous work.[1,2,6,7] It has also previously been shown that conductive films of ligand-stripped ITO nanocrystals can be switched between NIR-blocking and NIR-transmissive states in electrochemical half-cells using liquid electrolytes.[1,2] For half-cell configurations, it was demonstrated that the charging in the ITO electrodes is pseudocapacitive. Injection of electrons into the ITO conduction band is concomitant with the build up of cationic charge at the ITO–electrolyte interface, as necessary for charge balance, and an EDL. As a result, the extent of capacitive charging of the ITO NC active layers, and the charging kinetics, can be expected to depend on the spatial arrangement of ion- and electron-conducting domains in the working electrode, the relative length scales of those domains, and the topology of their interfaces.

In this work, conductive films of ITO nanocrystals were readily obtained by casting 'bare' nanocrystal inks[20,21] (i.e., colloidal ITO nanocrystals, chemically stripped of their coordinating organic ligands) onto ITO-coated glass substrates. After thermal treatment to ensure dispersant removal, the resulting microporous ITO NC frameworks were homogeneous over large areas (Figure 10.7a,b). Alongside these unarchitectured (i.e., randomly close-packed) ITO films, I generated conductive mesoporous ITO architectures using block copolymers to direct the assembly of naked ITO NCs. This additional processing step allowed me to arrange the ITO nanocrystals into periodic, well-controlled 3-D architectures at the electrode surface, thereby defining to a high degree of precision the structure of the electrode on length scales relevant for interfacing the ITO framework with the supporting electrolyte. Three poly(*N,N*-dimethylacrylamide)-*block*-polystyrene (PDMA-*b*-PS) block copolymer architecture directing agents (ADAs) were synthesized and employed to assemble different ITO frameworks: PDMA_{20k}-*b*-PS_{20k} (Figure 10.7c,d), PDMA_{10k}-*b*-PS_{60k} (Figure 10.7e,f), and PDMA_{20k}-*b*-PS_{60k} (Figure 10.7g,h). Mesoporous ITO frameworks generated using this process had ~60% pore volume, as determined by RBS analysis.

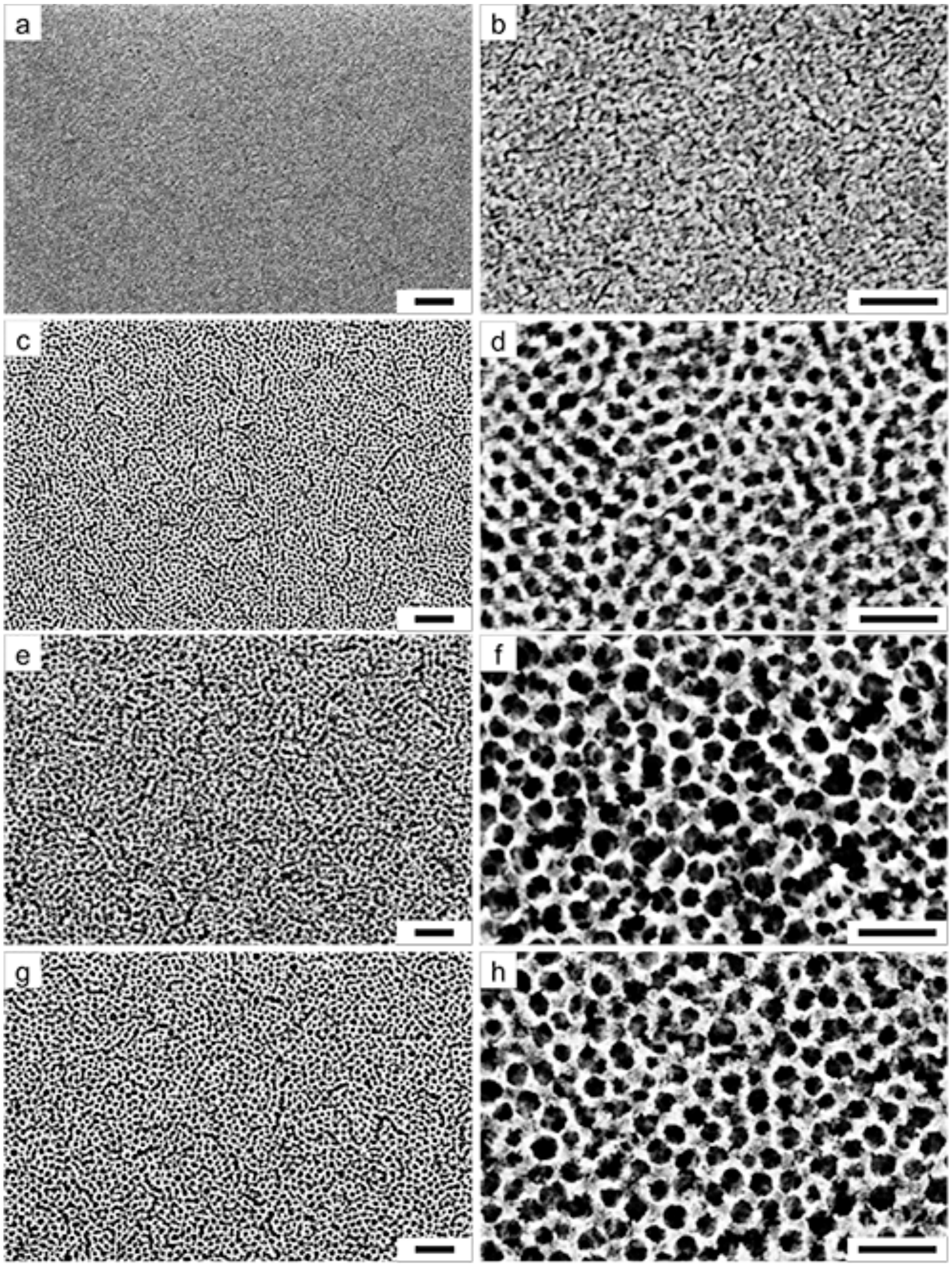

Figure 10.7. SEM of NIR-selective electrochromic ITO NC films: (a,b) randomly packed films at ~34% overall microporosity; (c,d) frameworks assembled with $\mathrm{PDMA_{20k}}$-*b*-$\mathrm{PS_{20k}}$; (e,f) $\mathrm{PDMA_{10k}}$-*b*-$\mathrm{PS_{60k}}$; (g,h) or $\mathrm{PDMA_{20k}}$-*b*-$\mathrm{PS_{60k}}$ exhibited ~60% overall porosity. Scale bar = 100 nm.

As seen in the SEM (Figure 10.7) and GISAXS (Figure 10.8), I showed the meso ITO frameworks were tunable with respect to the periodicity of the ITO framework's porosity, as well as the average thickness of its walls and pore dimensions (Table 10.1). Using the range of block copolymers I synthesized, the critical dimensions of the mesoporous ITO NC architectures could be tuned; the periodicity ranged 32 to 48 nm, and pore size from

29 to 37 nm. Independent tuning of the PDMA and PS microdomain molecular weights translated to nearly independent control over wall thickness (from 9 to 13 nm) and pore size, respectively. The regularity with which these ITO frameworks were configured in all dimensions allowed for the first systematic investigation of how different ITO architectures influenced the performance characteristics of NIR-selective electrochromic devices.

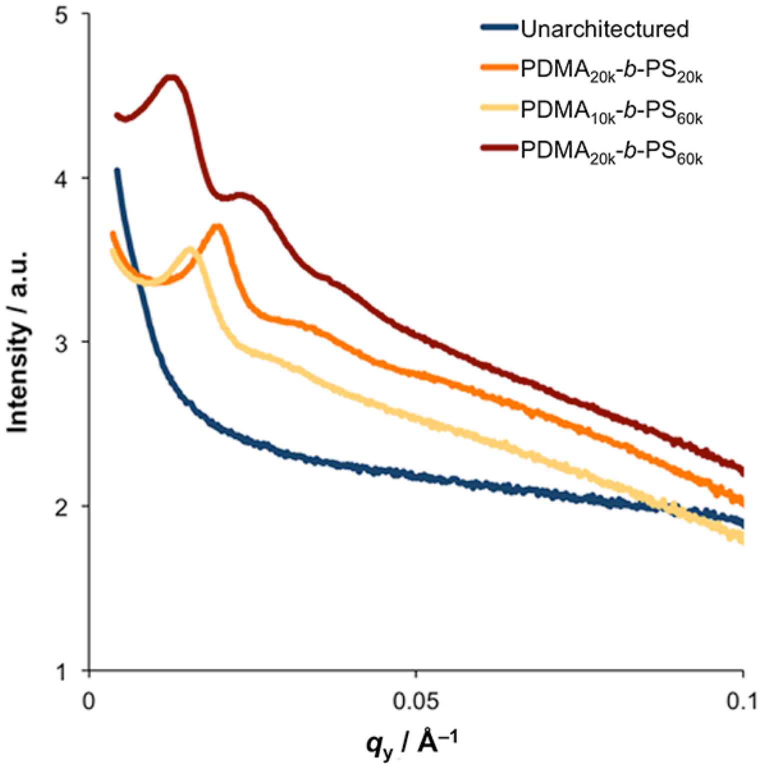

Figure 10.8. GISAXS line profiles along the in-plane scattering axis for unarchitectured and architectured ITO NC films.

Table 10.1. Periodicity, pore size, and wall thickness for mesoporous ITO NC frameworks.

ITO architecture-directing agent	**ITO framework periodicity[a] (nm)**	**ITO framework pore size[b] (nm)**	**ITO framework wall thickness[b] (nm)**
PDMA$_{20k}$-*b*-PS$_{20k}$	32	29 ± 7	12 ± 2
PDMA$_{10k}$-*b*-PS$_{60k}$	40	35 ± 7	9 ± 2
PDMA$_{20k}$-*b*-PS$_{60k}$	48	37 ± 6	13 ± 3

[a] Determined by GISAXS from in-plane scattering data. [b] Determined by ImageJ analysis of SEM images.

To understand the effect of mesostructuring ITO on electrode performance, the porous electrodes were first interrogated in electrochemical half-cells using propylene carbonate-$LiClO_4$ as a supporting electrolyte. Separate lithium reference and counter electrodes were used for all spectroelectrochemical measurements. As a control, unarchitectured films of the same thickness were compared alongside those that were mesoarchitectured using the block copolymers. Upon capacitive charging of the ITO frameworks, step-wise over a potential range of 4 V to 1.8 V relative to Li/Li^+, the plasmon absorbance was readily tunable in all films (Figure 10.9). This process was electroreversible.

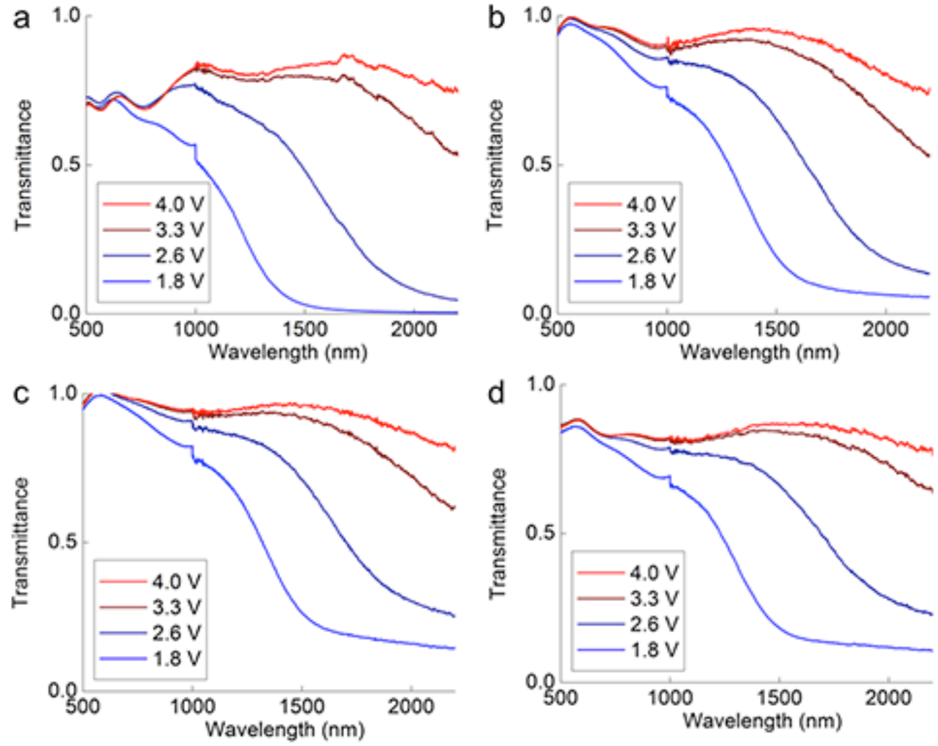

Figure 10.9. Spectroelectrochemistry of NIR-selective electrochromic ITO NC films in the presence of liquid electrolyte using separate Li foils as counter and reference electrodes: (a) ~340 nm thick, randomly packed films at ~36% overall microporosity; (b) ~300 nm thick film assembled with $PDMA_{20k}$-*b*-PS_{20k}; (c) ~390 nm thick film assembled with $PDMA_{10k}$-*b*-PS_{60k}; and (d) ~400 nm thick film assembled with $PDMA_{20k}$-*b*-PS_{60k}. Architectured ITO films (b–d) exhibited ~60% overall porosity.

Qualitatively, the extent of switching from a NIR-transmissive state to NIR-blocking state was determined by the film thickness and ITO volume fraction. Quantitatively, it was useful to compare the coloration efficiency[2] (CE) of different ITO films (Table 10.2). The unarchitectured film showed a 56 % greater change in optical density at 1750 nm for a given charge-per-unit area than the most efficient mesoporous framework, which was directly attributed to its 60 % higher ITO NC content per unit volume. Among the hierarchically porous ITO frameworks, which had similar ITO volume fractions, those assembled with the smallest block copolymer, PDMA$_{20k}$-*b*-PS$_{20k}$, exhibited the greatest CE. The architectured mesoporous ITO films showed significant modulation of the NIR portion of the solar spectrum despite their significantly lower volume fraction of NCs relative to unarchitectured films (~30 % ΔT_{NIR} for architectured vs. 37 % ΔT_{NIR} for unarchitectured films).

Table 10.2. Quantitative analysis of ITO NC-derived NIR-electrochromic electrodes immersed in propylene carbonate containing 100 mM $LiClO_4$. Separate Li foils were used as reference and counter electrodes.

	Unarchitectured	**PDMA$_{20k}$-*b*-PS$_{20k}$**	**PDMA$_{10k}$-*b*-PS$_{20k}$**	**PDMA$_{20k}$-*b*-PS$_{60k}$**
CE (cm^2 C^{-1})[a]	493	316	207	178
ΔT_{solar} (%)	18	15	14	14
ΔT_{NIR} (%)	37	30	27	27
ΔT_{lum} (%)	1	2	2	2
τ_{bleach} (s)[b]	2.22	0.98	0.92	0.92
Specific capacity ($C g^{-1}$ ITO)[b]	24.5	50.4	40.6	52.8

[a] Coloration efficiency (CE) determined by ΔOD/charge-per-unit-area at 1750 nm. [b] Determined by analysis of chronoamperometry data with voltage swings of 1.8 V and 4 V, averaged over 5 cycles.

In order to understand differences in ITO capacitive charging responsible for NIR-switching, chronoamperometry was carried out in liquid electrolyte on all films. Here, ITO active-layer electrodes were held at a constant potential, either at 1.8 V or 4.0 V vs. Li/Li^+, and current was allowed to flow until equilibrium was reached (Figure 10.10). It was possible to extract a half-life for ITO discharging (i.e., bleaching) by fitting the current decay to a simple exponential;[2] half-lives for the current decay, τ_{bleach}, are reported in Table 10.2.

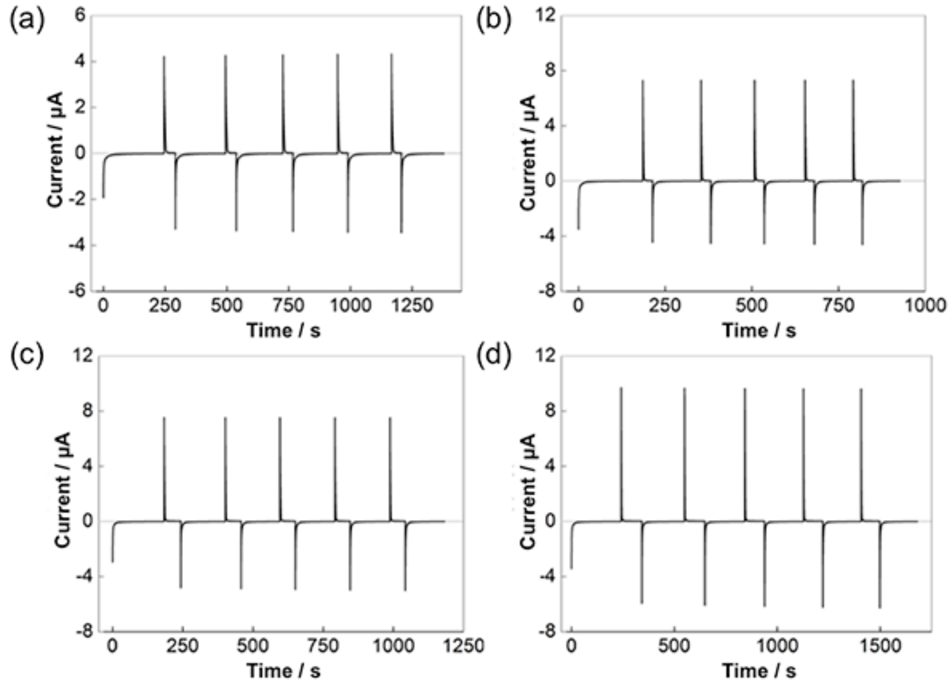

Figure 10.10. Chronoamperometry data for ITO nanocrystal films: (a) unarchitectured film; hierarchically porous films assembled using (b) PDMA$_{20k}$-*b*-PS$_{20k}$, (c) PDMA$_{10k}$-*b*-PS$_{60k}$, or (d) PDMA$_{10k}$-*b*-PS$_{60k}$ block copolymer as architecture-directing agents. A voltage swing of 1.8 and 4.0 V vs. Li/Li$^+$ was used for all films.

The switching for each of the three mesoporous ITO frameworks was faster than that observed for unarchitectured ITO film. Among different mesoporous ITO frameworks, however, there were no significant differences in τ_{bleach}. The extent of capacitive charging was calculated by integrating the chronoamperometry data and normalizing to the mass of ITO on the electrode (Table 10.2). These data further distinguished capacitive charging in architectured frameworks compared to unarchitectured ITO films. Notably, frameworks with the thickest walls gave the largest specific charging capacity measured; this capacity was nearly double that measured for unarchitectured films. For film with thinner ITO frameworks, the specific capacity was ~80% of that observed for either of the films with thicker walls. Thus, ITO utilization and charging kinetics are both significantly improved upon by simply arranging the ITO NCs into mesoporous conductive frameworks.

The responsiveness of all four types of ITO NC films to capacitive switching was further interrogated by cyclic voltammetry (CV). All films were cycled between 1.8 V and 4.0 V vs. Li/Li$^+$ at a linear scan rate of 100 mV s^{-1}, 10 mV s^{-1}, or 1 mV s^{-1}. The specific capacity was calculated by integrating the *i*–*V* curves and normalizing to the mass of ITO on the electrode. These data were reported for 4 charge/discharge cycles at each of the scan rates (Figure 10.11).

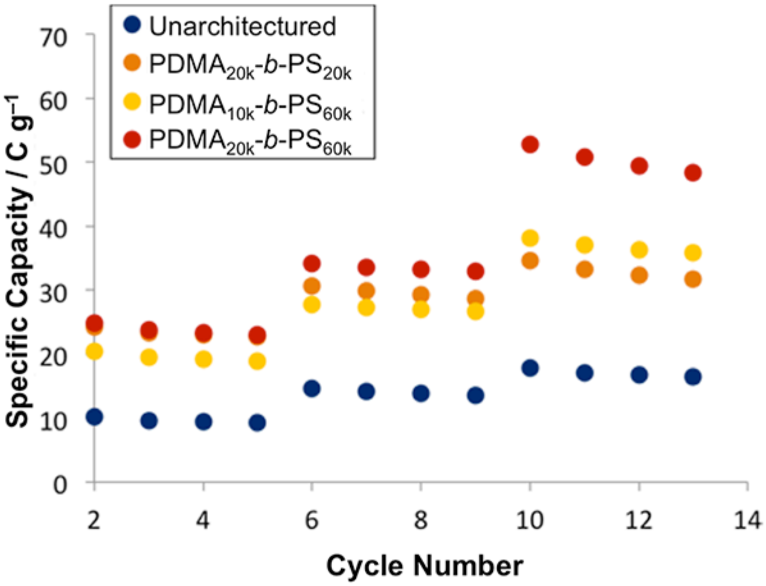

Figure 10.11. Specific capacity for ITO working electrodes in propylene carbonate containing 100 mM $LiClO_4$ extracted from cyclic voltammetry and ITO electrode mass. Data reported for cycles 2–5, 6–9, and 10–13 were obtained at linear scan rates of 100 mV s^{-1}, 10mV s^{-1}, and 1 mV s^{-1}, respectively

In all cases, the arrangement of ITO NCs into mesoporous conductive frameworks enhanced the charging current and, ultimately, the specific capacity. It was useful to consider the thermodynamic limits for capacitive charging at a specified potential, which was determined for all films using chronoamperometry. Any deviation from this thermodynamic limit would indicate kinetic limitations in ion transport imposed by the architecture's network of ITO–electrolyte interfaces and the concentration of ions in the pores. For example, the thermodynamic limit for the specific capacity of ITO frameworks derived from $PDMA_{20k}$-*b*-PS_{60k} was 52.8 C g^{-1}. The specific capacity extracted from the CV for the same film at the slowest scan rate (1 mV s^{-1}) ranged from 52.7 to 48.4 C g^{-1}; the slight decrease was ascribed to an irreversible surface Sn redox process as we have observed previously.[2] This indicated that ion transport through the hierarchically porous ITO framework was not limiting at this scan rate. By contrast, for random, close-packed ITO films, the CV-derived specific capacity was ~17 C g^{-1}, which was 69 % of the theoretical maximum determined by chronoamperometry. Thus ion transport was limiting in these microporous films, even at slow scan rates.

For the three different types of ITO frameworks the degree to which ion transport was kinetically limited depended strongly on their pore dimensions. At the slowest scan rate (1 mV s^{-1}), ITO films assembled using $PDMA_{20k}$-*b*-PS_{20k}, $PDMA_{10k}$-*b*-PS_{60k}, and $PDMA_{20k}$-*b*-PS_{60k} reached 63%, 91%, and 100% (respectively) of their theoretical specific capacity, as determined by chronoamperometry; thus, the larger pore architectures most readily approached their theoretical charging capacity. For all films, as the scan rate was increased, capacitive charging became kinetically limited by ion transport to the electrolyte–ITO interface. The extent to which capacitive charging was kinetically limited for the different hierarchically porous ITO frameworks converged at the highest scan rates to a value that exceeded that of the unarchitectured films by a factor of 2–2.5. These data point to enhanced charging kinetics in all of the hierarchically porous frameworks, suggesting that the pore structure allowed for more expedient coupling of the ion and electron transport in the multiphasic electrodes.

Given the improved ITO utilization and enhanced capacitive charging kinetics offered by nanocrystal networking into hierarchically porous frameworks, I next aimed to realize these performance gains in solid-state NIR-selective electrochromic devices, which are reported here for the first time. In order to realize this goal, two additional advances beyond developing electrode architectures were necessary: the first was identification of a suitable counter electrode; and the second was identification of a polymer electrolyte that could be configured between the working and counter electrodes in the device. With respect to the former, I was ultimately successful in using ~60 % microporous CeO_2 nanocrystal counter electrodes.[22–24] These provided suitable charge storage capacity for device switching, obviated the need for thick films that might have otherwise contributed to undesirable optical scattering, and were optically transparent across the entire spectral range of interest. With respect to the latter, we aimed for a transparent plasticized polymer electrolyte (PPE) that could be easily deposited onto both electrodes, would flow readily into the electrode pores, and would exhibit sufficient room temperature ionic conductivity as necessary for fast device switching. These criteria were fulfilled by a poly(vinyl butyral)–based PPE[27–29] that was plasticized with trimethylolpropane propoxylate (PO/OH); the PPE's room temperature ionic conductivity was determined to be ~1 x 10^{-7} S cm^{-1} using electrochemical impedance spectroscopy (Figure 10.6a).

NIR-selective electrochromic heteromaterial frameworks, where electron and ion conducting domains are reciprocally arranged in space with controllable mesoscale periodicity, were generated by first assembling bare ITO nanocrystals into hierarchically porous electrodes, as shown in Figure 10.7. For these solid-state devices, an electrode generated from $PDMA_{20k}$-*b*-PS_{20k} architecture-directing agent was tested alongside an electrode composed of unarchitectured NC film. The PPE was subsequently deposited onto the ITO-based electrode and thermally treated to relieve the film of volatile organics. The solid-state device was then configured by positioning the CeO_2 nanocrystal electrode, similarly coated with PPE, on the stack in a manner that allowed for contacts to be made to each electrode. The stack was then thermally pressed to ensure reliable interfacing. In this construction the PPE separated the ITO- and CeO_2-based electrodes by ~50 mm.

Because neither electrode was polarized prior to assembling the stack, it was necessary to perform a break-in cycle to induce charge, which was then available to switch the device repeatedly. To do so, a –4 V bias was applied across the device for a total of 6 min, which oxidized the PPE at the CeO_2 electrode and resulted in charge injection into the ITO active layer. No build-up of a solid–electrolyte interphase was anticipated due to the protic nature of both polymer and plasticizer, which allowed for the oxidation of primary and secondary alcohols at these potentials to yield protons alongside aldehydes (for PO/OH) and ketones (for PVB); local sequestration of electrochemically-generated protons at the CeO_2 surface was also likely. It was relatively straightforward to track the extent of PPE oxidation by monitoring the ITO plasmon absorption during the break-in step (Figure 10.12).

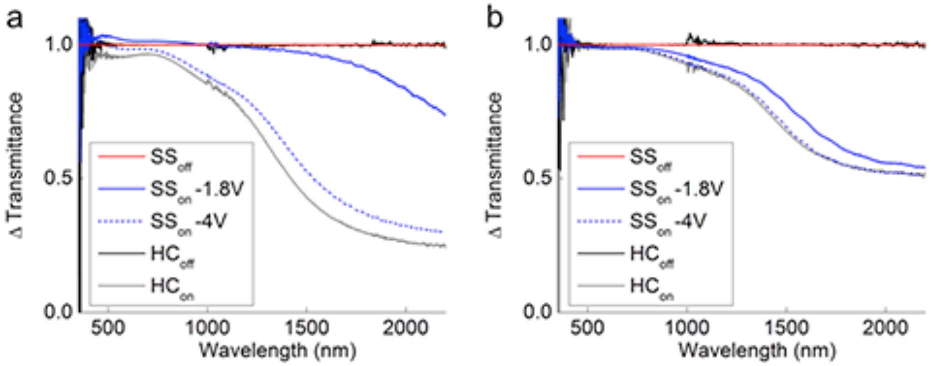

Figure 10.12. Optical modulation by NIR-selective electrochromic ITO NC electrodes, and those same electrodes in solid-state NIR-selective electrochromic devices: ~258 nm unarchitectured ITO active layers (a) are shown alongside ~309 nm hierarchically porous ITO active layers (b) generated using PDMA$_{20k}$-*b*-PS$_{20k}$ architecture-directing agents. NIR-switching of the ITO electrodes in half-cell (HC) configurations are shown for both NIR-transmissive (black) and NIR-blocking (grey) states. For solid-state (SS) devices, an initial break-in step was carried out by applying a –4 V bias across the device; ITO charging at that potential after 6 min signifies the maximum extent of NIR-blocking available to the device (dotted blue). Under normal operation, SS devices were switched between –1.8 V and +1.8 V to achieve NIR-blocking (solid blue) and NIR-transmissive (solid red) states, respectively.

Reversible NIR-switching of the solid-state devices was achieved by applying potentials that did not further degrade the PPE: specifically, +/–1.8 V was found to be adequate. When cycled at these potentials, the solid-state devices employing unarchitectured ITO active layer electrodes exhibited far more modest NIR-modulation than expected on the basis of their performance in the half-cell spectroelectrochemical measurements (Figure 10.12a). On the other hand, when solid-state devices were configured instead with the PPE–ITO electrochromic heteromaterial frameworks, the full range of NIR-modulation anticipated on the basis of half-cell measurements was achieved (Figure 10.12b). The coloration efficiency and specific capacity of these devices were more than double those of the devices assembled from unarchitectured electrodes (Table 10.3 and Figure 10.13).

Table 10.3. Quantitative analysis of ITO NC-derived NIR-electrochromic electrodes integrated into solid-state devices.

	Unarchitectured ITO	**PDMA$_{20k}$-*b*-PS$_{20k}$ architectured ITO–PPE heteromaterial frameworks**

CE (cm^2 C^{-1})[a]	210	501
ΔT_{NIR} (%)	3.8	8.3
τ_{bleach} (s)[b]	4.8	7.55
Specific capacity (C g^{-1} ITO)[b]	2.85	6.78

[a] Coloration efficiency (CE) determined by ΔOD/charge-per-unit-area at 1750 nm. [b] Determined by analysis of chronoamperometry data with voltage swings of –1.8 V and +1.8 V, averaged over 10 cycles.

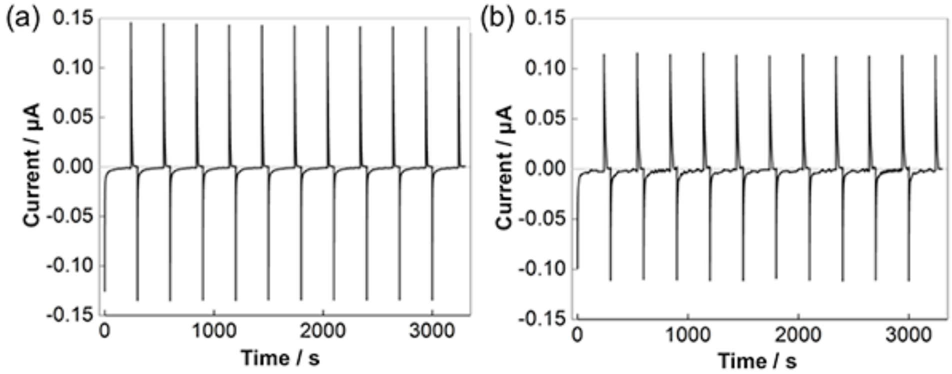

Figure 10.13. Chronoamperometry data for solid-state devices configured with NIR-switchable ITO nanocrystal electrodes: (a) unarchitectured ITO NC active layer; (b) hierarchically porous ITO framework active layer generated using PDMA$_{20k}$-*b*-PS$_{20k}$ architecture-directing agents. A two-electrode configuration was used with –1.8 and +1.8 voltage swings for 4 min and 1 min, respectively.

The specific capacity was enhanced to an even greater extent than in the liquid electrolyte (Table 10.2); both observations can be understood as originating from the mesoscopic segregation of interfaces, which reduced inefficiencies in the framework charging since there is less overlap in the EDL compared to microporous case, wherein charged interfaces are only 0.5–2 nm apart. The deeper charging achieved for the mesostructured electrodes was associated with slower charging kinetics (higher τ_{bleach}), when compared to the unarchitectured ITO-based devices; nevertheless, this switching speed is still attractive for a NIR-selective electrochromic smart window technology.

Additional insight into the coupled mesoscale charge transport phenomena in the solid-state devices was obtained by cycling the potentials between –1.8 V and +1.8 V at a linear scan rate of 100, 10, or 1 mV s^{-1} (Figure 10.14).

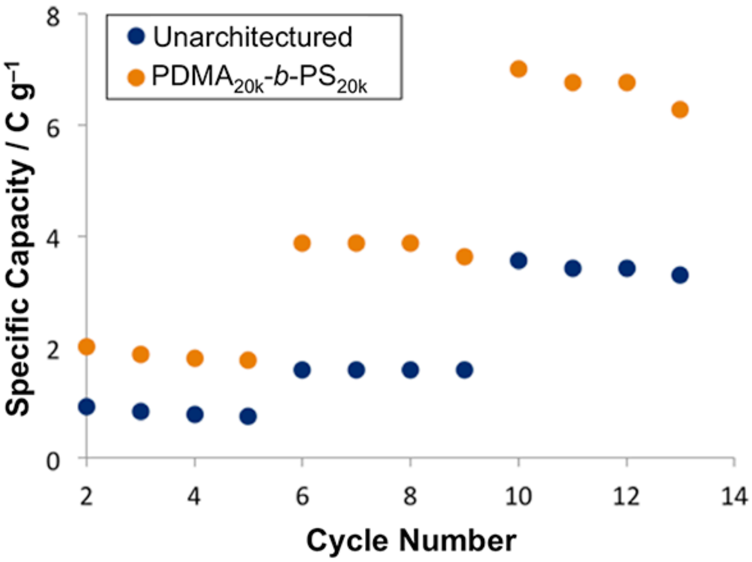

Figure 10.14. Specific capacity for ITO working electrodes in solid-state devices, extracted from cyclic voltammetry and ITO electrode mass. Data reported for cycles 2–5, 6–9, and 10–13 were obtained at linear scan rates of 100 mV s^{-1}, 10 mV s^{-1}, and 1 mV s^{-1}, respectively.

As before with the analysis of the NIR-electrochromic ITO electrodes in half-cells, the thermodynamic limits for charging capacity were, to a first approximation, indicated by the data obtained from chronoamperometry when the device was held at either −1.8 V or +1.8 V and charge was allowed to flow in the device until equilibrium was reached (Table 10.3). Indeed, at slow scan rates, both devices reached their theoretical maximum charging capacity. Both devices likewise saw significant decreases from that maximum as the scan rate was increased. For devices configured with unarchitectured, microscale-interfacing ITO–PPE electrodes, the specific capacity measured at a scan rate of 100 mV s^{-1} was only 22 % of the theoretical maximum, while for devices configured with $PDMA_{20k}$-*b*-PS-architectured ITO–PPE heteromaterial frameworks, 27 % of its theoretical maximum was reached. At all scan rates, the NIR-electrochromic ITO–PPE heteromaterial frameworks saw greater active material utilization.

10.4 Conclusions

In this chapter I showed that NIR-selective electrochromic active layers based on ITO nanocrystals, when arbitrarily deposited onto electrodes as microporous films, were limited in their capacitive switching due to overlap in electrical double layers throughout the film. This charging inefficiency was improved significantly by assembling the ITO nanocrystals into hierarchically porous and periodically ordered mesoscale frameworks. Doing so also allowed for their infiltration with an ion-conducting polymer electrolyte. These NIR-electrochromic ITO-polymer electrolyte heteromaterial frameworks represented a modular class of multiphasic electrodes featuring spatially segregated domains for ion and electron transport with definable length scales and interfacial topologies. They provided new insight into the relationship between capacitive charging kinetics and thermodynamics as it relates to the NIR-electrochromic performance in solid-state devices. We also showed that solid-state devices realize their maximum performance when heteromaterial frameworks are used as the NIR-switchable working electrode. My analysis also suggested that their deployment as a smart windows technology might require further investigation into critical mesoscale transport phenomena underpinning their basic operation.

10.5 References

1. Garcia, G.; Buonsanti, R.; Runnerstrom, E. L.; Mendelsberg, R. J.; Llordes, A.; Anders, A.; Richardson, T. J.; Milliron, D. J. "Dynamically Modulating the Surface Plasmon Resonance of Doped Semiconductor Nanocrystals" *Nano Lett.* **2011**, *11*, 4415−4420.
2. Garcia, G.; Buonsanti, R.; Llordes, A.; Runnerstrom, E. L.; Bergerud, A.; Milliron, D. J. "Near infrared Spectrally Selective Plasmonic Electrochromic Thin Films" *Adv. Opt. Mater.* **2013**, *1*, 215−220.
3. Li, S.-Y.; Niklasson, G. A.; Granqvist, C. G. "Plasmon-induced near-infrared electrochromism based on transparent conducting nanoparticles: Approximate performance limits" *Appl. Phys. Lett.* **2012**, *101*, 071903-1–071903-3.
4. DeForest, N.; Shehabi, A.; Garcia, G.; Greenblatt, J.; Masanet, E.; Lee, E. S.; Selkowitz, S.; Milliron, D. J. "Regional performance targets for transparent near-infrared switching electrochromic window glazings" *Build. Sci.* **2013**, *61*, 160–168.
5. Buonsanti, R.; Milliron, D. J. "Chemistry of Doped Colloidal Nanocrystals" *Chem. Mater.* **2013,** *25*, 1305–1371.
6. Mendelsberg, R. J.; Garcia, G.; Milliron, D. J. "Extracting reliable electronic properties from transmission spectra of indium tin oxide thin films and nanocrystal films by careful application of the Drude theory" *J. Appl. Phys.* **2012**, *111*, 063515-1–063515-9.
7. Mendelsberg, R. J.; Garcia, G.; Li, H.; Manna, L.; Milliron, D. J. "Understanding the Plasmon Resonance in Ensembles of Degenerately Doped Semiconductor Nanocrystals" *J. Phys. Chem. C* **2012**, *116*, 12226–12231.
8. Granqvist, C. G. *Handbook of Inorganic Electrochromic Materials*. Elsevier, New York, 1995. Print.
9. De Trizio, L.; Buonsanti, R.; Schimpf, A. M.; Llordes, A.; Gamelin, D. R.; Simonutti, R.; Milliron, D. J. "Nb-Doped Colloidal TiO_2 Nanocrystals with Tunable Infrared Absorption" *Chem. Mater.* **2013**, *25*, 3383–3390.
10. Buonsanti, R.; Llordes, A.; Aloni, S.; Helms, B. A.; Milliron, D. J. "Tunable Infrared Absorption and Visible Transparency of Colloidal Aluminum-Doped Zinc Oxide Nanocrystals" *Nano Lett.* **2011**, *11*, 4706−4710..
11. zum Felde, U.; Haase, M.; Weller, H. "Electrochromism of Highly Doped Nanocrystalline SnO_2:Sb" *J. Phys. Chem. B* **2000**, *104*, 9388–9395.
12. Xu, J. M.; Li, L.; Wang, S.; Ding, H. L.; Zhang, Y. X.; Li, G. H. "Influence of Sb doping on the structural and optical properties of tin oxide nanocrystals" *CrystEngComm* **2013**, *15*, 3296–3300.
13. Llordes, A.; Garcia, G.; Gazquez, J.; Milliron, D. J. "Tunable near-infrared and visible-light transmittance in nanocrystal-in-glass composites" *Nature* **2013**, *500*, 323−326.
14. Llordes, A.; Hammack, A. T.; Buonsanti, R.; Tangirala, R.; Aloni, S.; Helms, B. A.; Milliron, D. J. "Polyoxometalates and colloidal nanocrystals as building blocks for metal oxide nanocomposite films" *J. Mater. Chem.* **2011**, *21*, 11631-11638.

15. Buonsanti, R.; Pick, T. E.; Krins, N.; Richardson, T. J.; Helms, B. A.; Milliron, D. J. "Assembly of Ligand-Stripped Nanocrystals into Precisely Controlled Mesoporous Architectures" *Nano Lett.* **2012**, *12*, 3872–3877.
16. Rauda, I. E.; Buonsanti, R.; Saldarriaga-Lopez, L. C.; Benjauthrit, K.; Schelhas, L. T.; Stefik, M.; Augustyn, V.; Ko, J.; Dunn, B.; Wiesner, U.; Milliron, D. J.; Tolbert, S. H. "General Method for the Synthesis of Hierarchical Nanocrystal-Based Mesoporous Materials" *ACS Nano* **2012**, *6*, 6386–6399.
17. Rauda, I. E.; Saldarriaga-Lopez, L. C.; Helms, B. A.; Schelhas, L. T.; Membreno, D.; Milliron, D. J.; Tolbert, S. H. "Nanoporous Semiconductors Synthesized Through Polymer Templating of Ligand-Stripped CdSe Nanocrystals" *Adv. Mater.* **2013**, *25*, 1315–1322.
18. Rivest, J. B.; Buonsanti, R.; Pick, T. E.; Zhu, L.; Lim, E.; Clavero, C.; Schaible, E.; Helms, B. A.; Milliron, D. J. "Evolution of Ordered Metal Chalcogenide Architectures through Chemical Transformations" *J. Am. Chem. Soc.* **2013**, *135*, 7446–7749.
19. Milliron, D. J.; Buonsanti, R.; Llordes, A.; Helms, B. A. "Constructing Functional Mesostructured Materials from Colloidal Nanocrystal Building Blocks" *Acc. Chem. Res.* **2014**, *47*, 236–246.
20. Dong, A.; Ye, X.; Chen, J.; Kang, Y.; Gordon, T.; Kikkawa, J. M.; Murray, C. B. "A Generalized Ligand-Exchange Strategy Enabling Sequential Surface Functionalization of Colloidal Nanocrystals" *J. Am. Chem. Soc.* **2011**, *133*, 998–1006.
21. Rosen, E. L.; Buonsanti, R.; Llordes, A.; Sawvel, A. M.; Milliron, D. J.; Helms, B. A. "Exceptionally Mild Reactive Stripping of Native Ligands from Nanocrystal Surfaces by Using Meerwein's Salt" *Angew. Chem. Int. Ed.* **2012**, *51*, 684–689.
22. Bhosale, A. K.; Tarwal, N. L.; Shinde, P. S.; Kadam, P. M.; Patil, R. S.; Barman, S. R.; Patil, P. S. "Effective utilization of spray pyrolyzed CeO_2 as optically passive counter electrode for enhancing optical modulation of WO_3" *Solid State Ionics* **2009**, *180*, 1324–1331.
23. Brezesinski, T.; Wang, J.; Senter, R.; Brezesinski, K.; Dunn, B.; Tolbert, S. H. "On the Correlation between Mechanical Flexibility, Nanoscale Structure, and Charge Storage in Periodic Mesoporous CeO_2 Thin Films" *ACS Nano* **2010**, *4*, 967–977.
24. Ozer, N. "Optical properties and electrochromic characterization of sol–gel deposited ceria films" *Sol. Energy Mater. Sol. Cells* **2001**, *68*, 391–400.
25. Gilstrap Jr., R. A.; Capozzi, C. J.; Carson, C. G.; Gerhardt, R. A.; Summers, C. J. "Synthesis of a Nonagglomerated Indium Tin Oxide Nanoparticle Dispersion" *Adv. Mater.* **2008**, *20*, 4163–4166.
26. Liu, Y.; He, S.; Maeda, H. "Wet Chemical Preparation of Well-dispersed Colloidal Cerium Oxide Nanocrystals" *Chem. Lett.* **2007**, *36*, 764–765.
27. Saito, Y.; Okano, M.; Kubota, K.; Sakai, T.; Fujioka, J.; Kawakami, T. "Evaluation of Interactive Effects on the Ionic Conduction Properties of Polymer Gel Electrolytes" *J. Phys. Chem. B* **2012**, *116*, 10089–10097.

28. Li, Y.; Wang, J.; Tang, J.; Liu, Y.; He, Y. “Conductive performances of solid polymer electrolyte films based on PVB/$LiClO_4$ plasticized by PEG_{200}, PEG_{400} and PEG_{600}” *J. Power Sources* **2009**, *187*, 305–311.
29. Kraft, A.; Rottman, M.; Heckner, K.-H. “Large-area electrochromic glazing with ion-conducting PVB interlayer and two complementary electrodeposited electrochromic layers” *Sol. Energy Mater. Sol. Cells* **2006**, *90*, 469–476.
30. Largeot, C.; Portet, C.; Chmiola, J.; Taberna, P.-L.; Gogotsi, Y.; Simon, P. “Relation between the Ion Size and Pore Size for an Electric Double-Layer Capacitor” *J. Am. Chem. Soc.* **2008**, *130*, 2730–2731.
31. Brezesinski, T.; Wang, J.; Polleux, J.; Dunn, B.; Tolbert, S. H “Templated Nanocrystal-Based Porous TiO_2 Films for Next-Generation Electrochemical Capacitors” *J. Am. Chem. Soc.* **2009**, *131*, 1802–1809.

Chapter 11

Nanocomposite architecture for rapid, spectrally-selective electrochromic modulation of solar transmittance

Adapted from:

Jongwook Kim, Gary K. Ong, Yang Wang, Gabriel LeBlanc, Teresa E. Williams, Tracy M. Mattox, Brett A. Helms, and Delia J. Milliron. "Nanocomposite Architecture for Rapid, Spectrally-Selective Electrochromic Modulation of Solar Transmittance" *Nano Letters* 2015, **15**, 5574-5579.

11.1 Introduction

In principle, composite materials can combine and enhance the advantageous properties of two or more components. In practice, judicious arrangement of matter is essential to avoid deleterious interactions that can result from simple blending.[1] In nanoscale composites, structural organization takes on even greater importance as distinct physical and chemical properties can emerge from confinement and from the high density of interfaces. Significant performance gains therefore can be realized when the critical length scales and spatial relationships in nanocomposite materials are deliberately designed and fabricated, or architected, to meet a functional purpose.

Electrochemical and photochemical systems (e.g., batteries, fuel cells, photovoltaic cells, and electrochromic devices) have long been major targets for exerting control over nanoscale architecture in the effort to meet complex performance criteria, which requires coordinated and efficient transport of electrons, ions, and molecular species.[2–8] In some of the most elegant examples of architected composites, battery electrodes with both high rate capability and high capacity have been constructed by using an electronically conductive mesostructured framework to mechanically support and "wire up" an insulating, but high-capacity active material.[1,4] In these examples, the framework component is selected to mitigate a deficiency (poor electronic conductivity) of the active material. In other instances, two active materials with complementary properties have been blended to form a large interfacial area central to the material's functionality. This is the case for polymer blend photovoltaic cells, where n- and p-type semiconducting polymers transfer charge across the interface,[9,10] and for reported nanocrystal-in-glass electrochromic materials, in which the interface between near-infrared- and visible-light modulating components enhances the optical switching contrast.[11] However, the random mixing of components in active material blends can be detrimental, because transport pathways are tortuous and can contain dead ends. Such composites could benefit from more deliberate architecting of their mesoscale structure,[12] incorporating, perhaps, the use of a scaffold as the primary component to support the addition of the second component. As previously decribed in Chapter 6, colloidal nanocrystal frameworks (CNFs) provide a tunable and robust platform; choice of nano builidng material also imparts functionality. In the example elaborated in this chapter, I investigate a nanocomposite metal oxide electrochromic material that utilizes a templated mesoscale framework architecture to achieve rapid switching and unprecedented dynamic range for modulating visible (Vis) and near-infrared (NIR) transmittance.

11.2 Experimental

MATERIALS. Oleic acid, oleyl amine, tungsten(IV) chloride (WCl_4), isopropanol (iPrOH), *n*-hexanes, trimethyloxonium tetrafluoroborate (MeO_3BF_4), lithium bis(trifluoromethanesulfonyl)imide (Li-TFSI), Tetrabutylammonium bis-trifluoromethanesulfonimidate (TBA-TFSI), acetonitrile (ACN), *N,N*-dimethylformamide (DMF), propylene carbonate (PC), and tetraglyme were obtained from Aldrich and used as received. ITO-coated glass substrates (20 mm×20 mm×1.1 mm; 200 Ω sq^{-1} sheet resistance) were purchased from Diamond Coatings Limited.

NANOCRYSTALS. Decaniobate-POMs ($[Nb_{10}O_{26}]^{6-}$) were prepared as previously reported and stored in a dispersion of 1:1 $EtOH/H_2O$.[13] To prepare WO_{3-x} NCs, a mixture of oleic acid (20 mL) and oleyl amine (2 mL) was degased under vacuum at 120 ˚C for 1 h. After purging with N_2 and increasing the temperature to 300 ˚C, a dispersion of WCl_4 (340 mg) in oleic acid (4 mL) was injected. The reaction mixture quickly turned dark blue and after stirring for 10 min the reaction was cooled to room temperature. The mixture was transferred into a glove box, precipitated by adding an excess volume of iPrOH, centrifuged, and the resulting pellet was dispersed in hexane (10 mL) (Figure 11.1a).

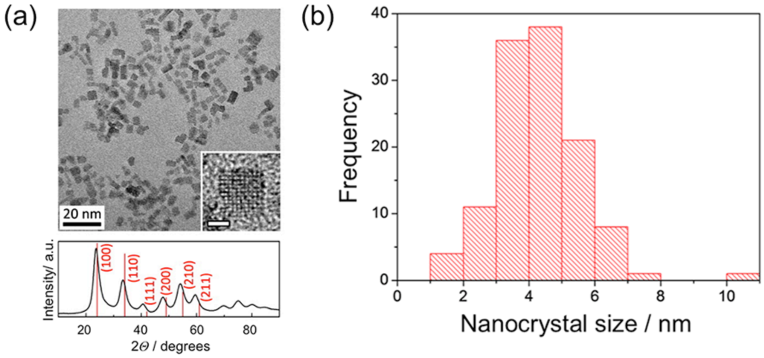

Figure 11.1. Size-distribution analysis for WO_{3-x} NCs. (a) Top: Low- and (inset) high-resolution BF-TEM images (inset scale bar = 2 nm); Bottom: X-ray diffraction pattern of the synthesized WO_{3-x} nanocrystals (black) and the reference pattern for the cubic WO_3 phase (indexed red bars; JCPDS 041−0905); (b) Histogram of the WO_{3-x} nanocrystal size distribution, manually measured from the TEM images ($d = 4.3 \pm 1.3$ nm; $n = 120$).

PREPARATION OF LIGAND-STRIPPed NANOCRYSTALS. In a typical ligand stripping,[14] a 1 mL dispersion of WO_{3-x} NCs in hexanes (10 mg mL^{-1}) was combined with 5 mL of MeO_3BF_4 dissolved in ACN (10 mg mL^{-1}) and stirred overnight. The NCs were precipitated by adding an excess volume of toluene, and then centrifuged, and the resulting pellet was dispersed in DMF.

PREPARATION OF MESOPOROUS NANAOCRYSTAL FRAMEWORKS. I synthesized polystyrene-*block*-poly(*N*,*N*-dimethylacrylamide) PS_{60k}-*b*-$PDMA_{10k}$ BCP as previously described.[15] The micelle solution was prepared by first dissolving PS_{60k}-*b*-$PDMA_{10k}$ in DMF (60 mg mL^{-1}), then combining 200 µL of ethanol with 100 µL of BCP before stirring for 16 h at ambient temperature. 100 μL of a dispersion of ligand-stripped WO_{3-x} NCs in DMF (70 mg mL^{-1}) was added and stirred for an additional 16 h at rt. Substrates were prepared by spin-coating the BCP–NC assembly onto a prepared ITO-glass substrate with a 1 s ramp to 800 rpm, then held for 1 min; 3 coatings were used to achieve desired film thicknesses. Thermal annealing to remove the BCP ADA was performed in air in a quartz tube furnace at 400 ˚C for 1 h, then cooling to rt.

NbO_x GLASS IN-FILLING. A solution of Decaniobate-POM was spin-coated at 2000 rpm on the prepared WO_{3-x} nanocrystal framework. The POM concentration (140 mg mL^{-1}) was optimized to fill the entire mesopore volume of the framework but not to leave an over-layer on the surface of the nanocrystal film (260 nm thick composite film). Thermal annealing to decompose POMs and condense into NbO_x glass was performed in air in a quartz tube furnace at 400 ˚C for 30 min, generating the interfacial pore channels.

PREPARATION OF UNARCHITECTURED, PURE WO_{3-x} NANOCRYSTAL FILMS. A dispersion of ligand-stripped WO_{3-x} NCs in DMF were deposited by spin-coating a prepared, ITO-glass substrate with a 1 s ramp to 800 rpm, then held for 1 min. Thermal annealing was performed in air in a quartz tube furnace at 400 ˚C for 1 h, then cooling to rt.

PREPARATION OF PURE, NbO_x GLASS FILMS. A solution of Decaniobate-POM (140 mg mL^{-1}) was spin-coated at 2000 rpm on a prepared, ITO-glass substrate. Thermal annealing to decompose POMs and condense into NbO_x glass was performed in air in a quartz tube furnace at 400 ˚C for 30 min.

ELECTROCHEMICAL METHODS. A homebuilt spectroelectrochemical cell installed in a nitrogen glove box was used for the electrochemical operations and the *in situ* optical measurements. The WO_{3-x}, NbO_x, and WO_{3-x}–NbO_x composite films were placed as working electrodes in the cell connected to the spectrometer and the light source with fiber–optic cables. For the standard Li^+ ion charging experiment, a three-electrode configuration with a single Li foil as counter and reference electrodes was used with 0.1 M Li-TFSI in tetraglyme as electrolyte. For the purely capacitive charging experiment, a Pt foil counter electrode and an Ag/Ag^+ reference electrode, calibrated against a Li foil reference electrode (+3.0 V), were used with 0.1M TBA-TFSI in PC to prevent Li^+ ion contamination. A Bio-logic VMP3 potentiostat was used for chronoamperometry (CA) and cyclic voltammetry (CV) studies, and the optical transmission spectra were collected in-situ. The cycling stability was measured upon CV cycling in between 1.5–4 V (*vs.* Li) with the sweep rates selected to obtain the charge capacity above 70% of the saturated values under CA in between 1.5–4 V (30 mV sec^{-1} for pure WO_{3-x}, 20 mV sec^{-1} for WO_{3-x}–NbO_x composite, and 10 mV sec sec^{-1} for pure NbO_x). The charge capacities measured during charging and discharging were identical for each cycle.

11.3 Results and Discussion

As described previously, it was established that degenerately doped metal oxide nanocrystals can effectively modulate NIR transmittance through electrochemical charging and discharging of the free electrons responsible for their localized surface plasmon resonance (LSPR) absorption.[16–18] Considering the fact that solar NIR is most intense at shorter wavelengths (i.e., 700−1300 nm) we hypothesized that nanocrystals with LSPR absorption in this spectral range would be ideal for dynamic solar control (Figure 11.2).

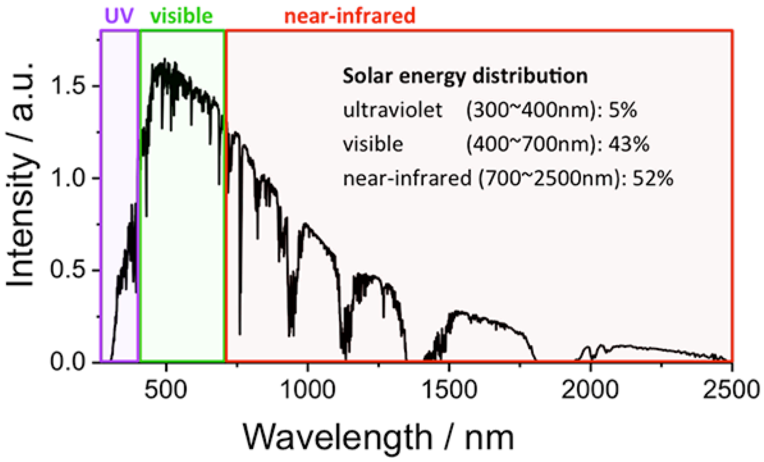

Figure 11.2. Normalized solar radiation intensity spectrum. Ultraviolet (UV), visible (Vis), and near-infrared (NIR) regions are indicated, respectively, as purple, green, and red.

To this end, WO_{3-x} NCs were selected to serve as the first active component in this new nanocomposite architecture. Both interstitially-doped and oxygen vacancy-doped tungsten oxide nanocrystals[19,20] can exhibit LSPRs at shorter wavelength than substitutionally doped transparent conducting oxides such as tin-doped indium oxide (ITO)[21−23] or aluminum-doped zinc oxide (AZO).[24] A new synthetic route for WO_{3-x} nanocrystals was developed, yielding nanocrystals with a small average size (Figure 11.1). Based on our prior work with ITO nanocrystals we expected these small nanocrystals to produce the strongest optical modulation when electrochemically charged.[16]

Examining the X-ray diffraction pattern of the WO_{3-x} nanocrystals (Figure 11.1a) showed their lattice was significantly distorted from the cubic WO_3 phase; this distortion was ascribed to a large number of oxygen vacancies, which generated a strong LSPR absorption peak centered at 875 nm in wavelength (Figure 11.3a). Traces indicate spectra acquired at, from top to bottom, 0, 1, 5, 10, 20, 30, 50, 70, 110, 150, 235, 380, and 1300 min after exposure to air. Inset pictures show the solution cuvette used for this measurement at 0, 50, and 1300 min.

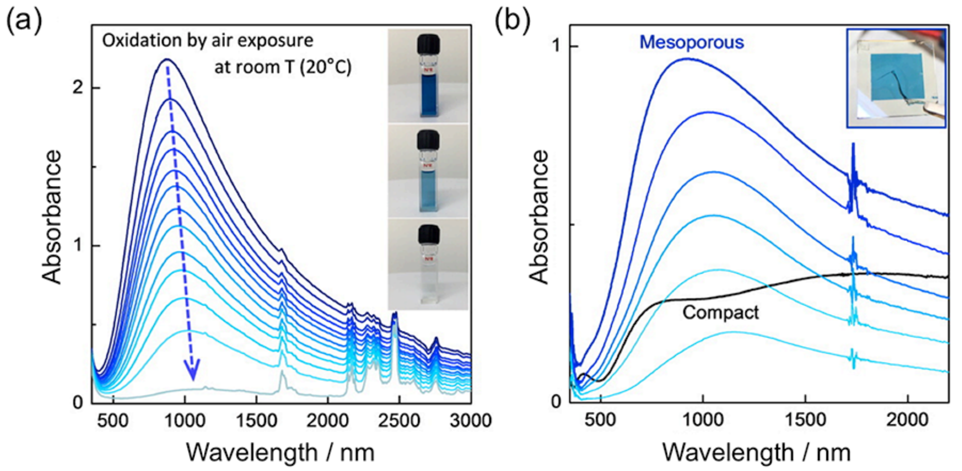

Figure 11.3. Tungsten oxide nanocrystals for NIR modulation: (a) Vis-NIR absorbance spectra of a colloidal dispersion in tetrachloroethylene: (b) electrochemically switched [*vs.* Li/Li$^+$ in 0.1 M Li-TFSI/tetraglyme] absorbance spectra of WO_{3-x} nanocrystal films on ITO coated glass. Blue lines are for a mesoporous film prepared by block copolymer templated assembly (thickness = 280 nm; porosity = 71%), showing a gradual increase of the LSPR peak with a blue-shift ($\Delta\lambda \sim 250$ nm) at different charging states. Black line is for a randomly packed film (saturated at 1.5 V) prepared with the same volume of WO_{3-x} nanocrystals per unit area (thickness = 108 nm, porosity = 28%). The inset picture shows a fully charged mesoporous film sample.

This LSPR band overlapped well with the NIR region of the solar spectrum (Figure 11.2) while maintaining relatively high Vis (390−700 nm) transparency with minor absorption in the red range. The series of LSPR spectra in Figure 11.3a showed fast oxidative decay under air exposure followed by a red-shift ($\Delta\lambda \sim 200$ nm) and finally bleaching to a fully transparent state, as indicated by the color change observed in the sample solution. This rapid environmental response was likely facilitated by the small nanocrystal size, which we hypothesized should likewise enable fast electrochemical modulation of the LSPR.[16,17]

In fact, we found that it was necessary to arrange the WO_{3-x} nanocrystals into a mesoporous framework architecture in order to realize an electrochromic response that resembled the spectral response found in solution (Figure 11.3b). To do so, WO_{3-x} NCs were assembled by means of a sacrificial micellar block copolymer (poly(*N,N*-dimethylacrylamide)-*b*-polystyrene, PDMA-*b*-PS) architecture-directing agent (ADA). As previously described, PDMA-*b*-PS BCP micelles were unique in their ability to provide access to well-ordered colloidal nanocrystal frameworks from ligand-stripped nanocrystals by assembling these components in solution, then creating a BCP-NC-composite architecture film by spin-coating.[15] After thermal removal of the BCP-ADA, the assembled framework contained densely distributed spherical mesopores visible by SEM (Figure 11.4a).

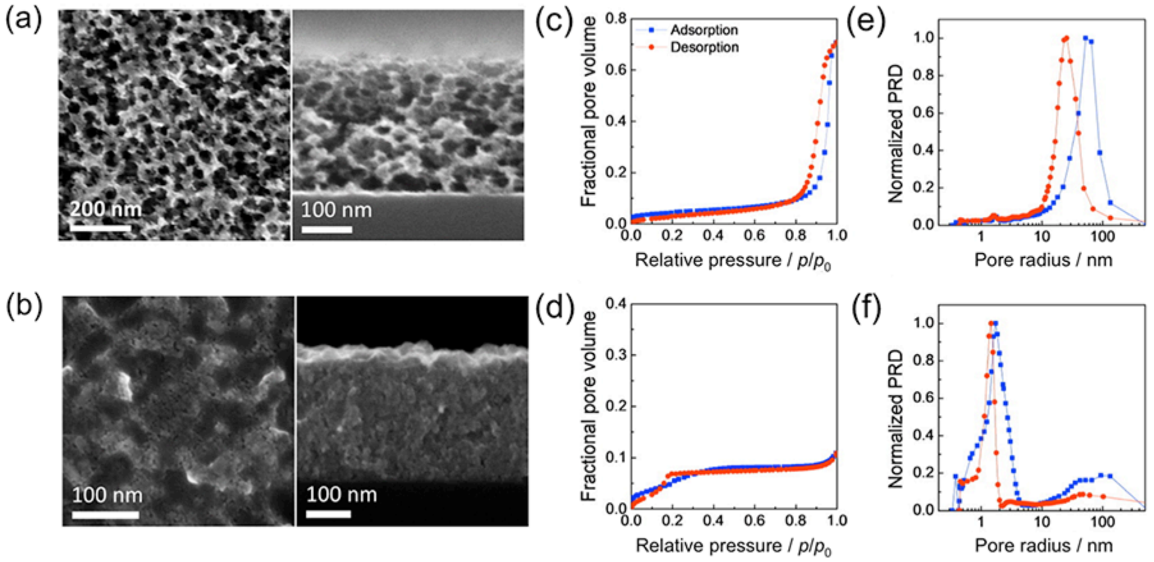

Figure 11.4. Mesoporous (WO_{3-x}) and mesostructured (WO_{3-x}–NbO_x) nanocomposite framework architectures. Scanning electron microscopy (SEM) images (left: top down; right: cross section) of: (a) mesoporous WO_{3-x} nanocrystal framework film; (b) architected composite film after in-filling with NbO_x glass. Toluene adsorption−desorption isotherms for: (c) mesoporous WO_{3-x} framework; (d) mesostructured composite. Normalized pore radius distributions (PRD) for: (e) mesoporous WO_{3-x} framework; (f) mesostructured composite.

Analysis by ellipsometric porosimetry[25] (EP) (Figure 11.4c–f, Table 11.1, and Figure 11.5a–d) revealed the mesoscale pore size and the high porosity of the mesoporous WO_{3-x} nanocrystal framework, which can be compared to a randomly packed, unarchitectured film of the same nanocrystals that has smaller pores and much lower porosity.

Table 11.1. Characteristics of Pore Networks in Electrochromic Films Characterized by Ellipsometric Porosimetry

	Porosity (%)	**Pore radius, cage (nm)**	**Pore radius, neck (nm)**
Unarchitectured WO_{x-3}	28	5.7	3.7
Mesoporous WO_{x-3}	71	53	26
Mesostructured WO_{x-3}–NbO_x	9	1.7	1.5
Pure NbO_x	0	n/a	n/a

Figure 11.5 shows EP spectra (Ψ, the amplitude ratio, and Δ, the phase difference) obtained for all four samples: randomly packed, unarchitectured WO_{3-x} nanocrystal film;

mesoporous WO_{3-x} nanocrystal framework; mesostructured WO_{3-x}–NbO_x composite film; and pure NbO_x glass film. The two extremes, $p = 0$ and $p = 1$ are shown for clarity, represented by blue circles and red circles, respectively. Also shown are their theoretically fitted lines by using Lorentz oscillator model and Cauchy dispersion law.

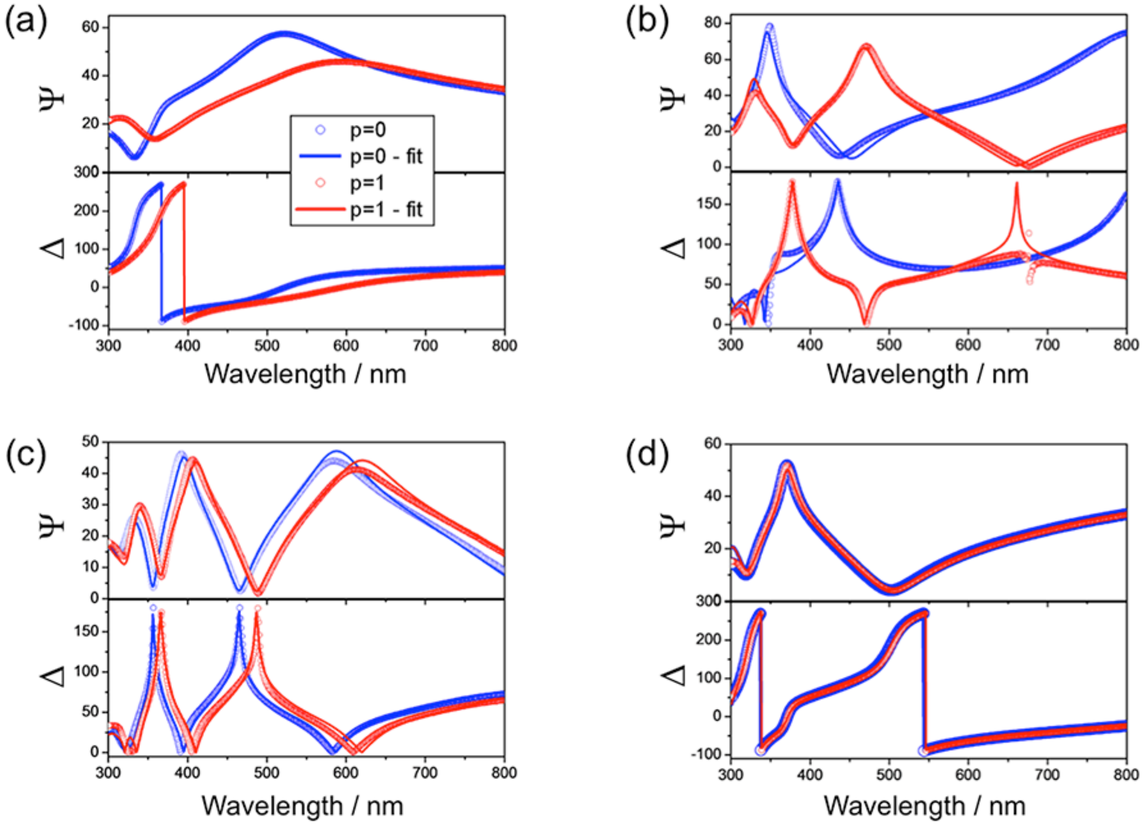

Figure 11.5. Ellipsometric porosimetry data and fitting: (a) unarchitectured WO_{3-x} nanocrystal film; (b) mesoporous WO_{3-x} nanocrystal framework; (c) mesostructured WO_{3-x}–NbO_x composite film; (d) pure NbO_x glass film.

The moderate spectral shift seen in Figure 11.5a indicated the typical moderate porosity of randomly packed nanocrystal films; the large shift in Figure 11.5b corresponded to the large porosity resulting from the block copolymer-templated mesoporous framework. The zero-shift in Figure 11.5d indicated that NbO_x glass film was compact without pores, and the small shift in Figure 11.5c, together with the pore radius distribution (Figure 11.4f) implied the efficient NbO_x in-filling and generation of the small pore channels.

When electrochemically charged with Li^+ ions, WO_{3-x} nanocrystals deposited on the working electrode (ITO-coated glass) acquired electrons as free carriers generating the LSPR. The mesoporous WO_{3-x} framework film exhibited rapid and reversible plasmonic electrochromism upon cycling (Figure 11.3b), showing spectral changes similar to those of the environmental oxidation process shown in Figure 11.3a. By contrast, a nanocrystal film made without the block copolymer showed a broad, red-shifted optical response that can be explained by strong LSPR coupling among the nanocrystals, which were densely packed in three dimensions.[26] The mesostructured film had a clear aspect without haziness in both colored and bleached states, consistent with the mesopore dimensions lying far below the visible wavelengths. The specific charge capacity of the nanocrystal framework was more than double that of a dense nanocrystal film (16.2 *vs.* 7.5 mC cm^{-2}, respectively) with the same loading, facilitating strong modulation of the LSPR.[18]

To better understand the origin of electrochromism in the mesoporous WO_{3-x} framework, a purely capacitive charging process was enforced by using an electrolyte containing bulky molecular cations (tetrabutylammonium, TBA^+), which cannot intercalate into the crystal lattice. The coloration using TBA-TFSI was 84% of that using Li-TFSI, indicating that capacitive charging can account for most of the light absorbance (Figure 11.6b). The blue trace indicates a mesoporous framework prepared by the block copolymer templated assembly (thickness = 280 nm; porosity = 71%), switched in Li-TFSI electrolyte. The red trace indicates the same sample switched in TBA–TFSI electrolyte thus in the purely capacitive regime. The black trace is for the unarchitectured WO_{3-x} film (saturated at 1.5 V) prepared with the same volume of WO_{3-x} nanocrystals per unit area (thickness = 108 nm, porosity = 28%). A high level of the capacitive contribution was similarly reported for few-nanometer diameter TiO_2 nanocrystals.[27] The strong, NIR-selective modulation obtained with plasmonic WO_{3-x} nanocrystal frameworks therefore was distinguished from the electrochromism typically found in amorphous and mixed-phase tungsten oxide films, which have a broader characteristic spectrum that may include contributions due to polaronic absorption.[28,29]

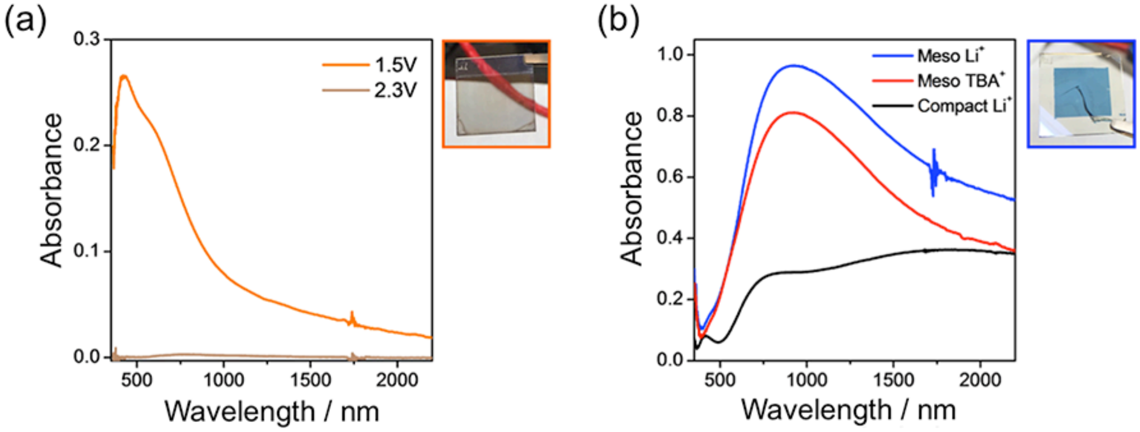

Figure 11.6. Electrochemically switched optical spectra of electrochromic films. (a) Absorbance spectra of a pure NbO_x glass film collected after saturation at 1.5 V (orange) and 2.3 V (brown) *vs.* Li reference electrode, in Li-TFSI electrolyte. The measurement was baselined with the same sample at the fully bleached state at 4 V. It is clearly shown that NbO_x does not optically switch at 2.3 V, which allows dual-band modulation in the composite film. Inset photo was taken after fully charging at 1.5 V and shows a moderate darkening of NbO_x in the visible (Vis) range. (b) Absorbance spectra of pure WO_{3-x}

nanocrystal films. Inset photo was taken after full charging (1.5 V *vs.* Li/Li$^+$) of a mesoporous film sample.

To complement the NIR optical response of the WO_{3-x} nanocrystals, a second active component, amorphous NbO_x, was selected that exhibited electrochromism mostly in the Vis range. NbO_x glass was similarly used in previous work as the visible light-modulating component of ITO nanocrystal-in-glass electrochromic composite films.[11] When NbO_x was electrochemically charged, localized polaronic states give rise to its characteristic absorption,[11,30] which increased in extinction at shorter visible wavelengths so that the film has a brown tint (Figure 11.6a). This spectrum made an ideal complement to the red-to-NIR plasmonic absorption of electrochemically charged WO_{3-x} (Figure 11.3b); together, the absorption of these two component materials covered the full spectrum of solar radiation. Thermal decomposition of the poyloxometalate (POM) cluster salt, $(NMe_4)_6[Nb_{10}O_{28}]\cdot 6H_2O$,[31] was a convenient route to electrochromic NbO_x glass, particularly as this POM is water-soluble. Optical quality films were prepared by spin-coating from aqueous ethanol (1:1 mixture) then annealing at 400 ˚C.[11]

To organize these two ideal electrochromic components–WO_{3-x} nanocrystals for NIR control and NbO_x for visible light control–into an architected nanocomposite, the mesopores of a WO_{3-x} nanocrystal framework were backfilled with POM. After annealing, an interpenetrating glass network was formed within the WO_{3-x} nanocrystal framework.[32] The mostly-dense composite was found to be 9% porous by ellipsometric porosimetry (Figure 11.4d–f and Table 1). The small mesopores detected by porosimetry (cage = 1.7 nm; neck = 1.5 nm) were seen by SEM to be open at the film surface (Figure 11.4b).

Upon electrochemical charging, the NbO_x-filled WO_{3-x} composite architecture exhibited completely independent and reversible electrochromic switching of the two metal oxide components. The transmittance spectra of the 260 nm-thick composite film revealed dual-band Vis and NIR modulation at different charging voltages (Figure 11.7a). When applying 4 V [*vs.* Li/Li$^+$], the film was transparent both in the NIR and Vis ranges ("bright mode") as both WO_{3-x} and NbO_x are fully discharged. At 2.3 V, WO_{3-x} nanocrystals were selectively charged, recovering free electrons that gave rise to LSPR absorption in the NIR range. In this "cool mode", the film blocked most transmission in the NIR range; in a typical commercial or residential window, this would reduce solar heat gain while maintaining a high Vis transmittance useful for day lighting[33] (Table 11.2). At 1.5 V, NbO_x was reduced by Li$^+$ ion intercalation, inducing polaronic absorption of Vis light, resulting in a "dark mode". The short wavelength absorption tail of the further charged WO_{3-x} also contributed to Vis (red edge) blocking in the dark mode, optimally complementing the NbOx spectrum to produce a largely neutral tint (Figure 11.7a).[34]

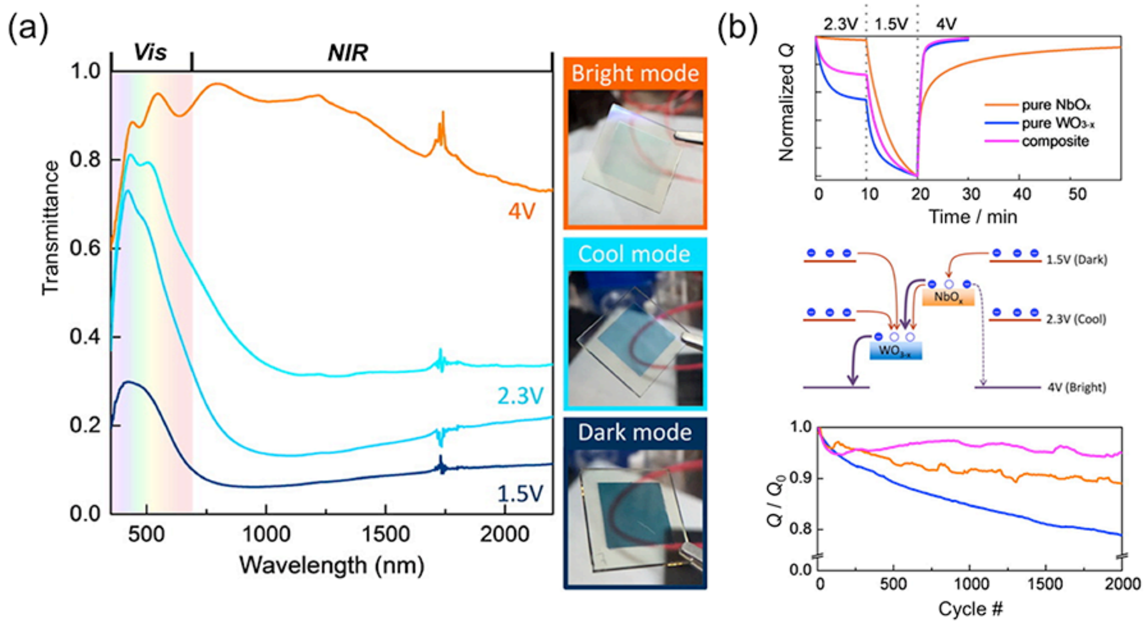

Figure 11.7. Optical and electrochemical performance of architected nanocomposite films. (a) Transmittance spectra of the 260 nm-thick WO_{3-x}–NbO_x composite film on a ITO-coated glass at different switching potentials [*vs.* Li/Li_+ in 0.1 M Li-TFSI/tetraglyme] and the corresponding photos of the sample. (b) Normalized charging profiles following potentiostatic steps for three different films: mesoporous WO_{3-x} nanocrystal framework (blue), NbO_x glass (orange), and the architected WO_{3-x}–NbO_x composite film (magenta). The discharging profile (at 4 V) of the composite film overlaps almost exactly with that of the empty WO_{3-x} framework. (c) Schematic energy diagram showing the charge flows in the architected composite at different switching potentials. Orange arrows indicate charging at 2.3 and 1.5 V. The dotted gray arrow indicates slow, direct discharging of NbO_x and the thick gray arrows indicate fast discharging of WO_{3-x} and NbO_x through WO_{3-x} according to the observed kinetics shown in (b). (d) Normalized charge capacity profiles of the same three films over 2000 cycles. Each sample was cycled by cyclic voltammetry between 1.5−4 V with a sweep rate selected to obtain a charge capacity above 70% of the saturated values under chronoamperometry at 1.5 and 4 V: (NbO_x at 10 mV s^{-1}, WO_{3-x} at 30 mV s^{-1}, and WO_{3-x}–NbO_x at 20 mV s^{-1}).

Table 11.2. Integrated solar transmittances (T) in the Vis, NIR, and total solar ranges for the architected WO_{3-x}–NbO_x composite film

Mode	T_{Vis}	T_{NIR}	T_{solar}
Bright	0.93	0.91	0.92
Cool, after 1 min	0.73	0.36	0.54
Cool, after 3 min	0.54	0.16	0.35
Dark	0.22	0.07	0.14

The color indices (CIELAB space) calculated from the dark-mode spectrum ($L^* = 54$; $a^* = -11$; $b^* = -22$) indicated a blue-gray color that was aesthetically desirable for window applications. Earlier studies on electrochromic materials have focused on single-band Vis modulation mostly achieving a limited dark mode transmittance value or poor color neutrality.[35] NIR transmission has so far been controlled most successfully with static coatings. This composite film was the first dual-band electrochromic material with an unprecedented dynamic optical range and Vis-NIR selectivity satisfying the optical performance criteria for practical energy-saving smart windows.

Despite its low 9% porosity, the architected composite was very active electrochemically and exhibited higher optical contrast than either of the component materials (Table 11.2). In the NIR, the composite achieved 2.8-fold higher contrast than a randomly packed, unarchitectured WO_{3-x} nanocrystal film and 80% of that found in the 70% porous WO_{3-x} framework (based on the integrated absorbance between λ = 450−2200 nm). Meanwhile, in the architected composite NbO_x obtained a 1.4-fold enhancement of optical contrast (absorbance at λ = 450 nm) compared to a pure NbO_x film, which may reflect structural changes to the glass network, as observed in previous work on randomly structured nanocrystal-in-glass composites.[11]

Besides this high optical contrast, the architected composite exhibited remarkably rapid switching; most notably the discharging of NbO_x was dramatically accelerated compared to pure NbO_x. It has been reported that switching time for tungsten oxide films can be reduced down to several seconds by introducing mesoporous structures.[36,37] Switching of the WO_{3-x} nanocrystal film is thus much faster than that of a compact NbO_x film (Figure 11.7b, top panel). Within the architecture, however, the spectral signature of reduced NbO_x was the first to bleach, indicating NbO_x was discharged first, followed by the WO_{3-x} component (Figure 11.8). In fact, both components could be discharged as rapidly as a pure WO_{3-x} mesoporous framework (Figure 11.7b). The fast kinetics and high optical contrast suggested efficient access by the electrolyte to the active materials in the composite architecture. We hypothesized that small mesoporous channels were effectively templated along the WO_{3-x} framework during POM decomposition. The similar neck and cage dimensions observed by ellipsometric porosimetry were consistent with the presence of a highly efficient network of porous channels that permit electrolyte access so that Li^+ ions could be transferred across all three interfaces ($WO_{3-x} \leftrightarrow NbO_x$, $WO_{3-x} \leftrightarrow$ electrolyte, $NbO_x \leftrightarrow$ electrolyte), allowing the most kinetically facile pathway to be autonomously selected. Therefore, as depicted in Figure 11.7b (middle panel), a cascade discharging of NbO_x through WO_{3-x}, rather than the slower direct discharging of NbO_x, was promoted by the mesoscale architecture.

To better understand the nature of the porous network, a composite film with the same architecture but covered with a thin, dense layer (40 nm) of pure NbO_x was fabricated and compared to the performance of a WO_{3-x}–NbO_x composite film. Ellipsometric porosimetry of a pure NbO_x film prepared from the POM revealed no apparent porosity, so this layer was considered to effectively block electrolyte access to the mesopores. Incorporating this over-layer completely changes the spectroelectrochemical characteristics of the composite, which now no longer exhibited either selective Vis-NIR modulation or fast switching, although strong optical modulation could still be observed at long times (Figure 11.8). The wide orange trace in each indicated the fully bleached, Vis- and NIR-transparent “bright mode”, with the light blue trace acquired 3 minutes after applying 2.3 V, which is the "cool mode" spectrum. The dark blue trace was acquired after 10 minutes of applying 1.5 V, which is the 'dark mode' spectrum. The thin orange traces were collected at 30 second intervals after applying 4 V from the 'dark mode'.

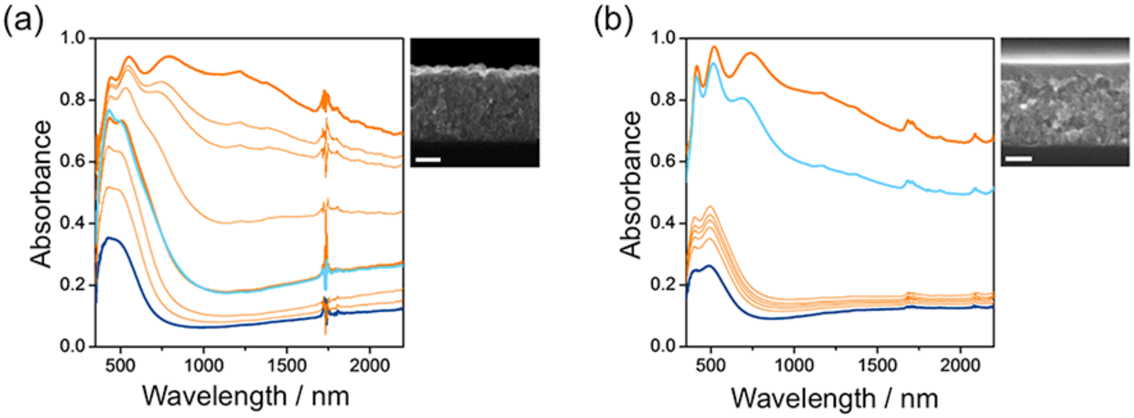

Figure 11.8. Optical switching kinetics of WO_{3-x}–NbO_x composite films: (a) evolution of transmittance spectral for the architected WO_{3-x}–NbO_x composite film, exposed at the film's surface (inset: cross-sectional SEM; scale bar = 100 nm); (b) evolution of transmittance spectral for the architected WO_{3-x}–NbO_x composite film, coated with 40 nm-thick NbO_x on the film's surface (inset: cross-sectional SEM; scale bar = 100 nm).

For the WO_{3-x}–NbO_x composite films exposed at the surface, the fast bleaching in the Vis range, thus fast discharging of NbO_x, turned the film back to the 'cool mode' within 90 seconds and a followed fast discharging of WO_{3-x} allowed a full bleaching to the 'bright mode' in another two minutes (Figure 11.8a). On the contrary, for the NbO_x-coated composite film, 'cool mode' performance was poor because WO_{3-x}–now covered with NbO_x– could not be switched independently (Figure 11.8b). When applying 1.5 V, the transmittance in Vis and NIR ranges decreased simultaneously as both WO_{3-x} and NbO_x were charged together. The slow kinetics were especially apparent for discharging; it took ~10 hours to fully bleach this sample back to the 'bright mode' while constantly applying 4 V because the overlayer of NbO_x effectively generated a barrier for ion extraction from the WO_{3-x}.

Other methods for in-filling of a mesoporous framework, such as atomic layer deposition,[38] typically result in conformal coatings and core−shell structures, as the affinity of the two components was a prerequisite for deposition. The trade-off between electrochemical activity and the pore-filling ratio was thought to be inevitable. My result suggests this hurdle can be overcome by introducing interface-sharing pore channels, which are produced in this work by a straightforward glass condensation process. As an added advantage, the electrochemical instability of the WO_{3-x} nanocrystal film was also mitigated, as evaluated by a cycling durability test. Only 5.7% of the charge capacity of the architected composite was lost after 2000 cycles, whereas single component WO_{3-x} and NbOx films lost 21% and 11%, respectively (Figure11.7b, bottom panel). This difference may result from the composite architecture being mechanically robust compared to the potentially degradable morphology of the unsupported nanocrystal framework.

11.4 Conclusions

In summary, I showed that every aspect of the nanocomposite architecture contributed to its electrochemical efficiency. Having been effectively templated by the WO_{3-x} framework, the pore channels formed an open network permitting the infiltration of the electrolyte to be in contact with both WO_{3-x} and NbO_x, so that each component could be switched independently *via* electrochemical charging and discharging. Ion intercalation depth was also reduced to the size of the WO_{3-x} nanocrystals and the size of the NbO_x mesodomains, as determined by the periodicity of the framework; this scaling could minimize the switching time. Furthermore, the coexistence of the pore channels with the covalently linked WO_{3-x}−NbO_x heterointerface established a redox cascade based on the relative alignment of the redox potentials, which favorably enhanced the charging and discharging kinetics. The optical dynamic ranges of both active components were enhanced by the designer architecture. The results demonstrated here not only represented a practical dual-band electrochromic performance for energy-saving smart windows but also exemplified a broadly applicable approach toward constructing highly functional electrochemical materials (e.g., batteries, supercapacitors, and solar cells) by a synergistic arrangement of multiple components and their interfaces at the mesoscopic scale.

11.5 References

1. Munch, E.; Launey, M. E.; Alsem, D. H.; Saiz, E.; Tomsia, A. P.; Ritchie, R. O. "Tough, bio-inspired hybrid materials" *Science* **2008**, *322*, 1516−1520.
2. Ji, X.; Lee, K. T.; Nazar, L. F. "A highly ordered nanostructured carbon-sulphur cathode for lithium-sulphur batteries" *Nat. Mater.* **2009**, *8*, 500−506.
3. Zheng, G.; Yang, Y.; Cha, J. J.; Hong, S. S.; Cui, Y. "Hollow carbon nanofiber-encapsulated sulfur cathodes for high specific capacity rechargeable lithium batteries" *Nano Lett.* **2011**, *11*, 4462−4467.
4. Liu, N.; Lu, Z.; Zhao, J.; McDowell, M. T.; Lee, H.-W.; Zhao, W.; Cui, Y. "A pomegranate-inspired nanoscale design for large-volume-change lithium battery anodes" *Nat. Nanotechnol.* **2014**, *9*, 187−192.
5. Zhang, H.; Yu, X.; Braun, P. V. "Three-dimensional bicontinuous ultrafast-charge and -discharge bulk battery electrodes" *Nat. Nanotechnol.* **2011***, 6*, 277−281.
6. Zukalová, M.; Zukal, A.; Kavan, L.; Nazeeruddin, M. K.; Liska, P.; Grätzel, M. "Organized Mesoporous TiO2 Films Exhibiting Greatly Enhanced Performance in Dye-Sensitized Solar Cells" *Nano Lett.* **2005**, *5*, 1789−1792.
7. Scherer, M. R. J.; Steiner, U. "Efficient Electrochromic Devices Made from 3D Nanotubular Gyroid Networks" *Nano Lett*. **2013**, *13*, 3005−3010.
8. Choi, S. Y.; Mamak, M.; Coombs, N.; Chopra, N.; Ozin, G. A. "Electrochromic Performance of Viologen-Modified Periodic Mesoporous Nanocrystalline Anatase Electrodes" *Nano Lett.* **2004***, 4*, 1231−1235.
9. Yu, G.; Gao, J.; Hummelen, J. C.; Wudl, F.; Heeger, A. J. "Polymer Photovoltaic Cells: Enhanced Efficiencies via a Network of Internal Donor-Acceptor Heterojunctions" *Science* **1995**, *270*, 1789−1791.
10. Halls, J. J. M.; Walsh, C. A.; Greenham, N. C.; Marseglia, E. A.; Friend, R. H.; Moratti, S. C.; Holmes, A. B. "Efficient photodiodes from interpenetrating polymer networks" *Nature* **1995**, *376*, 498− 500.
11. Llordes, A.; Garcia, G.; Gazquez, J.; Milliron, D. J. "Tunable near-infrared and visible-light transmittance in nanocrystal-in-glass composites" *Nature* **2013**, *500*, 323−326.
12. Li, G.; Shrotriya, V.; Huang, J.; Yao, Y.; Moriarty, T.; Emery, K.; Yang, Y. "High-efficiency solution processable polymer photovoltaic cells by self-organization of polymer blends" *Nat. Mater.* **2005**, *4*, 864−868.
13. Llordes, A.; Hammack, A. T.; Buonsanti, R.; Tangirala, R.; Aloni, S.; Helms, B. A.; Milliron, D. J. "Polyoxometalates and colloidal nanocrystals as building blocks for metal oxide nanocomposite films" *J. Mater. Chem.* **2011**, *21*, 11631-11638.
14. Rosen, E. L.; Buonsanti, R.; Llordes, A.; Sawvel, A. M.; Milliron, D. J.; Helms, B. A. "Exceptionally Mild Reactive Stripping of Native Ligands from Nanocrystal Surfaces by Using Meerwein's Salt" *Angew. Chem. Int. Ed.* **2012**, *51*, 684–689.
15. Buonsanti, R.; Pick, T. E.; Krins, N.; Richardson, T. J.; Helms, B. A.; Milliron, D. J. "Assembly of Ligand-Stripped Nanocrystals into Precisely Controlled Mesoporous Architectures" *Nano Lett*. **2012**, *12*, 3872–3877.

16. Garcia, G.; Buonsanti, R.; Runnerstrom, E. L.; Mendelsberg, R. J.; Llordes, A.; Anders, A.; Richardson, T. J.; Milliron, D. J. "Dynamically Modulating the Surface Plasmon Resonance of Doped Semiconductor Nanocrystals" *Nano Lett.* **2011**, *11*, 4415−4420.
17. Garcia, G.; Buonsanti, R.; Llordes, A.; Runnerstrom, E. L.; Bergerud, A.; Milliron, D. J. "Near infrared Spectrally Selective Plasmonic Electrochromic Thin Films" *Adv. Opt. Mater.* **2013**, *1*, 215−220.
18. Williams, T. E.; Chang, C. M.; Rosen, E. L.; Garcia, G.; Runnerstrom, E. L.; Williams, B. L.; Koo, B.; Buonsanti, R.; Milliron, D. J.; Helms, B. A. "NIR-Selective Electrochromic Heteromaterial Frameworks: a Platform to Understand Mesoscale Transport Phenomena in Solid-State Electrochemical Devices" *J. Mater. Chem. C* **2014**, *2*, 3328−3335.
19. Manthiram, K.; Alivisatos, A. P. "Tunable Localized Surface Plasmon Resonances in Tungsten Oxide Nanocrystals" *J. Am. Chem. Soc.* **2012**, *134*, 3995−3998.
20. Mattox, T. M.; Bergerud, A.; Agrawal, A.; Milliron, D. J. "Influence of Shape on the Surface Plasmon Resonance of Tungsten Bronze Nanocrystals" *Chem. Mater.* **2014**, *26*, 1779−1784.
21. Choi, S.-I.; Nam, K. M.; Park, B. K.; Seo, W. S.; Park, J. T. "Preparation and Optical Properties of Colloidal, Monodisperse, and Highly Crystalline ITO Nanoparticles" *Chem. Mater.* **2008**, *20*, 2609−2611.
22. Kanehara, M.; Koike, H.; Yoshinaga, T.; Teranishi, T. "Indium Tin Oxide Nanoparticles with Compositionally Tunable Surface Plasmon Resonance Frequencies in the Near-IR Region" *J. Am. Chem. Soc.* **2009**, *131*, 17736−17737.
23. Lounis, S. D.; Runnerstrom, E. L.; Bergerud, A.; Nordlund, D.; Milliron, D. J. "Influence of Dopant Distribution on the Plasmonic Properties of Indium Tin Oxide Nanocrystals" *J. Am. Chem. Soc.* **2014**, *136*, 7110−7116.
24. Buonsanti, R.; Llordes, A.; Aloni, S.; Helms, B. A.; Milliron, D. J. "Tunable Infrared Absorption and Visible Transparency of Colloidal Aluminum-Doped Zinc Oxide Nanocrystals" *Nano Lett.* **2011**, *11*, 4706−4710.
25. Baklanov, M. R.; Mogilnikov, K. P.; Polovinkin, V. G.; Dultsev, F. N. "Determination of pore size distribution in thin films by ellipsometric porosimetry" *J. Vac. Sci. Technol., B: Microelectron. Process. Phenom.* **2000**, *18*, 1385−1391.
26. Agrawal, A.; Kriegel, I.; Milliron, D. J. "Shape-Dependent Field Enhancement and Plasmon Resonance of Oxide Nanocrystals" *J. Phys. Chem. C* **2015**, *119*, 6227−6238.
27. Wang, J.; Polleux, J.; Lim, J.; Dunn, B. "Pseudocapacitive Contributions to Electrochemical Energy Storage in TiO_2 (Anatase) Nanoparticles" *J. Phys. Chem. C* **2007**, *111*, 14925−14931.
28. Granqvist, C. G. "Electrochromic Tungsten Oxide Films: Review of Progress 1993–1998" *Sol. Energy Mater. Sol. Cells* **2000**, *60*, 201−262.
29. Niklasson, G. A.; Granqvist, C. G. "Electrochromics for smart windows: thin films of tungsten oxide and nickel oxide, and devices based on these" *J. Mater. Chem.* **2007**, *17*, 127−156.

30. Özer, N.; Rubin, M. D.; Lampert, C. M. “Optical and electrochemical characteristics of niobium oxide films prepared by sol-gel process and magnetron sputtering A comparison” *Sol. Energy Mater. Sol. Cells* **1996**, *40*, 285−296.
31. Villa, E. M.; Ohlin, C. A.; Balogh, E.; Anderson, T. M.; Nyman, M. D.; Casey, W. H. “Reaction Dynamics of the Decaniobate Ion $[H_xNb_{10}O_{28}]^{(6-x)-}$ in Water” *Angew. Chem.* **2008**, *120*, 4922−4924.
32. Llordes, A.; Hammack, A. T.; Buonsanti, R.; Tangirala, R.; Aloni, S.; Helms, B. A.; Milliron, D. J. “Polyoxometalates and colloidal nanocrystals as building blocks for metal oxide nanocomposite films” *J. Mater. Chem.* **2011**, *21*, 11631−11638.
33. DeForest, N.; Shehabi, A.; Garcia, G.; Greenblatt, J.; Masanet, E.; Lee, E. S.; Selkowitz, S.; Milliron, D. J. “Regional performance targets for transparent near-infrared switching electrochromic window glazings” *Build. Environ.* **2013**, *61*, 160−168.
34. Beaujuge, P. M.; Ellinger, S.; Reynolds, J. R. “The donor–acceptor approach allows a black-to-transmissive switching polymeric electrochrome” *Nat. Mater.* **2008**, *7*, 795−799.
35. Granqvist, C. G. “Electrochromics for smart windows: Oxide-based thin films and devices” *Thin Solid Films* **2014**, *564*, 1−38.
36. Ozkan, E.; Lee, S.-H.; Liu, P.; Tracy, C. E.; Tepehan, F. Z.; Pitts, J. R.; Deb, S. K. “Electrochromic and optical properties of mesoporous tungsten oxide films” *Solid State Ionics* **2002**, *149*, 139−146.
37. Deepa, M.; Srivastava, A. K.; Sood, K. N.; Agnihotry, S. A. “Nanostructured mesoporous tungsten oxide films with fast kinetics for electrochromic smart windows” *Nanotechnology* **2006**, *17*, 2625–2630.
38. George, S. M. “Atomic Layer Deposition: An Overview” *Chem. Rev.* **2010,** *110,* 111−131.

Conclusions and outlook

This dissertation focused on investigating the interactions between polymeric materials and colloidally synthesized nanocrystals in order to gain insight into controlling their assembly into higher-order architectures. Through solution-phase chemistry techniques each class of material was shown to be highly tunable (e.g., composition, size, shape), which allowed for the ability to impart unique functionality to their composite structures and a broader range of application space for device fabrication. Of particular note was the application of these techniques for the development of novel device architectures that incorporated mesoscale porosity into electrodes for energy storage/efficiency devices.

The interface between polymeric (i.e., soft) and nanocrystal (i.e., hard) materials was shown here to be a key factor in determining assembly outcomes. Thus, my investigation into how to impart aqueous dispersibility to ligand-stripped nanocrystals leveraged their cationic surfaces into the design of polymeric materials used to 'wrap' the nanocrystal and allow for transfer into water. New insight was gained into interactions between organic materials and open coordination sites on nanocrystal surfaces while maintaining the nanocrystal's original electronic properties. Though a range of PEO-based polymers were demonstrated in this work, further investigation into other side-chains or incorporation of additional functionality to the polymer backbone could lead to more advanced bio-based applications such as imaging, sensing, or drug delivery through choice of nanocrystal component.

It was the discovery that cationic nanocrystal surfaces formed stable, dative-type coordination with *N,N*-dimethylformamide (DMF) that led to the discovery of poly(*N,N*-dimethylacrylamide)-*block*-polystyrene (PDMA-*b*-PS) as a new class of architecture-directing agent (ADA) for the preparation of colloidal nanocrystal frameworks. With its DMF-like polymer backbone, I determined that stable assemblies were achievable through favorable energetic interactions between ligand-stripped nanocrystals and the PDMA corona of PDMA-*b*-PS micelles. I investigated facile solution deposition techniques (e.g., spin casting, dip coating, and drop casting) for a wide range of nanocrystal sizes and types, with a chemical-free thermal anneal removing all organic materials and revealing the desired porous framework. Through my experiments, the insight gained into the energetic interactions responsible for the assembly between these two chemically disparate materials ultimately led to the development of a simple procedure scaling across materials systems and allowing for a high degree of synthetic and structural tunability in the resulting architectures.

To further understand their assembly outcomes I investigated local and long-range order as a function of both nanocrystal size and loading, using varying polymer block sizes of PDMA-*b*-PS. One challenge was how best to make use of the large and varied amount of information gained from characterization by X-ray scattering and electron imaging. Here I applied novel mathematical and image analysis techniques to quantitatively assess framework architectures, thereby validating qualitative assessments of order, segmentation of phases, and pore structure. I developed tools for a quantitative description of order-to-disorder for frameworks generated from a range of nanocrystal loadings and identified the minimum volume fraction required to form stable, ordered architectures. This analysis could ultimately find impact in lower in materials costs for researchers looking to implement nanocrystal-based porous electrodes into next generation devices.

The fabrication of an all solid-state electrochromic device in which the active layer was composed of precisely-arranged tin-doped indium oxide nanocrystals was the proof of concept experiment to demonstrate the functionality imparted by a colloidal nanocrystal framework *vs*. a random closed packed active layer. A significant challenge in fabricating devices from these types of random arrangements of nano building units is trying to overcome mass or ion transport bottlenecks that occur due to significant overlap of the electrical double layer. My experiments showed greater than a two-fold increase in both specific capacity and coloration efficiency for a colloidal nanocrystal framework-based solid-state device, proving that active material utilization and charging kinetics were greatly improved by arranging nanocrystals into a precise film architecture. Additionally, demonstrating the ability to backfill pores with a secondary active material imparted even greater functionality to the device with its ability to independently modulate not only near-IR but also visible light. These discoveries could lead to a new generation of energy saving window technologies based upon solution phase chemistry and deposition techniques.

I envision several opportunities for future work based upon the synthesis and characterization techniques I developed in this dissertation. Firstly, forming assemblies from BCP micelles and two distinct types of NC materials–either different sizes or shapes–can allow for an interesting fundamental study on determining the placement of each material at the corona of the micelle and, ultimately, within the framework. This can lead to the ability to further tailor choice of nano building unit to form more advanced composite materials for a broader range of device applications. Secondly, the image analysis techniques described for 2–D SEM images of colloidal nanocrystal frameworks can find use in analyzing 3–D representations of the same, generated from STEM tomography. Of interest from this analysis would be the determination of pore structure and NC placement throughout the entire thickness of the film. In taking both ideas forward, my hope is that microscopy can be a useful tool to inform on how to describe and characterize assembly fundamentals as chemically disparate materials interface and discriminate by type, size or shape.